Sede Amministrativa: UNIVERSITÀ DEGLI STUDI DI PADOVA
Dipartimento di Fisica e Astronomia “Galileo Galilei”

SCUOLA DI DOTTORATO DI RICERCA IN ASTRONOMIA
CICLO XXXI

Observations of young stars to understand how planets form

Tesi redatta con il contributo finanziario
dell’Istituto Nazionale di Astrofisica

Direttore della scuola: Ch.mo Prof. Giampaolo Piotto
Supervisore: Dr. Raffaele Gratton
Co-supervisore: Dr. Serena Benatti

Valutatori Esterni:

Prof. Artie Hatzes
Prof. Francesco Pepe

Dottoranda: Ilaria Carleo

Sommario

Prima della scoperta dei pianeti extrasolari, il nostro Sistema Solare era l'unico esempio conosciuto di sistema planetario e per spiegare le sue proprietà fu elaborata una teoria di formazione che prevedeva la nascita della stella da una nube di gas e polvere, e la formazione di un disco circumstellare. Nelle regioni piú esterne, dove le zone di formazione sono estese e i materiali ghiacciati sono abbondanti, i nuclei rocciosi crescono velocemente e attirano gas formando un'atmosfera. Nelle regioni piú interne, invece, le zone di formazione sono piú piccole, i materiali ghiacciati assenti e i nuclei rocciosi non riescono ad accrescere gas, essendo piú piccoli. Dunque, questo scenario di formazione planetaria prevede pianeti rocciosi all'interno e pianeti gassosi all'esterno.

La scoperta del primo pianeta Gioviano caldo (ovvero pianeti extrasolari giganti con periodi orbitali minori-uguali di $\sim$ 10 giorni), 51 Peg b (Mayor & Queloz, 1995), che orbita intorno alla sua stella con un periodo dieci volte minore ($P = 4.23$ giorni) del periodo Mercurio intorno al Sole, ha messo a dura prova le nostre assunzioni sulla formazione planetaria, ponendo molti dubbi anche sulla formazione del nostro Sistema Solare. Inoltre, le successive scoperte che hanno rivelato una straordinaria diversificazione nelle proprietà degli esopianeti, hanno dimostrato chiaramente che le caratteristiche del Sistema Solare rappresentano solo una di tante combinazioni possibili.

Tutto ciò ha comportato un accresciuto interesse nel campo della scoperta e caratterizzazione dei pianeti extrasolari. Sono state sviluppate diverse teorie per spiegare le origini e le proprietà dei Gioviani caldi. Queste si dividono in tre classi principali: *a*) *formazione in situ* (Boss, 1995), per cui un pianeta si forma vicino alla propria stella e la sua orbita rimane invariata; *b*) *migrazione nel disco* (Lin & Papaloizou, 1986),che prevede la formazione di un pianeta lontano dalla stella, poi, con la successiva migrazione all'interno del disco protoplanetario, l'orbita del pianeta diminuisce da molte Unità Astronomiche (UA) a centesimi di un UA; *c*) *migrazione mareale ad alta eccentricità* (Wu & Murray, 2003), in cui il pianeta viene sbalzato in un'orbita molto eccentrica a causa di interazioni con un altro pianeta o un compagno stellare distante, e successivamente l'orbita viene circolarizzata per effetto mareale. Nella Sezione 1.2 vengono descritte in dettaglio queste teorie di formazione.

Osservare stelle giovani (stelle di sequenza principale, PMS) sta diventando sempre piú importante in questo contesto, poiché danno la grande opportunità di studiare i sistemi planetari nelle loro prime fasi di formazione e ciò permette di testare i modelli di evoluzione dei pianeti (Sezione 1.3). Il metodo delle velocità radiali (RV) è il piú adatto ad identificare pianeti con orbite strette come i Gioviani caldi. Altri metodi sono meno adatti, infatti l'imaging diretto puó solo rivelare pianeti a grande distanza dalla stella, mentre il metodo dei transiti riduce il campione a causa della sua bassa statistica (solo un pianeta su 10 transita), ma le missioni spaziali attuali e future possono avere un contributo cruciale per questo studio. Inoltre, GAIA puó fornire tra qualche anno dati molto utili, come le soluzioni orbitali. Dettagli sui metodi per la ricerca di esopianeti e le rispettive sensibilità sono discussi nella Sezione 1.1.

Sfortunatamente, le stelle giovani sono molto attive e le osservazioni sono rese complicate dalle macchie stellari, i getti, l'accrescimento e dischi circumstellari. Il forte campo magnetico di queste stelle induce variazioni intrinseche di RV con ampiezze simili o maggiori al segnale Kepleriano, dunque l'attività stellare puó mimare o coprire la presenza di un compagno. Per questo motivo un'indagine con il metodo delle RV ha successo solo se caratterizzata dalla capacità di distinguere tra segnale indotto dall'attività e segnale indotto da un pianeta. Negli ultimi anni sono state sviluppate molte tecniche per affrontare il problema del rumore stellare

(Dumusque et al., 2017). Qui elenco i metodi piú usati: *a*) *La correlazione tra il Bisettore (BIS) e le RV* (Hatzes et al., 1997) permette di capire la variabilità del profilo delle righe spettrali dovuta all'attività stellare. Queloz et al. (2001) ha trovato una forte anti-correlazione tra RV e BIS quando la variazione di RV è dovuta all'attività. La mancanza di tale correlazione va fortemente a favore dell'origine planetaria della modulazione di RV, ma puó non essere trovata alcuna correlazione se le righe d'assorbimento non sono spettroscopicamente risolte; *b*) *Altri indici d'attività* possono essere l'emissione delle righe del Calcio II H e K o H_α. Queste righe sono molto utili quando si studia la correlazione tra le RV e la loro emissione, soprattutto nella banda visibile; *c*) *Le osservazioni multi-banda* sono un potente strumento per superare il limite imposto dall'attivitá stellare. In particolare, accoppiare osservazioni nel vicino infrarosso e nel visibile permette di separare quasi immediatamente il contributo dovuto all'attivitá, poiché il jitter delle RV dovuto all'attività è ridotto nell'infrarosso rispetto alla banda visibile, mentre la variazione di RV dovuta a un moto Kepleriano non dipende dalla lunghezza d'onda; *d*) *I Processi Gaussiani (GP)* (Haywood et al., 2014) consistono in una tecnica Bayesiana capace di mitigare il rumore correlato in un insieme di misure, come l'attività stellare nei dati RV. Questo metodo modella l'attività ed aiuta a separare il suo contributo dal segnale planetario. I GP sono molto utili ed efficaci quando il campione di dati è molto grande (centinaia di punti).

Una descrizione piú dettagliata sui metodi usati per modellare l'attività stellare é descritta nella Sezione 1.3.1.

La spettroscopia multi-banda simultanea è stata valutata da GAPS2.0, una collaborazione costituita dalla maggior parte della comunità esoplanetaria Italiana, portando alla realizzazione di GIARPS tra il 2014 e il 2017, che permette di osservare simultaneamente con HARPS − N nella banda visibile e GIANO − B nella banda infrarossa. Nel Capitolo 2 viene descritto in dettaglio il progetto GIARPS. Lo scopo scientifico di GAPS2.0 è quello di esplorare il campo della formazione ed evoluzione planetaria con enfasi sulle regioni interne dei sistemi planetari, osservando stelle giovani a diverse età e identificando e caratterizzando i loro pianeti. Dalle proprietà esoplanetarie osservabili (parametri orbitali, frequenza dipendente dall'età, composizione atmosferica) è possibile capire i processi fisici che sono responsabili della generazione di Gioviani caldi.

Un programma pilota, effettuato nell'Autunno-Inverno del 2017, ci ha permesso di testare la metodologia multi-banda e di ottimizzare la strategia per la rimozione del segnale dovuto all'attività. Questo lavoro di dottorato riguarda l'analisi di alcuni casi di Gioviani caldi pubblicati in letteratura. Sono state fatte osservazioni di queste stelle con la modalità GIARPS sia durante il programma pilota che durante i primi mesi del Large Program iniziato ad Aprile 2018. I primi risultati sono discussi nel Capitolo 3 e mostrano due casi di pianeti eliminati (Sezioni 3.2 - 3.5) e di un pianeta confermato (Sezione 3.4), dimostrando la fattibilità del nostro programma e la potenzialitá della tecnica della spettroscopia multi-banda.

Abstract

Before the discovery of the first exoplanets, our Solar System was the only known example of a planetary system and a formation theory was conceived to explain its properties. The star was formed by a cloud of gas and dust collapsing into a disk. In the outer regions, since material feeding zones were large and icy materials abundant, solid cores formed, quickly grew and accreted gaseous atmospheres, while in the inner regions, rocky cores could not accrete gas because they were small, feeding zones were poor and icy materials absent. So the planetary formation picture only consisted in rocky planets inside, gas giant outside.

The discovery of the first Hot Jupiter (HJ, giant extrasolar planets with orbital periods shorter than ~ 10 days), 51 Peg b (Mayor & Queloz, 1995), that orbits ten times closer to its host star ($P = 4.23$ days) than Mercury to the Sun, challenged our assumptions about planet formation, putting in doubt also the ideas about the formation of our Solar System. Moreover, the following discoveries, that revealed the diversity of the exoplanets characteristics, clearly demonstrated that most of the gross features of the Solar System are only one result within a wide range of possibilities. This consideration raised the interest in the field of exoplanet discovery and characterization. Different theories were developed in order to explain the origins and properties of HJs. The three main classes of HJ origin theory are: *a*) *in situ formation* (Boss, 1995), that predicts the formation of a planet nearby its host star, remaining on the orbit where it formed; *b*) *disk migration* (Lin & Papaloizou, 1986), for which a planet forms far from its host star and, when the proto-planetary disk moves towards the star, it can shrink the orbit of a giant planet from several AU to hundredths of an AU; *c*) *high-eccentricity tidal migration* (Wu & Murray, 2003), in which the planet is pumped into a very eccentric orbit as a result of gravitational interactions with other planets or with a distant stellar companion, followed by tidal dissipation which circularises the planet's orbit. Sec. 1.2 provides a more detailed description of these formation theories.

Observing young stars (pre-main sequence stars, PMS) is becoming very important in this context, because they give the opportunity to study the planetary systems in their earlier formation phases and calibrate and test the evolutionary models for planets (Sec. 1.3). While the direct imaging method can only detect massive planets at wide separation from their host stars, the radial velocity (RV) method is more suited to identify planets on close orbits, like HJs. The transit method reduces the sample because of its low statistics of transiting events (only about 1/10 of exoplanets transits), but current and future space missions can have a crucial contribution to this study. Also GAIA can provide very useful data in few years. Details on methods to search for exoplanets and their corresponding sensitivities are discussed in Sec. 1.1.

Unluckily, young stars are very active and the observations are made complicated by star spots, jets, accretion, and circumstellar disks. The strong magnetic field of these stars induces intrinsic RV variations with amplitudes similar or even larger than the Keplerian signal, so that the stellar activity can mimic or cover the presence of a companion. For this reason a successful RV survey of young stars should be characterized by the capability of distinguishing between the activity-induced and planet-induced RV modulation. In last years a lot of techniques were developed in order to deal with the RV stellar noise (Dumusque et al., 2017). Here I list the most used methods: *a*) *Bisector (BIS) Velocity Span and RV correlation* (Hatzes et al., 1997) allows to understand the variability of the line profile due to the stellar activity. Queloz et al. (2001) found a very strong anti-correlation between RVs and BIS when the RV variation is due to the stellar activity. The lack of correlation strongly support the

planetary origin of the RV modulation, but no correlation can also occur if the absorption lines are not spectroscopically resolved; *b*) *Other activity indices* can be the emission of H and K lines of Ca II or H_α. These lines are very useful when investigating the correlation between RVs and their emission, especially in the visible regime; *c*) *Multi-wavelength observations* are a powerful tool to overcome the limits imposed by the stellar activity. In particular coupling near-infrared (NIR) and visible (VIS) observations allows to immediately disentangle the activity contribution, because the RV jitter due to the activity is reduced in the NIR respect to the VIS range. On the other hand, if the RV variation is due to a Keplerian motion it is wavelength-independent; *d*) *Gaussian processes (GP) regression* (Haywood et al., 2014) is a Bayesian technique able to mitigate the correlated noise in a set of measurements, as the stellar activity in RV data. This method models the activity and helps to distinguish its contribution from the planetary signal. The GPs are very useful and effective when the dataset of radial velocities is very large (hundreds data points). A more detailed description of the methods used for modelling the stellar activity is reported in Sec. 1.3.1.

Simultaneous multi-band spectroscopy has been evaluated from GAPS2.0, a collaboration among most of Italian exoplanetary community, leading to the realization of GIARPS, between 2014 and 2017, that allows to simultaneously observe with HARPS − N in the VIS range and GIANO − B in NIR range. In Chapter 2 the GIARPS Project is described in details. The scientific aim of GAPS2.0 is to explore the realm of planet formation and evolution with emphasis on the inner regions of planetary systems, observing young stars at different ages and identifying and characterizing their planets. From the observable exoplanetary properties (orbital parameters, age-dependent frequency, atmospheric composition) it is possible to understand the physical processes responsible for generating HJs.

A pilot program, performed in Autumn-Winter 2017, allowed us to test the multi-wavelength methodology and to optimize the strategy of removal of activity signal at very young ages. This PhD work concerned the analysis of some case of claimed HJs. The observations of these targets in GIARPS mode were performed during the pilot program and also during the following Large Program started in April 2018. The first results are discussed in Chapter 3 and show two cases of disclaimed planets (Sec. 3.2 - 3.5) and one confirmed planet (Sec. 3.4), demonstrating the feasibility of our program and the potentiality of the multi-band spectroscopy technique.

Contents

List of Figures

List of Tables

Chapter 1

Scientific background

The search for exoplanets has led to more than 3700 discoveries through various detection techniques (see the European site Extrasolar Planet Encyclopedia[1] and the NASA Exoplanet Archive site[2]). About 700 of known exoplanets have been detected with high-precision stellar radial velocity (RV) measurements in the visible wavelength region. In Sec. 1.1 I describe the different methods with the corresponding sensitivity and applicability to different types of stars. Twenty years after the seminal discovery of 51 Peg-b by Mayor & Queloz (1995), the RV technique is still one of the most important method to discover planetary systems, and RV measurements are required to confirm and characterize planetary candidates found by photometric surveys.

The most favourable targets for RV measurements are solar-type stars (F, G, and K spectral types). They are generally observed at visible wavelengths for several reasons (Bean et al., 2010): these stars are bright at wavelength shorter than $1\mu m$ (visible region) where the spectra are rich in deep and sharp spectral lines, so a good Doppler shift measurement is possible; spectrograph technology operating in the visible region is more advanced relative to instruments operating at other wavelengths.

The most accurate RV measurements have been made with HARPS (Pepe et al., 2004, Lovis et al., 2006) and HIRES (Vogt et al., 1994). With a precision close or below 1 m s^{-1}, those instruments could reach planets down to a few Earth masses with short period orbits. Most discoveries are giant gaseous planets, hot-Neptunes and Jupiters, of short periods (few days). A few planets with masses between 1 and 10 Earth masses (super-Earths) have been discovered. Such small objects may be detected in favourable cases (inactive star) if they are close to the star, so that they are expected to be very hot due to the strong stellar irradiance. However, detection of such small planets around solar-type stars requires several tens to a few hundreds of high-quality RV points.

In the last years less massive stars, M-dwarfs, have become more interesting targets for various reasons, one of these being that M-dwarfs are more likely to host detectable rocky planetary companions (Bean et al., 2010). Since this kind of stars peaks in the NIR range, this led to the advent of high-resolution NIR spectrographs. Another scientific topic that can take advantage of NIR spectroscopy is the study of exoplanetary formation and evolution, aimed to explain the observed diversity of planetary systems. For this science, the observations are focused on the young stars. Sec. 1.2 provides an overview of the different planets

---

[1] http://exoplanet.eu/

[2] https://exoplanetarchive.ipac.caltech.edu/

origin theories, while Sec. 1.3 describes the case of the research for Hot Jupiters (HJs) around young stars to give constraints to the theories. Anyway, both late-M stars and young stars can be very active and the RV variations can be confused with a modulation due to the stellar activity rather than a companion. Measuring radial velocities from NIR spectra can overcome this issue, since the jitter related to activity is reduced relative to visible measurements, because in the NIR the contrast between stellar spots or plagues and the rest of the stellar disk is reduced. The raising interest for measuring high precision RVs from NIR spectra led to build more precise spectrographs for NIR spectral region, even if they don't reach yet the sub-m s^{-1} precision of optical instruments. In Sec. 1.3.1 I describe some methods aimed to deal with the stellar activity that affects the RV measurements.

1.1 Exoplanet search methods

From the properties of planets, one can derive several observable quantities that can lead both to the detection and the characterization of planets. Those properties can be roughly divided into two categories:

- Dynamical signatures, which signal the presence of a companion by the orbital motion of the host stars among the barycenter of the star-planet system (variation in radial velocities, astrometric signature)
- Information coming from the measurement of the light of the combined star-planet system (transits) or of the planet itself, separate from the star (direct imaging)

Figure 1.1 summarizes the detection methods considered to date, also giving an indication of the lower mass limits which are expected in the near future.

Figure 1.2 shows the Period-Mass diagram (logarithmic scale) of currently (August, 20 2018) confirmed planets with different methods. It is clear that each method is sensitive to a specific region of the diagram. In the following I present the main exoplanets research methods, discussing the motivation of their specific mass-period coverage.

1.1.1 Dynamical signatures

The motion of a single planet orbiting a star causes the star to undergo a reflex motion about the star-planet barycentre, with orbital semi-major axis $a_* = a \cdot (M_p/M_*)$ and period P. This results in the periodic perturbation of three observables, all of which have been detected (albeit in different systems): in radial velocity, in angular (or astrometric) position, and in time of arrival of some periodic reference signal.

Radial velocity signal

The velocity amplitude K of a star of mass M_* due to a companion with mass $M_p \sin i$ (where i is the orbital inclination, that is the angle between the plan of orbit and the plan of sky) with orbital period P and eccentricity e is (e.g. Cumming et al. 1999):

$$K = \left(\frac{2\pi G}{P}\right)^{1/3} \frac{M_p \sin i}{(M_p + M_*)^{2/3}} \frac{1}{(1-e^2)^{1/2}}. \tag{1.1}$$

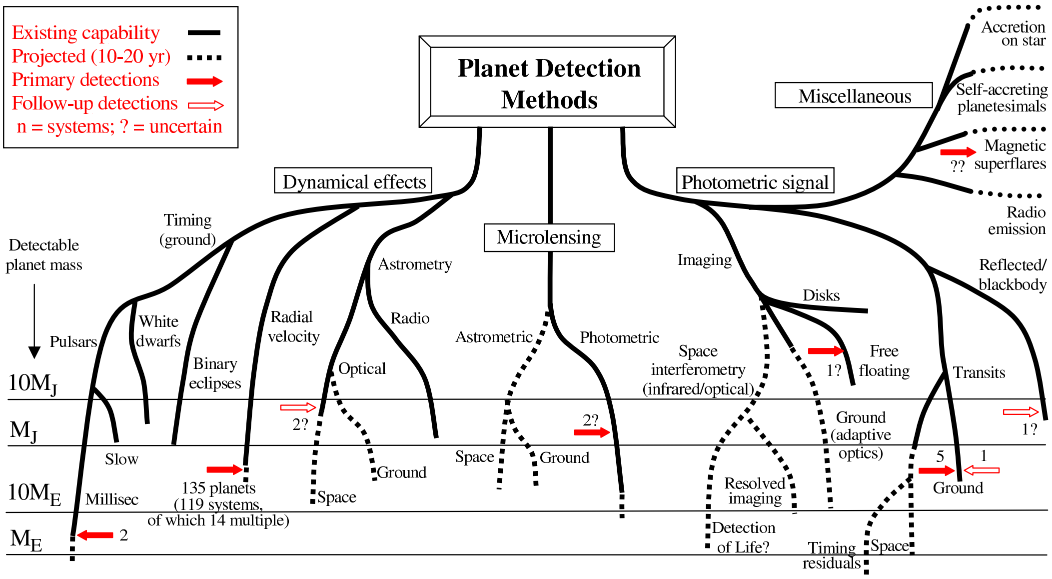

Figure 1.1: Detection methods for extra-solar planets, adapted from Perryman et al. (2005). The lower extent of the lines indicates, roughly, the detectable masses that are in principle within reach of present measurements (solid lines), and those that might be expected within the next 10 years (dashed). The (logarithmic) mass scale is shown at left. The miscellaneous signatures to the upper right are less well quantified in mass terms. Solid arrows indicate (original) detections according to approximate mass, while open arrows indicate further measurements of previously-detected systems. '?' indicates uncertain or unconfirmed detections. The figure takes no account of the numbers of planets that may be detectable by each method.

In a circular orbit the velocity variations are sinusoidal, and for $M_p \ll M_*$ the amplitude reduces to:

$$K = 28.4 \left(\frac{P}{1 \text{ year}}\right)^{-1/3} \left(\frac{M_p \sin i}{M_{Jup}}\right) \left(\frac{M_*}{M_\odot}\right)^{-2/3} \quad \mathrm{m\,s^{-1}} \tag{1.2}$$

where the period P and the semi-major axis a are related by Kepler's Third Law:

$$P = \left(\frac{a}{1 \text{ AU}}\right)^{3/2} \left(\frac{M_*}{M_\odot}\right)^{-1/2} \quad \text{year.} \tag{1.3}$$

The semi amplitude of this radial velocity curve is about $K = 12.5$ m s^{-1} with a period of 11.9 yr in the case of Jupiter orbiting the Sun, and about 0.1 m s^{-1} for the Earth. The $\sin i$ dependence means that orbital systems seen face on ($i = 0$ if seen by an observer at the pole of the orbit) result in no measurable radial velocity perturbation and that, conversely, radial velocity measurements can determine only $M_p \sin i$ rather than M_p, hence providing only a lower limit to the planet mass, since the orbital inclination is unknown with RV method only.

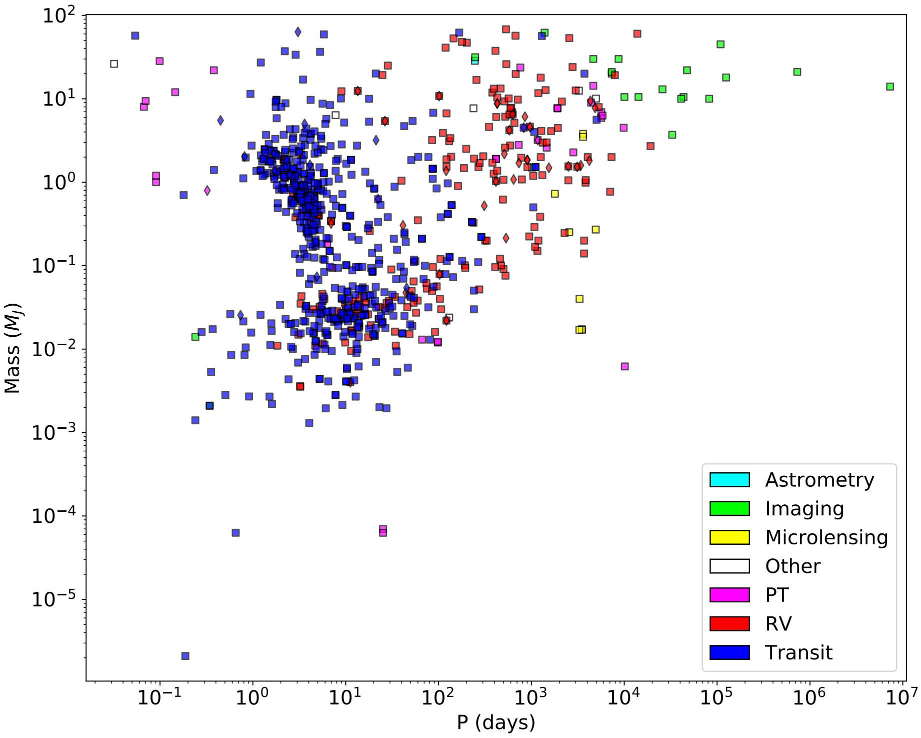

Figure 1.2: Planetary masses of confirmed exoplanets (as for August 2018) as function of their orbital periods. Different colours reprensent different discovery techniques, while diamonds are data where mass is actually $Msini$.

Although the radial velocity amplitude is independent on the distance to the star, signal-to-noise considerations limit observations to the brighter stars (typically $V < 8$ mag, $10-12$ for lower accuracy data). Equation 1.1 indicates that radial velocity measurements favour the detection of systems with massive planets, and with small a (and hence small P).

Astrometric signal

The principle of planet detection with astrometry is similar to that underlying the Doppler technique: the presence of a planet is inferred from the motion of its parent star around the common centre of gravity. In the case of astrometry the two components of this motion are observed in the plane of the sky; this gives sufficient information to solve for the orbital elements without the $\sin i$ ambiguity. The path of a star orbiting the star-planet barycentre appears projected on the plane of the sky as an ellipse with angular semi-major axis α given by:

$$\alpha = \frac{M_p}{M_*} \cdot \frac{a}{d} \tag{1.4}$$

where α is in arcsec when a is in AU and d is in pc (and M_p and M_* are in common units). This 'astrometric signature' is therefore proportional to both the planet mass and the orbital radius, and inversely proportional to the distance to the star.

Astrometry also has the advantage of being applicable to all types of stars. It is more sensitive to planets with larger orbital semi-major axes and hence complements radial velocity measurements. However, planets with large orbits have very large periods, and this limits the usefulness of this technique to separation of a few AU, simply because the time elapsed since the earliest high quality astrometric measurements for a star is typically less than 20 years and never larger than 30.

For multi-planet systems, astrometric measurements can determine their relative orbital inclinations (i.e., whether the planets are co-planar), an important ingredient for formation theories and dynamical stability analyses.

Pulsar timing

Although all orbital systems are affected by changes in light travel time across the orbit, in general there is no timing reference on which to base such measurements. A notable exception are radio pulsars[3], rapidly spinning highly-magnetised neutron stars, formed during the core collapse of massive stars (8–20 $M_\odot$) in a supernova explosion. Pulsars emit narrow beams of radio emission parallel to their magnetic dipole axis, seen as intense pulses at the object's spin frequency due to a misalignment of the magnetic and spin axes. There are two broad classes: 'normal' pulsars, with spin periods around 1 s, and of which several hundreds are known; and the millisecond pulsars, 'recycled' old ($\sim 10^9$ yr) neutron stars that have been spun-up to very short spin periods during mass and angular momentum transfer from a binary companion, with most of the 30 known objects still having (non-accreting) binary companions, either white dwarfs or neutron stars. The latter are extremely accurate frequency standards, with periods changing only through a tiny spin-down at a rate $\sim 10^{-19}\,\mathrm{m\,s^{-1}}$ presumed due to their low magnetic field strength (Bailes, 1996).

In the simplest case of a circular, edge-on orbit, the semi-amplitude of timing residuals due to planetary motion is (Hermes, 2017):

$$\tau_p \sim \left(\frac{M_p}{M_*}\right)\left(\frac{asini}{c}\right). \tag{1.5}$$

where a is the orbital semi-major axis with respect to inclination i, M_p is the mass of the companion, M_* is the mass of the pulsating star, and c is the speed of light. The extremely high accuracy of pulsar timing allows the detection of lower mass bodies orbiting the pulsar to be inferred from changes in pulse arrival times due to orbital motion.

It is not surprising, then, that the first planetary system discovered around an object other than our Sun was found around the 6.2-ms pulsar PSR 1257+12 ($d \sim 500$ pc), with at least two plausible terrestrial-mass companions (Wolszczan & Frail, 1992) having masses of 2.8 and 3.4 $M_\oplus$, and almost circular orbits with $a = 0.47$ and 0.36 AU, and period of 98.22 and 66.54 days respectively, close to a 3:2 orbital resonance.

1.1.2 Photometric detections

Transit depth and probability

The transit method aims at detecting the dimming of the stellar light by occultation due to an orbiting planet.

---

[3] pulsating white dwarfs can also be considered (see Mullally, 2009)

Transit experiments offer a relatively easy way to investigate the planet atmosphere, doing spectroscopy during the planet transit. Massive planets with short orbits (Hot Jupiters) can be observed from the ground, while planets down to Earth-mass or below can be detected from space, altough small planets can be detected from ground if around very small stars (see e.g. the case of the planets around TRAPPIST-1, Gillon et al. 2017)

The probability of viewing a planet transiting across the stellar disk with a suitable angle, depends on the distance of the planet to the central star (impact parameter). For close-in orbits it is about 10%, decreasing for more distant planets. The transit depth is the fractional reduction of the stellar intensity $\Delta L/L_*$ due to the planet transit and it depends on the ratio of the cross sections of the planet to the star (see eq. 1.6):

$$\frac{\Delta L}{L_*} \simeq \left(\frac{R_p}{R_*}\right)^2 \tag{1.6}$$

where R_p and R_* are the absolute radius of the planet and the star, respectively. The transit amplitude depends primarily on the relative angle of the planets and stellar disk. If the radius of the star can be estimated from spectral classification or stellar evolutionary models, then R_p can be estimated from equation 1.6. With knowledge of the period P and an estimate of the stellar mass M_* (also from spectral classification or via evolutionary models), the semi major axis of the orbit, a, can be derived from Kepler's law. Usually, transiting planet orbits have very low eccentricities. With the approximation of circular orbit, other observational parameters are given, to first order, by simple geometry (Deeg, 1998). Thus, the duration of the transit is defined as:

$$\tau = \frac{P}{\pi}\left(\frac{R_* \cos\delta + R_p}{a}\right) \simeq 13 \left(\frac{M_*}{M_\odot}\right)^{-1/2} \left(\frac{1}{1\ \mathrm{AU}}\right)^{1/2} \left(\frac{R_*}{R_\odot}\right) \quad \text{hours} \tag{1.7}$$

where δ is the latitude of the transit on the stellar disk, that depends on the inclination of the orbit.

With the other parameters estimated as above, δ can be derived from equation 1.7, and hence the orbital inclination from $\cos i = (R_* \sin\delta)/a$. The minimum inclination where transits can occur is given by $i_{\min} = \cos^{-1}(R_*/a)$, while the probability of observing transits for a randomly oriented system is $p = R_*/a = \cos i_{\min}$. Evaluation of i and p for realistic cases demonstrates that i must be very close to 90°, while p is very small, implying that only a small fraction of planets (∼10% for close-in planets, ∼1% for planets with semi-major axis of ∼1 AU) can ever be detected or monitored using this technique. Finally, the combination between RV and transit method allows to evaluate the actual planet mass, since the orbital inclination i is known.

Direct Imaging

The direct imaging technique consists in the occultation of the central star with a suitable device (e.g. a coronagraph) allowing to observe the light of a faint companion orbiting around it. The main parameter determining detectability of planets from direct imaging are the apparent separation and the luminosity contrast between the star and the planet.

From the detection point of view, in the case of direct imaging, the planets can be roughly divided into two classes, depending on the dominant source of planet luminosity:

- **Warm planets**, for which the intrinsic (thermal) flux dominates

- **Cold planets** that shines mainly thanks to the reflected light from the parent star

The separation between these two classes cannot be rigorously defined, since it depends on several factors: wavelength, age of the system, mass of the planet, albedo, orbital separation and luminosity of the parent star. Similarly there cannot be a rigorous distinction between intrinsic and reflected light, since stellar irradiation alters the atmospheric structure and models must consider the two contributions self-consistently.

Planets at young ages are mostly self luminous: their luminosity depends on age, mass and atmosphere composition, so the planet/star contrast does not depend on the planet distance to the star. These planets are cool, and then much more luminous in the near infrared than in the visible domain. The spectrum depends on the temperature, surface gravity and the presence/lack of dust in the planet atmosphere. Very dusty atmospheres have smooth spectra similar to black body, while where dust is negligible the spectra have peaks of the emission around wavelengths 1.05, 1.25, 1.6 and 2.1 micron depending on their effective temperature (i.e. mass/age). After a bright and short accretion phase, contraction and differentiation are the remaining energy sources of the planet. Initially (age of $\sim$1 Myr), the planet is still quite warm ($T \sim 2500K$) and may be quite bright with luminosity values that can be as large as 0.001 the Solar value for a 10 Jupter mass planet. The total luminosity is proportional to the square of the mass. Luminosity and temperature deal with age, the luminosity decreasing with the inverse of the age. At old ages, the intrinsic flux of planets becomes small (for stars older than the Sun, it remains dominant only for super-Jupiters/brown dwarfs companions) and thus their contrast strongly depends on the median distance from the star, and on reflective properties of the atmosphere: albedo and polarization level. For gas giant, the radius is weakly dependent on mass for old objects in the sub-stellar regime. Therefore, similar brightness values are expected for planets of different masses. The spectra should also look similar because temperature and the location and physical characteristics of clouds in the upper atmosphere (which deeply affect the emergent spectrum) are also not strongly mass dependent. Therefore, for these objects determination of mass requires detection of the reflex motion of the star. The reflected light is smaller in the near infrared (because the star flux and planetary albedo drop) and thus the optimal wavelength domain for such systems is from J to L-bands (1.25 to 3.7 μm) band.

Microlensing

Gravitational microlensing exploits the lensing effect of the general relativistic curvature of spacetime to detect planets: the light rays can be deflected by a strong gravitational field. So the light of a background star can be deflected by the gravitational field of a nearby star along the line of sight of the observer. Consequently, the nearby star acts as a lens and the background star appears more luminous. The magnification of the star is monitored as function of the time, as illustrated in Figure 1.3. A second peak in the light curve of the star suggests the presence of a planetary companion. To observe this effect the alignment of stars and observer is needed within the so-called Einstein radius, that depends on the mass of the lens, thus they are more frequent if one looks at regions of the Galaxy that are densely populated with stars.

Gravitational microlensing is important because it covers a region of the Period-Mass diagram complementary to other methods (long periods and small masses, see Fig. 1.2). It is probably the only method that could detect planets outside the Milky Way (Haswell, 2010).

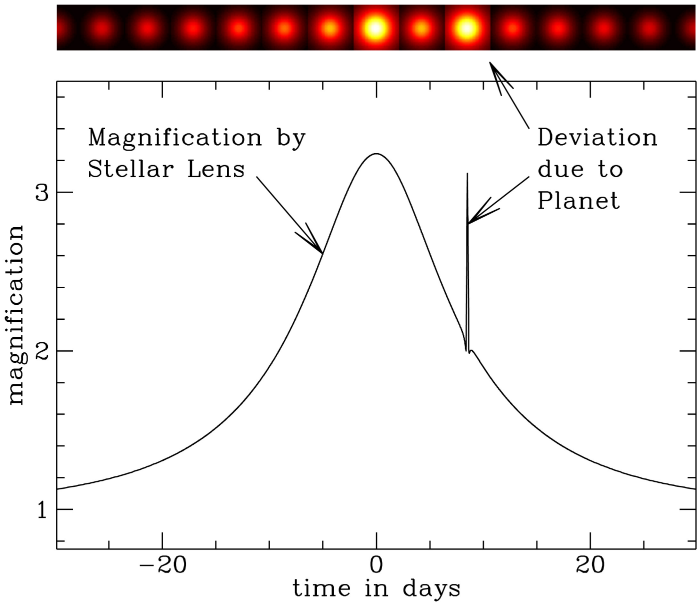

Figure 1.3: Gravitational microlensing: when background star, lens star and observer are aligned the light of background star is magnified due to the relativistic effect of curvature of the spacetime. If a planet is present another peak in the light curve occurs.

The great disadvantage of the microlensing method is that the microlensing events are rare and not repeatable and there is no opportunity for confirming and refining the observations.

1.2 Planetary formation and evolution

Since the discovery of the first Hot Jupiters (HJs, planets that orbits their host stars with a period shorter than $\sim$ 10 days) the unique example of a planetary system was our Solar System, with rocky planets in the inner regions and gaseous planets in the outer regions. This picture was immediately upended by the discovery of 51 Peg b (Mayor & Queloz, 1995) and theories of planet formation started to be revised. While HJs are relatively rare in the Galaxy (only 1% of Sun-like stars host one, and even less around M dwarfs, Johnson et al. 2010), they play a very important role in our understanding of the internal structure, atmospheric composition, and orbital architecture of giant planets outside our Solar System. The HJs are crucial for the theoretical work concerning several physical processes to solve a key question: *How do planetary systems form and evolve?* In addition, HJs are the easiest planets detected by the most successful techniques (transits and radial velocity variation).
The three main classes of HJs origin theory are in situ formation (Sec. 1.2.1), disk migration (Sec. 1.2.2) and high eccentricity tidal migration (Sec. 1.2.3). See Dawson & Johnson 2018 for a detailed review.

1.2.1 In situ formation

In situ formation is possible if gravitational instability (Boss, 1997) or core accretion (e.g. Perri & Cameron 1974) can occur close to the star. Rafikov 2005, 2006 asserted that none of these two mechanisms could operate at the typical locations of Hot Jupiters, so they must have formed further from their stars and migrated to their current close in orbits.

The gravitational instability occurs if the free-fall time due to self gravity is sufficiently rapid to overcome Keplerian shear, so that part of proto-planetary disk fragments into bound clumps. Toomre (1964) found a criterion for gravitational instability, for which close to the star the temperature increases, the pressure decreases and the rotation of the local gas is faster, working against the gravitational collapse. On the other hand, the high gas surface density supports the collapse. However, this last effect cannot compensate for the fast rotation and high termal pressure unless the gas density profile is steeper than $P^{-7/6}$, where P is the pressure. Even if the gas was dense enough to fragment the disk, these fragments would shear out before they could cool and contract because of the vicinity to the star. Rafikov (2005) found a criterion for the cooling of the disk fragments before they are rotationally sheared, but this assertion should be valid simultaneously to the previous criterion and this requires implausibly high temperatures and gas surface densities. Therefore no gravitational instability could be expected at short orbital periods.

The core accretion occurs when a rocky proto-planet core accretes many times its mass from the proto-planetary disk in order to form an HJ. The challenge is accreting enough mass before the gas disk dissipates. The gas accretion starts only if the rocky core is about 10 $M_\oplus$, i.e. if the timescale to grow the core is shorter than the disk lifetime (few Myr, Fedele et al. 2010) and if the amount of mass in the feeding zone[4] is sufficient to grow a 10 $M_\oplus$ core. While the first requirement is easy to meet at short orbital periods, the second one is difficult being the feeding zones close to the stars quite tiny. The 10 $M_\oplus$ core can be achieved by enhancing the solid surface density, but this leads to destabilize the disk (e.g. Schlichting 2014), or by

---

[4] The feeding zone represents the domain within which a dominant planetary embryo is able to significantly deflect the paths of other planetesimals towards itself and grow (D'Angelo et al., 2010).

accreting little pebbles that drift from the outer disk, but they cannot reach masses greater than 1 $M_{\oplus}$, so the HJs cannot be formed solely by this mechanism.

Recent studies (Lee et al. 2014, Lee & Chiang 2016, Batygin et al. 2016) suggested the formation of HJs starting from super-Earths (rocky planets with a mass between that of Earth and Neptune at short orbital periods). However, the occurance rate of the super-Earths' orbital periods has a steep decrease within 10 days (Lee & Chiang, 2017).

1.2.2 Disk migration

According to the disk migration theory, torques from the proto-planetary disk can move the orbit of a giant planet from several AU to handredths of an AU (Goldreich & Tremaine 1980, Ida & Lin 2008). While small mass planets do not perturb the density profile of the disk (type I migration), giant planets are massive and modify the disk radial density profile, deflecting the gas, and eventually creating a gap and forming inner and outer disks. As the disk viscously spreads, the gap and the planet are carried with it (type II migration, Lin & Papaloizou 1986).

Until 2014, most standard descriptions of disk migration theories were based on the idea that the disk is separated into an inner and outer region and gas is considered unable to cross the gap. Duffell et al. (2014) demonstrated that this assertion is incorrect and a significant amount of material passes through the gap on horseshoe orbits. However, one tricky point in the disk migration theories is that it predicts migration timescales much shorter than the lifetime of the protoplanetary disk. Dürmann & Kley (2015) claimed that the planet inside its gap is not necessarily at equilibrium with the gas, when the gas profile is itself at equilibrium with the planet. So the planet can actually migrate faster than the gas drifts, even in a stationary disk (Robert et al., 2018).

1.2.3 High eccentricity tidal migration

To turn a cold Jupiter into a Hot Jupiter its orbital angular momentum has to be reduced by a factor of 10 and its orbital energy by a factor of 100. While the disk migration can change the planet's energy and angular momentum simultaneously, the tidal migration needs two steps: first a perturber reduces the planet's angular momentum by perturbing the Jupiter onto a highly elliptical orbit, then the Jupiter tidally dissipates its orbital energy by interactions with the central star. These interactions can eventually decouple the planet from its perturber. Several mechanisms have been proposed for the eccentricity excitation, such as planet-planet scattering, (Chatterjee et al., 2008) that can take place if systems formed tightly packed (Jurić & Tremaine, 2008) or high eccentricities are generated by fly-bys (Shara et al., 2016), or secular interactions, that slowly exchange angular momentum between widely separated planets (Kozai, 1962). While in planet-planet scattering eccentricities are excited on a timescale of thousands of years, secular excitations occur on timescales that can range from millions of years to many billions of years.

None of the previous described Jupiter's origin theories can explain all the observational evidence, actually an observational evidence can be explained by more than one origin channel. One important observational constraint could be provided by the obliquity of HJs' host stars and the frequency of the counter-rotating planets. The host star obliquity is the angle between the star's spin angular momentum vector and the planet's orbital angular momentum vector. To date, many HJs are observed to be well-aligned with their host stars, but some are highly misaligned, even retrograde (Albrecht et al. 2012, Esposito et al. 2014). There are various methods to measure the stellar obliquity, one of these is the Rossiter-McLaughlin (RML) effect (Rossiter 1924, McLaughlin 1924), an anomaly in the radial velocity variation that occurs when a planet transits a star. Since the star rotates on its axis, one quadrant of the photosphere seems to come towards the observer, the opposite one seems to move away. The greater is the stellar rotational velocity the higher is this effect. From the shape of the RML effect, one can derive the ratio of the sizes between the planet and its host star, the rotational speed of the star and the stellar obliquity (the sky-projected spin-orbit angle).

HJs originated in situ or via disk migration are expected to maintain aligned orbits (Bitsch et al., 2013). On the other hand, the gravitational interactions with the gas disk could reduce the HJ's angolar momentum (high eccentricity tidal migration) and change its direction. So the distribution of stellar obliquities is related to the mechanisms for generating different planet eccentricities. This picture is further complicated by the empirical correlation between the spin-orbit relative orientation and the effective temperature of the host star (Winn et al., 2010): planets hosted by stars hotter than 6250 K show a wide distribution of obliquity, while planets around cooler stars are almost always well aligned. Moreover, also in the in situ or disk migration scenarios, planets may be misaligned by some recently proposed mechanisms, like binary perturber (Spalding & Batygin, 2015) or internal gravity waves (Rogers et al., 2012).

The interpretation of HJ host star obliquities is still ambiguous and not clearly linked to one or more origin theories. This field is still an uncharted territory to be understood. Observing properties of Hot Jupiters and their host stars, and studying the correlations among those properties, is a powerful tool to test theories of the planetary formation and evolution.

1.3 Observations of Hot Jupiters around Young stars

The detection of giant planets around young stars can address key questions in the astrophysics of planetary formation and migration, previously described. In fact, looking at young stars provides an opportunity to observe the architecture of planets in their infancy.

After more than 20 years of the first discoveries, exoplanetary science is now entering a mature phase, in which scientific goals are shifted toward the determination of the physical properties of planets and the origin of their observed, astonishing diversity. As discussed in the previous section, detections of extrasolar planets allow to measure the frequency of planets with different masses, sizes, orbital characteristics and host star properties, and are now beginning to probe the diverse outcomes of planet formation and evolution. The observed planetary properties (orbital architecture, internal structure, and atmospheric composition) are the result of the complex interplay between a variety of physical and dynamical processes operating on different timescales during formation and the successive orbital evolution. Those processes are in turn dependent on 'environmental' conditions, such as disk properties, multiplicity, and stellar radiation fields and involve mainly the migration processes. Planet-disk interaction (Baruteau et al., 2014), planet-planet scattering (Chatterjee et al., 2008) or in-situ formation (Batygin et al., 2016) are thought to be responsible for generating hot Jupiters (HJs) and Warm Jupiters, and are expected to produce observable effects that can be used to gauge their respective effectiveness. These effects include differences in orbital parameters (eccentricity and/or obliquity), migration timescales and age-dependent frequency of different systems. The orbital properties and frequencies of mature HJs are to-date rather well-determined.

A great limitation in the observations of young stars is caused by their high levels of activity. In the following section I describe some methods proposed for taking into account and/or modelling the intrinsic stellar activity.

1.3.1 Methods to deal with the stellar activity

The radial velocity of a star is defined to be the velocity of the center of mass of the star along our line of sight (Queloz et al., 2001) and the observational determination of a star's radial velocity is made by measuring the Doppler shift of spectral lines, that are also affected by the stellar activity. For this reason, the radial velocity variations can be due to either a possible companion or changes in the stellar atmosphere.

Several processes, other than barycentric motion, can cause apparent radial velocity variantions with different time scales: stellar oscillations, granulation and magnetic activity. Oscillations, caused by pressure waves (p-modes) that propagate to the surface of solar type stars, consist in dilatation and contraction of external envelopes. The typical lifetime of these oscillations in Solar type stars is few minutes (Schrijver & Zwaan, 2000) and typical RV amplitude induced by them is between 10 and 400 cm s^{-1}, depending on the star type and evolutionary stage. Granulation, due to the convective nature of the solar type stars, is an ensemble of hot fluid cells rising up to the surface, forming large and bright spots, until they become cool and dense enough to sink again. Since these cells move towards the observer, the granulation contributes to the spectrum as a convective blueshift. Typical timescales of this effect are several minutes (Title et al., 1989) to several hours (Del Moro et al., 2004), and the amplitude in RV variation on the order of the meter-per-second. On longer timescales, stellar surface features such as spots (regions cooler than the solar mean surface temperature), faculae (hotter photospheric structures) or plages (hotter cromospheric structures) induce photometric and spectroscopic variations that are modulated by the rotation period of the star. Since the starspots move together with the star, they come in and out of view as the star rotates, inducing an imbalance between the redshifted and blueshifted halves of the star and producing an asymmetry in the shape of the total line profile. These perturbations to the line profile lead to RV variations of the order of m s^{-1} (Huélamo et al. 2008, Makarov et al. 2009, Lagrange et al. 2010). These modulations can be much greater for more active and more rapidly rotating stars (Desort et al., 2007). The typical lifetime can range from hours to even years depending on the spectral type and age. Finally, longer period RV oscillations can be caused by stellar magnetic activity cycles, which have typical timescales of several years to decades (Gomes da Silva et al., 2012).

While the activity-induced signals due to stellar oscillations and granulation can be mitigated by adapting the observational strategy (Dumusque et al., 2011), signals caused by active regions on the stellar surface are harder to disentangle. Some techniques, described in the following, have been developed for overcoming this issue.

Bisector Velocity Span (BVS) The bisector consists in the midpoints between right and left points of the spectral line profile; it measures the general asymmetry of the lines of a spectrum. For a line profile with a perfect Gaussian shape, this would be a straight vertical line. In practice, the bisector shape is affected by the granulation: the granulation pattern is made of dark regions (that produce a redshifted line profile) surrounding bright granules (blueshifted line profile). The total line profile is the sum of these two profiles. Since the blueshifted effect dominates with respect to the redshifted one, the resulting line profile is asymmetric, and its bisector is curved at the top, with the typical C-shape. Active regions that reduce this net blueshift will thus produce smaller distortions producing a bisector that is variable with time as a consequence of the distortion of the spectral line.

One of the best techniques to interpret observed RV variations is to look for changes in the bisector line after applying the cross correlation function (CCF) method. The CCF is widely used to derive the radial velocities when the signal to noise ratio of the spectra is low. Most of works uses this method to derive radial velocity measurements, because of its simple application and moreover it is less dependent from the variability of telluric lines than other techniques, which require a more complex models of Earth's atmosphere (see Sec. 1.3.3 for a wide discussion on the impact of telluric lines on RV measurements). Since the CCF represents the mean shape of the lines in the whole spectrum, it provides additional information about the average features of the lines. In the cross-correlation method a mask composed of hundreds or thousands of spectral lines is convolved to the observed spectrum. The CCF profile may be fitted by a Gaussian (Queloz, 1995). The Gaussian parameters allow to determine radial velocities, as described in Section 2.9 (from center position), an information about line broadening (the Full Width at Half Maximum) that is related to the rotational velocity, while the equivalent width can be used as a metallicity estimate if the temperature of the star is known approximately.

From the CCF profiles one can perform a bisector analysis. By selecting two regions of the bisector at the top and bottom of the profile, one can measure possible bisector orientation changes that may be due to asymmetries in the distribution of light on the surface of a rotating star, due e.g. to activity. The difference between the two selected regions is the bisector velocity span widely used in this type of studies. Any correlation between radial velocity changes and line-bisector orientation leads to serious doubts on the reflex motion interpretation of the radial velocity variations. If the radial velocity is due to the presence of a companion, there is no change in bisector's shape or orientation.

Unfortunately, the lack of correlation does not ensure the presence of a planet (Prato et al., 2008) and the correlation is not always linear or easily detectable (Desort et al., 2007).

Other activity indicators Other kinds of correlation analysis can be performed between the RVs and some spectroscopic activity indicators, such as the emission of H and K lines of Ca II (Noyes et al. 1984,Isaacson & Fischer 2010) or H_α (Robinson et al., 1990, Strassmeier et al., 1990, Santos et al., 2010, Gomes da Silva et al., 2011). As discussed in (Sissa et al., 2016), the correlation of H_α with Ca II H&K indices is high for the most active stars but decreases at a lower activity level, and sometimes becomes an anti-correlation (Gomes da Silva et al., 2011). Similar results were also found by Cincunegui et al. (2007), who added, using simultaneous observations of stars with spectral type later than F, that the correlation is lost when studying individual spectra of single stars and there is no dependence on activity. The correlation between the averaged fluxes for the Ca II and H_α lines can be clarified by considering the dependence of the two indexes on the stellar colour or the spectral type, while the absence of a general relation between the simultaneous Ca II and H_α index can be due to difference in the formation region of the two lines (see also Gomes da Silva et al. 2014). Studying the solar spectrum as a prototype and extrapolating the results to other stars, Meunier & Delfosse (2009) discovered that plages and filaments in the chromosphere contribute differently to Ca II and H_α lines: while plages contribute to the emission of all these lines, the absorption due to filaments is remarkable only for H_α. Therefore the saturation of the plage filling factor seems to enhance the correlation between the two indexes in case of high stellar activity and low filament contribution. On the other hand, the anti-correlation between the emission in Ca II and H_α for low active stars seems to depend only on a strong filament contrast if the filaments are well correlated with plages (see also Gomes da Silva et al., 2014).

While Ca II and $H_\alpha$lines are dominant features in the optical range, He I at 1.083 μm and Brackett γ (Brγ) lines at 2.16 μm can be useful activity indicators in the NIR range.

Coupling Near-Infrared and Visible Spectroscopy With the increasing interest in observing M-dwarfs to search for Earth-like planets, in the last years the NIR band became more and more important because both the spectra of these stars peak between 1 and 2.5 μm and the stellar activity is reduced in the NIR. In the framework of the exoplanets field this is a great advantage, in fact while the activity signal is chromatic showing different amplitudes in differents wavelength bands, the Keplerian motion is independent on wavelength. The combination between VIS and NIR data provides a very useful information on the origin of RV variation. Since the first years of 2000s early results (Sec. 1.3.2) of combined VIS-NIR spectroscopy were presented to better study the stellar activity and to better understand the RV signals from young stars. These studies were performed with observations collected in different observatories and in different periods. This could prevent a correct interpretation of the stellar activity, since its behaviour could be different in different periods of the stellar activity cycle. Moreover, from a technical point of view, in order to obtain two datasets (VIS and NIR), a research team should submit two different proposals and observe the same target twice with two different instruments, with a consequent loss of observing time. The simultaneity certainly overcomes these issues and represents a huge potential in terms of science and time. CARMENES (Quirrenbach et al., 2014), GIARPS (Claudi et al. 2016, described in this thesis at Chap. 2) and NIRPS+HARPS (Bouchy et al., 2017) are the first examples demonstrating the technological efforts in this field. See Benatti (2018) for a detailed review on the multi-wavelength high resolution spectroscopy.

Gaussian Process Regression The Gaussian Process Regression (GPR) is a very powerful Bayesian method used to mitigate the contribution of the stellar activity noise in the RV data (e.g. Rasmussen & Williams 2006, Haywood et al. 2014). The exact shape of activity-induced RV signals is still poorly understood, and the sinusoidal models (Boisse et al., 2011), that fit the RV activity as the sum of sinusoidal signals at the rotational period of the star and its first harmonics, are not a perfect description of them. GPR allows to incorporate the noise due to the magnetic activity making minimal assumptions on its form as RV signal.

Usually a GPR consists in a quasi-period covariance kernel, a function described by some parameters, called hyperparameters, that represents the covariance between measurements at different epochs in terms of parameters that can be related to some physical properties of the star. The hyperparameters are: h that represents the amplitude of the correlations; θ is related to the rotation period of the star; w is the length (time) scale of the quasi-periodic component, linked to the size evolution of the active regions; λ is the correlation decay timescale that is related to the active regions lifetime. A series of Gaussian priors is set to perform this analysis, and a Markov Chain Monte Carlo (MCMC) algorithm is used to fit the RVs.

The strength of the GPR is that it is a non-parametric method and does not assume any physical model about active regions. On the other hand, the drawback consists in requiring a large numbers of data (order of hundreds) in order to have a reliable result.

In the following section, I list some previous work in this area, that made use of one or more of above-described methods to clean-up the stellar activity.

1.3.2 Previous work

One of the most interesting case in this framework concerned the very young star TW Hya ($\sim$ 10 Myr). Setiawan et al. (2008) announced the discovery of a giant planet orbiting this star: they analyzed high resolution optical spectroscopic observations and obtained significant periodic radial velocity variation. This result, together with the lack of correlation between the RV variation and the cross correlation function bisector (BIS) seemed to be a proof of the existence of a planet orbiting the star. Huélamo et al. (2008) studied the same object analyzing new optical and infrared data. The optical data were acquired with the CORALIE spectrograph at 1.2m Euler Swiss telescope in La Silla, Chile. Each measurement has an accuracy of about 10 m s^{-1}. These data were complemented by older RVs measurements of TW Hya obtained with HARPS (at the ESO's 3.6m telescope at La Silla Observatory) and FEROS (at the MPG/ESO 2.2-metre telescope at La Silla Observatory) spectrographs, finding a period of about 3.56 days and confirming the possible presence of a planet. To further test this hypotesis Huélamo et al. (2008) observed TW Hya over six nights in the infrared range with CRIRES, the CRyogenic high-resolution InfraRed Echelle Spectrograph mounted on the VLT (Kaeufl et al., 2004). To derive the RVs from the spectra they used the cross correlation method: the spectra were correlated with a telluric mask, developed with the HITRAN database (Rothman et al., 1998), and a stellar mask from PHOENIX models (Barman et al., 2005). They found a dependence of the optical RV amplitude with the used CCF mask; the infrared RV curve is almost flat with a scatter of 35 m s^{-1}. These results are inconsistent with optical orbital solution, so they concluded that the RV signal found for TW Hya is rather caused by a cool spot modulated by stellar rotation.

Prato et al. (2008) measured the RVs of the $\sim$ 2 Myr old T Tauri stars DN Tau, V836 Tau, and V827 Tau in visible and IR range with the Coude' echelle spectrograph at McDonald Observatory 2.7m Harlan J. Smith telescope, and CSHELL spectrograph at the NASA IRTF 3m telescope, respectively. They demonstrated that the correlation between radial velocity variations and line bisector slope changes is not sufficient to rule out starspots as a cause of radial velocity variations in the search for planets around young stars. In fact, the observed stars did not exhibit any BIS correlation, suggesting the presence of giant companions, but then IR spectroscopic data showed substantial reduction in RV amplitude, identifying the activity nature of the RV modulation.

Mahmud et al. (2011) observed the weak-line T Tauri star, Hubble I 4, with the Coude' and CSHELL spectrographs, obtaining visible and infrared radial velocities. They performed a periodogram analysis finding a peak at 1.55 days in both datasets, used to obtain phase-folded RV curves. A Keplerian orbit was fit to the optical data yielding a semi-amplitude of 1395±94 m s^{-1}. The same Keplerian orbit was also fitted to the infrared RVs with only the semi-amplitude as a free parameter, finding a value of 365±80 m s^{-1}. The difference of RV amplitudes in different wavelength ranges confirmed the activity-induced RV modulation, also supported by a very strong correlation between RVs and BIS values from optical data.

Bailey et al. (2012) presented the results of a high-resolution NIR RV analysis of twenty young stars in the βPic and TW Hya Associations. These spectra were acquired with NIRSPEC instrument at the 10m Keck II telescope. The determination of RVs was made using telluric absorption features as a wavelength reference. For each observation they created a model based on the combination of a telluric spectrum and a synthetically generated stellar spectrum. Both spectra were convolved by a parametrized instrumental profile and projected on a parametrized wavelength solution. The RV of the star was determined by minimizing the χ^2 of the fit. The RV precision achieved with this method was of 50 m s^{-1} for old field mid-M dwarfs. The observed RV dispersions for young stars were between 48 m s^{-1} and 197 m s^{-1}. These dispersions were affected by noise from stellar activity or stellar jitter. The contribution of this effect was determined by subtracting, in quadrature, the average instrumental noise of 46 m s^{-1}, and the calculated theoretical noise, equal to 40 m s^{-1}, from the observed dispersions. The dependence of stellar jitter with projected rotational velocity limited the precision of 77 m s^{-1} for the slowest rotating stars, 108 m s^{-1} for modest rotating stars, and 168 m s^{-1} for rapidly rotating stars. As expected, the NIR RV measurements decreased the RV noise caused by star spots by a factor of 3 compared to optical measurements, so no planet detection was obtained. The authors also determined the mass detection limits performing the Monte Carlo simulation at orbital periods shorter than 3, 10, 30 and 100 days. They obtained the average limits of 8.5, 13, 17, and 26 $M_{Jupiter}$, respectively.

Crockett et al. (2012) presented nine 1-3 Myr old stars of their multi-wavelength radial velocity survey of the Taurus–Auriga star-forming region. They performed visible and near-infrared observations with Coude' and CSHELL spectrographs, finding a typical reduction in RV amplitude in the NIR range by a factor of 2-3. Among these stars, they observed Hubble I, refining the analysis previously performed by Mahmud et al. (2011) with additional NIRSPEC data. They found a resolved RV modulation in the K band, but with a lower amplitude with respect to the optical curve, confirming its activity-induced nature. This result not only supports the argument that optical observations are not sufficient when looking for planets around young, active stars, but also NIR observations alone cannot be conclusive if they exhibit a modulation consistent with the presence of a companion.

Another target of their sample, CI Tau, showed an optical RV periodicity at 6.47 days, while the NIR periodicity was 10.87 days. While the NIR RVs did not phase with the VIS period and viceversa, they subtracted the NIR Keplerian fit from both datasets, obtaining a VIS phase-folded curve to 6.47 days clearer than the initial VIS fit. That led the authors to suggest that the optical RV modulation was a superposition of both spot and companion induced variabilities. In fact, later, Johns-Krull et al. (2016) claimed a young massive planet orbiting around this star with a period of 9 days. They used a larger sample spanning about 10 years consisting in visible data from the Coude' spectrograph and NIR data from CSHELL, NIRSPEC, Phoenix at the KPNO 4m Mayall telescope and IGRINS at the Harlan J. Smith 2.7 m telescope. They found that the full set of optical and IR RV measurements phase coherently with equal amplitudes to the 9 day period proposed by Johns-Krull et al. (2016).

Lagrange et al. (2013) observed 22 nearby young stars with ages $\leq$200 Myr and four other stars with ages greater than 200 Myr, in order to investigate the planet detection limits in young associations with RV data. They computed the detection limits with two methods, the rms-based method that measures the standard deviation of the RV series (Lagrange et al., 2009), and the local power analysis (LPA) method (Meunier et al., 2012). The detection limits depend on both the monitoring quality (time-span and sampling) and the characteristics of the stars (spectral-type, rotational velocity $vsini$, and activity/pulsations). No planets was found in their sample. They found that for low and moderately active stars the detection limits reach few Neptune masses for periods below 100 days. The best detection limits were obtained for low to moderate $vsini$ in the range 10-30 km s^{-1}, which are generally observed for stars older than 30 Myr. Detection limits increase at younger ages, but (sub-)Jupiter mass planets are still detectable.

Donati et al. (2016) announced the detection of the youngest HJ with the RV technique around the weak-line T Tauri star V830 Tau. They used ESPaDOnS and NARVAL spectropolarimeters, installed at the Cassegrain focus of the 3.6-m CFHT on top of Maunakea (Hawaii), and of the 2-m Bernard Lyot Telescope on top of Pic du Midi (France), respectively. They used the method of the Zeeman Doppler Imaging (ZDI) in order to reconstruct distributions of spots and plages at the stellar surface and model the activity, and the Least-Square Deconvolution (LSD), a multiline technique similar to cross-correlation, to derive line profiles with enhanced signal-to-noise ratio from thousands of spectral lines simultaneously. This method looks for the planet parameters that enable the best fit to the corrected LSD profiles. Then they filtered the initial RVs with this model. While the raw RV data exhibited the peak in the periodogram correspondent to the rotational period of 2.741 days, in the filtered RVs periodogram this peak disappeared and another significant peak at 4.93 days came up. Also the orbital curve showed an amplitude of 75 $\mathrm{m\ s^{-1}}$ against the initial amplitude of about 1 $\mathrm{km\ s^{-1}}$.

I present in this work my analysis on this targets with GIARPS observations in Sec. 3.3.

Yu et al. (2017) reported the detection of a HJ around the weak-line T-Tauri star TAP 26, from ESPaDOnS spectropolarimeter. They used different methods in order to search for a planetary signal in the observed data: filtering out the activity modelled by applying the ZDI method, the simultaneous fit of the planet parameters and the stellar activity (LSD method), and the use of Gaussian Process Regression to model the activity directly from the raw RVs. The planetary parameters found from all three methods are consistent each other, demonstrating the presence of a planet signature in the data with a period of 10.9 days.

For a list of confirmed/candidate planets younger than 1 Gyr see Table 1. in David et al. (2018). This table also includes the planet BD+20 1790b, that we ruled out (see Sec. 3.2), because their paper was published earlier.

However, the difficulties in dealing with the identification of planetary signals in presence of the very high magnetic activity levels of their hosts led to the retraction of some of the proposed HJs around young stars (see e.g. Carleo et al. 2018, described in this thesis at Sec. 3.2). The two claimed detections of HJs around WTTS in Taurus (Donati et al. 2016; Yu et al. 2017) from a sample of 20 objects points toward a frequency of HJs higher at very young ages with respect to that observed around old, field objects (1.0-1.5%).

1.3.3 The impact of telluric lines on RV measurements

Ground-based astronomical observations, in particular photometric and spectroscopic measurements, have to contend with the Earth's atmosphere, which presents absorption features that are resolved especially at high spectral resolution. These telluric absorption features result from rotational and vibrational transitions of several molecules including H_2O, O_2, O_3, CO_2, CH_4, and N_2O. Figure 1.4 by Smette et al. (2015) shows the absorption telluric spectrum in optical and NIR regimes, marking the major molecular species that contribute to the absorption.

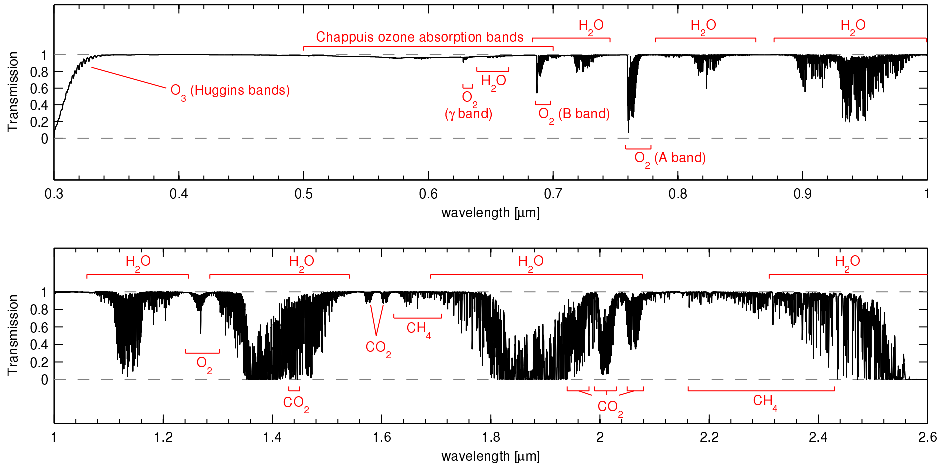

Figure 1.4: Synthetic absorption spectrum of the Earth's atmosphere. Figure taken by Smette et al. (2015).

While the optical region is dominated by broad absorption bands from ozone, narrow oxygen bands and some weak water vapour (H_2O) features, in the NIR regime strong roto-vibrational line systems of H_2O, CO_2 and O_3 hamper the J, H and K bandpasses. In addition, CH_4, O_2 and N_2O significantly contribute to the atmospheric transmission losses. Atmospheric transmission rapidly varies as a function of wavelength. The molecular species are distributed vertically through the atmosphere: H_2O, that dominates the whole telluric spectrum, and O_2, important at wevalengths <1.3 μm, are present at altitudes <5 km; CO and CH_4, that dominate the K band, is at 10 – 20 km; CO_2, important in the H band, is present at heights >30 km.

This rich set of absorption features provides a wavelength reference for RV measurements, as first proposed by Griffin & Griffin (1973). They used telluric O_2 lines as a wavelength reference, estimating a precision of 10 m s^{-1} for Doppler measurements of bright stars. However, while this does not require any hardware investment, telluric lines are likely not stable enough to provide a reference system for precision well below 10 m s^{-1}. In fact, temperature, pressure and chemical composition are variable seasonally, daily, and sometimes hourly. The absorbing molecules move with the wind, mainly horizontally, at velocities of 10 to 20 m s^{-1}, so the telluric absorption spectrum cannot be considered as a zero velocity reference. In addition, as described above, contributions of absorption regions come from a wide range of altitudes, and therefore pressures. This leads the shapes of telluric lines to be fundamentally asymmetric and their positions can change as the barometric pressure changes (Caccin et al., 1985). The shift due to wind and pressure is on the order of few tens of femtometers (Plavchan et al., 2015). Furthermore, the pressure broadens the H_2O lines that present widths of 0.01 nm and are resolved from high-resolution spectrometers. These lines of water vapour also significantly depend on atmospheric conditions and suffer significant temporal variations.

Variations in telluric absorption lines can impact broadband photometry when filters overlap with atmospheric features (e.g. Blake & Shaw 2011b, Berta et al. 2012), and also could affect ground-based transit spectroscopy observations (Mandell et al., 2011) and high-precision Doppler measurements, especially at NIR wavelengths. For this reason it is important to understand the impact of this complex Earth's atmosphere spectrum and separate its contribution from the scientific data. Different methods have been proposed, both empirical and physical. The most common method is to observe a telluric standard star (e.g. Vacca et al. 2003), that is an early-type star (mid B to late A) with very few or well determined intrinsic features. If there are no instrinsic features or are negligible (e.g. for low-resolution spectrographs), the simplest technique is to divide the target spectrum by the telluric one, removing the atmospheric absorption lines. However, telluric standard stars also have intrinsic stellar lines that are often not negligible (especially for high-resolution spectrographs), and the telluric correction leaves residuals in the final target spectrum. To overcome such a problem, Maiolino et al. (1996) proposed to use late FV and early GV, rather than A-type stars, as reference stars. They considered the high signal-to-noise ratio and high-resolution spectrum of the Sun, shifted to the appropriate radial velocity and convolved to the resolution of the observations. Dividing this solar spectrum to the observed GV star spectrum, they removed any intrinsic stellar features and obtained the correction telluric spectrum. However, this technique presents some practical problems, that are more evident when applying to high quality and resolution spectra: Hanson et al. (1996) specified that GV stars have many relatively faint metal lines that vary according to the age, chemical composition, *vsini* and temperature, making the match between these stars and the solar spectrum not so perfect. They then proposed to use an AV and a GV stars as telluric standards: the spectral regions of the AV star polluted by the H lines are replaced from the GV spectrum, and the resulting cleaned AV spectrum is divided from the object spectrum. The drawback of this method is the observing time necessary to observe two standard stars. As an alternative method, Vacca et al. (2003) presented a technique based on that one by Maiolino et al. (1996), observing and using an A0V star, as telluric standard, corrected from stellar features by fitting a high-resolution model of Vega's intrinsic spectrum.

The atmospheric spectrum has a high density of strong absorption lines and is affected by the same instrumental effects as the stellar spectrum, thus it provides a natural and intrinsically precise in-situ wavelength calibration. On the other hand, this empirical calibration has some disadvantages: observations of telluric standard stars are required, losing some telescope time, and it needs to be acquired at similar airmass and close in time to the science target. Also, the standard star should be bright enough in order not to compromise the final signal-to-noise ratio. For these reasons, in recent years, much effort has been put into developing physical calibration approaches, i.e. creating synthetic spectra of the Earth's atmosphere. The major advantage of this model technique is to avoid the intrinsic stellar lines problem and save precious telescope time. Seifahrt & Käufl (2008) performed the RV stability test of CRIRES, using a synthetic telluric spectrum as the wavelength rest frame reference. They obtained a constant RV with a precision of about 20 m s^{-1} for an M-giant star. They also investigated the intrinsic stability of the telluric lines at 4100 nm for features originated in the lower troposphere (SiO), obtaining an r.m.s. in the telluric RVs of about 10 m s^{-1}.

Details on the technique used for constructing the synthetic telluric spectrum are reported in Seifahrt et al. (2010), where the authors presented the LBLRTM (line-by-line radiative transfer code) method and input parameters to synthetise the telluric lines. In order to investigate the feasibility of the use of modeled Earth's atmopshere as wavelength calibrator and to remove it from stellar spectra, they compared the synthetic telluric spectrum to the observed one. In Fig. 1.5 by Seifahrt et al. (2010), this comparison is shown in the top panel, while middle and bottom panels show the subtraction and the division between the observed and computed telluric spectra, respectively.

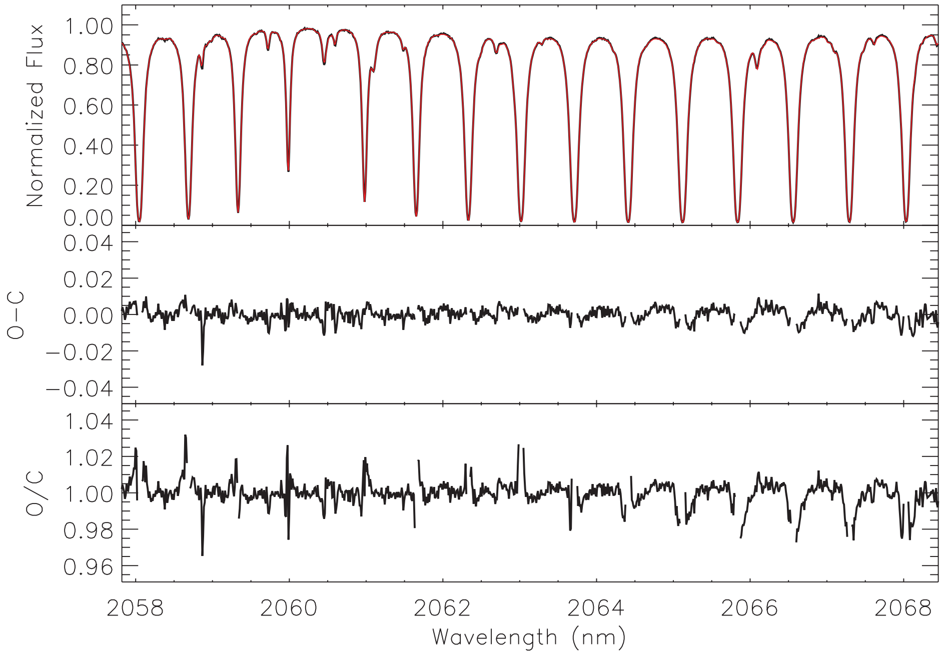

Figure 1.5: Figure taken by Seifahrt et al. (2010). *Top panel*: Comparison between observed (black) and synthetic (red) telluric spectra. *Middle panel*: the subtraction between observed and synthetic spectra. *Bottom panel*: the division between observed and synthetic spectra.

The model of the Earth's atmosphere spectrum matched the observed features up to 2% or better, demonstrating that it can be a good alternative to the usage of the telluric standard stars.

An important work on the stability of the atmospheric lines over long time scales and how these impact the RV measurements was performed by Figueira et al. (2010b), who carried out an extensive analysis of six years of archival HARPS data. They constructed a synthetic O_2 telluric mask from HITRAN database, cross-correlated it with Tau Ceti HARPS data and found an overall long-term Doppler precision of 10 m s^{-1}. Plotting the RVs over a full night as function of time, they obtained the top panel of Fig. 1.6, whose shape is justified in part by the changes in the bisector, as can be seen in the bottom panel of the same figure.

In fact, observing at different airmasses produces different absorption features. At higher airmass, much more molecules contribute to the absorption, producing larger, deeper and more asymmetric lines; this asymmetry impacts on the measured RVs. Moreover, also the pressure increase can contribute to the broadening and asymmetry of the absorption lines.

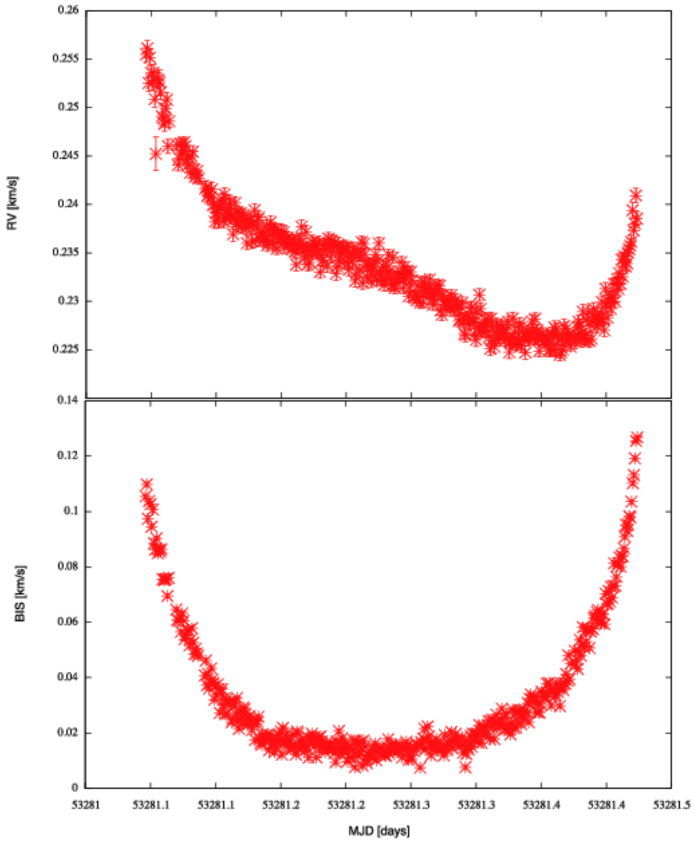

Figure 1.6: Figure taken by Figueira et al. (2010b). *Top panel*: RV values of Tau Ceti over a full night. *Bottom panel*: The corresponding bisector as a function of time.

However, as seen by the two figures, there should be other effects affecting the shape of the RV variations. The authors identified this effect in the horizontal wind and modeled the airmass and the wind patterns above the observatory with a simple, but physically motivated, model, described by the following formula:

$$\Omega = \alpha\left(\frac{1}{\sin\theta} - 1\right) + \beta\cos\theta\cos(\phi - \delta) + \gamma \tag{1.8}$$

where α is the proportionality constant associated to the airmass, β and δ are the average wind speed magnitude and direction, θ and ϕ are the telescope elevation and azimuth, respectively, γ is the zero-point of the RV. Taking into account this wind effect, the RV precision is improved to about 2 m s^{-1}, twice the photon noise. From this model, they found a predominant wind direction between N and NE of about 40 m s^{-1}, which perfectly agrees with the typical value for high-altitude winds on La Silla. They also found that on short time scales (1-8 days) and low airmass the precision is about 5 m s^{-1} without any telluric correction. This is due to the fact that the abundant species in the atmosphere, O_2 and CO_2, have a constant volume mixing ratio (v.m.r.) up to 80 km, so they are less sensitive to the short time scales weather variations.

The horizontal wind is one of the most important factors that impacts the variations in the telluric spectrum, that in turn affects the RV mesurements. Although with a different purpose than the astronomical science, it is worth to report the study by Stober et al. (2013) who investigated the horizontal winds through the MAARSY (Middle Atmosphere Alomar Radar System) on the island of Andoya in Northern Norway. The authors studied the nature of the mesospheric movements at 83.4 km, in particular the PMSE (Polar Mesospheric summer echoes) that are tracers of the atmospheric dynamics and allow to understand the variability of the horizontal winds.

The telluric modelling described in Figueira et al. (2010b) was also applied in a later work by Figueira et al. (2012), where the authors compared data from telluric standard stars observations and radiosonde measurements. During the site characterization for E-ELT (European Extremely Large Telescope) the atmospheric paramaters were studied. Among these, the Precipitable Water Vapour (PWV) is one of the major contributors to the opacity of the Earth's atmosphere, especially in the infrared range. The long time scale mean value of the PWV determines how good a site is for the IR astronomy. The goal of this work was to obtain the fitting parameters (α, β, γ and δ), from two different methods. The parameters derived from the telluric standards by the model described in the previous paper are compared with those obtained from the radiosonde measurements. While they cannot conclude anything about α and γ, the two approaches derived concordant results for wind magnitude and direction, β and δ in time segments of 2 hours.

A similar approach was previously adopted by Blake & Shaw (2011b), for the purpose of measuring NIR atmospheric extinction using GPS (Global Positioning System) receiver. They computed theoretical atmospheric spectra using the LBLRTM between 700 and 1050 nm, where the spectrum is dominated by the water vapour, highly variable in short timescales. Fitting these models with the high-resolution observations of A stars, they estimated the optical depths of H_2O absorption at different observing conditions (airmass), and compared this value with the PWV measurements by the GPS located at Apache Point Observatory, finding a strong correlation. Telluric templates matched line depths better than 2%, while regions with dense forest of lines have residuals of 5-10%. The authors simulated the impact of PWV variations on a long-term M dwarf survey, demonstrating that PWV changes have an effect of 0.003 to 0.004 mag, comparable to the signal from a super-Earth transiting a mid-M star. Moreover, changes in PWV can occur on short timescales, comparable to the duration of a transit. This method allows to empirically correct for extinction due to H_2O absorption and indicates that GPS measurements combined with the atmospheric models could be a powerful tool to improve the precision in NIR photometry, Doppler measurements and transiting surveys.

Thanks to the increased interest in Doppler measurements of cool, red stars, a substantial progress in near infrared instrumentation has been done until recently. Many authors have explored and developed different approaches to deal with the telluric lines, that are even denser in the NIR respect to the optical region. To cite some examples, Blake & Shaw (2011a) demonstrated the long-term stability of 10 m s^{-1}, simulating the impact of atmospheric variations on RV measurements of 100 late-M stars, using theoretical models of the composition of Earth's atmosphere. Rudolf et al. (2016) applied the method described by Seifahrt et al. (2010) to the X-Shooter spectrograph, whose spectral range spans from visible to NIR, and determined the abundances of the most dominant producers of telluric lines (H_2O, O_2, CO_2 and CH_4). Recently, Sameshima et al. (2018) introduced an hybrid method, that makes use of both telluric standard stars observations and theoretical models in order to extract the telluric spectrum from the observed one without the contamination of intrinsic stellar lines. This technique allows to reach accuracies better than 2% if the difference in airmass between the target and the telluric standard is $\lesssim 0.05$ and in time $\lesssim 1$ h. This result shows again that minimizing the time between the science and standard observations is crucial in NIR spectroscopy. As more and more NIR spectrographs are coming online, it is very important to be able to extract the maximum radial velocity information content by improving the telluric correction. In this context, a very instructive work is that by Figueira et al. (2016), where they simulated M-dwarf spectra with different rotational velocities, $vsini$, and spectral resolutions, and calculated the RV precision in three different conditions: the whole spectra as acquired from space, after discarding strongly telluric polluted regions with absorption deeper than 2%, and after applying a perfect telluric correction. In the following I report, as an example, one of their resulting plots (Fig. 1.7) with $vsini = 1$ km s^{-1}. The dashed lines represent the first case of simulated space observations, the circles the second case of partial correction, and the triangles the third case of a perfect telluric correction.

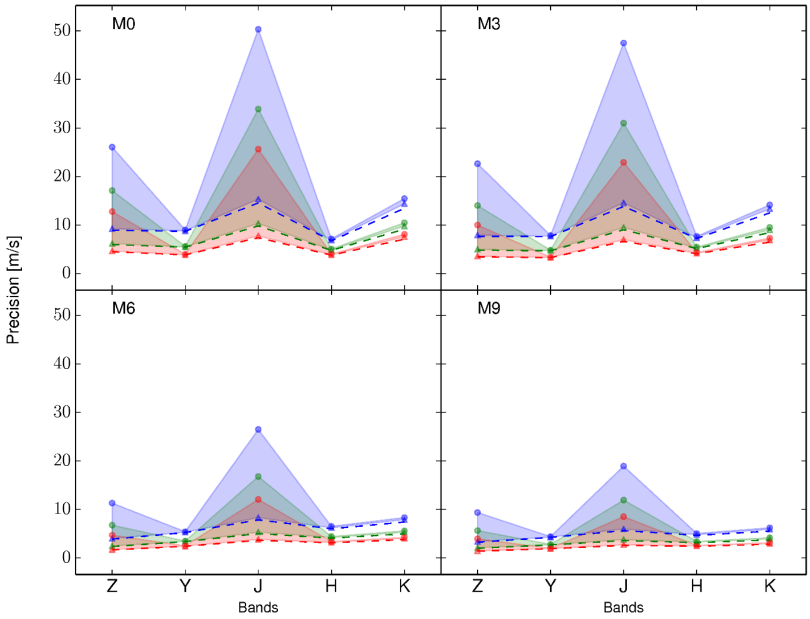

Figure 1.7: Figure taken by Figueira et al. (2016), showing precision achieved as a function of spectral band and four different spectral types. This plot represents the case of $vsini = 1$ km s^{-1}.

The general conclusion is that the most important parameter that influences the RV precision is the spectral type: late-M stars reach a precision twice better than early-M. Moreover, the modeling of the Earth's atmosphere has a significant impact on the regions discarded: fine-tuning of the rejection criteria could lead to different final precisions.

A similar work was conducted by Sithajan et al. (2016), who added the spectral coverage variable among the others. They simulated optical (0.38-0.62 μm), broad-optical (0.38-0.90 μm) and NIR (0.90-2.4 μm) spectroscopy observations, concluding that, since the NIR spectrograph can gain additional advantage of RV sensitivity over the optical one only for late M dwarfs and if telluric residuals can be subtracted to below 1%, the broad optical spectrograph can potentially be an optimal spectrograph for high precision RV surveys for low mass planets.

Overall, so far the RV precision in the infrared is worse than in the visible, mainly due to the denser presence of telluric lines at these wavelengths: up to now no NIR technique matched the precision achieved by visible methods, as the simultaneous Thorium calibration. The better NIR RV precision is around 5-10 m s^{-1} over periods of weeks against less than 1 m s^{-1} in the visible range with HARPS. Precise Doppler measurements will require improvements to the telluric correction techniques. This is also true for extremely precise new generation visible spectrographs like ESPRESSO, that aims for precision of ten cm s^{-1} (Pepe et al., 2010). In this regime, telluric lines with optical depth less than 2%, micro-telluric lines, become a disturbing factor in RV measurements: Cunha et al. (2014) found that the impact of micro-telluric lines on the RV calculation are already close to the precision of HARPS and become not negligible for more precise instruments. Figure 1.8 shows their result of the impact of micro-telluric lines as function of BERV (Barycentric Earth Radial Velocity) for different spectral type stars: a G-type star could be affected from this effect aliasing a planet.

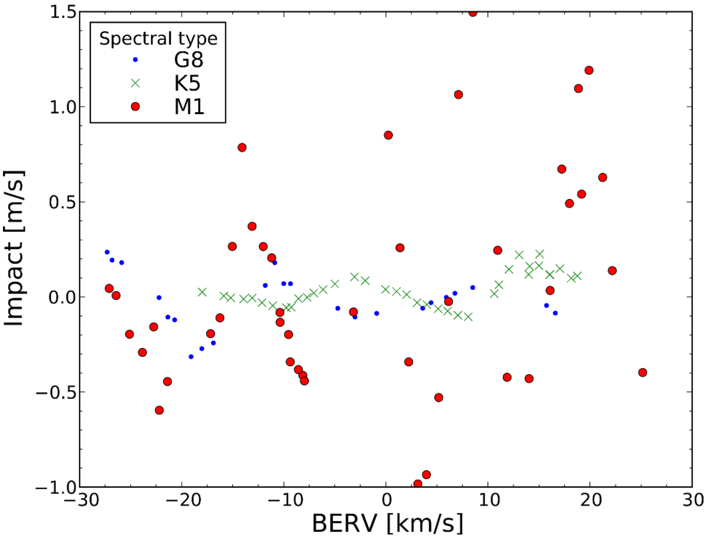

Figure 1.8: Figure taken by Cunha et al. (2014), showing the impact on RV measurements as a function of BERV for different spectral type stars.

Chapter 2

GIARPS

GIARPS (GIAno & haRPS – n, Claudi et al. 2017) is a project completely funded by WOW (see Sec. 2.1) devoted to have on the same focal station of the Telescopio Nazionale Galileo (TNG) both the high resolution spectrographs HARPS – N in the visible and GIANO in the NIR working simultaneously. This allows to have a unique facility in the northern hemisphere, providing cross-dispersed echelle spectroscopy at a high resolution ($\sim$ 110,000 in the VIS and 50,000 in the NIR) over a wide spectral range ($0.390 - 2.45\mu$m) in a single exposure.
In the following we describe in details the project, the instrument characteristics and the GIARPS realization and commissioning runs.

2.1 WOW and GAPS 2.0

WOW (A Way to Other Worlds) is a funding program in the framework of the *Progetti Premiali* of the Italian Ministry of Education, University, and Research. The purpose of the project is to fasten cooperation and sinergy within the Italian extrasolar planets community through the realization of several projects, all aimed towards the following main points:

1. The full exploitation of the planetary data obtained by the Italian community on national and international facilities.
2. The discovery of a few rocky planets around low mass stars, possibly in the habitable zone, with the Italian Telescope TNG.
3. An initial statistics of exoplanets (of various mass and temperature) in the solar neighbourhood and the estimate of their capability to host life.
4. A determination of the expected physical properties of exoplanetary atmospheres that will be observed with future planned instruments.
5. A *complete* database of the conditions that can be found in planetary atmospheres of our Solar System.
6. The definition of what is a biomarker.
7. Feasibility studies to improve the performance of already working facilities.
8. The definition of scientific requirements for the future instrumentations to be transformed in engineering requirements.

9. Feasibility analysis of new concepts for innovative instrumentations.

The last three points included funding of the refurbishment of GIANO based on the scientific requirements defined by the GAPS (Global Architecture of Planetary Systems, Covino et al. 2013) community, that gathers a large part of the Italian researchers working in the field of exoplanets. The GAPS project started in 2012, aiming to exploit the great capabilities of the HARPS – N high accuracy high-resolution spectrograph at TNG. It gathers more than 80 astronomers from several institutes of the Italian National Institute for Astrophysics (INAF) and Italian Universities (Padova, Torino and Milano). Technical and scientific support is also provided by a few collaborators from European and American Institutions. The original purpose of GAPS was the study and the characterization of the architectural properties of planetary systems through the radial velocity technique, by analyzing the distributions of planetary parameters and their correlations with those of the host star. After five years of HARPS – N observations and analysis, GAPS has developed an optimized observing strategy and new analysis tools, in particular for those objects which require many data and specific treatment of the RV time series, such as the more active stars.

In 2014 GAPS proposed to realize a new facility by joining existing equipment at the TNG, HARPS – N and GIANO, in order to have simultaneous multi-wavelength high resolution spectroscopy. In 2015 the GIARPS project, with Riccardo Claudi as Principal Investigator, Serena Benatti as Project Manager, and me as Instrument Scientist, took the first steps with the feasibility study and the subsequent hardware realization, supported by the specific effort from TNG and the Arcetri Observatory.

New perspectives are foreseen for GAPS using GIARPS that is now available at TNG with high impact on the exoplanetary research. The extension of the wavelength range will open to the GAPS community new scenarios and objectives in the study of the extra-solar planets. The second phase of the GAPS project called GAPS2.0 project, is focused on the study of a number of hot Jupiter atmospheres and the detection/confirmation of planets around a sample of young stars. At the beginning of 2018 GAPS has temporarily obtained the status of long program with GIARPS to start its new scientific program, that should be confirmed for further 4 years after the presentation to the TNG Time Allocation Committee and INAF Scientific Direction of the preliminary results. The first achievements of the RVs program on young stars are presented in Chapter 3.

2.2 The Visible arm: HARPS – N

Since April 2012 the high resolution echelle spectrograph HARPS – N Cosentino et al. (2012) is part of the equipment of the Telescopio Nazionale Galileo (TNG), after an agreement between the Italian National Institute of Astrophysics (INAF) and the HARPS – N Consortium[1]. HARPS – N is the Northern counterpart of HARPS Mayor et al. (2003), mounted at the ESO 3.6 m telescope in La Silla (Chile). Both of them are characterized by an extreme instrumental stability that allows radial velocities measurement with the highest accuracy available up to now, i.e. lower than 1 m s^{-1}. This accuracy will be improved in the near future by ESPRESSO (Pepe et al., 2010) at VLT. Figure 2.1 shows the internal errors of the HARPS – N radial velocity measurement as function of the SNR at 550 nm, for some of the

---

[1] Composed by Geneva Observatory (CH), INAF-TNG (Italy), CfA and Harvard University (USA), University of St. Andrews, Edinburgh, and Belfast (UK).

spectra collected in the framework of the GAPS project. For high values of SNR the typical HARPS – N internal errors range between 0.5 an 1 m s^{-1}.

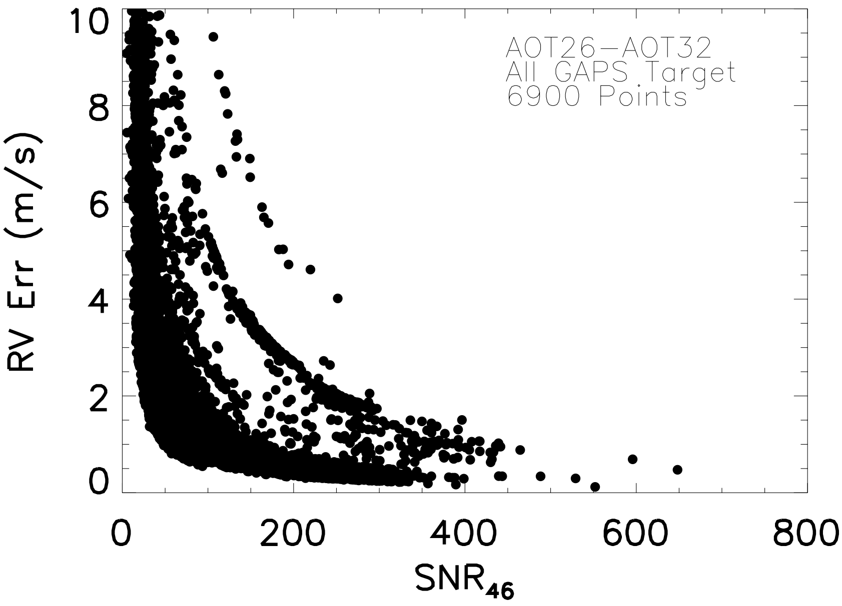

Figure 2.1: Typical internal errors of the HARPS – N radial velocity measurement as function of the SNR at the central order of the spectra.

HARPS – N is mounted at the Nasmyth B focus of TNG, and it covers the spectral domain from 390 to 690 *nm* with a mean resolution of 115,000. The instrument is composed by two main parts: the spectrograph, which is located in a separated room on the ground floor of the telescope building inside a vacuum vessel to minimize the vibrations and to ensure the required stability of temperature and pressure, and the Front End Unit (FEU), which is mounted on the Nasmyth B fork. These two modules are connected through an optical fiber link. The FEU is the first part of the instrument, where the incoming light from the telescope (or the calibration lamps) is injected into the fibers. The star image is maintained inside the entrance of the fiber thanks to a tip-tilt mirror acting together with the auto-guider system. The octagonal fiber link increases the light scrambling effect and guarantees a very high precision in radial velocity measurement, since it minimizes the spectrograph slit illumination changes due to the positioning error of the star in the fiber entrance. The two fibers have 1 arcsec aperture each: one is dedicated to the scientific object, while the second one is used for reference, e.g., the sky background or a Fabry-Perot interferometry [2]. The fiber entrance is re-imaged by the spectrograph optics onto a 4k×4k CCD, where echelle spectra of 69 orders are formed for each fiber. The spectrograph is mounted on a nickel plated stainless steel mount and contains no moving parts.

The HARPS – N integrated pipeline (Sosnowska et al., 2012) provides to the observer a complete reduced dataset only 25 seconds after the end of the exposure. The pipeline takes

---

[2] a laser comb reference is in realization and it is also partly funded by the WOW project.

into account the data images (calibration, bias, dark and scientific), performs quality control and executes a complete data reduction. The radial velocity measurement is performed through the application of the cross-correlation function (CCF) method. The acquired spectrum is cross-correlated with a specific template, called mask, that depicts the typical features of stars with different spectral types (see Pepe et al. 2002 and reference therein). The output is a set of data including the reduced frames, wavelength-calibrated spectra and the parameters of the CCF, e.g. the Full Width Half Maximum of the CCF, the radial velocities with the corresponding uncertainties, the bisector velocity span.

2.3 The NIR arm: GIANO/GIANO – B

At the beginning of 2015, TNG offered for the first time to the scientific community GIANO (Oliva et al., 2006), its new near infrared (NIR) high resolution echelle spectrograph. GIANO is a cross disperser echelle spectrograph; cross dispersion is provided by a sequence of three prisms used in double-pass mode. After the commissioning and science verification observing runs in 2013 and 2014, GIANO demonstrated its capability to fulfill the required performances, reaching for instance a reasonably good accuracy for the radial velocity measurements (~ 10 m s^{-1} on short time scales, Carleo et al. 2016). A single exposure with GIANO produces a spectrum ranging from Y to K band (0.95 - 2.45 μm) with a resolution of 50,000 (Origlia et al., 2014). Almost the whole spectral range is observed in a single exposure, with only small windows lost in the K-band, due to the optical design that creates curvature of the redder echelle orders, the edges of which fall outside the detector.

The GIANO spectrometer is mounted on a rigid aluminum bench, thermally connected to a LN2 tank. Following the light path of the instrument from the entrance window, the spectrometer includes a flat window, a cold stop, a filter wheel, a slit, the spectrometer optics (7 mirrors, 3 prisms used in double-pass mode, 1 echelle grating) and a $2\mathrm{k}^2$ HgCdTe detector array. All of these elements are included inside a vacuum chamber (see Figure 2.2) which is permanently connected to all the sub-systems (pipelines, valves, pumps, sensors, PLC), necessary to create, maintain, monitor and control the vacuum and the cryogenic status of the spectrometer. All the operations are performed and supervised by the PLC (Programmable Logic Computer), controlled through a dedicated panel.

GIANO was originally designed and realized to be mounted at the Nasmyth B focus of the TNG, directly fed by the light coming from the telescope. Anyway, due to scheduling issues of the TNG it was re-adapted and mounted at the Nasmyth A, and fed by IR-transmitting ZBLAN fibers. In this configuration (thereinafter GIANO – A) the instrument was composed by two main modules: the cryogenically cooled spectrograph and the warm preslit and interface system. The preslit system also included a fiber mechanical agitator and rackmount with the electronics and the calibration lamps. An additional rack–mount contained the detector warm electronics and controls.

The GIANO – A preslit box was optically connected to the spectrograph by a couple of fibers optics, used to simultaneously observe the target and the sky. The core diameter of each fiber was 85 μm (1 arcsec on sky), the distance between the two fiber centers was 250 μm (3 arcsec on sky). A third fiber was used for calibration, and can be illuminated either by a halogen lamp for flat–field or by an U–Ne lamp for wavelength calibration. The introduction of the fibers, due to constraints imposed by the telescope interfacing during the pre–commissioning phase, significantly reduced the end–to–end efficiency of the instrument.

Figure 2.2: GIANO vacuum vessel, fiber agitator, LN2 tank and the electronics in the Nasmyth A of TNG (Claudi et al., 2016)

It also introduced a non repeatable wavelength-dependent spectral modulation (modal noise)[3] that could not be corrected by flat-fielding, limiting the signal to noise ratio achievable in the spectra, regardless of the brightness of the star and integration time. For this reason GIANO – A used a mechanical agitator to decrease the effect of fiber modal noise. This mechanism worked quite well for diffuse sources like the calibration lamps, but for observation of scientific targets, the modal noise was amplified by effects related to the non-uniform illumination of the fiber (which also depended on the seeing conditions and on the tracking/guiding performances of the telescope). In stellar spectra acquired in non optimal observing conditions the residual modal noise could be as high as a few percent, especially at longer wavelengths (K band), thus limiting the overall signal-to-noise ratio.

The GIANO echellogram has a fixed format and includes about 50 orders, covering the 0.95-2.45 μm wavelength range. It has a full spectral coverage up to 1.8 μm, while at the longest wavelengths the spectral coverage is about 75% (see above). Due to an image slicer, each 2D frame contains four tracks per order, two for each fiber. Observations of science targets are generally performed by nodding-on-fiber, i.e., target and sky are taken in pairs and alternatively acquired on fiber A and B, respectively. From each pair of exposure an “A–B 2D–spectrum” was computed, then extracted and summed together for an optimal subtraction of the detector noise and of the sky background. An example of the positive (on A fiber) and negative (on B fiber) spectra of a target star obtained with GIANO – A is shown in Figure 2.3.

2.4 GIAno & haRPS – n: GIARPS

GIARPS is the new configuration of GIANO and HARPS – N that allows the simultaneous use of the two spectrographs, exploiting therefore a wide wavelength range (0.390 - 2.45 μm) with high resolution (115,000 in the visible and 50,000 in the NIR) obtained in a single

---

[3] The fiber mechanical agitator previously mentioned was needed to alleviate the strong modal noise generated by the ZBLAN fibers

Figure 2.3: Science 2D – spectrum obtained with the sum of each pair of A–B spectra.

exposure. The two instruments are also able to work separately, so with GIARPS the TNG provides three different observing modes for high resolution spectroscopy: *a*) HARPS–N only (maintaining the original optical configuration of the HARPS – N front end with the already existing mirror); *b*) GIANO only; *c*) both GIANO and HARPS – N splitting the light with a dichroic beam splitter.

The simultaneous use of the two spectrographs has been possible by moving GIANO from Nasmyth A to Nasmyth B focus of TNG, allowing the spectrograph to operate as originally designed. The main activity of the GIARPS project was therefore the modification of the configuration of GIANO, now called GIANO – B, that had to be fed by a new train of preslit optics instead of the fibers. This also provided a significant improvement in the instrument performances, since the modal noise was removed and efficiency increased.

A rigid structure fastened the GIANO – B dewar to the fork of the TNG (see Figure 2.4) by keeping the cryostat axis parallel to the elevation axis of the telescope. The structure was thought in order to sustain a burden of about 2000 kg and it is rigid enough to avoid vibration modes to those naturally generated by the movements of the telescope (jitter, tracking etc.). However, this structure is open, so that its temperature follows the variations in the Nasmyth room. While this has a minor impact on the radial velocity stability of GIANO – B, it requires a careful focusing of the system to avoid loses in the efficiency. The resulting structure is shown in the picture taken at the end of all operations (Fig. 2.5).

The new GIANO – B preslit optics is fully described in Tozzi et al. (2016): with reference to Figure 2.6 a brief description is given in the following. The light coming from the Nasmyth focus of the TNG meets at first a dichroic that reflects the visible light toward the HARPS–N front end unit (FEU) and transmits the near IR light to GIANO – B. This dichroic is mounted

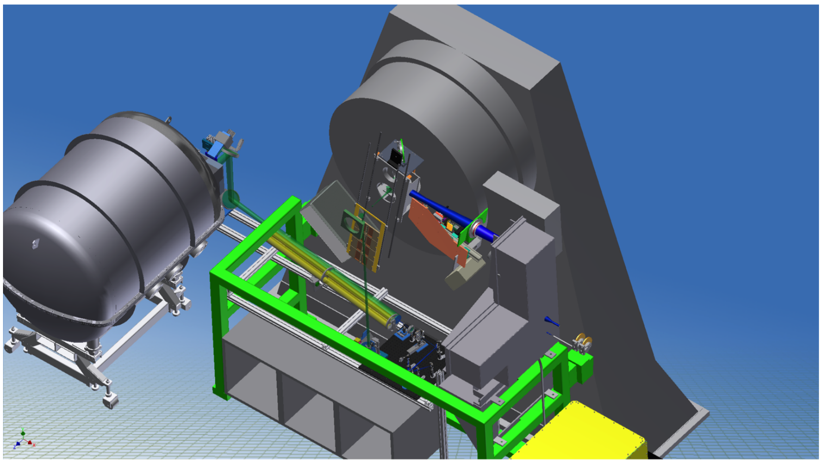

Figure 2.4: Mechanical solution for the housing of GIANO (left side) in Nasmyth B. The new preslit is located inside the SARG gage (green structure).

Figure 2.5: Picture of the final structure as mounted at TNG.

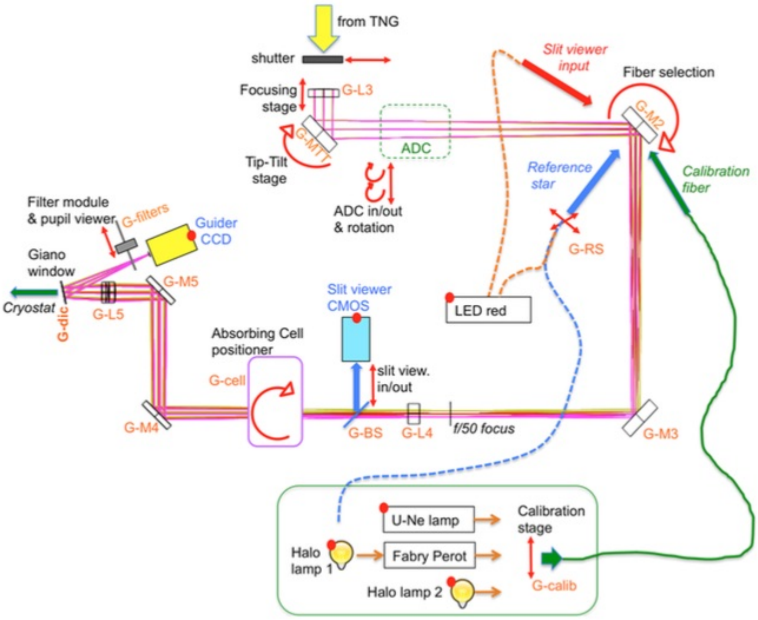

Figure 2.6: Scheme of the new optics for GIANO – B, necessary to obtain the and use it simultaneously with HARPS–N Tozzi et al. (2016).

on a slide in the Nasmyth box that allows to select the preferred observing mode. In the case of GIARPS observing mode, the dichroic is inserted. The near IR light is firstly directed towards the re-imaging module (the pick up module) inside the Nasmyth box of interface with the instruments. The pick up creates an intermediate focus below the de-rotator, in the volume previously allocated to the SARG spectrograph (Gratton et al., 2001). The light is then redirected towards the G-L3 module in order to correct and optimize the focusing of the stellar image onto the slit of the NIR spectrograph. Just after G-L3 there is a tip tilt mirror (G-MTT). The next optical elements, G-M2 (rotatory mirror) and G-M3 (fixed mirror) are used to select the calibration input from the calibration unit. The latter is beneath the preslit plane and is equipped with a U-Ne lamp, a halogen lamp and a Fabry Perot selectable by a translation stage.

After that, a rotating stage can be inserted to host an absorption cell that could equip GIANO – B in the near future. Actually, a feasibility study is ongoing and this kind of device would provide a stable reference spectrum for high precision radial velocity measurements. According to this study, to minimize systematic errors the gas cell will be filled with gases (in particular acethylene, ammonia and an isotopologue of methane) at very low value of pressure aiming to reduce the pressure-induced line-shifts and to exploit the intrinsically narrower lines for very accurate wavelength reference. Since for a given mixture of gases, a long cell filled at low pressure should be always preferred to a shorter cell filled at higher pressures, we use the maximum space/length available within the volume previously allocated to SARG, in order to have a 1.5m-long cell. In this configuration the light is brought inside the GIANO – B dewar by means of a set of optics (the periscope G-M4/G-M5 plus the re-imaging lens G-L5) that allows also to focus the light onto the entrance slit of the spectrometer. Finally, a slit viewer allows in daytime to find the exact position of the slit on the guiding camera, providing a better centering of the star during the night-time observations.

2.5 GIARPS Science case

The GIARPS science case is very broad, given the versatility of such an instrument and the large wavelength range. A number of outstanding science cases can be considered, in particular in the field of the exoplanet science.

Observation of hot planet atmospheres. Transiting extrasolar planets present a unique opportunity to study their atmospheres. Wavelength dependent variations in the height at which the planet becomes opaque to tangential rays will result in wavelength-dependent changes in the ratio of spectra taken in and out of the transit. Several groups (Swain et al. 2008; Swain et al. 2009; Beaulieu et al. 2010, Tinetti et al. 2010, Kreidberg et al. 2014, Stevenson et al. 2014, Evans et al. 2015, Evans et al. 2016) have pursued transmission spectroscopy and secondary occultation measurements detecting absorption signatures of several atoms (Hydrogen, Oxigen and Carbon in the visible and UV) and molecular signatures (in near and mid IR) from water, methane, carbon monoxide and dioxide. While most of these results have been obtained by space-based observations, several efforts to obtain ground based observations have been performed in the recent years, resulting in ground-based optical and NIR detection of transmission features (Redfield et al. 2008, Snellen et al. 2008, Sing et al. 2009, Sedaghati et al. 2017, Brogi et al. 2018, Casasayas-Barris et al. 2018) and eclipse measurements (Sing & López-Morales 2009, de Mooij & Snellen 2009, Croll et al. 2010,de Kok et al. 2013, Birkby et al. 2013, Nugroho et al. 2017). Ground-based transmission spectroscopy could also be very fruitful in the near IR, where high spectral resolution can resolve molecular absorption bands and can be used to combine the signal of tens to hundreds of individual molecular absorption lines (from e.g. water, CO, or methane). In this framework, GIARPS, with its resolution and wavelength range extending from visible to near IR, represents a good opportunity to obtain spectroscopic information on hot small mass companion atmospheres. The molecules that will mainly be targeting with GIARPS are O_2, H_2O, CO_2 and CH_4, which are all molecules with large broad absorption bands in the visual to near-infrared part of the Earth transmission spectrum (Pallé et al., 2009). In addition, during secondary eclipse, the planet passes behind the star and one can measure the planet's radiation directly by subtracting the photometric measurement during an eclipse from the measurement before or after the eclipse. Of about 1,000 transiting exoplanets, only a small fraction are bright enough ($V < 12$) to be suitable for atmospheric studies, but a larger number of candidates orbiting bright stars will be provided in the near future by the NASA TESS satellite, recently launched (Spring 2018).

Search for Giant planets around young nearby stars. Giant planets (GPs) play a crucial role for (exo)-planetary systems as they shape their final architecture, due to their strong impact on the dynamics and on the fate of lighter bodies in the system. They represent a significant part of the planets detected so far. However, we are far from having a complete knowledge of their occurrence, diversity and properties as GP exploration with RV or transit techniques is limited today to typically 5 AU from the stars (and even closer, 1 AU, for transiting planets). The outer population will remain mostly out of reach of deep imagers until the ELT era.

GAIA should allow to detect giant planets at separation of a few AU, up to distances of several tens of parsec, then including several thousand stars. However, this detection requires use of the full GAIA dataset, and should then be possible only with the latest release of GAIA data, later than 2022. Current release of GAIA data (DR2: April 2018) does not provide orbital solutions. Microlensing also allows in principle a quite good coverage of the separation-mass diagram. However, it only provides istantaneous images of systems, and can then be used only for statistical arguments. Detection of microlenses events including giant planets are slowly cumulating, but still a small number of such events have been found (Skowron et al., 2015).

Young stars (a few Myr to a few hundreds Myr) are then the only sources that could, in the near future, allow complete (mass-period) exploration of the giant planet population, using both current and next generation of planet imagers and high precision spectrographs. In fact, young GP have not completely cooled out and are still hot enough to be detected by direct imaging, and their detection from Doppler signal of the star is also within the reach of high resolution spectrographs, given that good enough precision can be reached despite the high activity levels of the host stars. Given their ages, young stars are also unique laboratories to study on–going formation processes and the building–up of planetary systems and get direct information on the associated timescales (e.g. migration of hot-Jupiters). In addition, young systems give the possibility to test and calibrate evolutionary models, and in particular the controversial mass-luminosities predictions at young ages: ”hot- start” and ”cold-start” models, which differ by the respective amounts of energy lost/available to heat the planet at early stages (Fortney et al., 2008). In this context, coupling imaging to RV data offers a unique opportunity to do so, by directly estimating/constraining the dynamical masses of imaged planets, as done in the case of β Pic b (Lagrange et al., 2012). Up to now, young stars have been mostly avoided in RV surveys as they are usually active, hence 1) more rapid rotators than their older counterparts (hence not well suited for masking techniques), and 2) their stellar jitters are higher than those of their Main Sequence counterparts, which a priori affects planet detectability. The first pioneering detection of a young HJ with the RV technique was recently announced around the weak-line T Tauri star V830 Tau using spectropolarimetry (Donati et al. 2016, Yu et al. 2017, Donati et al. 2017), after years of attempts marred by difficulties in dealing with the identification of planetary signals (both spectroscopic and photometric) in the presence of very high levels of activity of their young hosts.

Several studies (see e.g., Huélamo et al. 2008, Bailey et al. 2012, Prato et al. 2008, Mahmud et al. 2011, Crockett et al. 2012) have demonstrated that the stellar jitter is significantly lower in the IR, even for the most active stars. Also, it has been demonstrated that high resolution IR spectrographs such as VLT/CRIRES can reach precisions down to 5 m s^{-1} (see e.g., Seifahrt & Käufl 2008, Bean et al. 2010), allowing to detect close companions well within the planetary regime. The simultaneous use of high resolution and wide wavelength range from spectrographs like GIARPS, offer the unique opportunity to combine both techniques to constrain the giant planet population at all periods and test theories of planetary formation and evolution.

Search for hot planets around cool stars. The study of M-type stars is gaining momentum as an alternative ”fast track” method to discover and possibly characterize hot and temperate rocky exoplanets[4]. M–type stars are the most abundant type of stars in our

---

[4] It should be noticed that most cool M-stars are very active even at old ages (Robertson et al., 2013). A

Galaxy, and therefore obtaining statistics of planet occurrence and architecture around these stars is of great importance for understanding the physics of planet formation and evolution and its dependence on stellar host mass. Planet searches around M–type stars (with masses in the range of $0.1 \div 0.6$ $M_\odot$) have the main advantage of the larger RV signal, the smaller star-planet contrast and the shorter orbital period of the Habitable Zone (HZ). This has been exploited to find some of the low-mass Super-Earth exoplanets known so far both with RV (Mayor et al. 2009, Anglada-Escudé et al. 2012, Anglada-Escudé et al. 2016, Reiners et al. 2018) and transits (Charbonneau et al. 2009; Bonfils et al. 2013a, Gillon et al. 2016, Dittmann et al. 2017), although the current number of detections is still low compared with solar analogues. In spite of that, recent studies from ground–based RV programs carried out with state–of–the–art facilities (HARPS) indicate that Super–Earths with 6–10 Earth masses within the HZ of low-mass stars appear ubiquitous (Bonfils et al., 2013a). Recent analyses of Kepler data have only further corroborated this evidence (Dressing & Charbonneau 2013; Kopparapu 2013, Yang et al. 2014, Dressing & Charbonneau 2015). For the solar-neighbourhood sample, in particular, the abundance of planets as a function of mass and orbital distance is very loosely constrained. In addition, all the results obtained from RV surveys are only valid for M-type stars of spectral types earlier than M2 or M3 (mass of $\sim 0.4 M_\odot$. The faintness of the targets and the intrinsic stellar jitter have traditionally limited the investigation of even cooler and lower mass stars. Near–IR, high–precision (¡ 10 m s^{-1}) RV observations can be efficiently used to detect low–mass (potentially habitable) planets around stars with spectral types later than about M3. RV measured in the near–IR are also less susceptible to stellar activity noise, so, the amplitude of the RV signal is expected to be smaller in the NIR range than in the visible one (Reiners et al., 2013). The derivation of RV from both optical and NIR spectra (preferably simultaneously) provides then a unique opportunity to discriminate between stellar and Keplerian RV signals, and helps to confirm or retreat a planet candidate, in principle with only one dataset.

Search for giant planets in open clusters. More than 2000 extrasolar planets have been discovered so far, by employing different techniques. After the pioneering era, when the discovery of a single planet was a notable event, it is now time to start the more complex work of planet and planetary system taxonomy, trying to put some order among these detections and eventually understand why they are so different from each others. Nearly all planets known so far belong to isolated field stars, whose parameters (distance and age, above all) are still very uncertain. Consequently, the stellar mass and radius are affected by large errors, and this transfers directly on the precision we can estimate planet parameters. Errors increase with stellar distance, making the effort to put planet properties in context even more difficult.

Planet search in star clusters, in particular open clusters (OCs), offers an interesting and very appropriate laboratory. OC star distances and ages are much better measured than for field stars, and OCs span a wide range of parameters in terms of age, metallicity, stellar density. Main sequence stars are the best targets, as they have low stellar activity, and make (low mass) planet identification easier. Planet-star interaction is

---

consideration of the impact of activity on the atmospheres of planets around such star is beyond the scope of this thesis. However, it may significantly affect actual "habitability" of such planets (Roettenbacher & Kane 2017, Wheatley et al. 2017) more straightforward to measure than, e.g., in giant, evolved stars. OC stars are chemically homogeneous, so the effect of the presence of a planetary system on the host star chemistry can effectively investigate, including the possible link between lithium abundance and presence of planets proposed by Israelian et al. (2009). Most importantly, we can gather information useful to solve the long standing problem on how the planet frequency depends on stellar metallicity. For instance, are giant planets more frequent around metal rich stars because more metal rich environments are more effective in creating (massive) planets, or because of the pollution and planet cannibalism (Desidera et al., 2006) effects due to the presence of a planetary system orbiting the parent star? From the comparison of rotation and activity properties of planet hosts with those of other cluster members we get robust inference on the possible role of close-in planets on the evolution of stellar angular momentum (Lanza, 2010). On the other hand, planet formation might be influenced by the stellar environment, that may also affect the long-term evolution of the planetary system. Comparing properties of planetary systems in different environments if then of high interest.

Of course, these investigations need a statistically significant sample of planets and the number of planets discovered in OCs is still very small (Malavolta et al., 2016). A survey to search for giant planets around two intermediate-age, close OCs has been performed with HARPS – N within the GAPS large programme, targeting late F, G and early K stars. With GIARPS it is possible to extend the search to late K and M dwarfs, obtaining the broader search ever attempted in term of spectral range and stellar mass for giant planets in stars that share the same origin, exploring efficiently the MS of the clusters.

Not only exoplanets but also other science cases like young stars and proto–planetary disks, cool stars and stellar populations, moving minor bodies in the solar system, bursting young stellar objects, cataclysmic variables and X-ray binary transients in our Galaxy, supernovae up to gamma–ray bursts in the very distant and young Universe, can take advantage of the unicity of this facility both in terms of contemporaneous wide wavelength range and high resolution spectroscopy.

2.6 Preparatory work for GIARPS

Before the integration of GIARPS at TNG, a feasibility study as well as a scientific and technical preparation were necessary to define the major issues of the project. In this phase my direct contribution, as Instrument Scientist, concerned a study about the impact on the RVs due to the insertion of a gas cell in the optical path of GIANO – B (Sec. 2.6.1) and the statement of the requirements for a new Data Reduction Software (DRS) for GIANO – B to be optimized for the new long slit configuration (Sec. 2.6.2) and the GIARPS Calibration Plan (Sec. 2.7).

2.6.1 Simulation of RV measurements with the absorption cell

Simulation Purpose

In Carleo et al. (2016) I described my procedure for RV calculations (see also Sec. 2.9), that is based on two key points: the telluric lines are used as wavelength reference, and the Cross

Correlation Function (CCF) method determines the velocity for both the star and the telluric lines. Applying this method to various targets observed with GIANO in Nasmyth A, having different spectral types (from $K0V$ to $M8$), we reached different accuracy, mainly depending on the H magnitude of the target: for an H magnitude of about 5 we obtain an rms scatter of $\sim$ 10 m s^{-1}, while for an H magnitude of about 9 the standard deviation goes up to $\sim$ 100 m s^{-1}, as the Figure 2.7 shows. A discussion of the limiting factors in our RVs is given in Sec. 3.6. For bright sources, stability of the telluric reference is a significant contribution.

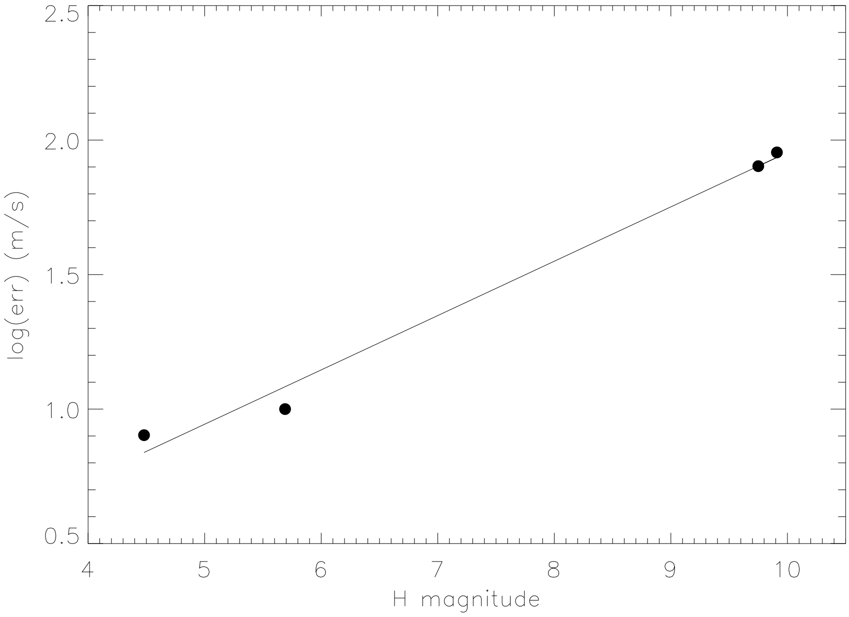

Figure 2.7: The error in the RV measurements depending on the H magnitude with the corresponding best linear fit.

A possible improvement in the precision of radial velocity measurements can then be reached with the introduction of an absorption gas cell in the GIANO optical path, providing a more reliable reference in comparison with the instability of the telluric spectrum. In order to understand how much this improvement can be relevant, our method has been applied simulating the presence of an absorption gas cell. In this preliminary approach, use of CCF method combines simplicity and enough accuracy needed in this analysis. A more detailed description is given in the following section.

Pre-reduction of the cells

The cells we considered contain a mixture of acethylene, ammonia and an isotopologue of methane at low pressure. Expected absorption spectra of these cells have been provided by Dr. Ulf Seemann, responsible for the feasibility study of the GIANO – B absorption cells. Three such spectra were available, one in HK band and two in J band. We have done a series of steps to adapt these cell spectra to the GIANO spectral format.

- *Conversion in wavelength*: First of all, being the original cell spectra in wave-number, we have converted the steps in wavelength.

- *Orders' creation*: The cell spectra were then divided into 50 orders, as in the case of the GIANO spectra.
- *Resolution reduction*: In the case of different resolutions among scientific spectra and cell spectra, it is necessary to uniform the spectral resolution. In our case, cells and GIANO spectra have a quite comparable resolution, so this point was unnecessary.
- *Re-sampling*: we re-sampled the cell spectra to have a very dense sampling and a constant step in RV.
- *Cell lines list and mask creation*: At this point we created a list of good lines in the cell spectrum, which allows to create the cell mask, similar to the mask used by the HARPS – N DRS. This mask was then employed for the measurement of radial velocities.

Results

The simulation of RV measurements with an absorption cell in the GIANO – B design was performed with the method described in Sec. 2.9, using the CCF method to compute the RVs. We were provided by three cell spectra: one for HK band and two for J band (named $J1$ and $J2$). We considered measurements of radial velocity obtained first with telluric lines as reference, and then with various combinations of the cells: $(J1, HK)$, $(J2, HK)$, $(J1, J2, HK)$, and finally using the HK cell alone. This analysis has led to some very promising results, summarized in the Table 2.1.

Table 2.1: Summary of the errors resulting from the RV measurements simulating the presence of the cell for different SNR.

	Median SNR 75	Min SNR 32	Median SNR 133	Min SNR 91
	Median int err (m s^{-1})	Max int err (m s^{-1})	Median int err (m s^{-1})	Max int err (m s^{-1})
Telluric	15	34	7	10
Cell J1+HK	12	25		
Cell J2+HK	12	25		
Cell J1J2+HK	12	25		
Cell HK	12	25	5	8

Comparison between telluric and cell analysis. After analysing the data, first with telluric lines and then with the cell simulation, we have found that the internal error in the first case is larger than in the second case. The Table reftab:errcell shows the results obtained for a target with a low signal-to-noise-ratio (SNR), and for another one with a higher SNR. In the first case the measurements of radial velocities with telluric lines as wavelength reference have a median internal error of 15 m s^{-1} corresponding to the median SNR (75), and the largest internal error is 34 m s^{-1} related to the lowest SNR (32). By using the cell simulation, the median internal error goes down to 12 m s^{-1} with the worst internal error of 25 m s^{-1}. These numbers do not change for all combinations of the cells, as explained in the following paragraph. Regarding the second target, the higher is the SNR, the lower is the internal error, leading to a better result, as represented in the Fig. 2.8 in terms of H magnitude and Fig. 2.9, in terms of SNR . Starting from the relation between the internal error and the SNR, we found that the radial velocities measurement with telluric spectra yields an error given by 1019/SNR [m s^{-1}], whereas with the HK cell the error is given by 775/SNR [m s^{-1}]. Hence the HK cell allows a gain of a factor of 1.3 in the internal errors.

Combinations between J and HK cells. As previously mentioned, in this simulations we considered measurements of radial velocity obtained for telluric lines and four combinations of the cells. In all cases we examined the contribution to the final RV provided by the individual orders of the specrtum. In all case we found that the RV measurements are mainly provided by HK spectrum, since the spectra of the $J1$ and $J2$ cells show lines in a small number of orders. So we can conclude that the HK cell is more optimized for RV extraction.

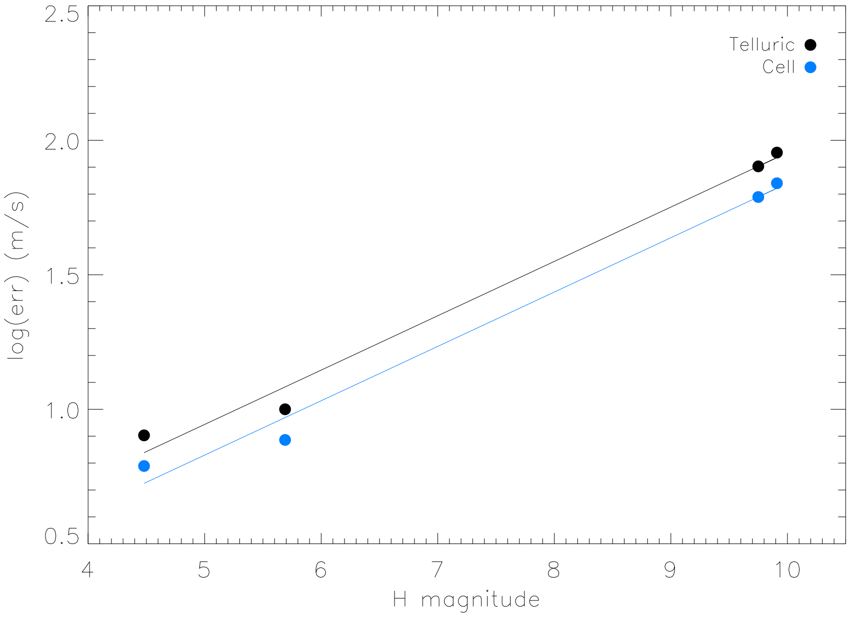

Figure 2.8: The error in the RV measurements depending on the H magnitude from telluric analysis (black dots) and from cell simulation (cyan dots) with the corresponding best linear fits.

To conclude, the possibility to use a cell during GIANO observations seems to lead to a significant improvement in the RV measurements for high SNR observations, while the loss of transmission, due to the stellar light absorption of the gas cell, is expected to offset the gain we could obtain for low SNR observations. Moreover, the HK cell alone is sufficient, considering that the addition of a J cell does not give further significant improvement.

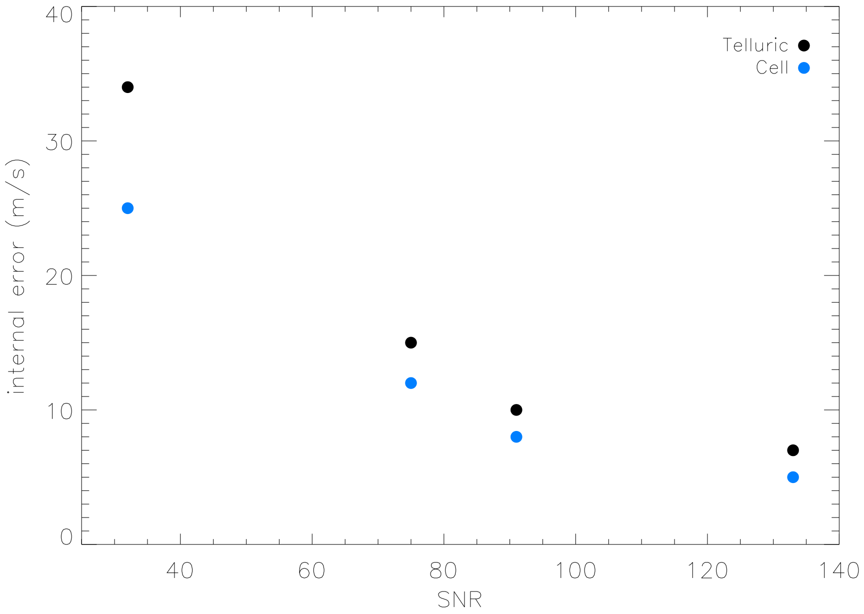

Figure 2.9: The error in the RV measurements depending on the SNR from telluric analysis (black dots) and from cell simulation (cyan dots).

2.6.2 Data Reduction Software requirements

The DRS for GIANO in the previous configuration (Nasmyth A and fiber-fed) performed standard echelle data reduction and additional procedures due to the particular appearance of GIANO spectra, i.e. the spectra by the two fibers further divided by a slicer, that resulted in 4 traces for each aperture. Once GIANO – B has been directly fed by the telescope and the instrumental configuration has been equipped with a long slit, the definition of the geometry of the apertures was completely changed and a new DRS was needed (we called this new DRS GOFIO, Rainer et al. 2018).

GOFIO processes all the calibration files (darks, flat-fields and wavelength calibration lamps) and the scientific images, observed both in the nodding and stare mode. According to the scientific target to observe, it is possible to select a specific type of acquisition, aiming to properly remove the thermal background which is crucial for infrared instruments. In the nodding mode (mostly used for point sources) the target is alternatively observed in two well defined positions of the slit and subsequently subtracted one to each other. A different method is used for extended objects, where the target is positioned in the center of the slit, which is entirely illuminated. In this case the background subtraction is performed by using sky spectra acquired close to the region of the target (stare mode).

I defined the requirements for GOFIO and its outputs. The first important request was to organize the DRS in clearly defined blocks or modules, each one executing well defined steps of the data reduction as well as the RV extraction. Furthermore, the software was required to be available in the following two modes:

Online or Pipeline mode : GOFIO should be available at the telescope providing real time data reduction during the observations. The online DRS displays information that the observer can use to check the instrument status and prioritize observations during the night (e.g. observe only bright targets if the SNR is lower than expected due to bad weather). At the end of every observation (providing a set of scientific and calibration raw files) the software processes the data with fixed parameters, providing reduced spectra that can be used for scientific analysis. The parameters are chosen to provide the most efficient (and fastest, if needed) data processing.

Offline or User mode : GOFIO should be available for offline data reduction either as a downloadable package or through a web interface. The offline DRS is required to be as customizable as possible. Offline mode also provides at least one tool for automatic calculation of RV from the extracted spectra.

The reduced calibration files are stored in a dedicated folder and inserted in the calibration database, which can be accessed by both the online and offline versions of GOFIO. The main purpose of the reduction software is to automatically process data obtained with the spectrograph, and provide spectra that can be used for immediate scientific analysis. For this reason it is important to have a user interface able to show specified information during the observations, like SNR and/or portion of spectrum on a graphical window, and specified output files after the observations. The full list of the GOFIO requirements and its outputs are reported in Appendix A.

2.7 Commissioning Plan

A third contribution I gave as Instrument Scientist of GIARPS was the preparation of the Commissioning Plan for GIARPS. This work is presented in this Section.

During the first semester of 2016, a commissioning plan was discussed and prepared. The upgrade of GIANO started with the design of a preslit optics (Tozzi et al., 2016) able to feed GIANO without the use of optical fibers. The validation of the new GIANO – B preslit and of the new configuration at the Nasmyth B focal station of the TNG was conducted in three different commissioning runs, between August 2016 and March 2017.

Some actions were necessary before starting the actual commissioning runs, in particular on the mid of July 2016 the support structure and the cover panels have been mounted on the ex SARG structure. At the end of August 2016 the new GIANO – B preslit was mounted. The periscope, consisting in two flat mirrors used to align the optical axis of the telescope interface with the optical axis of the spectrograph, have been installed. The sliding system has been mounted to allow the atmospheric dispersion compensator (ADC) to be inserted into or retracted from the optical beam. Electrical cables and fibers have been placed and tested and the periscope mirrors have been aligned towards the optics (triplet lens and dichroic) on the auxiliary bench.

Each commissioning run was aimed to validate and test different parts of the instrument. In the first run (August - September 2016), the preslit was integrated and aligned and the GAG (GIANO – B Auto Guide) tested and validated.

The second commissioning run (November 2016) started after the heating of the GIANO vessel, its translation from Nasmyth A to Nasmyth B, the subsequent cooling of the spectrograph and the preliminary alignment of the preslit with the instrument were successfully performed. The goal of the second commissioning was to test the new GIANO – B configuration, the calibration units and the scheduler, sequencer, preslit, autoguide softwares.

Finally, the third and last commissioning run (March 2017) aimed to optimize the GIANO – B performances and test the GIARPS mode, after mounting the dichroic in the optical path, aligning and focusing GIANO – B and HARPS – N. The results of the three commissioning runs are described in detail in Sec. 2.8.

Being the setup of GIANO – B largely new, I spent some time in La Palma to work on a new calibration plan for GIANO – B together with the instrument responsible, Francesca Ghinassi. We drew up a document describing the new calibration procedures and the corresponding hardware requirements, dividing them in three classes:

- **Science Calibrations (SCI)** are generally taken at night and cover a parameter range close to the one used for science observations. They should be available before the science observation or taken during the science observation in order to allow data reduction on line.
- **Technical Calibrations (TEC)** are generally taken in daytime and cover a large or complete range of the offered instrument setups and parameters.
- **Instrument Monitoring Calibrations (MON)** are taken routinely with a lower frequency (weekly/monthly) and basically concern with instrument parts (e.g. detectors) in order to monitor their performances and health over long periods of time.

The full calibration plan is reported in Appendix B.

2.8 Commissioning Results

My fourth contribution as Instrument Scientist of GIARPS consisted in the participation to the various commissioning runs at TNG and in the analysis of the data gathered in these runs, in order to verify that GIARPS worked properly and satisfied the instrument requirements. As mentioned in Sec. 2.4, the upgrade of GIANO started with the design of a preslit optics (Tozzi et al., 2016) able to feed GIANO without the use of optical fibers. The validation of the GIARPS preslit (see Sec. 2.8.1) and of the new configuration at the Nasmyth B focal station of the TNG (Sec. 2.8.2 and Sec. 2.8.3) was conducted in three different commissioing runs.

2.8.1 Preslit and Auto Guide commissioning

The first commissioning run was used to align the preslit and to check the pupil position and size. This was done for different elevation values of the telescope in daytime with artificial lights and for different stellar targets in night-time. The image acquisition of the target stars was performed by the Moravian G2-3200 CCD and guiding was done through the GIANO – B Auto Guider (GAG). It uses a CCD detector; combined with the use of a beam splitter that separates light between GIANO – B dewar and GIANO AG, this implies that only light in a restricted wavelength range in the z-band can be used for guiding.

The size of the autoguider field of view (FoV) was defined by observing a bright star (Vega), and moving it in the FoV according to well defined steps in pixels, while the GAG pixel scale was determined with two different methods: through the telescope off-sets and observing binary systems with known distance. For this task, I prepared in advance a sample of binary stars, starting from the Hipparcos online Catalogue and selecting those with parallax <5 arcsec to have a very slow proper motion, a declination > -20 degrees to be visible from TNG, and a z magnitude between 5 and 7 to not reach the saturation level. With these constraints, I obtained a sample of 39 binaries available for our tests. We finally used HIP10180, HIP102554 and HIP102132 to perform the observations.

The measurements from both methods, telescope off-sets and observing binaries, are consistent. The nominal scale value is of 0.028 arcsec/pixel while the measured FoV is 20×20 arcsec^2. For reference, the GIANO – B slit size is 6 ×0.5 arcsec, projected on sky.

In order to define the correct exposure times for the AG as a function of the stellar magnitude and the determination of the preslit photometric efficiency, I selected a sample of photometric standard stars with an I magnitude ranging between 4 and 13. Starting from three Catalogues, Oke (1990), Landolt (1992) and Calspec Database[5], I selected the stars visible from TNG. From this sample, we observed in particular the stars listed in Table 2.2.

Table 2.2: List of photometric standard stars with the corresponding I magnitude used to define the table of the exposure times for the Autoguide Software.

Star's name	I magnitude
ksi2 Ceti	4.3
10 Lac	5.2
HD159222	5.8
HD165459	6.7
BD+21 0607	8.4
BD+02 3375	9.1
TYC 568-1298-1	10.2
TYC 585-840-1	10.5
GSC 00543-01158	11.0
GSC 00447-00478	12.3
GSC 00543-01145	13.2
GSC 00543-01445	14.1

We performed with the GAG camera several observations of these photometric standard stars with several exposure times. These measurements were performed both with and without the insertion, in front of the GAG camera, of three neutral filters with different optical density, allowing to pass the 4.5%, 0.33%, and 0.02% of the light, respectively, useful to avoid the saturation of the detector due to the brighter objects. A table of stellar magnitudes with the related exposure times was constructed, observing photometric standard stars with different magnitudes. At this point the photometric efficiency (including atmosphere, telescope and Quantum Efficiency of the CCD) of the GAG was calculated at different exposure times, resulting around 1% as showed in the Fig. 2.10. Finally, we determined the limiting magnitude for the guiding camera in the I-band, that resulted to be 12 (without filters). A new version of the GAG software able to binning the detector of the camera, was released in May 2018. The photometric efficiency of GAG was checked and a new table of stellar magnitudes with the related exposure times was recompiled. In this new version, the camera allows observation of objects two magnitudes fainter. The limiting magnitude, with exposure time of 10 s, seeing~ 0.75 arcsec, at zenithal distance of 40deg, is then $z \sim 14$.

---

[5] http://www.stsci.edu/hst/observatory/crds/calspec.html

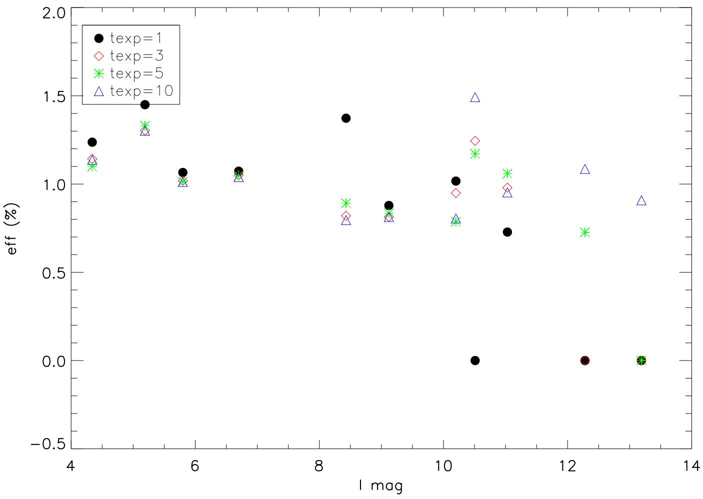

Figure 2.10: Efficiency (in percentage) of the preslit as function of I magnitude at different exposure times, without filters.

2.8.2 GIANO − B commissioning

In order to be prepared for this phase, the procedure for heating GIANO began in Septmeber 2016 for about one month, after which the moving and the mounting on the new platform were performed and the cooling procedure started.

The GIANO − B commissioning consisted first in the alignment of the spectrograph with the preslit system. Calibration frames were acquired in order to estimate the size of the slit of GIANO − B through the flat-field lamp and to check the stability of the U-Ne lamp. Fig. 2.11 shows the number of lines of the U-Ne spectrum for each order useful for the calibration. The selection of these lines is based on their intensity and on the fact that both the position on the detector and the wavelength of each line are well known. The total number of lines is 743, with 15 lines per order on average. Fig. 2.12 shows the flux of the U-Ne lines as function of wavelength: the most intense lines lie around 1100, 1800 and 2300 nm.

First observations with GIANO − B were performed in order to clock the overheads during an AB nodding exposure (see Section 2.8.4), resulting to be about 3 minutes, and to test the observation templates for the New Short Time Scheduler (NSTS) that is used to prepare, modify and schedule the Observing Blocks (OB). These blocks are predefined groups of available instrument and telescope commands and procedures that can be executed by the Sequencer Software. We, thus, observed both pointed (stars) and extended (Mars) sources to test both nodding and stare templates. Furthermore, I organized in advance a call for proposal (for both GIANO − B and GIARPS observations) within the GAPS team in order to select some scientific cases and perform the first GIANO − B (and later GIARPS, Sec. 2.8.3) observations during the commissioning. These observations were also useful to be compared with the GIANO − A spectra and calculate the preliminary estimation of the instrumental efficiency, acquiring photometric standard stars spectra.

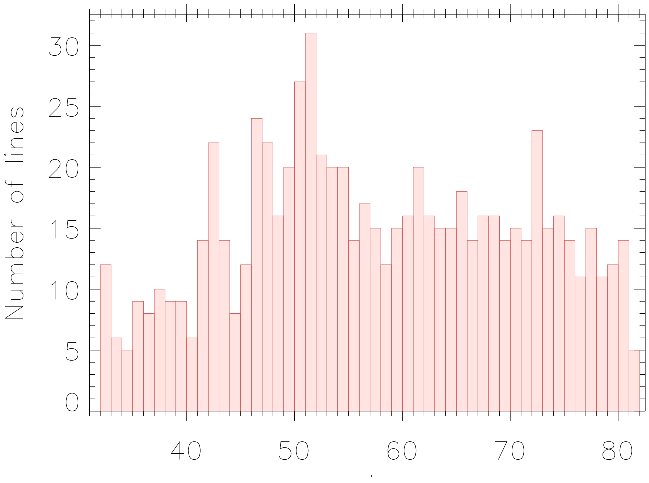

Figure 2.11: Number of U-Ne lines for each order.

2.8.3 GIARPS commissioning

During this last commissioning run the activities regarded the optimization of GIANO – B configuration, the sequencer and the autoguide final test, and the test of observations in GIARPS mode after mounting the dichroic. The focus and pointing model tests for GIANO – B were performed. Furthermore, in order to measure the actual efficiency of GIANO – B, without the loss of stellar flux due to the limited size of the slit and in a way independent of the seeing, we observe a standard star (HD 159222, Hmag = 5.08, spectral type = G1V) without the GIANO – B slit. The calculated efficiency was 15% in the K band (see Figure 2.13). This value agrees very well with the product of telescope, preslit and GIANO – B optic transmission.

After the dichroic was mounted and aligned to the system, we performed the first GIARPS–mode observations, testing the focus of both instruments with the dichroic. When the GIARPS mode is set, the GIARPS focus is the best compromise between the HARPS – N and the GIANO – B focus, choosing the optimized focus for HARPS – N, while GIANO – B is slightly out of focus. This does not have any important impact on RV measurements. Furthermore, we tested the new NSTS (New Short Time Scheduler) software adapted for GIANO – B and the GIANO – B sequencer (the commands dispatcher). We prepared and submitted the observing templates necessary to perform both nodding and stare observing modes and test the performances of the system. Just like the HARPS – N templates it executes the telescope slew and the pointing of the science target, then perform an AG acquire in order to show the target in the AG field of view. The user can center the target in the right position and run the exposure. At the end of the exposure, when the spectrum was stored in the disk, the new data reduction software, GOFIO (Rainer et al. 2018,see also Sec. 2.8.4) started the reduction. Details on the software that manages the creation of raw data files and coordinates the storing of data files into the TNG archive and the automatic start of GOFIO are provided in Harutyunyan et al. (2018).

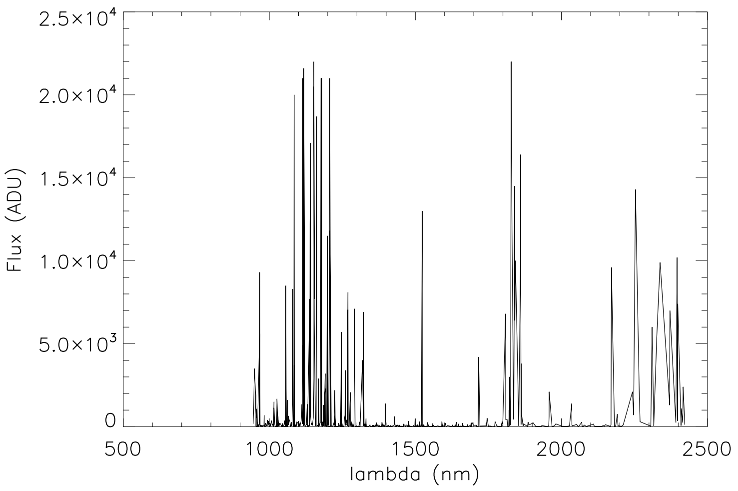

Figure 2.12: Flux of the U-Ne lamp's lines (ADU in 30 seconds) as function of the wavelength.

2.8.4 The GOFIO Pipeline

The different feeding of the GIANO – B spectrograph, from fibers to long slit, implied a different method to extract the spectra and provided the opportunity to create a dedicated data reduction pipeline. The GIANO – B reduction software, "GOFIO" Rainer et al. (2018), processes the calibrations as well as all the spectra in real time during the observing night, obtained with the nodding or stare acquisition modes.

GOFIO is part of the full online pipeline Harutyunyan et al. (2018) that manages the data flow from the observation to the archive. It has been successfully tested during the second and third GIARPS Commissioning runs, providing the extracted spectra used for instrument characterization and scientific validation. An off-line version of GOFIO will be available in the near future for GIANO – B/GIARPS users, allowing custom data reduction according to the scientific requirements of the observer and, if needed, computation of the radial velocity using telluric lines as a reference system (see Sect. 2.9). This will be possible through the implementation of GOFIO in the YABI workflow (Hunter et al., 2012) installed at IA2[6] at the INAF Observatory of Trieste.

2.9 Radial velocities with GIARPS: telluric method

HARPS – N RVs are extracted by its data reduction software (Pepe et al., 2002). I wrote the software required to extract radial velocities (RV) from GIANO and GIANO–B spectra following the approach described in Carleo et al. (2016). An ensemble of IDL procedures was created to measure RVs with the Cross Correlation Function (CCF) method (Baranne et al., 1979) and with telluric spectrum as wevelength reference. Anyway few changes to that version were added during the last year, that allowed to improve the accuracy of the RV measurements. The modifications mainly concerned the telluric subtraction (see Sec. 2.9.2)

---

[6] http://ia2.inaf.it.

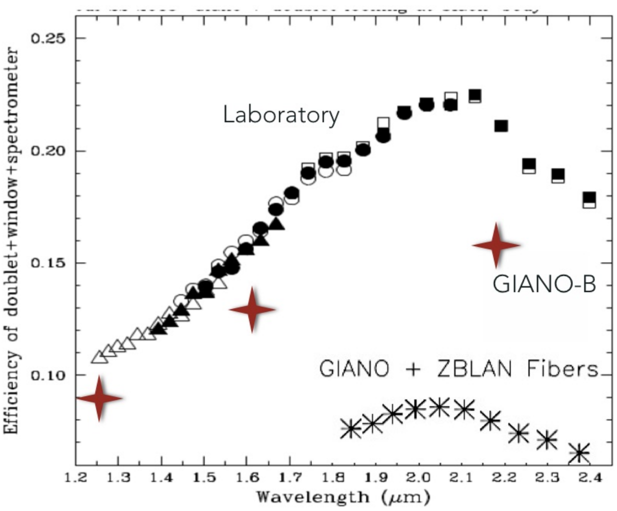

Figure 2.13: The measured efficiency of GIANO – B (red stars) compared with the efficiency measured in the laboratory at Arcetri observatory and the efficiency of GIANO fed by the fibers. Note that this measure was obtained without the GIANO – B slit. Note also that the laboratory measurements did not include telescope and preslit optics. Pnce the transmission of these components is taken into account, efficiency of GIANO – B agrees well with the laboratory measurements.

and mask construction (Sec. 2.9.3). This code will be ultimately implemented in GOFIO pipeline in order to have a completely automated computation procedure. However, results discussed in this thesis are obtained with an ensemble of IDL procedures that run off-line at OAPD (Astronomical Observatory of Padua) computers. Implementation in GOFIO will require some adaptation and translation into Python. Here the various steps of the RV extraction procedures are described in details.
Alternative methods for extraction of high precision RVs can be found in the literature. Perhaps, the most popular are those based on a match with a stellar template (e.g. TERRA, Anglada-Escudé & Butler 2012) or modelling of the observed spectrum as combination of a stellar spectrum and of a cell reference template (e.g. AUSTRAL, Endl et al. 2000).

2.9.1 Pre-reduction: spectrum normalization

Throughout my code, each individual order of the GIANO spectra is considered separately (i.e., they are never merged together). First of all, I re-sampled all original spectra to have a constant step in RV. This step is required to have uniform wavelength scales for all spectra. With the adopted method (CCF), a dense sampling allows to reduce RV errors because the wavelength of each spectral line is determined with an error that is at best equal to half this step due to consideration of the sampling theorem (Nyquist). However, execution of the procedure becomes slow when large files are used. The re-sampling should be made with the same step for stellar and telluric lines. In order to choose an appropriate step some tests were performed, applying to the analysis different step values (starting from 800 and going down until 100 m s^{-1}). The best compromise between accuracy and computation time is a step of 200 m s^{-1} that is small enough that uncertainties in the wavelength of the lines in the mask do not introduce avoidable noise, but large enough to keep time required for execution of the procedure reasonable (a few minutes per spectrum). Each individual order of the input spectrum was then re-sampled to the new grid, using a third degree cubic spline interpolation, and normalized to an approximate continuum. The normalization spectrum is obtained by dividing the spectra for a fiducial continuum. This was obtained either considering a cubic spline interpolation through local maxima within specified spectral window. In order to reduce the impact of cosmic rays and bad pixels, all spectral points with intensity normalized to a fiducial continuum larger than 1.2 were set at 1.2.

2.9.2 Subtraction of telluric contribution

In order to obtain the stellar spectrum cleaned from the telluric lines, I create the best spectrum of the Earth atmosphere (hereinafter, telluric spectrum) by making a median over several tens of high signal-to-noise spectra (>200) from a library acquired over time with GIANO – B. This best telluric spectrum is shifted to take into account small shifts in the dispersion zeropoints, and scaled in intensity to take into account the different airmass between telluric and science spectra, using an approach similar to the one adopted by the IRAF procedure TELLURIC. Finally, the obtained telluric spectrum is normalized to the intensity of the observed spectrum and subtracted from the science spectra. This approach, that determines the best shift and scale parameters, allows to minimize the RMS of the subtracted spectra. The subtraction yielded better results than a division of the spectra because a division leads to large errors in correspondence of strong telluric lines. As mentioned above, this procedure is applied separately to each individual order.

Fig. 2.14 shows an example of the subtraction of the telluric contribution from a science spectrum, using this procedure.

2.9.3 Masks preparation

Stellar Mask

The CCF method is performed by cross-correlating the spectrum with a template mask. This is a vector with dimension equal to the observed spectrum, whose components are all zero, except those for which the condition $|\lambda_{\rm spectrum} - \lambda_{\rm line,i}| < step$, is satisfied, where $step = \lambda_1 - \lambda_0$, $\lambda_{\rm spectrum}$ is the wavelength for the spectrum and $\lambda_{\rm line,i}$ is the wavelength of the mask lines. In general the list of lines should include as many lines as possible in order to maximize the RV signal. To optimize the result, lines should be weighted accordingly to their strength on the spectrum. We need to prepare two masks, for the stellar and telluric spectra, respectively. In order to measure absolute RVs, the wavelength of the mask should be given by laboratory data; this requires identification of each individual line in the mask[7].

---

[7] While not strictly needed in our method, but in order to validate our procedure for the preparation of the mask, we actually counter-identified 757 of the 1102 lines of the mask we obtained for the K2V star HD 3765 with those listed in the solar spectrum tables of Goldberg & Müller (1953), Mohler et al. (1953), and in the NIST atomic spectra database (www.nist.gov/pml/data/asd.cfm). The average offset between measured and tabulated wavelengths is 0.0090 nm, with an r.m.s. scatter for individual lines of 0.0162 nm. Lines in our mask not counter-identified with solar spectrum lines are all weak, having a reduced equivalent width $\log EW/\lambda < -5.1$, where EW is the equivalent width. Since HD 3765 is much cooler than the Sun, most spectral lines due to metals and molecules are stronger in its spectrum than in the Solar one. It is then not surprising that many lines that are weak in the spectrum of HD 3765 were not detectable in the Solar spectrum.

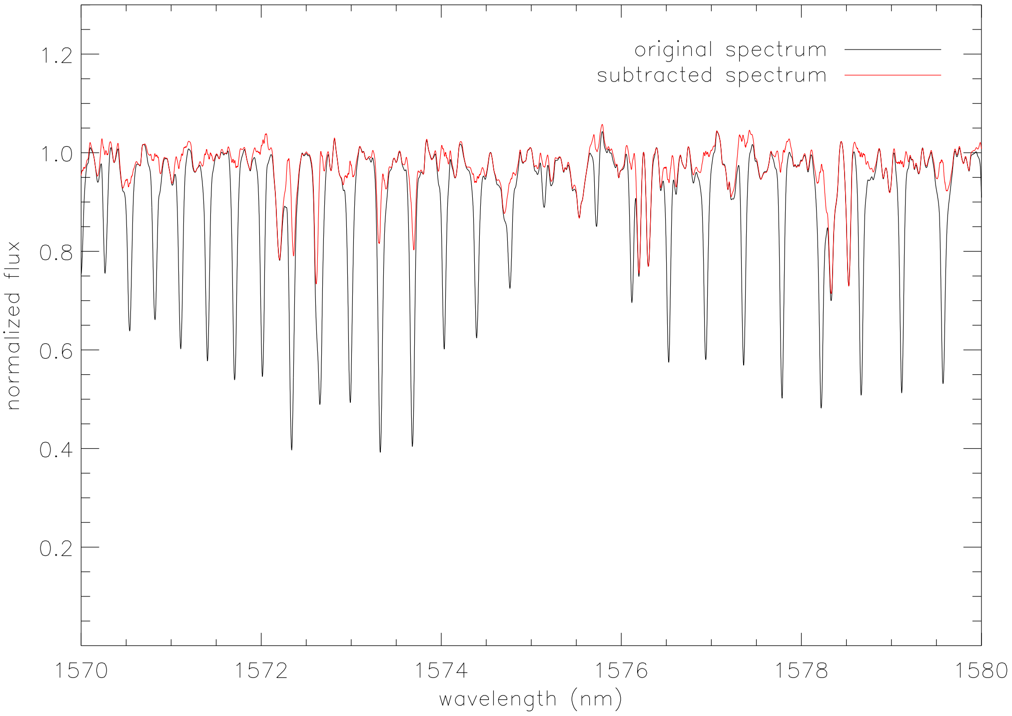

Figure 2.14: Example of the subtraction of telluric lines from science spectra.

However, we are interested here in variations of RVs rather than in their absolute values. In this case, what is important is that the same mask is used for all the spectra of a star, but the mask wavelengths do not need to be those observed at rest. A mask optimized for each individual star can be used.

We prepared an IDL procedure that automatically builds the list of lines and masks from the re-sampled, normalized and cleaned spectra (either stellar or telluric). The procedure works as follows. First, individual stellar spectra available for a given star are shifted at rest velocity and their median is then obtained. For this purpose, the intrinsic RV of the star is taken from the astronomical database SIMBAD (http://simbad.u-strasbg.fr/simbad/), while the barycentric correction BC is obtained through an IDL procedure previously prepared at OAPD. This obviously implies that the average RV measured with this mask will be that of the database. Previous tests showed that the BC procedure correctly gives the correction of RVs to the barycenter of the Solar System within a few hundredths of m s^{-1}, that is well enough for the present purposes. The weights, i.e. the values to be given to the mask at the wavelengths of each line, are set at the value of F_{center}, that is the central intensity of the line. This allows to weight the lines according to their intensity when computing the CCF.

Only for the purpose of creation of the mask, the spectrum is changed by sign and summed 1, so that the absorption lines now appear as emission lines with a maximum intensity of 1. The line list is obtained by dividing each order into 128 chunks; each of them was searched for lines using the following method. For each chunk, the wavelength yielding the maximum flux was found. A short interval around it was considered, where the spectrum was fitted by a four parameters Gaussian function: a_0 is the Gaussian height, namely the line intensity;

a_1 is the center of Gaussian, that represents central wavelength of line; a_2 is the Gaussian width, which gives the Full Width at Half Maximum (FWHM) of the line and a_3 is the local continuum. Finally, the central intensity of line is given by $I_{\text{center}} = a_0/a_3$. In order to avoid blended lines, which are present in several orders, the software looks for pairs of lines whose separation is less than a critical value: for such pairs, only the line with the highest intensity is left in the mask list.

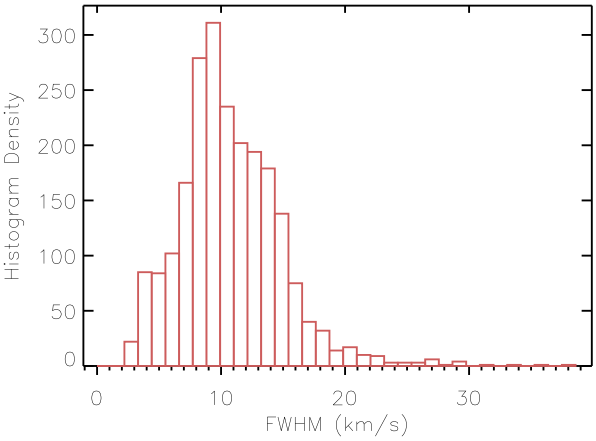

Figure 2.15: Density histogram of Full Width Half Maximum.

To further clean the line list from artifacts, only the lines with a value of the FWHM in agreement with that expected for the rotational velocity of the star and the spectral resolution of the spectrograph should be considered. We then inspected the density histogram of the FWHM (Fig. 2.15) obtained for a slowly rotating star. This clearly shows that the value of this quantity peaks at ~ 9 km s^{-1}, in agreement with the expected value given the GIANO spectral resolution. Therefore only values of $0.5\ R < FWHM < 2.5\ R(1 + 4a_0^2)$, with $R = \frac{\lambda_{\text{center}}}{50000} = \frac{a_1}{50000}$ were kept. While this is appropriate for slowly rotating stars, the most appropriate value of R shall in general be adopted considering the rotational velocity of the star. This is taken into account by the code. Fig. 2.16 shows an example of the creation of stellar mask using this procedure.

Telluric Mask

The telluric mask is built considering a line list that includes about 2000 lines, obtained from the best telluric spectrum. As telluric lines have a different profile respect to stellar lines, this can impact on the measure of RVs. In order to solve this inconvenient, only telluric lines with an intensity similar to the stellar ones are chosen. Fig. 2.17 shows an example of the creation of telluric mask using this procedure.

2.9.4 Subtraction of stellar contribution

Not only the stellar spectra can be contaminated by the telluric contribution, but also there can be a contamination of stellar lines in the telluric spectra. This may reduce accuracy of the RVs measured from telluric lines. To avoid this issue, the stellar spectra (not yet cleaned by telluric contribution) are subtracted by a stellar template, which is created by the

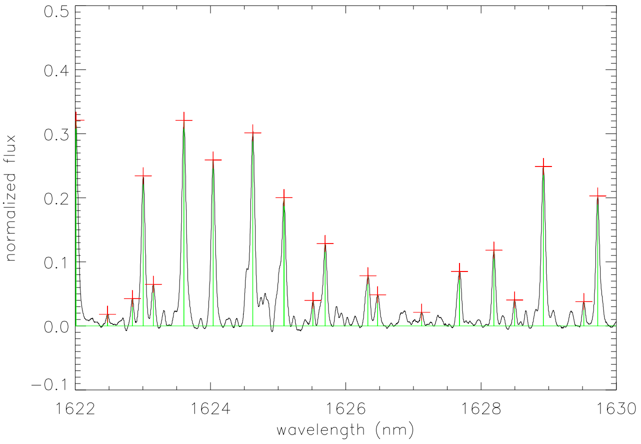

Figure 2.16: Example of stellar mask in a specified window of spectral range. Crosses are the values of the central intensities of the lines selected for the mask.

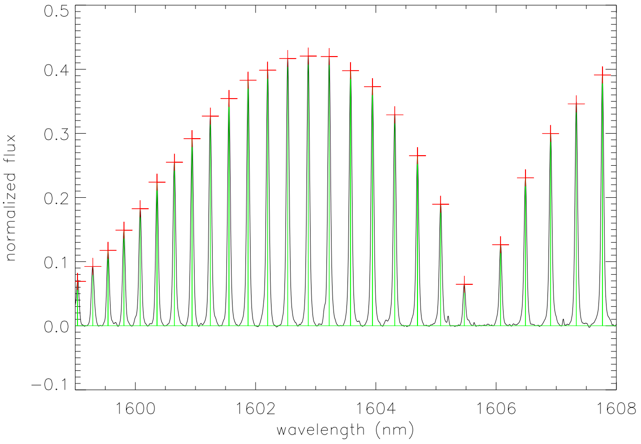

Figure 2.17: Example of telluric mask in a specified window of spectral range. Crosses are the values of the central intensities of the lines selected for the mask.

median of stellar spectra (that was used for stellar mask, see Sec. 2.9.3) re-shifted by a factor $\lambda_m = \lambda_0(1 + \frac{v_{geo}}{c})$, where λ_m is the measured wavelength, λ_0 is the wavelength at rest, $v_{geo} = v_{He} - BC$ is the geocentric velocity given by the difference between the heliocentric velocity and the barycentric correction, and c is the speed of light. This allows to create a telluric spectrum without the stellar lines contribution.

Therefore, for each science observation we obtained two cleaned spectra: the stellar spectra without telluric lines, and the telluric spectra without the stellar contribution. These spectra are used for the derivation of the stellar RV and of the rest RV corresponding to the telluric spectrum.

2.9.5 High precision RVs

At this point, using an IDL procedure, RVs of both telluric and stellar lines are finally measured with the CCF method, including the following steps:

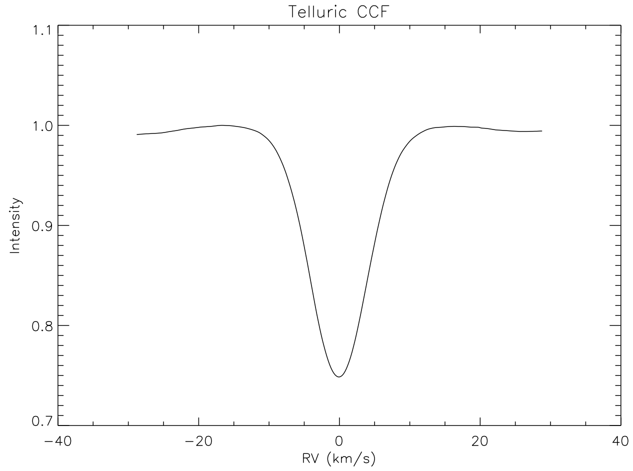

Figure 2.18: Total Cross Correlation Function of telluric spectrum.

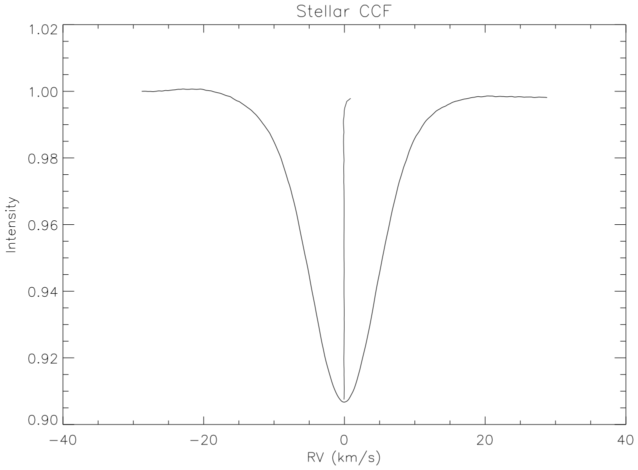

Figure 2.19: Total Cross Correlation Function of HD3765 star with the corresponding bisector.

1. **Reading input files**: the procedure works on the normalized stellar spectra subtracted by telluric contribution and on the normalized telluric spectra subtracted by stellar contamination, as input files (Sec 2.9.2 - 2.9.4).

2. **Telluric CCF for individual orders and error estimation**: In order to obtain the RV of the telluric lines, the telluric mask is cross-correlated with the normalized subtracted telluric spectra (Sec. 2.9.4) for each order and a Gaussian fit is subsequently executed for every CCF. The Gaussian fit provides four parameters which allow to obtain the FWHM and the RV. The centering error for each order is measured.

3. **Stellar CCF for individual orders and error estimation**: Likewise, in order to obtain the RVs of the star, the stellar mask is cross-correlated with normalized subtracted spectra of the star (Sec. 2.9.2), but in this case, the intrinsic RV of the star has to be corrected by a factor $bb = \frac{v_{\text{barycentric}} - BC}{step}$, where $v_{\text{barycentric}}$ is the RV of the star with respect to the barycenter of the Solar System. The center of the line on the CCFs are then measured for each order obtaining the RVs with their errors, depending on FWHM, intensity and S/N.

4. **Weighted CCF**: The total weighted CCF for each spectrum is calculated for both the telluric (Fig. 2.18) and the star (Fig. 2.19). Moreover the bisector is calculated for each spectrum: Fig. 2.19 is an example of the CCF for the RV-standard star HD 3765 and the corresponding bisector with the typical C-shape due to the granulation on the stellar surface (for more details on BIS see Sec. 1.3).

5. **Order selection**: A number of spectral orders shows a paucity of lines in the corresponding masks, as well as poor S/N due to a low atmospheric transmission at the relevant wavelengths. As expected, those orders show very large errors in the RV measurement, so we assign a null weight in the final solution. Since the accuracy is roughly proportional to the square root of the number of orders, using only parts of an order would complicate the code and the calculation with a negligible gain, so we decide to fully reject or use an order. Basically we reject:

   - in the telluric spectra, all the orders with a measured RV that exceeds more than 1 km s^{-1} in absolute value the value of the Earth's atmosphere lines, i.e. 0 km s^{-1};
   - in the standard RV stars spectra, all the orders with a measured RV that exceeds more than 1 km s^{-1} the tabulated RV of the star.

   A second selection is based on the value of the central intensity of the CCFs for the individual orders. The orders dominated by strong water vapour bands present very strong peaks in the telluric CCF and are located at the edges of each Y, J, H and K band. Few telluric lines are present at shorter wavelengths, making our methodology hard to apply in the Y band. For this reason we exclude it from our study. During the analysis we have found that, both for stellar and telluric lines, the best results are obtained when the central intensity of the CCF ranges between 0.2 and 0.4. The RV scatter is actually larger for orders with either weaker or stronger CCF intensity. In particular, for those orders with higher CCF intensity, the RV from stellar CCF is very unstable, probably due to the strong contamination by telluric lines. After the application of our selection criteria we can proceed with the analysis, using approximately half of the available orders. In these orders we still expect some spectrum-to-spectrum variations in radial velocities correlated with overall intensity of the telluric lines, due to the imperfect decontamination of the spectra. An example of order selection is presented in Table 2.3: most of selected orders lie between the telluric absorption bands.

6. **RV**: The RV for each spectrum was calculated by a Gaussian fit to the total CCF profile, providing the intensity, FWHM and RV values of the total CCF. The final RV for each spectrum is calculated by subtracting the telluric RV, RV_{tell}, from the stellar one RV_{star}: $RV = RV_{star} - RV_{tell}$, and the internal error is given by the final error, which takes into account the weight of each order.

Table 2.3: Example of order selection for the RV-standard star HD 159222. For each order a weight is calculated as square of the inverse of the standard deviation between all the available exposures.

Order	Weight	Band
0-2	0.0	K
3	13.8	
4	29.0	
5-8	0.0	
9-11	0.0	H
12	20.4	
13	21.9	
14	302.4	
15	104.1	
16	53.6	
17	85.3	
18	93.8	
19	0.0	
20-26	0.0	J
27	23.3	
28	23.0	
29	64.7	
30	14.5	
31	18.0	
32	34.3	
33-37	0.0	
38	17.1	Y
39	44.6	
40	31.2	
41	31.2	
42	15.8	
43	18.7	
44	24.8	
45	0.0	
46	18.4	
47-49	0.0	

7. **Internal Error Estimation**: The total error for the i-th order is given by the quadratic sum of both telluric and stellar contributions, and the final error for each spectrum, assumed that S/N is only given by statistics of photons, is obtained weighting each order considered for the analysis. For further considerations on the GIANO errors, see the Sec. 3.6. Moreover, since we re-sampled all spectra with a step of 200 m s^{-1} in RV, each line has an associated wavelength error of half this step, i.e. 100 m s^{-1}. Since about 1000 lines are used for RV determinations, the resulting error for this source of noise is $100/\sqrt{N_{lines}} \sim 3$ m s^{-1}, where N_{lines} is the number of lines. This is not entirely negligible, though it does not dominate the noise.

2.9.6 Bisector analysis

A measure of the asymmetry of the bisector is given by the Bisector Velocity Span (BVS). This is defined by comparing the position of the bisector at two flux levels of the profile of CCF (the top range lies around the 25% of the flux and bottom range around the 75%). The BVS is the difference between the median position of the bisectors in these two ranges. The uncertainties on this quantity is calculated by considering the fractions of the CCF used for the derivation of the BIS, resulting in $\sqrt{10}\sigma_{RV}$, where σ_{RV} is the RV error.

The bisector analysis is important for two reasons:

- the RV of a star is defined to be the velocity of the center of mass of the star along our line of sight (Queloz et al., 2001). The observational determination of a star's RV is made by measuring the Doppler shift of spectral lines. The RV variations can be due to either a possible companion or changes in the stellar atmosphere. One of the best ways to interpret observed variations is to look for changes in the BVS of the stellar CCF. Any correlation between RV changes and line-bisector orientation leads to serious doubts on the reflex motion interpretation of the RV variations. If the RV is due to changes in center-of-mass velocity of the star, there is no change in bisector's shape or orientation.

- In addition, in our analysis BVS significantly different from zero in the telluric CCF's may signal an asymmetric slit illumination. In this case, we might try to apply a correction based on the observed correlation between this quantity and the RVs. We applied this correction to some of the GIANO – A spectra, where misalignments between the fibers ends and the slit migth occur. No such correction was needed for GIANO – B spectra.

2.9.7 Weighted RV

Starting from the RVs measured through the CCF method from each order, the weighted average RVs and their corresponding errors are determined for each exposure. This approach takes into account the weight of single orders, some of them affected by telluric lines and thus contributing in different ways to the determination of the RVs. In this thesis we report, for each target, the weighted average RVs and the corresponding BIS values obtained from the CCF analysis.

2.10 Radial velocities with GIARPS: cell technique method

While the optical instruments have an extreme environmental stabilization or with the simultaneous reference method (e.g. HARPS at the ESO La Silla 3.6m telescope and HARPS – N at TNG, Fischer et al. 2016) or by placing an Iodine gas cell in the telescope optical path (e.g. HIRES at the 10m Keck Telescope, Vogt et al. 1994), in absence of a cell the NIR RVs are extracted using telluric lines as reference. This limits the RV precisions, because of the atmospheric instability (see also Sec. 1.3.3). Gas absorption cells have recently been developed also for the NIR spectrographs, such as the ammonia gas cell used by Bean et al. (2010) on the CRIRES spectrograph at the VLT, allowing unprecedented RV precision in the NIR. A similar gas cell was designed for GIANO – B (Seemann U. et al. , 2018), thanks to the GIARPS project, to have precise RVs on the few $\mathrm{m\ s^{-1}}$ level. Since an absorption gas cell was thought to be added to the new GIANO – B configuration, a collaboration between the Astronomical Observatory of Padua and the University of Texas at Austin allowed me to spend some months in Austin to develop an adapted version of the AUSTRAL code written by Prof. Michael Endl (Endl et al., 2000) to measure RVs in the NIR through the cell technique from GIANO – B spectra.

The AUSTRAL code is a modeling technique software aimed to obtain high precision RVs from ESO CES (Coudé Echelle Spectrometer, La Silla) and SARG (TNG) spectra. It combines single components of a spectrum taken with the absorption cell technique (the instrumental profile, IP; the high resolution Fourier Transform Spectrum of the cell, FTS; the stellar template without the cell) creating a synthetic spectrum that will be matched to the observations through the Maximum Entropy optimization method (MEM). My contribution at Austin aimed to adapt this code to the GIANO – B spectra acquired with the cell.
The steps I worked on are:

Gas cell template The AUSTRAL technique requires a very high resolution spectrum of the gas cell (FTS). Since our gas cell spectrum was at R = 50,000, and since the real gas cell FTS was not available, I created a simulated FTS (R = 500,000) by deconvolving the cell spectrum with an appropriate Gaussian (Fig. 2.20).

IP modeling I performed the convolution between the FTS spectrum and the GIANO's IP (that is the starting IP for AUSTRAL) and then downsampled it to the GIANO's resolution. The resulting spectrum is the input for AUSTRAL, that models the IP through the MEM algorithm. A new IP is created ($IP_{AUSTRAL}$). Figure 2.21 shows the GIANO and AUSTRAL IPs.

Stellar template The observed spectrum of the star without the gas cell is deconvolved, again with MEM algorithm, with the $IP_{AUSTRAL}$ created in the previous step, in order to obtain an intrinsic stellar spectrum without the instrumental effects. This spectrum represents the stellar template (Fig. 2.22).

Observation tamplate At this point, the observation model is the combination of the cell and stellar templates convolved with the $IP_{AUSTRAL}$. This combined spectrum is matched to the observed spectrum (that I simulated since a GIANO's spectrum through the gas cell does not exist), and RVs are measured.

This work, conducted in Spring 2016, was a preliminary activity, since GIANO spectrograph was not yet moved to Nasmyth B, so the GIANO spectra were the ones acquired with the

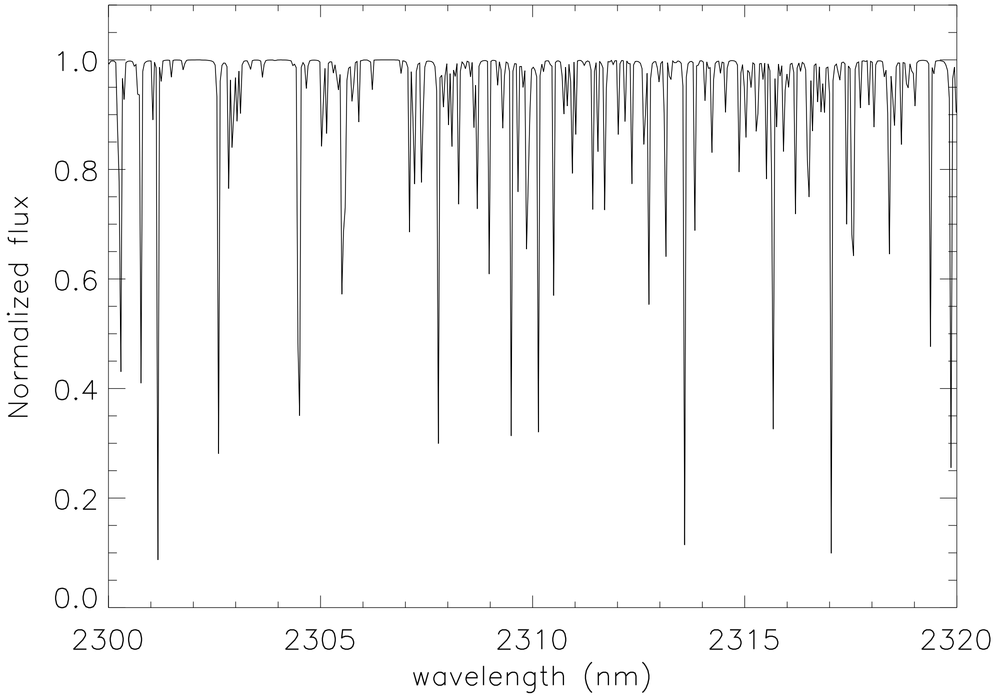

Figure 2.20: Portion of the FTS spectrum at R=500,000.

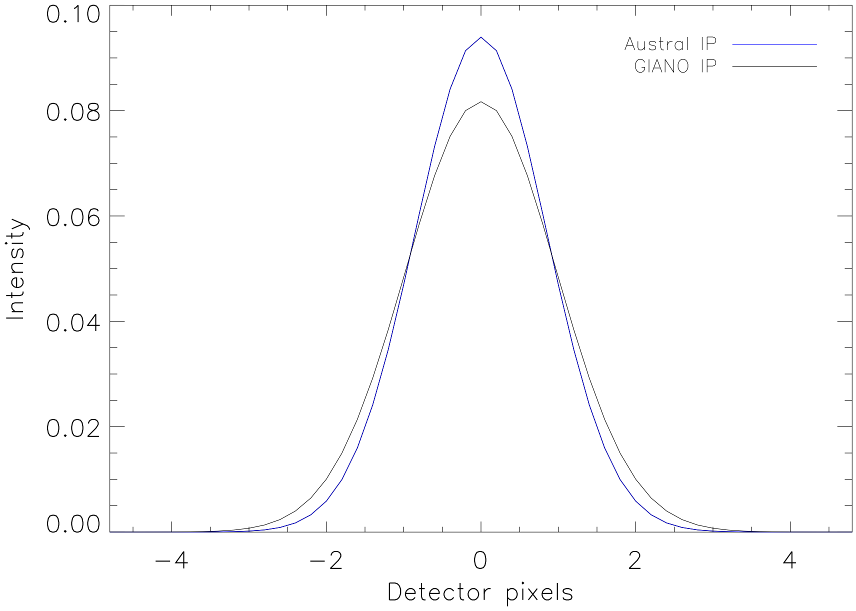

Figure 2.21: GIANO's IP in black and the resulting $IP_{AUSTRAL}$ in blue.

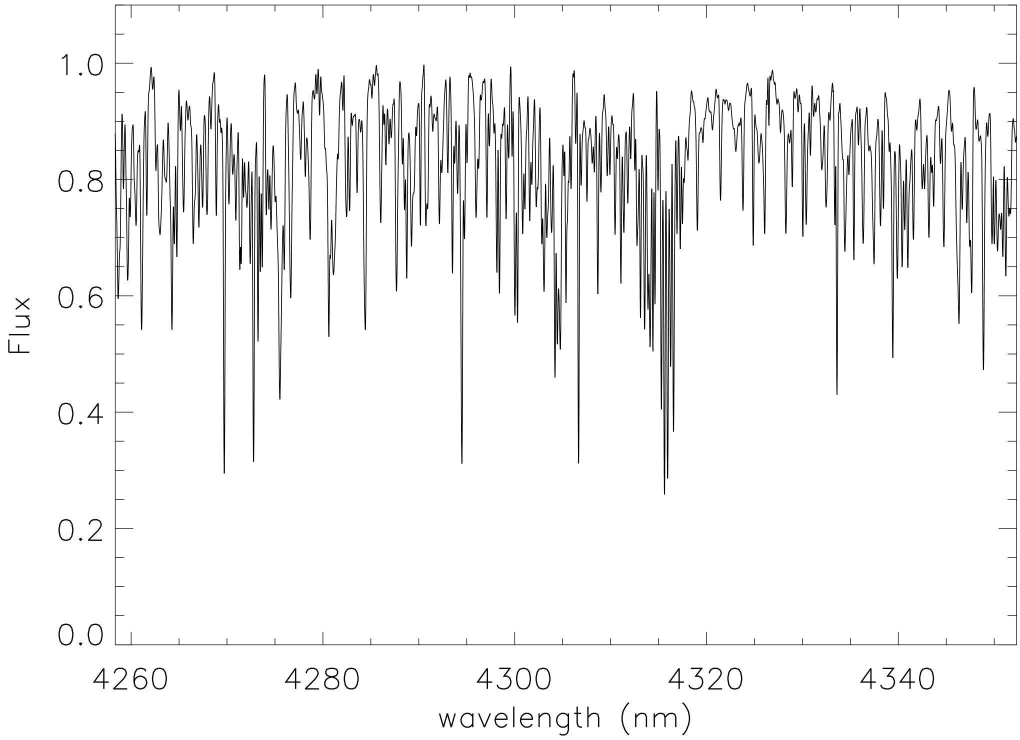

Figure 2.22: Stellar template for one order.

fibers. Moreover, since a gas cell is not yet present in the optical path, the observed spectrum through the cell was simulated to have AUSTRAL inputs.
Currently, the gas cell on GIANO – B is not yet available and some study is being conducted in order to evaluate its implemantation.

2.11 Current status of GIARPS and Perspectives

At the end of the 2017 Spring GIARPS has been delivered to the TNG in order to finish the instrument integration mainly with the Telescope Software environment and to be offered to the scientific community.

Some important activities were done also after the commissioning runs, as the development of the binning for the GIANO – B Auto Guider in order to optimize the guide during the observations and gain some magnitudes, the development of GIANO – B Exposure Time Calculator (it can be accessed through the following link: https://tngweb.tng.iac.es/giano-b/etc/). Moreover, an Observer's manual has been written[8] in order to have instructions for both GIANO – B and GIARPS observations.
The main open points are the followings:

- The GIANO – B command dispatcher: the GIANO – B NSTS version is under construction. At the moment it is possible to perform a couple of AB – AB Nodding and

---

[8] http://www.tng.iac.es/instruments/giano-b/resources/GIANO-B_Observer_Manual.pdf

use the spectrograph in stare observing mode. Most of the calibration templates are already built, other will follow also due to the future implementation of the Fabry-Perot system and the possible presence of absorption cell.

- Absorption Cells: The RVs from GIANO – B spectra are measured by using the CCF (cross-correlation function) method (see Section 2.9), with the telluric spectrum as wavelength reference. The use of this technique allows a precision of about 8 m s^{-1} for bright stars (H$\leq$ 5 mag) and about 100 m s^{-1} for fainter stars (tipically H$\sim$ 9 mag). The introduction of the absorption cell will allow more precise RV measurements with internal errors of about 3 m s^{-1}, due to the fact that absorption cell is more reliable in comparison with the instability of the telluric spectrum.

- RVs measurement: the GOFIO pipeline (Sec. 2.8.4) at the moment is limited to the on – line production of completed reduced and wavelength calibrated GIANO – B spectra. GOFIO will be implemented in the YABI workflow and it will be possible to process off – line the spectra to extract the RV value.

- Fabry–Perot: at this moment the wavelength calibration is made by means of an U–Ne Lamp. A step further in the wavelength calibration precision (and so in the RV measurement) could be achieved with the larger number of lines given by a Fabry Perot System coupled with the calibration box of GIANO – B. The GIANO – B Fabry Perot system is described in Tozzi et al. (2016).

Chapter 3

Results

We used HARPS – N and GIANO in its various configurations to examine the feasibility of a program focused on the search and characterization of very young Hot Jupiters. As seen in Chapter 1, HJs might possibly form through different mechanisms: type I migration or a jumping Jupiter scenario followed by a tidal circularization of the orbits. These two scenarios lead to different frequency and properties of HJs, at very young ages. However, detection of very young HJs is made difficult by the high activity level of the stars.

The existence of a number of very young HJs have been claimed in the literature. Observations of radial velocities obtained over a wide range of wavelenghts, as possible with GIARPS, may be used to test these claims and to strenghten the determination of the frequency of very young HJs and of their orbital parameters.

The first pioneering result that showed the potentiality of an instrument like GIARPS, was obtained from partially simultaneous VIS-NIR observations, from GIANO and HARPS – N, and regards the detection of a substellar companion with minimum mass of 10.78 ± 0.12 M_J and an orbital period of 101.54 ± 0.05 days around the K giant star TYC 4282-605-1 (González-Álvarez et al., 2017). This target was at first monitored with the VIS spectrograph HARPS – N at TNG, showing a RV modulation that could have been caused by a planet or stellar oscillations. A second dedicated monitoring has been arranged combining observations with HARPS – N and GIANO, in its first configuration, obtaining thus quasi-simultaneous observations. Since the two spectrographs were mounted at the two opposite Nasmyth foci of the telescope, a certain amount of time was necessary to change the telescope configuration, so the time difference between the VIS and the NIR spectra in the same night was of about a few hours, that is a very short time compared to the period of the candidate. The two datasets show that the VIS and NIR RV semi-amplitudes are compatible, providing the detection of the planet, avoiding to perform two separated observing runs with a VIS and a NIR instrument. This work is the very first example of cooperation between two spectrographs that would have been part of the GIARPS instrument. The published version of this work is reported in Appendix C, where my main contribution concerned the calculation of NIR RVs with my RV code.

In this chapter I describe the scientific results obtained from the GIARPS commissioning runs observations and the results from the first semester of the GAPS2.0 large program. In addition, RV data acquired with GIANO – A are also examined. In Sec. 3.1 the instrumental stability is discussed from two RV-standard stars RV measurements, then Sec. 3.2 is focused on the results from RVs of the star BD+20 1790, that confirmed the retraction of the Hot Jupiter claimed orbiting this star. I described the GIARPS RV measurements of V830 Tau in Sec. 3.3, HD 285507 in Sec. 3.4, and AD Leo in Sec. 3.5): these are all cases for which the presence of HJs was claimed.

3.1 RV standard stars

Some radial velocity standard (RV–std) stars were observed with GIANO – B in order to test instrument performances and determine the GIANO – B stability. In particular, I report the analysis on the RV standard stars HD 3765 (Sec. 3.1.1) and HD 159222 (3.1.2).

3.1.1 HD 3765

HD 3765 is a K2V star with magnitudes V=7.36, J=5.69, H=5.27, and K=5.16 (Cutri et al., 2003). It has a low activity level (Strassmeier et al. 2000, Martínez-Arnáiz et al. 2010) and a constant RV (RV jitter of 2.4 m s^{-1}) (Batten 1983, Isaacson & Fischer 2010).

We observed this star first with GIANO – A. Here I report the results described in Carleo et al. (2016).

Twenty-three GIANO – A spectra of HD 3765 were acquired in seven nights, with typical S/N values of 130 and internal errors in RVs from 4.5 to 10 m s^{-1}. The original r.m.s. of the RVs we obtained was 28 m s^{-1}. Most of this scatter is probably due to mechanical vibrations and drifts between the warm-preslit system (that includes the fiber, the slicer and the re-imaging optics) and the cryogenic spectrometer (see Tozzi et al., 2014, for more details). This was partly removed using the telluric line reference, that reduces the r.m.s. scatter of the stellar RVs from an original value of 610 to 28 m s^{-1}. However, even once corrected for the telluric reference, the RVs show significant correlations on the BVS of both the stellar and telluric CCFs (see Fig. 3.1 and Fig. 3.2). Removing these correlations, by subtracting the best fit function from the RVs, the r.m.s. decreases to 14 m s^{-1} for individual observations and 8 m s^{-1} averaging observations taken in the same night. Table 3.1 summarizes the final result for each spectrum of HD 3765. The resulting RV values after corrections are plotted against the Julian Days in Fig. 3.3.

We also observed HD 3765 over three months in GIARPS mode: the thirteen NIR spectra have a typical SNR values of 163 and internal errors in RVs of 25 m s^{-1} (see Tab. 3.2), while the 22 VIS counterparts have a typical SNR of 200 and internal errors in RVs of 0.3 m s^{-1}. The GIANO – B RVs (Table 3.3) were obtained with the method described in Sec. 2.9, while HARPS – N RVs (Table 3.4) were processed by the HARPS – N pipeline (DRS) through the YABI workflow.

Fig. 3.4 shows the resulting RVs both in visible (blue points) and near-infrared (red points) ranges. While the VIS RVs present a rms scatter of 2.3 m s^{-1} in very good agreement with the jitter known from previous observations, the NIR RVs have an rms scatter of 25 m s^{-1} over three months, and neglecting two outliers it goes down to 16 m s^{-1}.

We may conclude that the short-term stability evaluated for the previous GIANO configuration, with data obtained in 7 consecutive nights in pretty stable environmental conditions, is 8 m s^{-1}. This can provide an indication of the actual short-term performance of GIANO

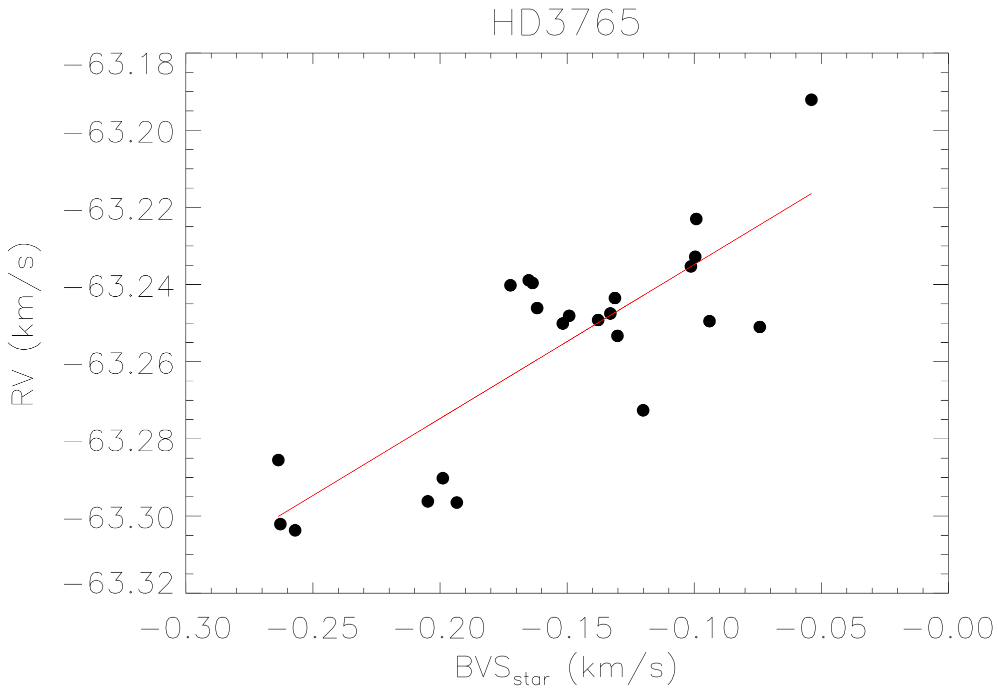

Figure 3.1: Correlation between GIANO – A RV values and the stellar bisector velocity span for HD 3765. The best linear fit is represented by a red line

– B. The long-term stability (over a half semester) is obtained with GIANO – B and it is ∼16 m s^{-1}, but since the observations were obtained during the first months of operation of GIANO – B, a series of maintenance services to the spectrograph could have produced RV offsets or drifts, as happened for AD Leo analysis (see Sec. 3.5 and App. D). For this reason, we have just started a new collection of HD 3765 spectra that should be obtained in a more stable and nominal condition, in order to have a better estimation of the long-term stability.

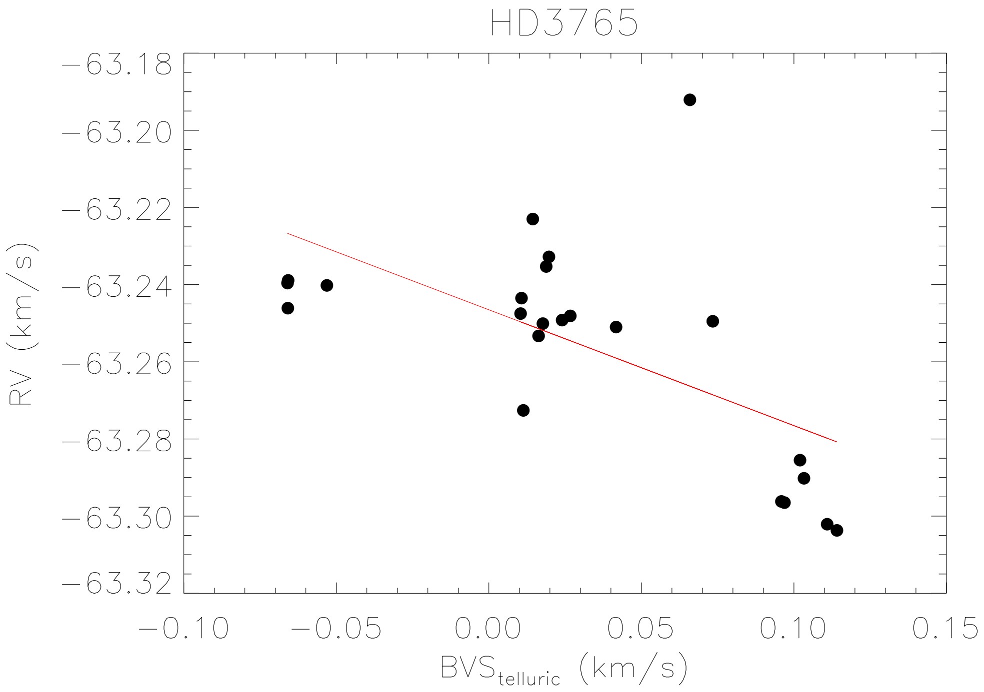

Figure 3.2: Correlation between GIANO – A RV values and the telluric bisector velocity span for HD 3765. The best linear fit is represented by a red line.

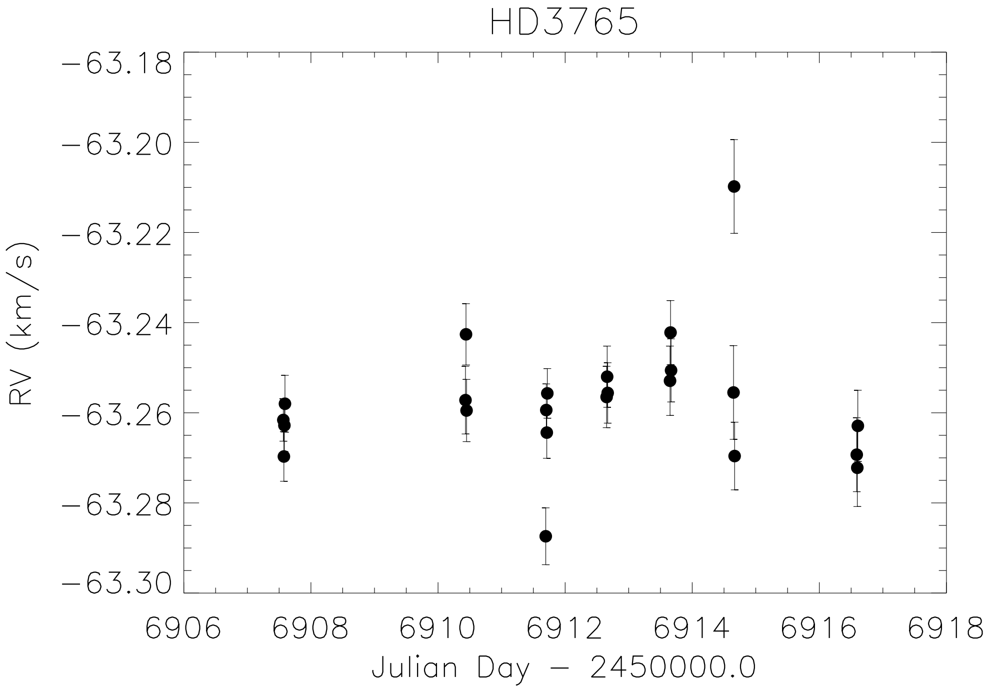

Figure 3.3: GIANO – A radial velocity values against the Julian Days for HD 3765, after correction for the systematic trend seen with the bisector velocity span of the telluric lines.

Table 3.1: GIANO – A results for HD3765. For each observation we have RV value, its internal error, the bisector velocity span of both telluric and star.

JD-2450000	Original RV (km s^{-1})	RV after correction (km s^{-1})	Final Error (km s^{-1})	BVS_{star} (km s^{-1})	BVS_{tell} (km s^{-1})
6907.56615741	-63.2389	-63.2616	0.0047	-0.1651	-0.1651
6907.57447917	-63.2461	-63.2697	0.0055	-0.1618	-0.0659
6907.58274306	-63.2396	-63.2628	0.0058	-0.1636	-0.0660
6907.59107639	-63.2402	-63.2580	0.0063	-0.1723	-0.0531
6910.43225694	-63.3021	-63.2572	0.0075	-0.2628	0.1109
6910.44055556	-63.2855	-63.2426	0.0068	-0.2636	0.1020
6910.44886574	-63.3037	-63.2595	0.0069	-0.2570	0.1141
6911.69504630	-63.2726	-63.2874	0.0063	-0.1201	0.0113
6911.70334491	-63.2475	-63.2594	0.0058	-0.1330	0.0104
6911.71164352	-63.2533	-63.2644	0.0057	-0.1302	0.0163
6911.71994213	-63.2435	-63.2557	0.0055	-0.1312	0.0107
6912.65265046	-63.2492	-63.2565	0.0068	-0.1378	0.0240
6912.66100694	-63.2481	-63.2520	0.0068	-0.1492	0.0267
6912.66934028	-63.2501	-63.2556	0.0067	-0.1517	0.0177
6913.65021991	-63.2353	-63.2529	0.0077	-0.1013	0.0188
6913.65861111	-63.2230	-63.2422	0.0071	-0.0992	0.0144
6913.66699074	-63.2328	-63.2506	0.0070	-0.0996	0.0197
6914.65011574	-63.2495	-63.2555	0.0104	-0.0940	0.0734
6914.65855324	-63.1921	-63.2098	0.0104	-0.0539	0.0659
6914.66695602	-63.2510	-63.2696	0.0075	-0.0742	0.0417
6916.58828704	-63.2962	-63.2693	0.0082	-0.2048	0.0959
6916.59723380	-63.2965	-63.2722	0.0086	-0.1934	0.0969
6916.60608796	-63.2902	-63.2629	0.0079	-0.1989	0.1033

Table 3.2: Summary of the spectroscopic data of HD 3765. For each dataset we list the instrument used for the observations, the number of spectra, the typical SNR, the RV nominal internal error (σ_{RV}), the RV r.m.s. scatter, and the peak-to-valley value of the RVs.

Instrument	N_{spectra}	SNR	σ_{RV} (ms^{-1})	RV r.m.s. (ms^{-1})	Peak-to-valley (ms^{-1})
GIANO – B	14	163	25.0	16.0	51.7
HARPS – N	22	205	0.3	2.3	7.1

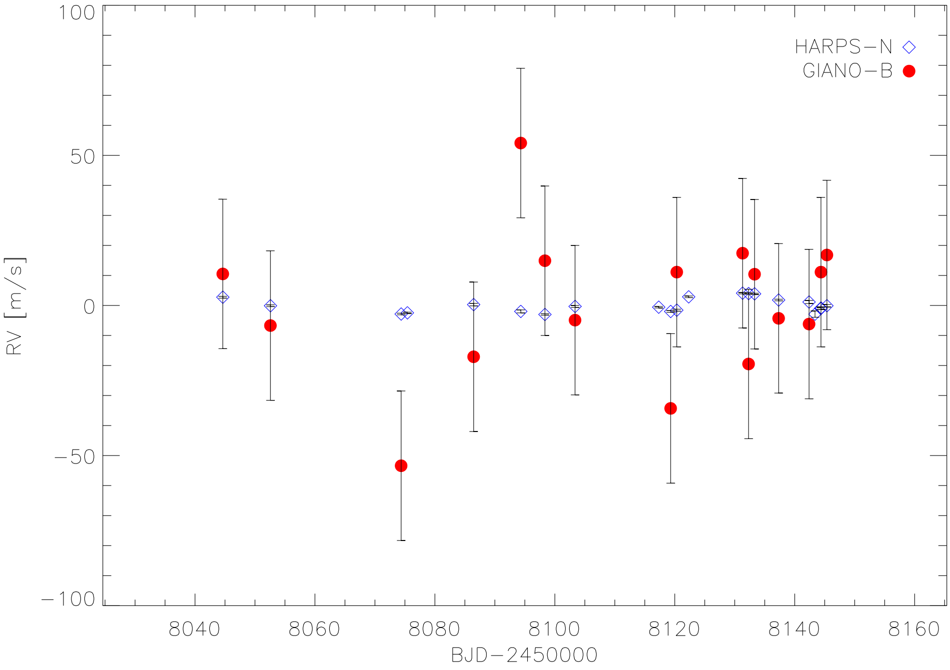

Figure 3.4: Radial velocities of the standard star HD 3765 from GIANO – B (red points) and HARPS-N (blue empty diamonds) spectra.

Table 3.3: Time series of HD 3765 from GIANO – B data. For each observation we list radial velocities (RV) and the bisector span (BIS) with the corresponding uncertainties.

JD-2450000	RV (km s^{-1})	σ_{RV} (km s^{-1})	BIS (km s^{-1})	σ_{BIS} (km s^{-1})
8044.6283912	0.073	0.025	0.026	0.005
8052.5756829	0.056	0.025	0.029	0.004
8086.4604167	0.045	0.025	0.021	0.004
8098.3465741	0.077	0.025	0.044	0.003
8103.3688889	0.058	0.025	0.028	0.003
8119.3134722	0.028	0.025	0.024	0.003
8120.3320255	0.074	0.025	0.027	0.003
8131.3076968	0.080	0.025	0.027	0.003
8132.3067014	0.043	0.025	0.009	0.003
8133.3059028	0.073	0.025	-0.032	0.003
8137.3186458	0.058	0.025	0.016	0.003
8142.3934838	0.056	0.025	0.022	0.004
8144.3778125	0.074	0.025	0.050	0.004
8145.3661343	0.079	0.025	0.035	0.003

Table 3.4: Time series of HD 3765 from HARPS – N data. For each observation we list radial velocities (RV) and the bisector span (BIS) with their related uncertainties.

JD-2450000	RV (km s^{-1})	σ_{RV} (km s^{-1})	BIS (km s^{-1})	σ_{BIS} (km s^{-1})
7944.6169299	-63.0773	0.0002	0.0102	0.0005
8044.6377734	-63.0735	0.0003	0.0105	0.0006
8052.5854038	-63.0763	0.0003	0.0097	0.0006
8074.3825627	-63.0791	0.0003	0.0103	0.0005
8075.4133771	-63.0787	0.0002	0.0086	0.0004
8086.4684090	-63.0760	0.0004	0.0104	0.0008
8094.3208140	-63.0782	0.0005	0.0131	0.0010
8098.3547519	-63.0792	0.0002	0.0116	0.0005
8103.3764748	-63.0766	0.0003	0.0098	0.0006
8117.3237640	-63.0768	0.0003	0.0112	0.0005
8119.3184981	-63.0782	0.0003	0.0098	0.0006
8120.3375930	-63.0778	0.0003	0.0108	0.0007
8122.3237605	-63.0734	0.0003	0.0086	0.0006
8131.3125197	-63.0721	0.0002	0.0083	0.0005
8132.3116015	-63.0723	0.0002	0.0073	0.0004
8133.3105559	-63.0724	0.0002	0.0087	0.0004
8137.3208510	-63.0744	0.0003	0.0094	0.0005
8142.3980010	-63.0751	0.0005	0.0027	0.0010
8143.3857416	-63.0791	0.0011	0.0154	0.0021
8144.3653698	-63.0773	0.0003	0.0034	0.0006
8144.3818961	-63.0771	0.0004	0.0030	0.0008
8145.3692090	-63.0763	0.0004	0.0063	0.0008

3.1.2 HD 159222

HD 159222 is a G1V star with magnitudes V=6.56, J=5.34, H=5.08, and K=5.00 (White et al., 2007). Although this star is listed in RV standard stars catalogues (Crifo et al., 2010), some works (Martínez-Arnáiz et al. 2010, Radick et al. 2018) state that it is an active star with $logR'_{HK}$ = -4.48, thus subject to intrinsic RV activity modulation.

We acquired 15 spectra of HD 159222 over 10 months in GIARPS mode: the NIR spectra have a typical SNR values of 141 and internal errors in RVs of 31 m s^{-1} (see Tab. 3.5), while the VIS counterpart a typical SNR of 148 and internal errors of 0.8 m s^{-1}.

Table 3.6 and Table 3.7 list the GIANO – B and HARPS – N RVs, respectively, and Fig. 3.5 shows the resulting RVs both in visible (blue points) and near-infrared (red points) ranges. While the VIS RVs present a rms scatter of $\sim$ 4 m s^{-1}, the NIR RVs have an rms scatter of 24 m s^{-1}. This dispersion may be related to different factors: HD 159222 is a G-type star, so in the NIR domain the number of stellar lines is lower with respect to a K-type star, like HD 3765, and this leads to a less accurate RV measurement; on the other hand, the long period of these observations (spanning from May 2017 to March 2018) may be affected by technical operations that could impact the instrumental stability, as happened for AD Leo observations (see Sec. 3.5 and App. D).

Table 3.5: Summary of the spectroscopic data of HD 159222. For each dataset we list the instrument used for the observations, the number of spectra, the typical SNR, the RV nominal internal error (σ_{RV}), the RV r.m.s. scatter, and the peak-to-valley value of the RVs.

Instrument	N$_{\text{spectra}}$	SNR	σ_{RV} (m s^{-1})	RV r.m.s. (m s^{-1})	Peak-to-valley (m s^{-1})
GIANO – B	15	141	31.0	23.6	78.0
HARPS – N	35	148	0.8	3.9	14.9

Table 3.6: Time series of HD 159222 from GIANO – B data. For each observation we list radial velocities (RV) and the bisector span (BIS) with the corresponding uncertainties.

JD-2450000	RV (km s^{-1})	σ_{RV} (km s^{-1})	BIS (km s^{-1})	σ_{BIS} (km s^{-1})
7904.4239931	-0.252	0.031	-0.004	0.083
7904.4277431	-0.237	0.031	-0.030	0.083
7904.4314699	-0.264	0.031	0.002	0.089
7914.4359722	-0.216	0.031	-0.047	0.040
7914.4419792	-0.234	0.031	-0.040	0.041
7955.4662731	-0.256	0.031	0.037	0.024
7961.4586574	-0.228	0.031	0.020	0.032
7961.4688079	-0.214	0.031	0.023	0.034
7962.5019907	-0.231	0.031	0.022	0.037
8044.3186574	-0.253	0.031	-0.012	0.041
8053.3438542	-0.198	0.031	-0.006	0.094
8062.3195370	-0.266	0.031	0.031	0.055
8072.2986458	-0.188	0.031	0.039	0.051

8185.7190278	-0.215	0.031	-0.005	0.071
8209.6759491	-0.216	0.031	-0.029	0.117

Table 3.7: Time series of HD 159222 from HARPS – N data. For each observation we list radial velocities (RV) and the bisector span (BIS) with their related uncertainties.

JD-2450000	RV (km s^{-1})	σ_{RV} (km s^{-1})	BIS (km s^{-1})	σ_{BIS} (km s^{-1})
7904.4263052	-51.5044	0.0007	-0.0039	0.0014
7904.4289556	-51.5057	0.0007	-0.0042	0.0014
7904.4313978	-51.5025	0.0006	-0.0018	0.0012
7904.4340251	-51.5040	0.0008	-0.0029	0.0016
7904.4365830	-51.5050	0.0008	-0.0050	0.0016
7914.4370378	-51.5005	0.0005	-0.0006	0.0009
7914.4396419	-51.5009	0.0004	0.0008	0.0009
7914.4422692	-51.4995	0.0005	0.0018	0.0009
7914.4448850	-51.4994	0.0005	0.0018	0.0009
7914.4475007	-51.5000	0.0005	0.0003	0.0010
7914.4500702	-51.4995	0.0005	0.0018	0.0010
7944.4780023	-51.4937	0.0006	-0.0055	0.0011
7955.4701805	-51.5040	0.0004	-0.0036	0.0008
7955.4727846	-51.5042	0.0004	-0.0050	0.0008
7955.4754350	-51.5044	0.0004	-0.0010	0.0008
7961.4623532	-51.5032	0.0006	-0.0074	0.0011
7961.4649226	-51.5051	0.0006	-0.0035	0.0011
7961.4676077	-51.5028	0.0006	-0.0037	0.0012
7962.4543414	-51.5003	0.0006	-0.0018	0.0012
7962.4568876	-51.5009	0.0006	-0.0031	0.0012
7962.4595033	-51.4995	0.0006	-0.0037	0.0011
7962.4954857	-51.4986	0.0006	-0.0033	0.0011
7962.4980435	-51.4995	0.0006	-0.0047	0.0012
7962.5006475	-51.4996	0.0006	-0.0010	0.0012
8044.3176762	-51.5000	0.0005	-0.0041	0.0011
8044.3203382	-51.5012	0.0006	-0.0037	0.0012
8053.3425049	-51.4969	0.0020	-0.0069	0.0040
8053.3453752	-51.4946	0.0027	-0.0108	0.0053
8062.3180362	-51.5062	0.0009	-0.0001	0.0017
8062.3207676	-51.5060	0.0010	-0.0028	0.0020
8062.3233486	-51.5042	0.0010	0.0006	0.0020
8068.3194799	-51.4913	0.0020	-0.0144	0.0039
8185.7195187	-51.5037	0.0008	-0.0021	0.0016
8209.6781174	-51.4938	0.0011	-0.0018	0.0022
8209.6806869	-51.4939	0.0012	-0.0009	0.0024

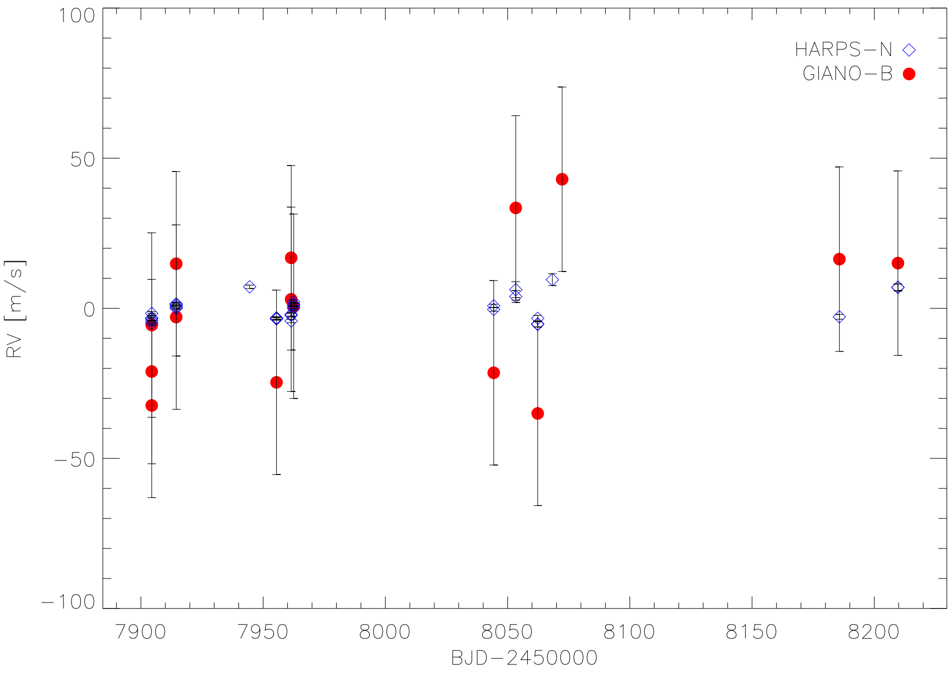

Figure 3.5: Radial velocities of the standard star HD 159222 from GIANO-B (red points) and HARPS-N (blue empty diamonds) spectra.

3.2 BD+20 1790

In this section, I present the analysis of the RV measurements of a debated Hot Jupiter (HJ) around BD+20 1790, presented in Carleo et al. (2018). BD+20 1790 (V429 Gem, K5Ve, V=9.9, Jeffries 1995) is a very active star ($\log R'_{HK} = -3.7$, Hernán-Obispo et al. 2015, hereafter HO15) and probable member of the AB Dor moving group (Torres et al., 2008) with an age of 149^{+51}_{-19} Myr (Bell et al., 2015). After dedicated spectroscopic observations, Hernán-Obispo et al. 2010 (hereafter HO10) interpreted the RV variations of this target as being due to the presence of a massive HJ with a period of 7.8 days. Figueira et al. (2010a) questioned the planet, providing CORALIE RVs showing a clear correlation with the bisector span (BIS), thus attributing the RV variations to photospheric processes. Later, HO15 reported a new RV and activity study exploiting a larger spectroscopic and photometric dataset supporting again the presence of a HJ around BD+20 1790. Finally, Gagné et al. (2016) published a small number of CSHELL NIR RVs with no conclusive results.

In Carleo et al. (2018) we ruled-out the presence of the planetary companion thanks to multi-wavelength observations.

3.2.1 Instruments

The instruments used for this survey includes HARPS – N and GIANO – B, whose characteristics are extensively described in Chapter 2. Moreover, we used IGRINS spectrograph and REM photometry.

IGRINS (Immersion Grating Infrared Spectrometer) (Mace et al., 2016) is the cross-dispersed NIR spectrograph, mounted alternatively at the Harlan J. Smith 2.7 m telescope (McDonald Observatory, TX, USA) and at the 4.3 m Discovery Channel Telescope (Lowell Observatory, AZ, USA), with a resolving power of R=45,000 (Yuk et al., 2010, Park et al., 2014). It covers the H and K windows, from 1.45 to 2.5 μm in a single acquisition.

REM (Rapid Eye Mount; Chincarini et al. 2003) is a 60 cm robotic telescope located at the La Silla station of the European Southern Observatory (ESO, Chile). The telescope hosts two instruments: REMIR, an infrared imaging camera, and ROS2, a visible imager. The two cameras can also observe simultaneously the same field of view thanks to a dichroic placed in front of the telescope focus. The ROS2 camera is equipped with a back-illuminated CCD (2048×2048 pixels, 13.5 micron pixels size, 0.58 arcsec/pixel plate scale), which has a corrected 9.8×9.8 arcmin field of view, and observes simultaneously through the four Sloan/SDSS g,r,i,z filters. The REMIR camera is equipped with a Hawaii I CCD (512×512 pixels, 1.2 arcsec/pixel plate scale), which has a corrected 10×10 arcmin field of view, and it is equipped with zJHK filters.

3.2.2 Observations and data reduction

In this section we describe the data acquired from each instrument. The spectroscopic datasets are presented in Sects. 3.2.2, 3.2.2, and 3.2.2, and a complete summary of them, including the uncertainties of the RVs measurements (obtained as explained before), the typical signal-to-noise ratio (S/N), the RV r.m.s., and the peak-to-valley amplitude, is reported in Table 3.8. The photometric observations are described in Sec. 3.2.2.

GIANO/GIANO – B

We collected spectra of BD+20 1790 with TNG instrumentation in three different observing campaigns (see Table 3.10). The first dataset consists of 18 observations with GIANO (March 28 – April 3, 2016), supported by quasi-simultaneous photometry with the REM telescope (see below). The second dataset (seven spectra) was acquired during the commissioning of GIANO – B in November 2016. The third one contains five spectra of GIANO – B obtained during the GIARPS commissioning in March 2017. Two of them are acquired in GIARPS mode in order to test the simultaneity of GIANO – B and HARPS – N observations. One additional HARPS – N spectrum was later collected without the NIR counterpart because GIANO – B was temporarily unavailable.

Table 3.8: Summary of the spectroscopic data presented in this work. For each dataset we list the instrument used for the observations, the number of spectra, the spectral range, the typical SNR, the RV nominal internal error (σ_{RV}), the RV r.m.s. scatter, and the peak-to-valley value of the RVs.

Instrument	N_{spectra}	Spect. range (μm)	SNR	σ_{RV} (kms^{-1})	RV r.m.s. (kms^{-1})	Peak-to-valley (kms^{-1})
GIANO/GIANO – B	18	0.95 - 2.45	72	0.036	0.130	0.384
HARPS – N	20	0.38 - 0.69	35	0.029	0.280	1.036
IGRINS	29	1.45 - 2.5	134	0.059	0.109	0.384

GIANO – A data were reduced with the IRAF package ECHELLE and the dedicated scripts collected in the GIANO_TOOLS[1] package, while GIANO – B spectra are processed with the dedicated pipeline GOFIO (Rainer et al., 2018).

We obtained a set of 30 NIR RVs over one year (listed in Table 3.10), with the method described in Carleo et al. (2016), in which the telluric lines are used as wavelength reference and the CCF method is used to determine the stellar RV. For this purpose, we constructed two suitable digital masks that include about 2000 stellar lines and a similar number of telluric lines. After the correction of the spectra to the barycentre of the solar system, the procedure performs the cross correlation of individual orders of the normalized spectra with the appropriate masks (both stellar and telluric), with the derivation of individual CCF. Through a weighted sum of the CCFs of the individual orders, we obtain the final stellar and telluric CCFs. These are fitted with Gaussian profiles to derive the stellar and telluric RV, respectively. The latter are finally subtracted from the former, providing the relative stellar RVs. The uncertainties are then evaluated taking into account the photon statistics. In the present analysis we consider a slightly different approach, which takes into account the weight of the single orders, some of them being affected by telluric lines and thus contributing in different ways to the determination of the RVs. Starting from the RV of individual orders, we calculate the weighted average RV for each exposure and its corresponding error. As a final step, we derive the bisector velocity span (BIS, as in Carleo et al. 2016) of the CCF and we

---

[1] Available at the TNG webpage: `http://www.tng.iac.es/instruments/giano/giano_tools_v1.2.0.tar.gz`.

calculate the uncertainties on this quantity by considering the fractions of the CCF used for the derivation of the BIS, resulting in $\sqrt{10}\sigma_{RV}$, where σ_{RV} is the RV error.

HARPS – N

HARPS – N RVs are extracted with the usual data reduction software (DRS, Pepe et al. 2002) by cross-correlating the observed spectrum with a numerical mask that depicts the spectral features of a K5 star. To work with uniform RV values, we processed our HARPS – N spectra and the ones collected by HO15 (except for one spectrum with very low signal-to-noise ratio at JD 2456681) with the current HARPS – N DRS through the YABI workflow. Since this facility allows us to customize the re-processing, we enlarge the width of the CCF to take into account the quite large $v \sin i$ of this star (10.03±0.47 km s^{-1}, López-Santiago 2005) and the consequent line broadening. The resulting RVs are listed in Table 3.11, together with the CaII activity indicator, logR'$_{HK}$, obtained with the dedicated tool of the HARPS – N DRS (the method is provided in Lovis et al. 2011) also available on YABI, and the BIS (see e.g. Queloz et al. 2001) estimated as in Lanza et al. (submitted), starting from the computed CCF of the DRS. The usually adopted uncertainty for the BIS is twice the value of the RV uncertainty, on the basis that the BIS slope is calculated using the top and lower half of a single line measurement. However, this occurs in the ideal case in which the bins of the CCF used for the estimation of the bisector are not correlated, therefore, in our case the multiplying factor is increased to 2.5 to avoid an underestimation of the uncertainties (see the justification in Lanza et al. 2018).

IGRINS

The 29 spectra of BD+20 1790 collected with IGRINS over one year, from April 2016 to March 2017, are reduced with the IGRINS Pipeline Package.[2] We acquired three different datasets, since the run with IGRINS installed at the Discovery Channel Telescope (DCT) occurred in between the two runs at the McDonald (McD) Observatory (see Table 3.8). The RV measurements (Table 3.12) are obtained with the same procedure used for GIANO, adapted to the spectral format of IGRINS.

REM

During the first run with GIANO we obtained quasi-simultaneous photometry with REM from May 30 to April 4, 2016. We used tasks within IRAF for bias correction and flat fielding, and the technique of aperture photometry to extract magnitude time series for BD+20 1790 and for other stars detected in the frames, which were selected as candidate comparison stars. In particular we identified two stars that were found to be non-variable and were used as comparison (C) and check (CK) stars (C: 2MASS 07233899+2025102, J = 11.23 mag, H = 11.43 mag, K = 11.17 mag; CK: 2MASS 07234597+2025328, J = 12.15 mag, H = 11.97 mag, K = 11.91 mag). We measured a standard deviation σ_{C-CK} = 0.014 mag in their differential light curve. The visible and infrared magnitudes of BD+20 1790 were computed differentially with respect to the comparison star. After averaging the six consecutive differential magnitudes

---

[2] `https://github.com/igrins/plp`.

obtained on each night with ROS2, we obtained a time series of six average *griz*-band differential magnitudes and four JHK-band differential magnitudes for the subsequent analysis. The average standard deviation associated with the nightly averaged magnitudes, which we consider as our photometric precision, is $\sigma < 0.015$ mag for all filters, and $\sigma \simeq 0.04$ mag for the H and K magnitudes.

3.2.3 Data analysis

Spectroscopic data

First, we reproduced the orbital fit of the VIS RVs as presented in HO15 (with SARG, FOCES, and HERMES data only) with a Keplerian function[3] as in Desidera et al. (2011). Our model is displayed in the upper panel of Fig. 3.6 as a dashed line together with the VIS data used for the fit, represented by grey dots. The obtained RV semi-amplitude is 926.8 ± 34.6 ms^{-1} and the period is 7.7827 ± 10^{-4} days, in good agreement with the result proposed by HO15. As in HO15, we were not able to obtain a solution including their HARPS – N data so we only over-imposed them to the fitting function. We observe a poor match that by itself casts some doubt on a Keplerian interpretation of the RV variation.

Our phase-folded NIR RVs are shown as well in Fig. 3.6 (lower panel): GIANO – A and GIANO – B RVs (red dots) show an r.m.s. scatter of 129.6 ms^{-1}, while IGRINS RVs (light blue dots) show an r.m.s. scatter of 109.2 ms^{-1}. The r.m.s. scatter of the whole NIR dataset is 119 ms^{-1}. Finally, the black asterisks represent new HARPS – N data (two of them have the NIR simultaneous counterpart). Figure 3.6 shows that the amplitude of NIR RVs (calculated as the difference between maximum and minimum RVs) is 437.3 ms^{-1}, four times lower with respect to the optical one reported in HO15 and interpreted as a signature of a hot Jupiter. Therefore, according to our data we can exclude any companion with those characteristics, ascribing the observed variation to phenomena of stellar origin.

Actually, the Spearman rank correlation between RVs and BIS, in this case for the whole HARPS – N dataset (HO15 and the three epochs presented here) is -0.92, with a very high statistical significance (p-value = $2 \cdot 10^{-8}$, evaluated through the IDL Astronomy Library routine `SAFE_CORRELATE`; see Table 3.9 for a summary of the measured correlations between RVs and activity indices of the whole dataset), showing an unambiguous linear trend (Fig. 3.7). After subtracting this correlation from the HARPS – N RVs time series, the resulting residuals show an r.m.s. of 61.1 ms^{-1} and the Generalized Lomb-Scargle (GLS) periodogram (Zechmeister & Kürster, 2009) does not show any significant periodicity (i.e. with an amplitude larger than four times the standard deviation of the power spectrum, corresponding to a false alarm probability (FAP) larger than 0.01). As further evidence that the original HARPS – N RVs are modulated by the stellar rotation of 2.801 ± 0.001 d (the photometric period by HO10), in Fig. 3.8 we fit them with a Keplerian function by using as a first guess that period, obtaining a very good agreement with our model (P=2.80150±2$\cdot 10^{-5}$ d, K=0.449±7.370 kms^{-1}, e=0.065±0.018).

We also investigated the other activity indices available from HARPS – N, for example $\log R'_{HK}$ as described in Sect 3.2.2, and the CCF asymmetry indices: the ΔV (a measure of the RV shift produced by the exclusive contribution of the asymmetry of the CCF; see Nardetto et al. 2006 and Figueira et al. 2013) and the $V_{\mathrm{asy(mod)}}$ (the modified version of the index V_{asy} by Figueira et al. 2013 for which the dependence from the RV shift is removed), presented in

---

[3] We adopted the IDL least-squares MPFIT package available at `http://purl.com/net/mpfit`.

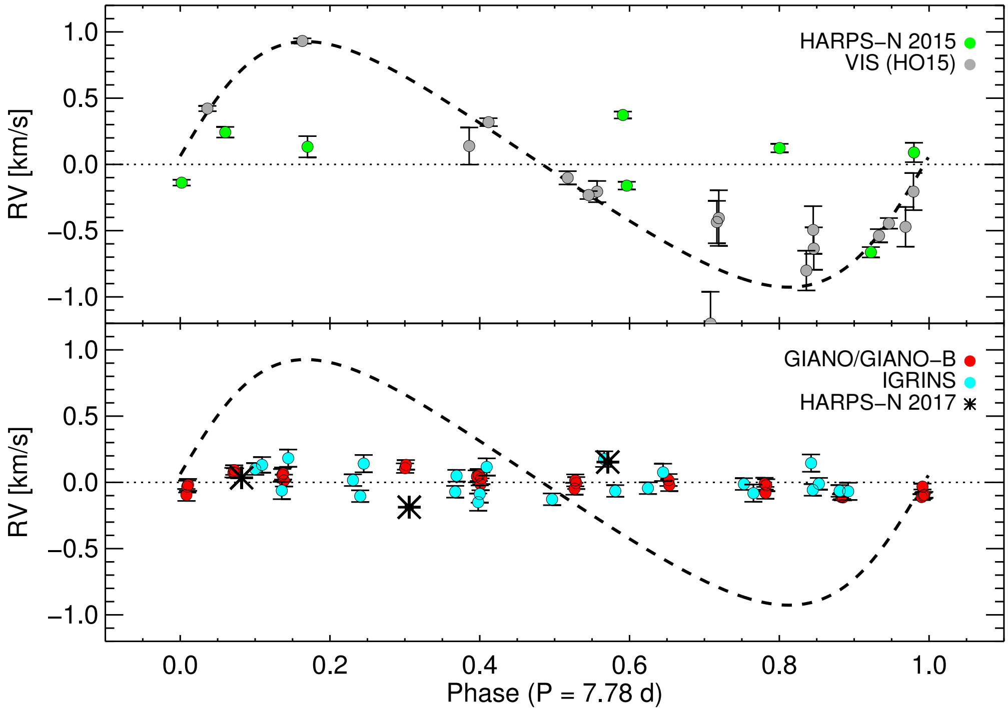

Figure 3.6: Orbital fit at 7.78 days found by HO15 compared to phase-folded visible and NIR RVs. Top panel: Orbital fit (black dashed line) obtained with the visible data (FOCES, SARG, and HERMES RVs from HO15, grey dots) and HARPS-N 2015 RVs (green dots). Bottom panel: Orbital fit (black dashed line), GIANO – A/GIANO – B (red dots), IGRINS (light blue dots), and HARPS-N 2017 (black asterisks, two acquired in GIARPS mode) RVs.

Table 3.9: Summary of the values of Spearman (ρ) correlation coefficients and corresponding p-values between RVs and activity indicators.

Parameters	ρ	p-value
HARPS – N (2015, 2017):		
RV - BIS	−0.92	$2 \cdot 10^{-8}$
RV residuals - BIS	0.39	0.13
RV - $\log R'_{HK}$	0.23	0.45
RV - $\mathrm{v}_{\mathrm{asy(mod)}}$	0.89	$2 \cdot 10^{-7}$
RV - ΔV	−0.91	$1 \cdot 10^{-7}$
RV - Hα	−0.35	0.22
GIANO,GIANO – B:		
RV - BIS	−0.14	0.44
RV - HeI	−0.08	0.65
IGRINS:		
RV - BIS	0.13	0.48
RV - Brγ	0.12	0.51

Lanza et al. (2018).[4] Finally, we also checked the correlation with the Hα index derived as in Sissa et al. (2016). As for the BIS, the other asymmetry indices show significant correlation with RVs, while we find weak correlations with $\log R'_{HK}$ and H_α indicators (Table 3.9).

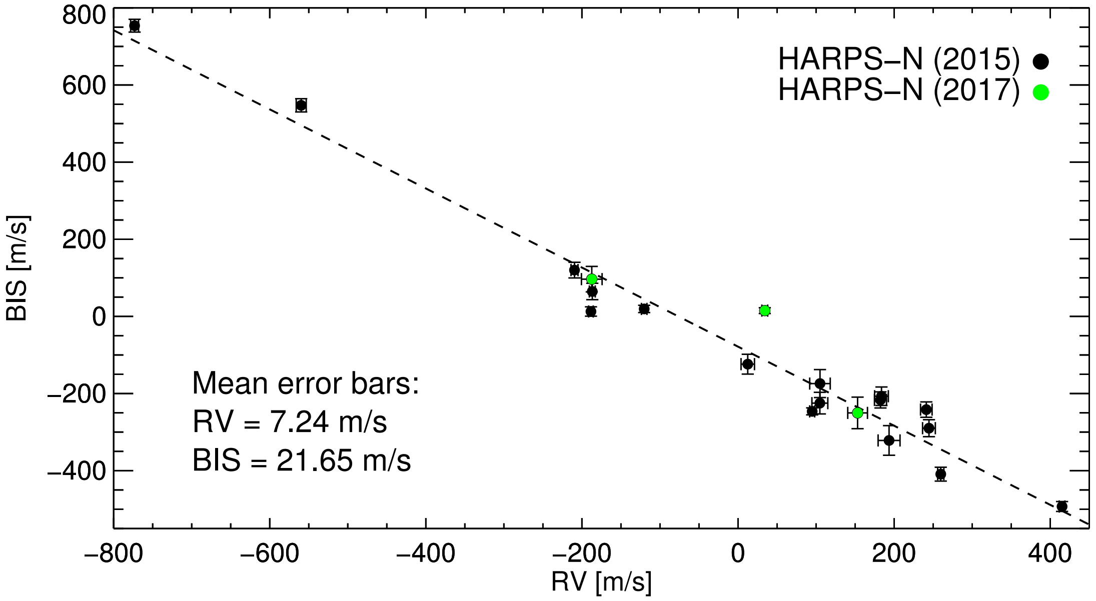

Figure 3.7: Correlation between RVs and BIS for HARPS – N data (HO15 and the three new epochs in this work).

We then focused our attention on the NIR data. We computed the GLS for both GIANO and IGRINS RVs even if the sampling is not suitable for a proper periodogram analysis (too few and too sparse points) or for a proper resolution of the known photometric period. The periodograms are quite noisy and do not exhibit any significant periodicity. Only for GIANO did we investigate the FAP (estimated by generating 10,000 artificial RV curves obtained from the real one, keeping the epochs of observations fixed but making random permutations of the RV values) of a peak at 7.74 d responsible for the apparent signal of the GIANO data when phase-folded with the orbital period proposed by HO15 (red dots in Fig. 3.6, lower panel). This test returned a FAP of 24.4%, so this periodicity is probably produced by random noise. We also noticed a small amount of power corresponding with the photometric period of the star, but it appears to be related to the GIANO data sampling according to the analysis of the window function. No prominent periodicity is found either when examining the GLS of the whole NIR dataset, which is obtained by applying a quite negligible RV offset between the two instruments (5 m s^{-1}). In order to investigate a possible correlation between NIR RVs and activity indicators, we first measured the Spearman coefficient for GIANO and GIANO – B data, in particular between the BIS and the RVs, the BIS and HeI index at 1.083 μm

---

[4] See a description of the $V_{\mathrm{asy(mod)}}$ in the poster "Line asymmetry indicators to detect stellar activity effects in radial velocity measurements" by Lanza et al., available at: `https://sites.google.com/a/yale.edu/eprv-posters/home`.

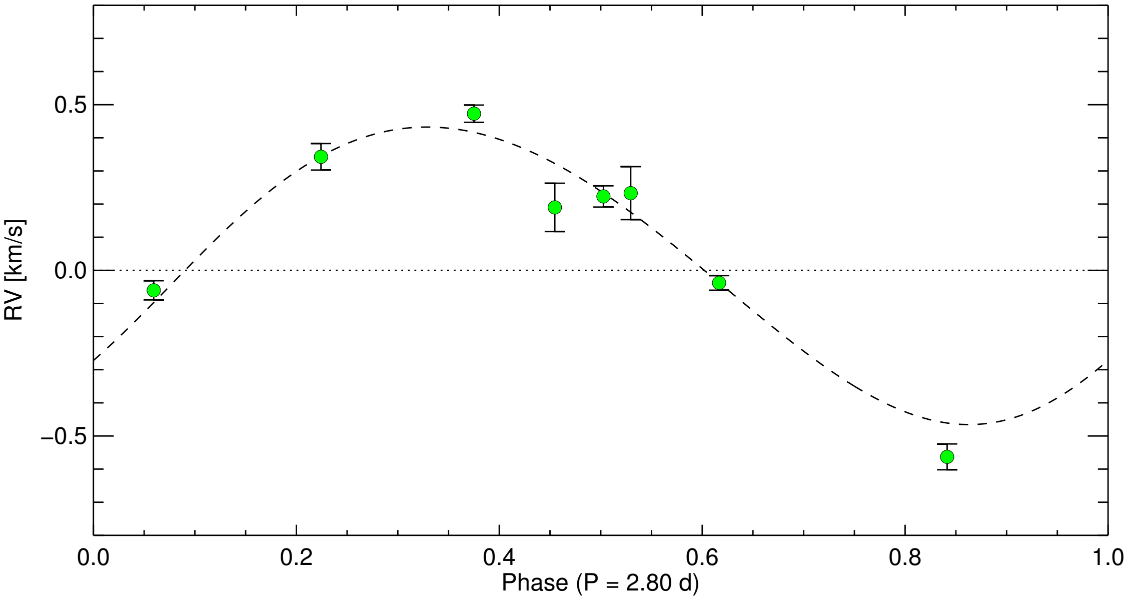

Figure 3.8: Phase-folded HARPS – N RVs (2015, reprocessed from HO15 dataset) at stellar rotational period.

(extracted as in Robertson et al. 2016), and between the HeI index and the RVs, but we found no strong correlation (Table 3.9), mainly due to the uncertainties in the measurements. A similar analysis was performed for the IGRINS data. Since the HeI line is out of the spectral coverage of IGRINS, we investigated the impact of the activity on RVs through the Brackett γ (Brγ) emission line at 2.16 μm (not available in the GIANO spectra because of the discontinuity among the orders), extracted as in Robertson et al. (2016). As in the case of GIANO, no significant correlation was found between RVs and these indicators (Table 3.9). Apparently our NIR radial velocities for BD+20 1790 are not highly sensitive to activity.

Photometric data

We used the GLS and the CLEAN (Roberts et al., 1987) periodogram analyses to search for significant periodicities in the BD+20 1790 photometric time series related to its rotation period. As an example, the GLS and CLEAN periodograms are plotted in Fig. 3.9 for the case of the g filter. The solid black line represents the normalized power versus period, whereas the dotted red line is the spectral window function. The horizontal red dashed line represents the power level corresponding to a FAP = 0.01 (confidence level of 99%, obtained with 1,000 moke light curves as in Sect. 3.2.3).

Our periodogram analysis of the photometric variation confirmed the already known stellar rotational period P = 2.76 ± 0.04 days (corresponding to the most powerful and significant peak in the periodogram, indicated with a red mark), slightly lower than the literature value possibly because of the short baseline of the observations (six consecutive nights) or the effect

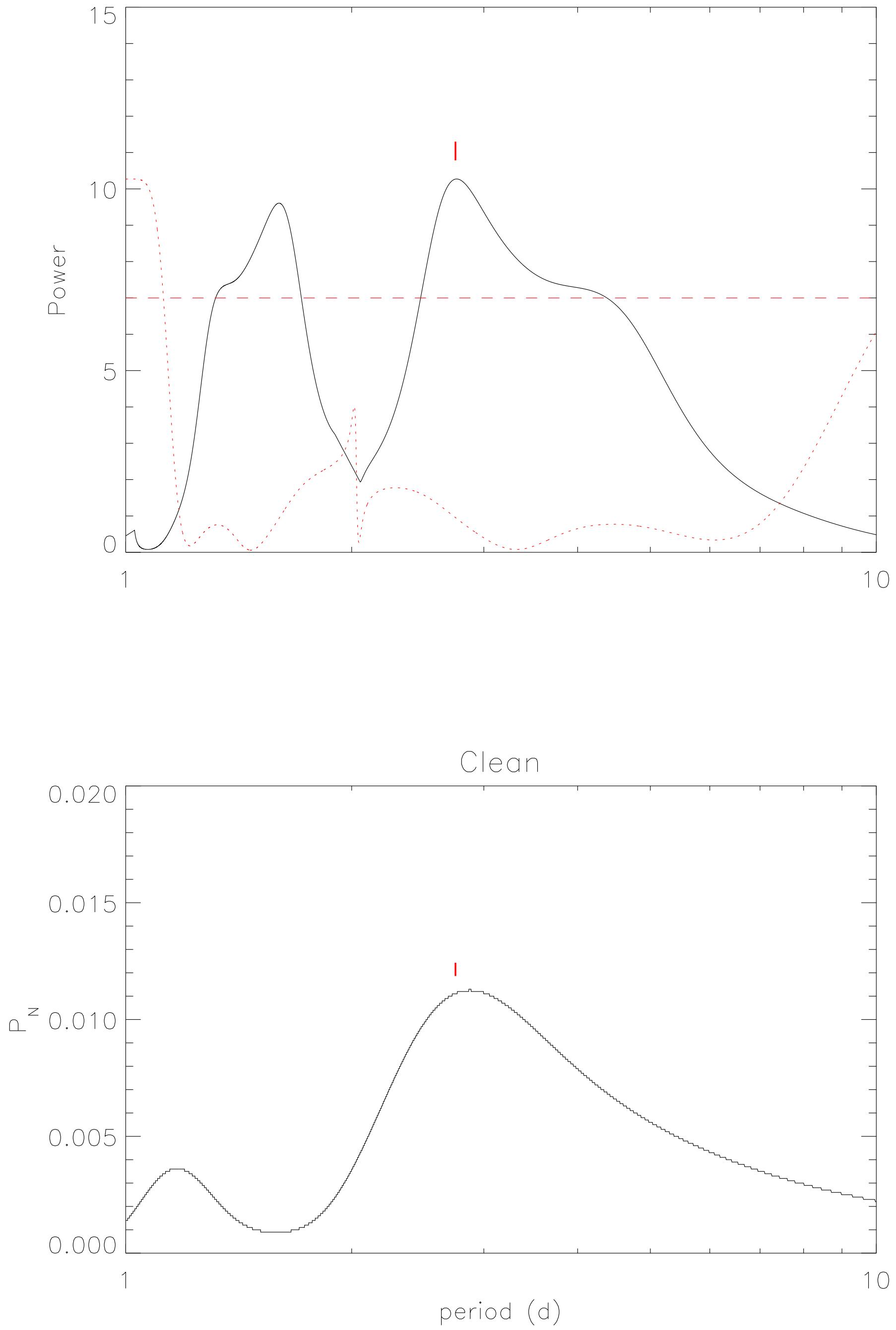

Figure 3.9: Top panel: Generalized Lomb-Scargle periodogram of the g-band photometric time series of BD+20 1790. The solid black line is the normalized power versus period, the dotted red line is the spectral window, and the horizontal dashed line indicates the power level corresponding to a FAP = 0.01. Bottom panel: CLEAN periodogram. The red mark is the most powerful and significant peak in the periodogram.

of differential rotation. The uncertainty on the period is calculated following the prescription of Lamm et al. (2004). We note that the secondary power peak in the GLS periodogram is absent in the CLEAN periodogram, which has the capability of effectively removing alias frequencies arising from the data sampling.
In Fig. 3.10 we plot the differential light curves of BD+20 1790 phased with the rotation period P = 2.76 d, using different colours for different filters. The solid lines represent sinusoidal fits to the phased magnitude computed using the rotation period. The peak-to-peak amplitudes of the sinusoidal fits measured in different filters are reported as labels in the figure. We observe that the REM light curves show different amplitudes in the different bands: unexpectedly, the amplitudes at longer wavelengths are greater than those at shorter wavelengths and the NIR modulation is almost in anti-phase with respect to the optical modulation in the *gri* passbands (the maximum of the light curves are located at ~ 0.8 for the *gri* filters, at ~ 0.1 for z and at ~ 0.2 for JHK). Moreover, the amplitudes of the optical light curves are a factor of approximately seven smaller than in other seasons (cf. the light curves in Fig. 3 in HO15). This could be due to a transient phase of peculiar activity during the REM observing season (that covered a very short period) with respect to what was observed in past campaigns. This particular variability is also supported by the comparison between our HARPS – N RVs and the ones in HO15, as noticed also by Figueira et al. (2010a) with CORALIE data.

3.2.4 Discussion

The present investigation adds another important piece of evidence to the multi-wavelength characterization of the RV variations in late-type stars. Our results show that the amplitude of the NIR RV modulation in BD+20 1790 is generally a factor of $2-3$ smaller than in the optical band, in agreement with the results obtained by Crockett et al. (2012) for very active young stars. This indicates that brightness inhomogeneities, whose contrast is generally smaller in the NIR than in the optical passband, are mainly responsible for the RV variations via line profile distortions. Other effects, such as quenching of convective blueshifts (e.g. Lanza et al. 2011) or line profile distortions produced by the Zeeman effect (Reiners et al., 2013), are probably less important in these very active and moderately rapidly rotating ($v \sin i \geq 10$ km s^{-1}) stars. Nevertheless, an intriguing result is the small amplitude of the RV variations in the NIR as measured by GIANO contemporaneously to the REM observations that show a remarkable NIR rotational modulation in the J, H, and K passbands. To interpret these results, we first consider a simple model for the wide-band photometric variations, including the effects of both dark and bright spots. Several models for the simultaneous photometric and RV variations of late-type stars have been proposed (e.g. Boisse et al. 2012; Dumusque et al. 2014; Herrero et al. 2016). They include the effects of solar-like faculae whose contrast increases towards the limb. Here, we consider a hot spot in the photosphere that has a constant contrast at different limb positions, similarly to the behaviour generally assumed for a cool spot.

From the stellar $v \sin i$, radius, and rotation period (from HO10), we estimated an inclination of the stellar spin axis to the line of sight of $\sim 50°$. With a simulation we then reproduced the sinusoidal shapes, amplitude ratio, and phase difference of the optical and the NIR light curves by assuming a circumpolar active region, always in view, consisting of two co-spatial components (as observed in e.g. V410 Tau, Rice et al. 2011): a cool feature (hereinafter "cool spot") covering a fraction $f_{\rm s}$ of its total area and a hot feature (hereinafter

"hot spot") covering the remaining fraction $1 - f_{\rm s}$.
Therefore, the average brightness of the active region at wavelength λ can be written as

$$I_{\rm a} = f_{\rm s} B(T_{\rm c}, \lambda) + (1 - f_{\rm s}) B(T_{\rm h}, \lambda), \tag{3.1}$$

where, for simplicity, we assume that the brightness of each component is given by a Planck function $B(T, \lambda)$, with $T_{\rm c}$ being the temperature of the cool spot and $T_{\rm h}$ that of the hot spot. Those temperatures verify the inequality: $T_{\rm c} < T_{\rm phot} < T_{\rm h}$, where $T_{\rm phot}$ is the temperature of the unperturbed photosphere. The contrast of the active region is $C_{\rm s} = 1 - (I_{\rm a}/I_{\rm phot})$, where $I_{\rm phot}$ is the brightness of the unperturbed photosphere. For an active region dominated by the cool spot, $C_{\rm s} > 0$ because $I_{\rm a} < I_{\rm phot}$, while for an active region dominated by the hot spot, $C_{\rm s} < 0$.

For BD+20 1790, we assume $T_{\rm phot} = 4410$ K (HO15), while for the cool and the hot spots we assume temperatures $T_{\rm c} = T_{\rm phot} - 1000$ K and $T_{\rm h} = T_{\rm phot} + 1000$ K, respectively. Those temperature differences are typical of young and active stars such as Weak T-Tauri stars (cf. Rice et al., 2011, Koen, 2016). The contrast is plotted versus the fraction of the active region covered by the cool spot in Fig. 3.11 for the optical wavelength $\lambda_{\rm opt} = 636$ nm and the NIR wavelength $\lambda_{\rm NIR} = 1705$ nm. Those values correspond approximately to the mean wavelengths of the *gri* bands and of the *JHK* bands, respectively.

We see that for a restricted range of $f_{\rm s}$, that is $0.65 < f_{\rm s} < 0.67$, the contrast in the optical is negative and small, while that in the NIR is positive and remarkably larger. This leads to a rotational modulation of the optical flux remarkably smaller than, and in anti-phase with, the rotational modulation in the NIR as illustrated by the synthetic light curves in Fig. 3.12 computed with the model in Sect. 3.2 of Lanza (2016). Specifically, these light curves were computed for an inclination of the spin axis to the line of sight $i = 50°$, considering an active region of an area of 20% of that of the star's disc, centred at a latitude of 60°. The quadratic limb-darkening coefficients at the two wavelengths were taken from Claret et al. (2012), while $C_{\rm s}(\lambda_{\rm opt}) = -0.02$ and $C_{\rm s}(\lambda_{\rm NIR}) = 0.15$ corresponding to $f_{\rm s} \simeq 0.665$ in our simple irradiance model (cf. Fig. 3.11). For simplicity, we assumed that the spot contrasts did not depend on the position on the disc.

The present model is simply illustrative. The amplitudes of the synthesized light curves are remarkably smaller than those observed in BD+20 1790, which may require a larger filling factor of the active region and/or larger temperature contrasts. For example, in the case of LkCa 4, Gully-Santiago et al. (2017) found a filling factor as large as 86%, which would imply an amplitude larger by a factor of approximately four in the case of the present model.
We finally notice that the variable characteristics of the activity of this star with time might explain why past studies obtained quite different values for the r.m.s. scatter of the RVs, and then different interpretations of the nature of this object.

As previously mentioned, the small amplitude of the RV modulation in the NIR as measured by GIANO contemporaneously with REM photometry is intriguing. Assuming that the depth of the spectral lines relative to their adjacent continuum is constant and considering a spot with a contrast $C_{\rm s}$ at latitude ϕ with a filling factor $f_{\rm s}$, we expect an RV modulation approximately of $C_{\rm s} f_{\rm s} v \sin i \cos\phi$ (cf. Saar & Donahue 1997; Desort et al. 2007) that is $\approx 0.75 - 1.0$ km s^{-1} for a spot at $\phi = 60°$, which is remarkably higher than what has been observed. A cool spot at a higher latitude would reduce the amplitude of the NIR wide-band flux modulations; a quenching of the convective shifts or the Zeeman effect also do not appear to be viable explanations because they increase the effect of a cool spot on

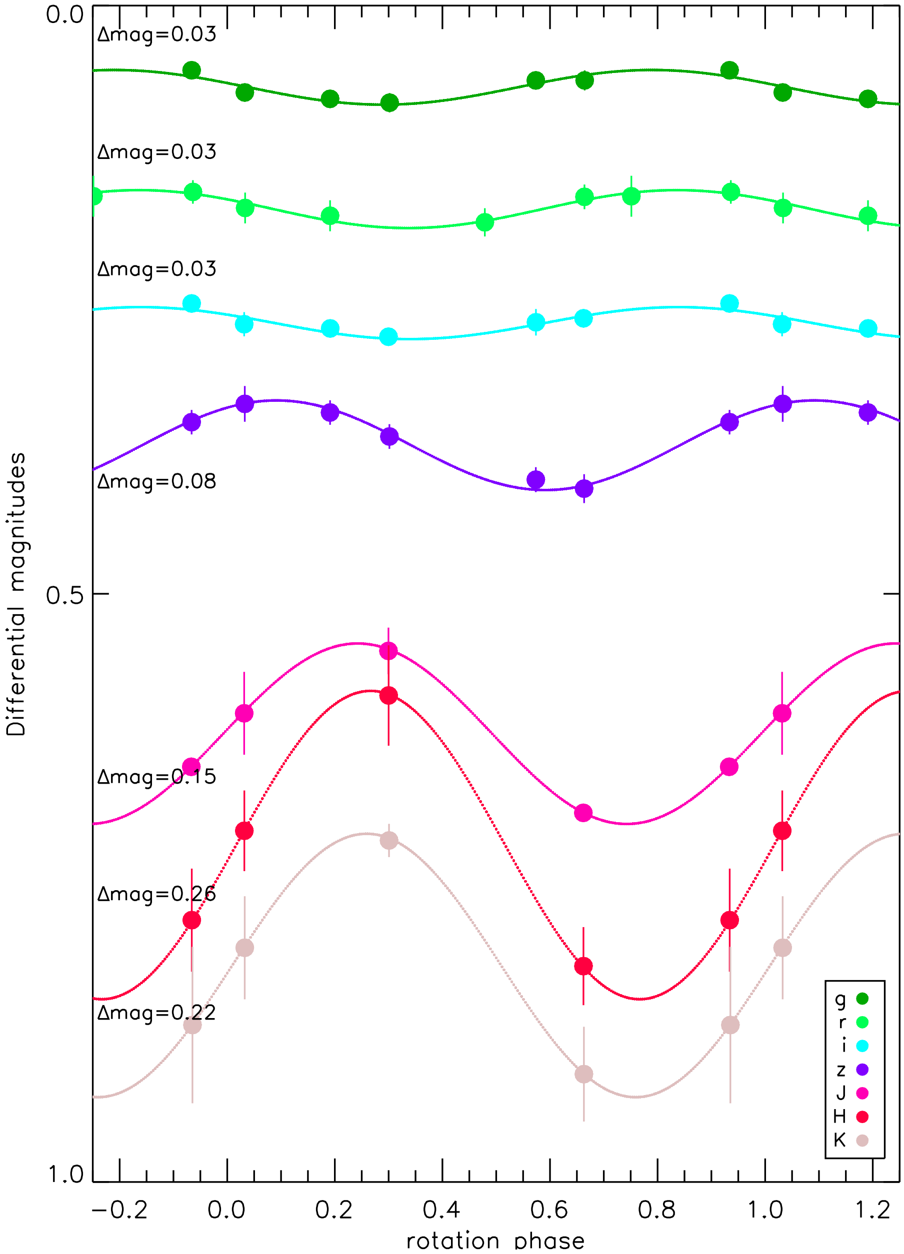

Figure 3.10: Differential lightcurves of BD+20 1790 phased with the rotation period P = 2.76d in different photometric bands. The solid line is a sinusoidal fit to the data with the same period. Labels show the peak-to-peak amplitudes of the lightcurves.

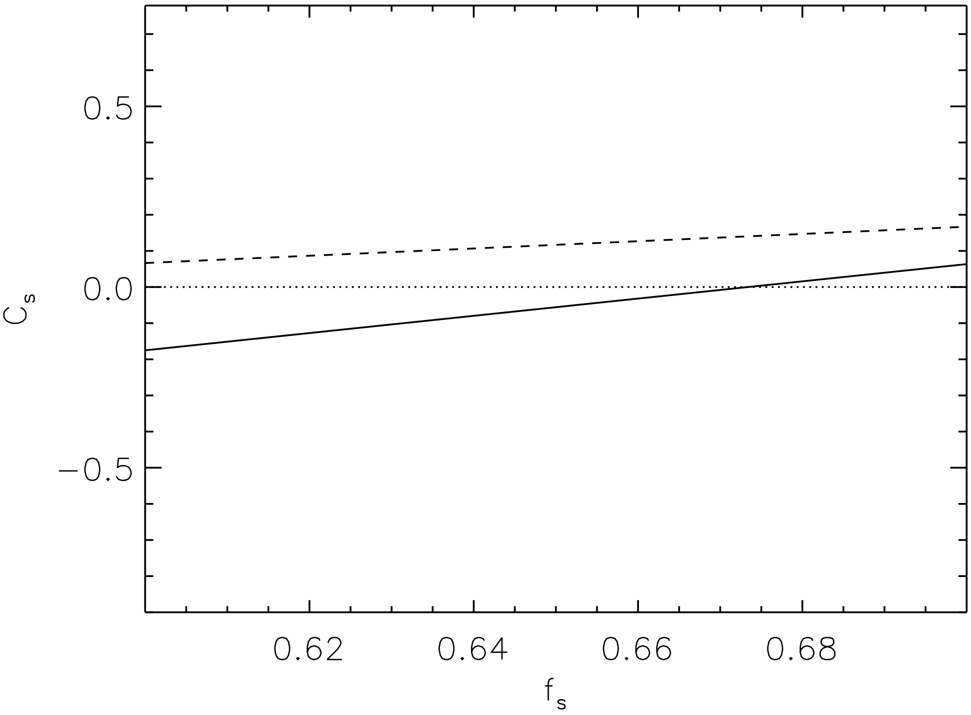

Figure 3.11: Contrast of an active region consisting of co-spatial cool and hot spots versus the fraction of its area covered by the cool spot. Two wavelengths are considered: $\lambda_{\rm opt} = 636$ nm (solid line) and $\lambda_{\rm NIR} = 1705$ nm (dashed line).

the RV at NIR wavelengths (Reiners et al., 2013). Nevertheless, the variation of the relative depths of the spectral lines in the NIR cannot be neglected and it is the dominant effect in the cool spot responsible for the large photometric modulation in the infrared. The relative line depths are strong functions of the continuum opacity and of the degree of element ionization both remarkably varying in a cool spot area with respect to the unperturbed photosphere. In general, these effects produce a remarkable increase of the relative depths of the spectral lines in the cool spot. This compensates for the decrease of the continuum intensity in the spot, reducing the distortions of the spectral line profiles and yielding an RV variation in the NIR smaller than expected from the wide-band photometric variation in the case of constant relative line depths. In any case, a quantitative analysis is not warranted by our data, since a larger number of observations would be required. This scenario suggests a need to better investigate this kind of target, since they might go through specific activity phases during which the VIS and NIR RV amplitudes are similar, possibly resulting in false positives. Looking at the curve phase shifts might give crucial information in these cases (see e.g. the recent result by Hatzes et al. 2018 for the K-giant γ Draconis).

With this work we dismiss the presence of the claimed hot Jupiter around BD+20 1790, which is a very peculiar target from the point of view of stellar activity, as confirmed by our photometric monitoring with REM almost contemporary to the first spectroscopic run with GIANO. Surprisingly, REM light curves show larger amplitudes at longer wavelengths and the NIR curve is almost in anti-phase with respect to the visible one. This has been explained with a photometric model that includes a mixture of cool and hot spots in the same active region.

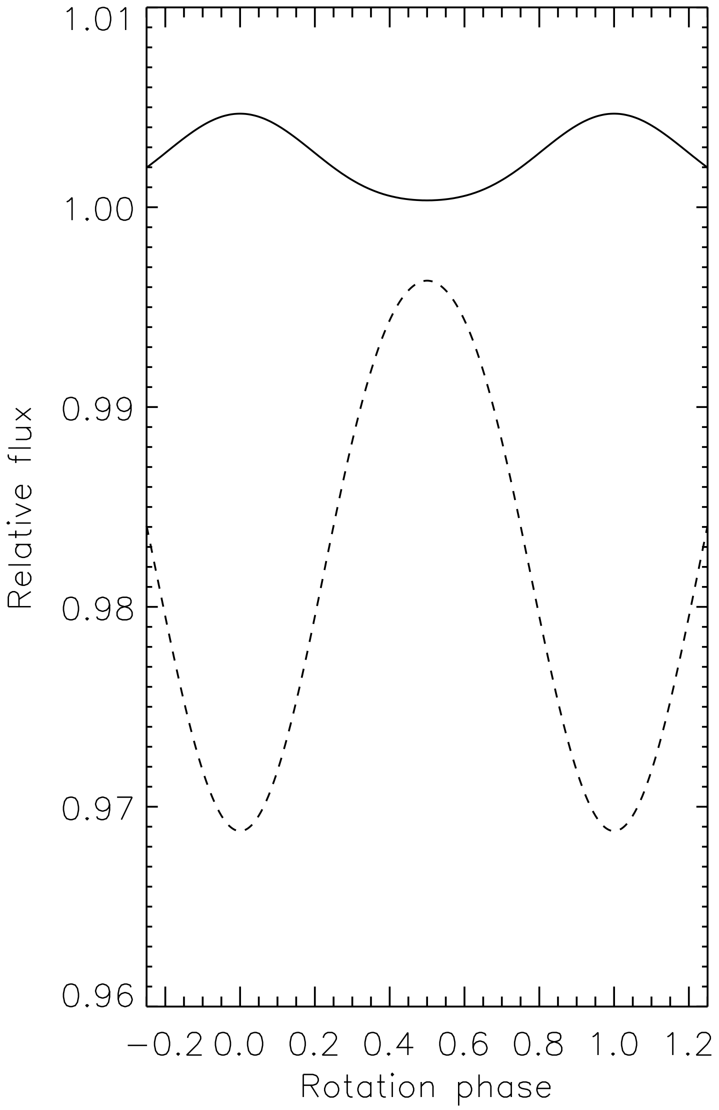

Figure 3.12: Light curves showing the rotational modulation of the flux at two wavelengths $\lambda_{\rm opt} = 636$ nm (solid line) and $\lambda_{\rm NIR} = 1705$ nm (dashed line). The amplitudes correspond to a spot having an area of 0.2 of the stellar disc.

Multi-band spectroscopy is known to be crucial in the search for exoplanets around young and active stars: here we present the first contribution of a new facility, GIARPS, which adds further value to this method thanks to the simultaneous observations in VIS and NIR bands. Our result clears the current census of hot Jupiters from the only previously known case orbiting a star between 20 to 200 Myr old (Rizzuto et al., 2017, David et al., 2018). The paucity of hot Jupiters in this age range might be explained by the time dependence of planet migration mechanisms (Mann et al. 2018 [5]) or simply by small number statistics. Further investigations are needed to achieve a firm conclusion on this key issue for the evolution of planetary systems.

Table 3.10: Time series of BD+20 1790 from GIANO and GIANO – B data. For each observation we list radial velocities (RV) and the bisector span (BIS) with the corresponding uncertainties.

Dataset	JD-2450000	RV (km s^{-1})	σ_{RV} (km s^{-1})	BIS (km s^{-1})	σ_{BIS} (km s^{-1})
GIANO	7475.8302179	8.476	0.045	0.090	0.071
	7475.8387828	8.539	0.045	0.138	0.074
	7475.8473007	8.552	0.045	0.082	0.076
	7476.8292450	8.626	0.045	0.289	0.076
	7476.8378800	8.637	0.045	0.106	0.069
	7476.8463629	8.584	0.045	0.232	0.073
	7478.8578259	8.616	0.045	0.043	0.083
	7478.8768308	8.626	0.045	0.128	0.083
	7478.8946776	8.556	0.045	0.036	0.078
	7478.9032996	8.602	0.045	0.124	0.076
	7479.8734209	8.523	0.045	0.123	0.049
	7479.8819158	8.586	0.045	0.017	0.052
	7479.8917888	8.566	0.045	0.106	0.054
	7480.8530107	8.588	0.045	0.226	0.076
	7480.8612976	8.550	0.045	0.147	0.072
	7481.8545340	8.560	0.045	-0.005	0.071
	7481.8631110	8.491	0.045	0.178	0.070
	7481.8715830	8.550	0.045	0.119	0.067
GIANO – B	7716.7390467	8.256	0.022	0.183	0.026
	7716.7477729	8.263	0.022	0.177	0.026
	7716.7564760	8.253	0.022	0.208	0.025
	7717.5770302	8.256	0.022	0.125	0.039
	7717.5857217	8.335	0.022	0.141	0.036
	7717.5945405	8.266	0.022	0.170	0.031
	7717.6046440	8.273	0.022	-0.016	0.036
GIANO – B	7821.4345852	8.474	0.036	-0.007	0.085
	7821.4436589	8.498	0.036	-0.014	0.084
	7827.4492982	8.440	0.036	0.332	0.087
	7827.4575966	8.460	0.036	0.274	0.090

---

[5] `https://keplerscience.arc.nasa.gov/cluster-workshop/talks/k2clusters-13-andrew-mann.pdf`.

	7827.4658833	8.437	0.036	0.094	0.092

Table 3.11: Time series of BD+20 1790 from HARPS – N data, from HO15 and GIARPS commissioning, uniformly reduced with the new HARPS – N DRS version. For each observation we list radial velocities (RV), $\log R'_{HK}$, and the bisector span (BIS) with their related uncertainties.

JD-2450000	RV (km s^{-1})	σ_{RV} (km s^{-1})	BIS (km s^{-1})	σ_{BIS} (km s^{-1})	$\log R'_{HK}$	$\sigma_{\log R'_{HK}}$
6293.496128	7.818	0.004	0.019	0.009	-3.982	0.002
6293.694395	7.750	0.004	0.065	0.021	-3.984	0.003
6293.768482	7.726	0.005	0.120	0.020	-3.995	0.003
6346.563090	8.021	0.003	-0.247	0.009	-3.944	0.002
6347.423110	7.374	0.007	0.547	0.017	-3.977	0.004
6347.601234	7.163	0.005	0.754	0.017	-3.989	0.004
6348.543400	8.113	0.008	-0.217	0.021	-4.016	0.007
6348.548909	8.113	0.010	-0.207	0.024	-4.041	0.008
6348.620652	8.167	0.009	-0.290	0.022	-4.018	0.008
6348.626160	8.166	0.008	-0.242	0.020	-4.022	0.007
6349.437201	8.017	0.015	-0.174	0.036	-3.946	0.011
6349.442721	8.027	0.011	-0.225	0.028	-3.955	0.008
6679.499824	8.346	0.004	-0.493	0.013	-3.972	0.003
6679.680352	8.177	0.004	-0.409	0.018	-3.887	0.002
6682.562820	8.137	0.015	-0.322	0.038	-3.941	0.011
6682.666891	7.945	0.009	-0.124	0.026	-3.966	0.007
6796.370888	7.748	0.003	0.013	0.012	-4.030	0.003
7821.424255	7.690	0.013	0.097	0.033	-4.023	0.009
7823.488210	8.031	0.013	-0.250	0.041	-3.946	0.009
7827.465395	7.915	0.004	0.015	0.008	-3.991	0.003

Table 3.12: Time series of BD+20 1790 from IGRINS data. For each observation we list radial velocities (RV) and the bisector span (BIS) with the corresponding uncertainties.

Dataset	JD-2450000	RV (km s^{-1})	σ_{RV} (km s^{-1})	BIS (km s^{-1})	σ_{BIS} (km s^{-1})
IGRINS@McD	7417.80148148	8.106	0.059	-0.249	0.062
	7418.77283564	8.220	0.059	0.025	0.029
	7419.81490740	8.146	0.059	-0.420	0.065
	7421.84695601	8.037	0.059	-0.127	0.075
	7475.63379629	8.133	0.059	0.438	0.065

	7476.61835648	8.161	0.059	0.221	0.062
	7503.59172453	8.205	0.059	-0.030	0.051
IGRINS@DCT	7671.96244213	8.285	0.065	0.362	0.054
	7673.95834490	8.015	0.065	0.270	0.056
	7675.86873842	8.178	0.065	0.339	0.047
	7713.04495370	8.219	0.065	0.143	0.060
	7732.03075231	8.248	0.065	0.117	0.054
	7742.97497685	8.244	0.065	0.464	0.078
	7793.85260416	8.021	0.065	0.228	0.043
	7794.84053240	8.035	0.065	0.345	0.033
	7796.74128472	8.041	0.065	0.181	0.072
	7798.78775463	7.953	0.065	0.396	0.047
IGRINS@McD	7825.74646990	8.018	0.044	0.318	0.063
	7827.67596064	8.131	0.044	-0.125	0.053
	7828.69434027	8.046	0.044	0.136	0.056
	7829.75975694	7.958	0.044	-0.053	0.071
	7862.63905092	7.964	0.044	-0.101	0.053
	7864.69674768	7.973	0.044	0.144	0.055
	7875.58734953	7.925	0.044	0.026	0.053
	7876.59074074	8.079	0.044	0.213	0.055
	7877.58625000	7.902	0.044	0.134	0.055
	7878.58519676	7.986	0.044	0.179	0.058
	7879.58496527	8.017	0.044	-0.006	0.053
	7880.58305555	7.965	0.044	-0.023	0.052

Table 3.13: Time series of BD+20 1790 from REM data with different filters. For each observation we list the differential magnitudes with the corresponding uncertainty.

Filter	JD-2450000	Δm (mag)	$\sigma_{\Delta m}$ (mag)
g	7477.52744	-1.960	0.005
	7478.58315	-1.985	0.004
	7479.57717	-2.002	0.007
	7480.59303	-1.984	0.008
	7481.59388	-2.012	0.009
	7482.61009	-2.010	0.008
r	7477.52744	-2.687	0.013
	7478.58315	-2.722	0.017
	7479.58383	-2.732	0.016
	7480.59303	-2.725	0.012
	7481.59283	-2.753	0.011
	7482.61159	-2.756	0.013

i	7477.52822	-3.100	0.007
	7478.58392	-3.109	0.011
	7479.57717	-3.129	0.007
	7480.58715	-3.104	0.006
	7481.58804	-3.124	0.008
	7482.60679	-3.122	0.010
z	7477.52744	-3.318	0.010
	7478.58315	-3.279	0.011
	7479.57717	-3.344	0.010
	7480.59196	-3.348	0.011
	7481.59097	-3.320	0.012
	7482.61009	-3.409	0.015
J	7479.57544	-3.756	0.006
	7480.58707	-3.839	0.020
	7481.58691	-3.687	0.005
	7482.60688	-3.756	0.035
H	7479.57789	-3.527	0.044
	7480.58792	-3.762	0.043
	7481.58772	-3.575	0.033
	7482.60755	-3.734	0.034
K	7479.58154	-3.850	0.067
	7480.59008	-4.003	0.014
	7481.58988	-3.801	0.040
	7482.60970	-3.904	0.044

3.3 V830 Tau

In this Section I present the RV measurements of the star V830 Tau, an active 2 Myr-old weak-lined T Tauri star. It is an M0 star with magnitudes V=12.1, J=9.3, H=8.6, and K=8.4 (Cutri et al., 2003), with a *vsini* of 30.5 km s^{-1} (Donati et al., 2015).

Donati et al. (2016) collected 48 spectra with ESPaDOnS and NARVAL (twin spectropolarimeters installed at the Cassegrain focus of the 3.6-m CFHT on top of Maunakea, Hawaii, and of the 2-m Bernard Lyot Telescope on top of Pic du Midi, France, respectively), claiming the youngest Hot Jupiter found to date, with a period of 4.93 ± 0.05 days and a semi-amplitude of 75 ± 12 m s^{-1}.

Given the fast rotation and extremely high activity of this possibly still accreting star, detection of RV variations due to a planet around this star is extremely difficult and requires a detailed modelling of the activity signal that is more than an order of magnitude larger than the planet signal. This modelling may be done using e.g. Gaussian Processing technique (e.g. Rasmussen & Williams 2006, Haywood et al. 2014), that however requires a specific observing strategy, with a dense covering of RVs of the order of several tens of observations for each season, possibly repeated over few years. Since we have data of a single season with GIARPS, we can only obtain preliminary conclusion from our dataset. We plan to continue the monitoring of this target in future seasons to strengthen our results.
We monitored this star over one semester in GIARPS mode (Autumn-Winter 2017) to investigate the nature of the RV variation. Summary of the available data from HARPS – N and GIANO – B and their properties are presented in Table 3.14. The dataset is composed of 47 GIANO – B spectra and 22 HARPS – N spectra. The number of spectra was limited by telescope time assignment and bad weather. The dataset is quite small compared with the need for application of sophisticated analysis methods such as Gaussian Processes. These results are then very preliminary. HARPS – N RVs were processed by both HARPS – N DRS through the YABI workflow and TERRA pipeline (Anglada-Escudé & Butler, 2012) and listed in Table 3.16. DRS is the usual method based on the Cross Correlation Function used with HARPS. TERRA pipeline uses a multiparameter fit of each observed spectrum with a stellar template obtained from the stellar spectra themselves.

Table 3.14: Summary of the spectroscopic data of V830 Tau. For each dataset we list the instrument used for the observations, the number of spectra, the typical SNR, the RV nominal internal error (σ_{RV}), the RV r.m.s. scatter, and the peak-to-valley value of the RVs. We report the HARPS – N results from two different approach, DRS and TERRA.

Instrument	N_{spectra}	SNR	σ_{RV} (km s^{-1})	RV r.m.s. (km s^{-1})	Peak-to-valley (km s^{-1})
GIANO – B	47	27	0.769	0.946	4.032
HARPS – N (DRS)	22	28	0.033	1.235	4.067
HARPS – N (Terra)	22	28	0.037	0.379	1.315

GIANO – B data were reduced by the online GOFIO pipeline (Rainer et al., 2018) and the GIANO – B RVs were obtained with the method described in Sec. 2.9 and listed in Table 3.15.

HARPS – N DRS data I computed the GLS and the orbital fit, using a Keplerian function, for HARPS – N data both for DRS and TERRA RVs. The HARPS – N - DRS periodogram (Fig. 3.13) exhibits a periodicity at 2.7405 days (FAP 9.65%), while the corresponding fitting model (Fig. 3.14) has a RV semi-amplitude of 1876.6 ± 17.4 m s^{-1} and a period of 2.7420 ± 0.0001 days. This is the known rotational period of the star (see Donati et al. 2015). However, in spite this signal is due to the activity, I try to remove it using a Keplerian fit. After subtracting this Keplerian fit, the r.m.s. of residuals is 378 m s^{-1} and its periodogram exhibits a peak at 14.5 days. Looking at the periodogram, a peak around the orbital period (red vertical dashed line in the periodgram, Fig. 3.13) rose up, even if with very low significance. The corresponding curve for residual RVs phased to 14.5 days period is shown in Fig. 3.15. However, the curve fit did not provide reasonably good parameters. I also tried to phase both original and residual HARPS-N DRS RVs to the proposed planet period of 4.93 days, but no evident periodicity was found.

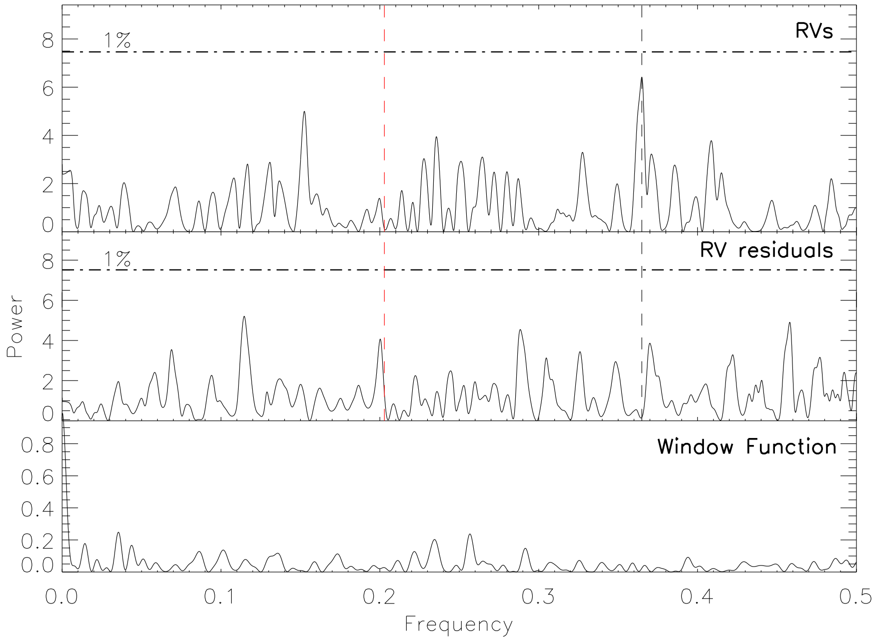

Figure 3.13: GLS of V830 Tau for HARPS – N DRS data. The black vertical dashed line is the rotational period at 2.7405 days, while the red vertical dashed line is the proposed planet period at 4.93 days.

HARPS – N TERRA data The HARPS – N - TERRA periodogram (Fig. 3.16) exhibits a periodicity at 2.7372 days (FAP 24%) , while the fitting model (Fig. 3.17) has a RV semi-amplitude of 485.0 ± 16.4 m s^{-1} and a period of 2.7399 ± 0.0007 days. The corresponding residuals have a scatter of 113 m s^{-1} and a peak in its periodogram at 2.093 days. Also in this case, looking at the periodogram (Fig. 3.16) a peak around the proposed orbital period came up. The phase-folded curve of the residual RVs at 2.0935 days is presented in Fig. 3.18.

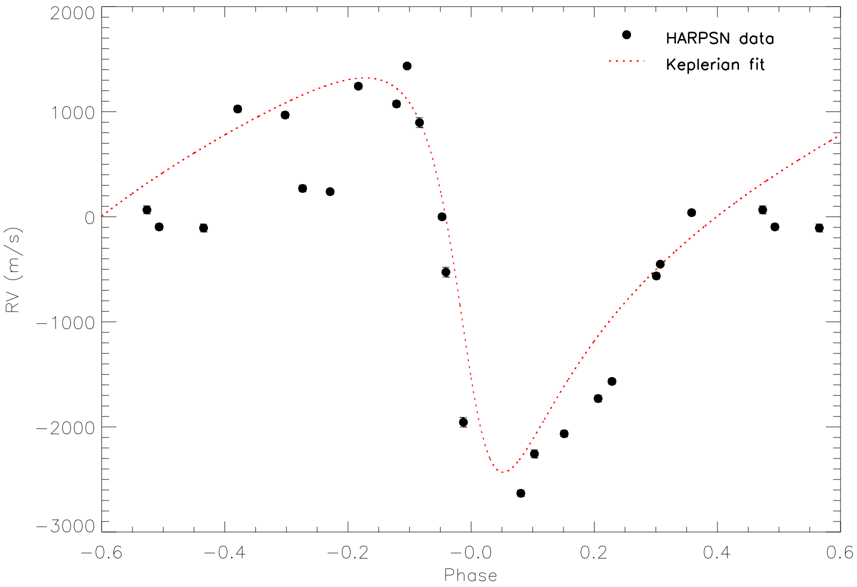

Figure 3.14: Keplerian fit (red dashed line) at 2.7420 days (rotational period) of V830 Tau with the HARPS – N DRS data (black dots).

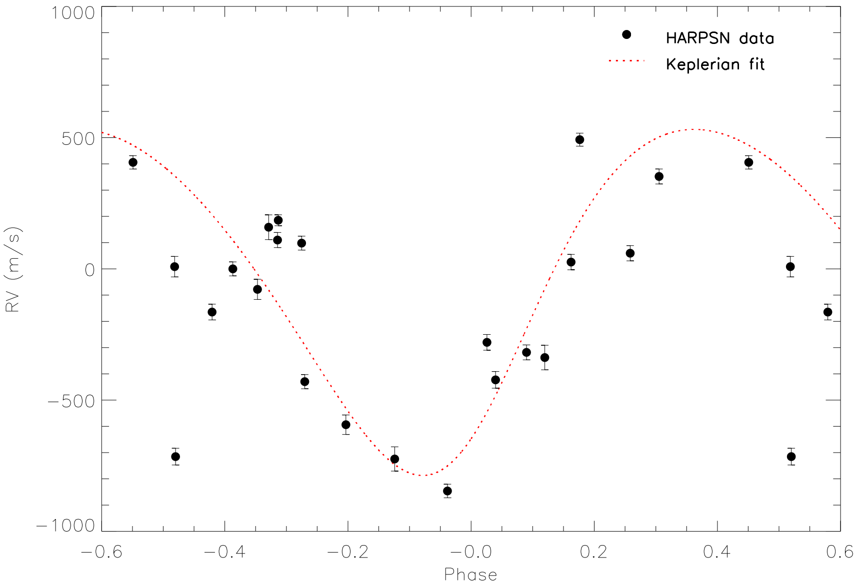

Figure 3.15: Keplerian fit (red dashed line) at 14.5 days of V830 Tau with the HARPS – N DRS residual RVs (black dots).

Also in this case, no accurated fitting parameters are provided and the phase-folded curves at 4.93 days of original and residual RVs did not exhibit any clear periodicity.

Another independent approach performed for this dataset was the fitting of a forth degree polynomial curve rather than a Keplerian curve, after phasing the data. The residual TERRA RVs obtained from the subtraction of this fit gave a quite good periodicity at the orbital period, providing a hint to support the planet claim.

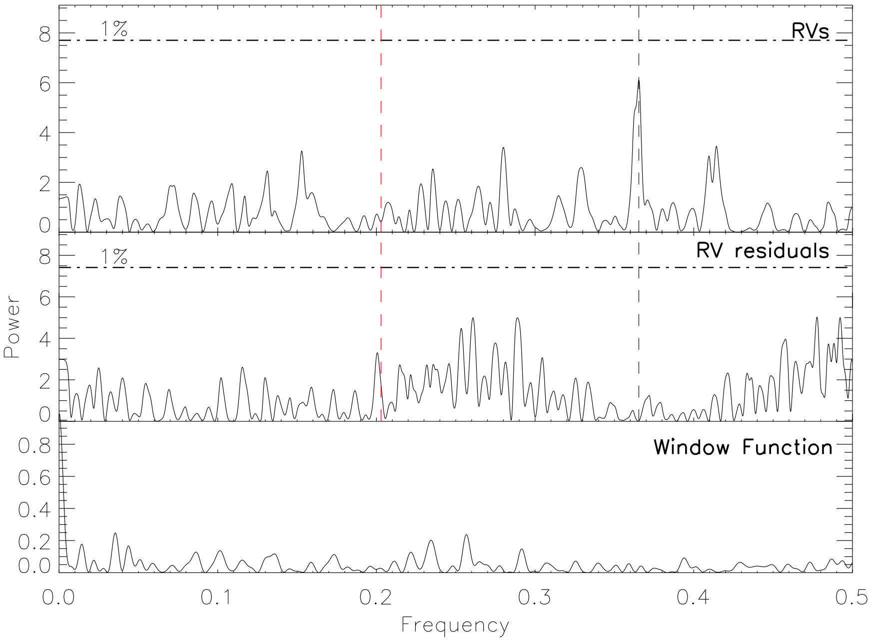

Figure 3.16: GLS of V830 Tau for HARPS – N TERRA data. The black vertical dashed line is the rotational period at 2.7405 days, while the red vertical dashed line is the proposed planet period at 4.93 days.

Fig. 3.19 shows the RVs provided by the two different RV calculation methods and the modulation amplitude is lower for TERRA RVs. The smaller amplitude of the activity signal found with TERRA with respect to DRS is a general feature of our analysis. It might be due to the fact that TERRA weights more regions close to the continuum respect to the CCF method, and then forming at larger optical depths that are less sensitive to activity. Moreover, the template-matching technique provides a significant increase in accuracy for M-dwarfs, for which the authors advise to use only orders redder than ~4400 Å.

GIANO – B data The GLS and Keplerian fit analysis was also performed for GIANO – B data. The NIR periodogram (Fig. 3.20) shows a significant periodicity of 2.7378 days (FAP = 0.1 %), and the NIR Keplerian fit (Fig. 3.21) provides a RV semi-amplitude of 976.0 ± 176.7 m s^{-1} and a period of 2.7369 ± 0.0026 days. Subtracting the Keplerian fit, the r.m.s. of the residuals is 676 m s^{-1} with a peak in the periodogram at 56.8068 days. The corresponding phase-folded curve to this period is illustred in Fig. 3.22. Again, I tried to phase both original and residual GIANO – B RVs at the orbital period of 4.93 days without finding any periodicity.

Summary of periods, semi-amplitudes and eccentricities obtained from data of the different instruments and different pipelines is reported in Tab. 3.17.

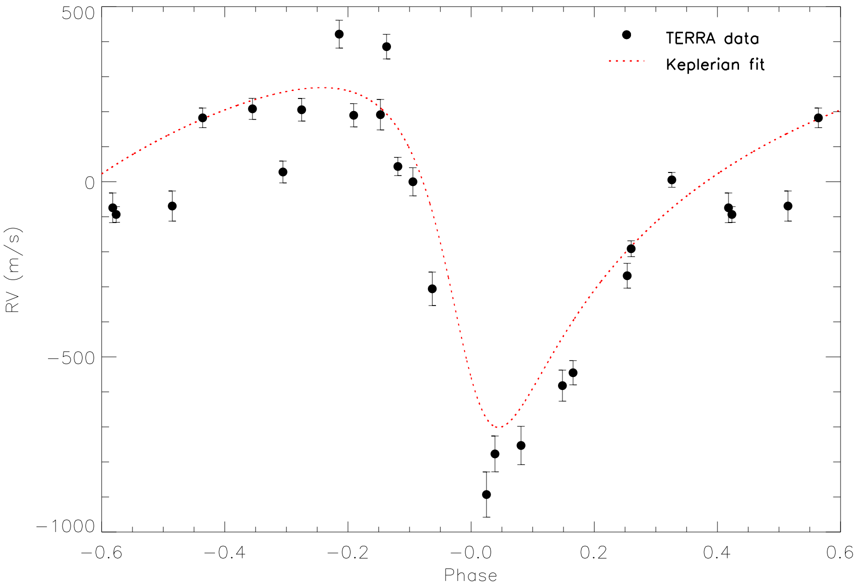

Figure 3.17: Keplerian fit (dashed line) at 2.7399 days (rotational period) of V830 Tau with the HARPS – N TERRA data (black dots).

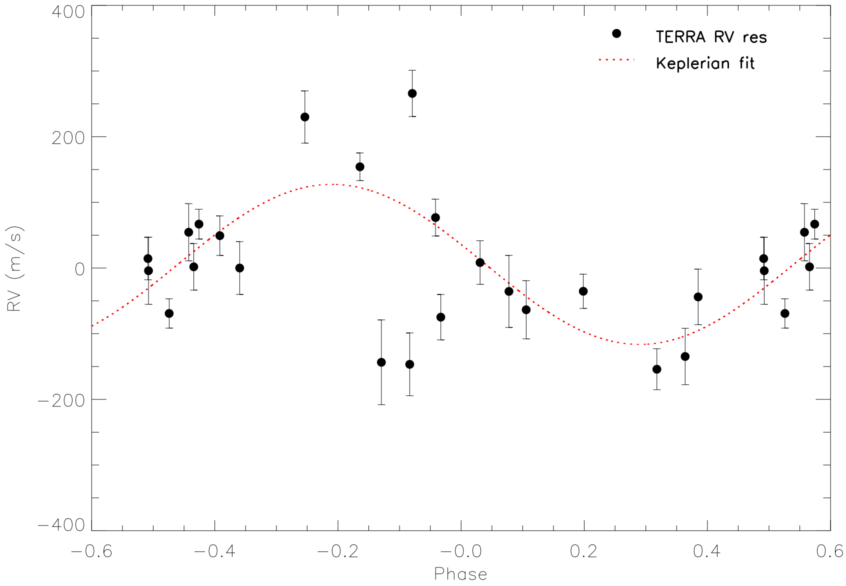

Figure 3.18: Keplerian fit (dashed line) at 2.0935 days (rotational period) of V830 Tau with the residual HARPS – N TERRA RVs (black dots).

Table 3.15: Time series of V830 Tau from GIANO – B data. For each observation we list radial velocities (RV) with the corresponding uncertainties.

JD-2450000	RV ($\mathrm{km\ s^{-1}}$)	σ_{RV} ($\mathrm{km\ s^{-1}}$)

8044.6446065	1.269	0.769
8044.6530440	1.136	0.769
8044.6614699	1.468	0.769
8050.6729977	0.165	0.769
8050.6816435	-0.631	0.769
8050.6903241	-1.055	0.769
8051.6106134	1.239	0.769
8051.6257639	1.149	0.769
8052.6593866	0.783	0.769
8052.6722107	0.752	0.769
8052.6806250	0.954	0.769
8072.4752315	0.348	0.769
8072.4836690	-2.564	0.769
8072.4921181	-1.884	0.769
8075.5588194	-1.397	0.769
8075.5672917	-0.383	0.769
8075.5757523	-0.945	0.769
8088.6395139	-1.559	0.769
8088.6479630	-0.504	0.769
8094.6942708	-1.385	0.769
8094.7031829	-0.648	0.769
8094.7121065	-0.981	0.769
8098.5742245	0.643	0.769
8098.5827083	0.657	0.769
8098.5911690	0.736	0.769
8112.4946296	1.184	0.769
8112.5035764	0.522	0.769
8112.5125347	0.881	0.769
8120.3598032	0.066	0.769
8120.3686574	0.041	0.769
8120.3774421	0.371	0.769
8121.5178472	-0.339	0.769
8121.5267708	-0.926	0.769
8121.5356829	0.039	0.769
8133.3250694	-0.545	0.769
8133.3602199	-0.799	0.769
8133.3721644	-0.282	0.769
8184.3363079	0.220	0.769
8184.3447454	0.611	0.769
8184.3531597	-0.516	0.769
8188.3473727	-1.162	0.769
8188.3562616	-0.654	0.769
8188.3651620	-0.938	0.769
8189.3573727	-0.249	0.769
8192.3455324	-0.756	0.769
8192.3539468	0.636	0.769

8192.3623727	0.710	0.769

Table 3.16: Time series of V830 Tau from HARPS – N data (DRS and TERRA). For each observation we list radial velocities (RV), and the bisector span (BIS) with their related uncertainties.

	DRS				TERRA	
JD-2450000	RV (km s^{-1})	σ_{RV} (km s^{-1})	BIS (km s^{-1})	σ_{BIS} (km s^{-1})	RV (km s^{-1})	σ_{RV} (km s^{-1})
8044.6623443	17.899	0.027	-0.312	0.053	0.113	0.026
8050.6902093	15.835	0.030	1.398	0.060	-0.684	0.055
8051.6285196	17.803	0.028	-0.070	0.057	-0.024	0.022
8052.6855394	18.973	0.029	-2.254	0.059	0.259	0.033
8072.4936655	15.643	0.039	1.237	0.078	-0.708	0.051
8074.7239238	18.796	0.047	-2.909	0.094	0.261	0.044
8075.5810286	16.333	0.027	1.983	0.054	-0.476	0.035
8094.7132243	16.169	0.032	1.997	0.064	-0.513	0.044
8098.5920652	18.925	0.029	-2.607	0.057	0.252	0.028
8102.5951016	15.267	0.030	1.946	0.060	-0.824	0.065
8103.6720437	17.965	0.038	-0.238	0.077	-0.005	0.042
8110.4874733	17.373	0.047	-23.577	0.094	0.069	0.040
8112.5135195	18.868	0.029	-2.442	0.058	0.278	0.030
8120.3762508	17.793	0.037	-2.364	0.074	0.000	0.043
8121.5333196	15.944	0.046	-0.164	0.092	-0.236	0.048
8133.3603884	17.336	0.029	0.086	0.058	-0.199	0.035
8133.3779797	17.448	0.021	0.037	0.042	-0.122	0.023
8137.3916473	18.139	0.026	0.363	0.052	0.275	0.032
8184.3484450	19.335	0.025	-2.809	0.050	0.455	0.035
8188.3575378	17.939	0.025	-0.294	0.051	0.075	0.021
8189.3671026	18.169	0.032	-0.200	0.064	0.097	0.031
8192.3573421	19.142	0.027	-2.063	0.053	0.491	0.040

Table 3.17: Summary of the periods, semi-amplitudes and eccentricities of V830 Tau resulting from the fitting model for each dataset.

Instrument/Pipeline	Period (days)	Semi-amplitude (m s^{-1})	Eccentricity
GIANO – B	2.7369 ± 0.0026	976.0 ± 176.7	0.42 ± 0.16
HARPS – N (DRS)	2.7420 ± 0.0001	1876.6 ± 17.4	0.51 ± 0.01
HARPS – N (Terra)	2.7399 ± 0.0007	485.0 ± 16.4	0.46 ± 0.02

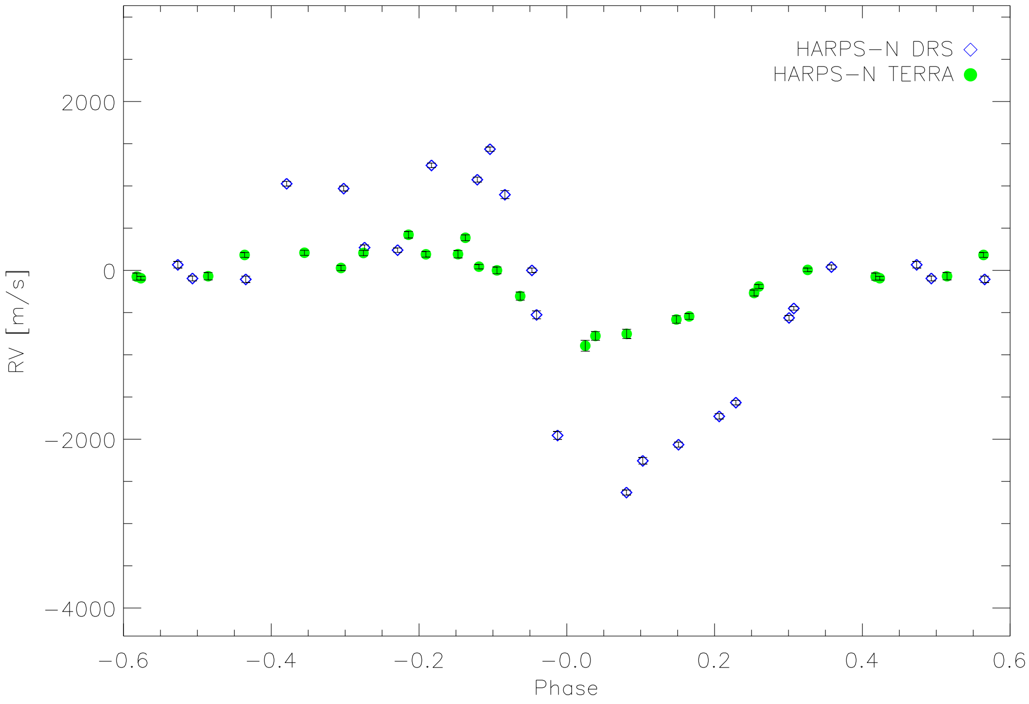

Figure 3.19: Comparison between DRS (blue diamonds) and TERRA (green dots) RVs with the TERRA orbital fit (dashed line).

3.3.1 Discussion

Figures 3.23 and 3.24 show the VIS orbital fit represented as dashed line, together with the phase-folded VIS-HARPS–N and NIR RVs (blue diamonds and red dots, respectively), and VIS-TERRA and NIR RVs, respectively.

From these first results, the NIR RVs seem to follow the VIS orbital curve, even if two different methods (DRS and TERRA) for VIS data give different amplitudes. This is due to the fact that the CCF method used by the DRS pipeline is more sensitive to the activity, in fact the visible DRS RVs show a very strong correlation with the bisector (Fig. 3.25) with a Pearson correlation coefficient of -0.86 and a Spearman coefficient of -0.79. After subtracting this trend, the DRS RVs have an r.m.s. of 651 m s^{-1} and no clear periodicity at the orbital period of 4.93 days.

However, the high uncertainties in RVs do not allow to understand the nature of the RV modulation, probably due to the fast rotation of this target. A hint toward the Keplerian nature could be supported by the strong correlation between GIANO – B RVs and visible RVs (both from DRS and TERRA values). To correlate VIS and NIR data, I averaged the GIANO – B RVs for each night. The final dataset is composed by 16 points. The correlation between the VIS - DRS and NIR data (3.26) shows a Pearson correlation coefficient of 0.77 and a Spearman coefficient of 0.79, while the correlation between VIS - TERRA and NIR RVs (3.27) has both coefficients equal to 0.68. Once subtracting these DRS and TERRA trends from NIR data, the original NIR RV r.m.s. of 946 m s^{-1} goes down to 531 m s^{-1} and 612 m

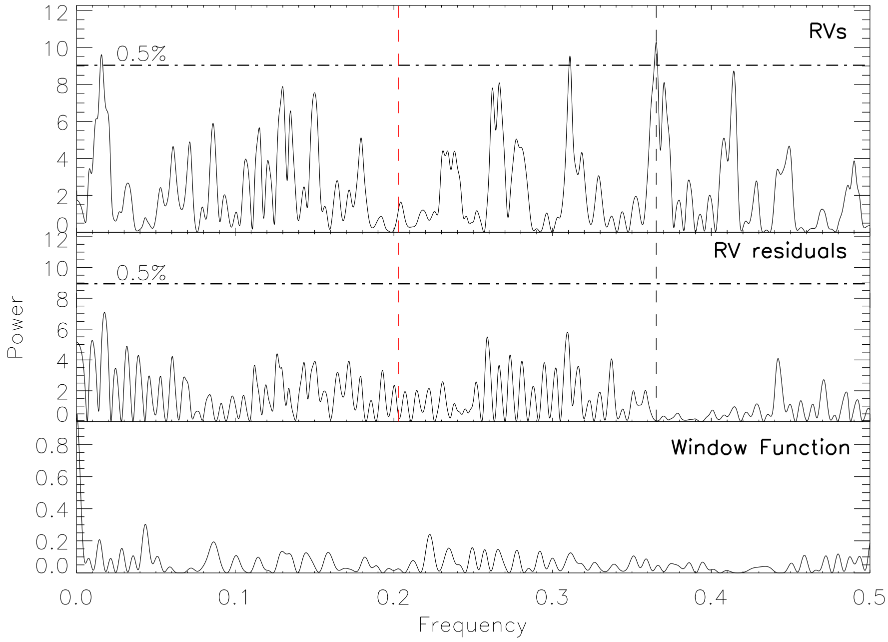

Figure 3.20: GLS of V830 Tau for GIANO – B data. The black vertical dashed line is the rotational period at 2.7405 days, while the red vertical dashed line is the proposed planet period at 4.93 days.

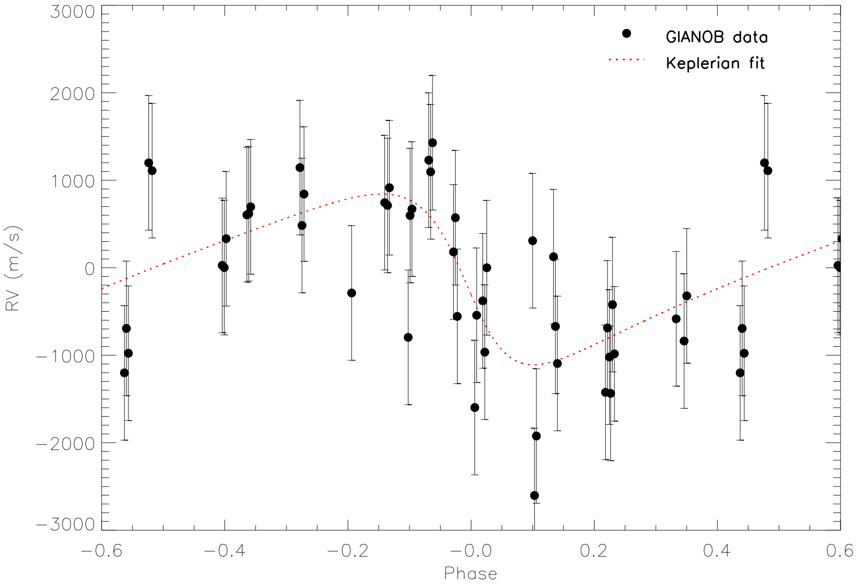

Figure 3.21: Keplerian fit (dashed line) at 2.7369 days of V830 Tau with the GIANO – B data (black dots).

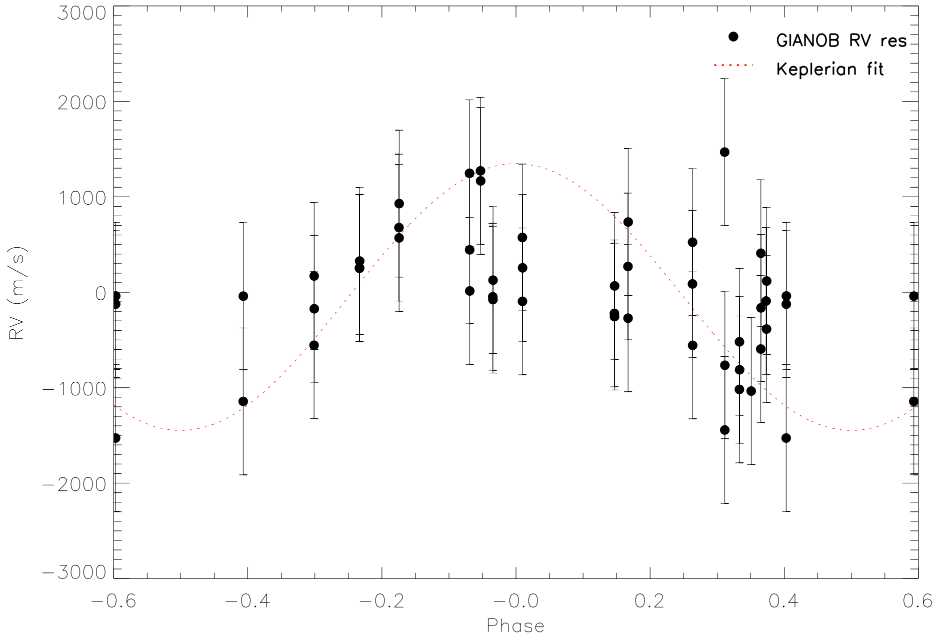

Figure 3.22: Keplerian fit (dashed line) at 56.8068 days of V830 Tau with the residual GIANO – B RVs (black dots).

s^{-1}, respectively. Both residual RVs do not exhibit any trend at 4.93 days.

As a preliminary test, the Gaussian Porcessing was performed on the combined GIARPS (HARPS – N TERRA + GIANO – B) data, obtaining an orbital period around 4.9 days, but discrepant amplitudes with respect to the published data, suggesting that a planet could be present and could be embedded by the strong activity clearly affecting our data. Anyway, the results remain unclear and inconclusive. A larger sample is needed for this target, so that we decided to go on observing it in order to rely on an independent dataset. An intensive monitoring is currently on going with GIARPS.

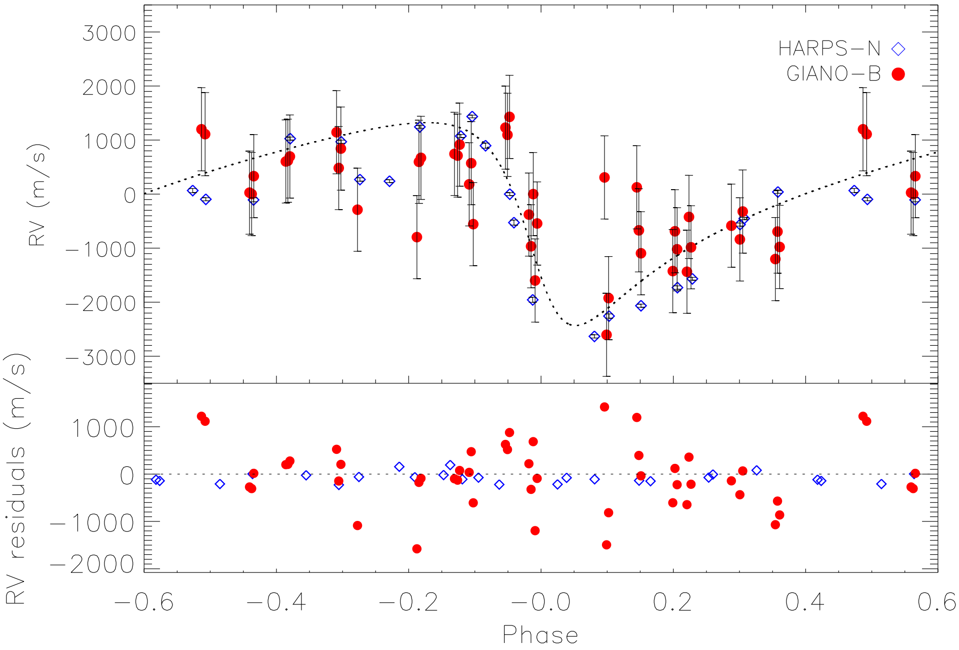

Figure 3.23: Keplerian fit (black dashed line) at 2.7420 days obtained with the visible data (HARPS – N- DRS, blue diamonds), with GIANO – B RVs (red dots) overplotted, with the corresponding residuals in the bottom panel.

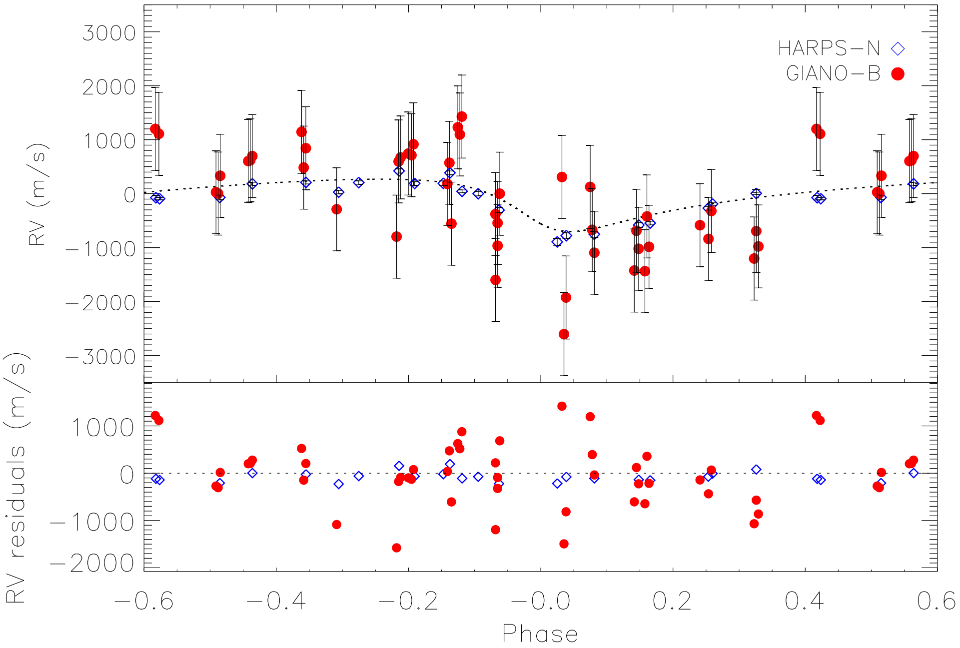

Figure 3.24: Keplerian fit (black dashed line) at 2.7399 days obtained with the visible data (HARPS – N - TERRA, blue diamonds), with GIANO – B RVs (red dots) overplotted, with the corresponding residuals in the bottom panel.

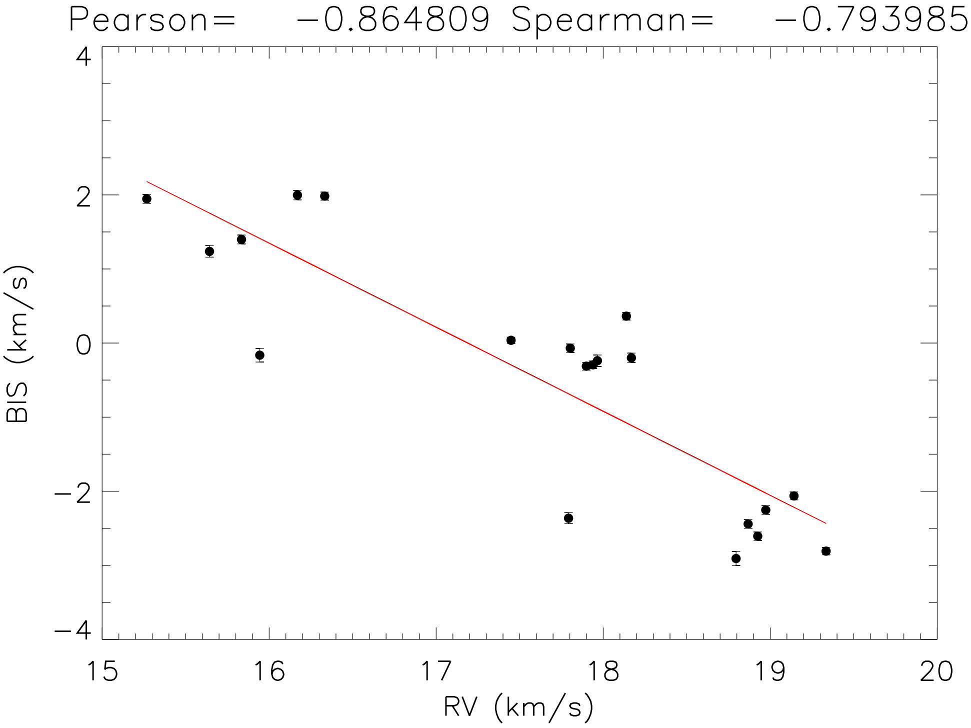

Figure 3.25: Correlation between VIS-DRS RVs and BIS of V830 Tau.

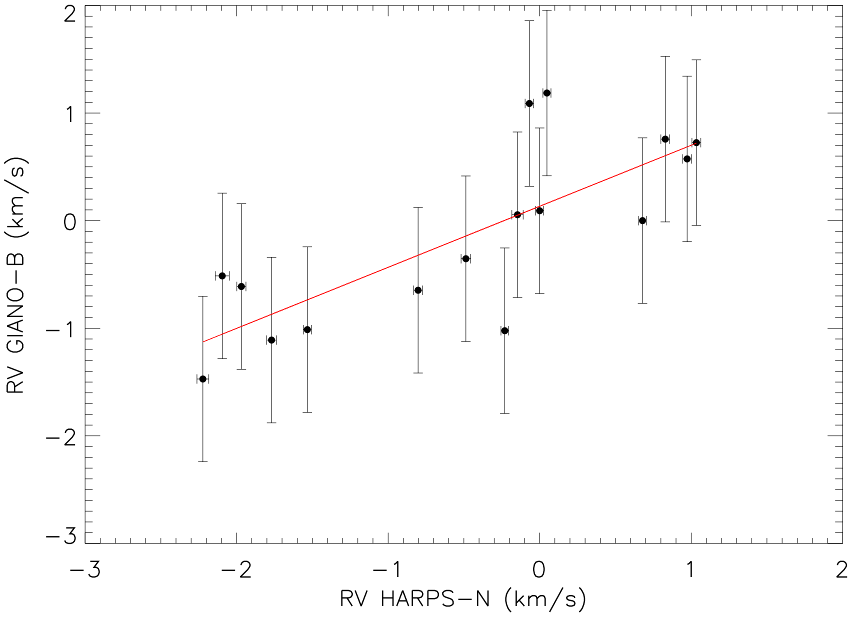

Figure 3.26: Correlation between VIS – DRS and NIR RVs of V830 Tau.

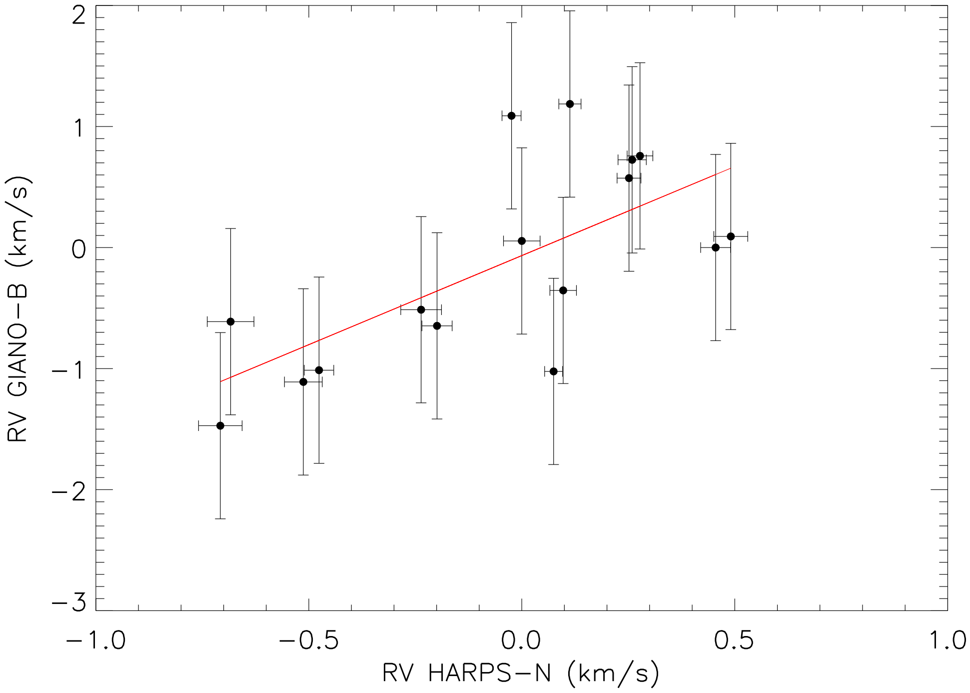

Figure 3.27: Correlation between VIS – TERRA and NIR RVs of V830 Tau.

3.4 HD 285507

In this Section I present the RV measurements of the star HD 285507, member of the Hyades open cluster (age 625 ± 50 Myr). It is a K4.5 star, chromospherically inactive (Quinn et al., 2014), with magnitudes V=10.5, J=8.4, H=7.8, K=7.7 (Cutri et al., 2003), $vsini$ = 3 km s^{-1} (Chaturvedi et al., 2016) and a rotational period of 11.98 days (Delorme et al., 2011).

Quinn et al. (2014) claimed a sligthly eccentric (e=0.086) Hot Jupiter around this star: RVs from TRES spectra (Tillinghast Reflector Echelle Spectrograph at the Fred L. Whipple Observatory in Arizona, Fűrész et al. 2008) show a variation of 89.5 m s^{-1} with a period of 6.0881 days. Since no correlation between RVs and S-index is found, they attributed the origin of RV variations to a companion of 0.917 M_J with a semi-amplitude of 125.8 m s^{-1}.

We monitored this star over one semester in 2018 observing it in GIARPS mode, in order to have multi-wavelength high resolution spectra that can allow us to immediately understand the RV nature. A summary of the available data from HARPS – N and GIANO – B and their properties are presented in Table 3.18. The dataset is composed of 30 GIANO – B spectra and 18 HARPS – N spectra. GIANO – B data were reduced by the online GOFIO pipeline, except for two observations of March, 6th, that GOFIO reduced using a UNe lamp acquired in January. This happens because GOFIO reduces the spectra with the last available lamp; since GIANO – B was not operative from January to March, the last available lamp was acquired in January (for more details, see also Appendix D). For this reason, I reduced these spectra again with the correct lamp.

Table 3.18: Summary of the spectroscopic data of HD 285507. For each dataset we list the instrument used for the observations, the number of spectra, the typical SNR, the RV nominal internal error (σ_{RV}), the RV r.m.s. scatter, and the peak-to-valley value of the RVs.

Instrument	N_{spectra}	SNR	σ_{RV} (km s^{-1})	RV r.m.s. (km s^{-1})	Peak-to-valley (km s^{-1})
GIANO – B	30	39	0.061	0.119	0.435
HARPS – N	18	42	0.003	0.105	0.298

The GIANO – B RVs (Table 3.19) were obtained with the method described in 2.9, while HARPS – N RVs (Table 3.20) were processed by HARPS – N DRS through the YABI workflow. VIS RVs through TERRA pipeline have the same values of the DRS ones, so hereinafter I only consider the DRS outputs.

HARPS – N data I computed the GLS for HARPS – N data (Fig. 3.28) and it exhibits a highly significant periodicity at 6.095 days, very close to the periodicity found by Quinn et al. (2014). The orbital fit is obtained from the VIS RVs, using a Keplerian function (as in Sec. 3.2). The obtained RV semi-amplitude is 143.2 ± 1.1 m s^{-1}, the period is 6.0981 ± 0.0008 days and the eccentricity 0.084 ± 0.009, and shows a very good agreement with the result proposed by Quinn et al. (2014). The VIS residuals from VIS orbital fit have a scatter of 10 m s^{-1} with a peak in the periodogram of 2.34 days that is, however, not highly significant (FAP 5%). Fig. 3.29 shows the orbital fit for the single planet solution (red dashed line) with the phase-folded HARPS – N data (black dots).

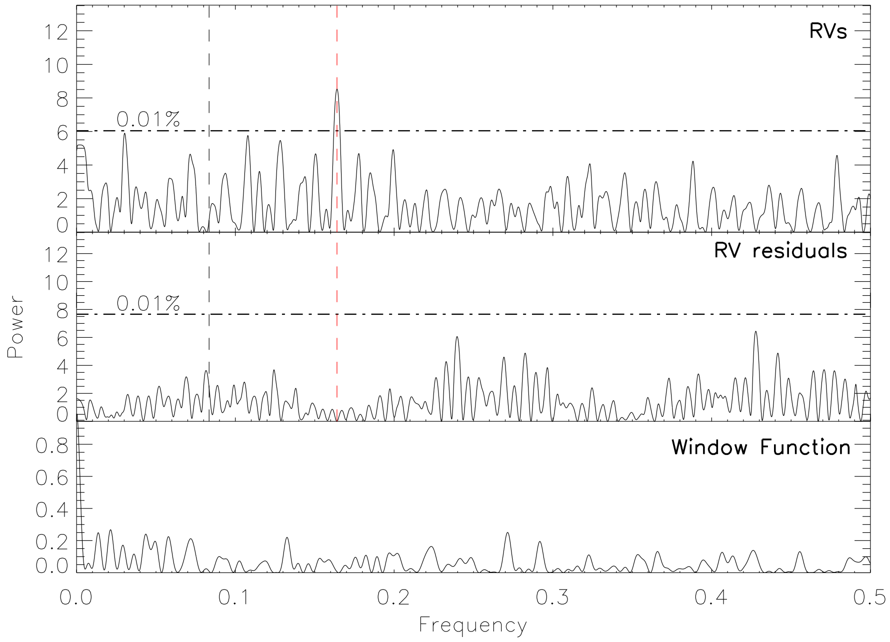

Figure 3.28: GLS of HD 285507 for HARPS – N data. The black vertical dashed line is the rotational period at 11.98 days, while the red vertical dashed line is the proposed planet period at 6.0881 days.

GIANO – B data The GLS and orbital fit analysis were also performed for GIANO – B data. The NIR periodogram (Fig. 3.30) shows a significant periodicity of 6.105 days, and the NIR orbital fit found a RV semi-amplitude of 148.5 ± 19.1 m s^{-1} and a period of 6.1061 ± 0.0122 days. After subtracting the NIR orbital fit, the r.m.s. of NIR residuals is 47.6 m s^{-1} and the corresponding periodogram shows a peak at P = 5.72 days that is not significant (FAP 30%). Fig. 3.31 shows the orbital solution (red dashed line) with the phase-folded GIANO – B data (black dots).

Summary of orbital parameters obtained from fitting data of the different instruments is reported in Tab. 3.21.

3.4.1 Discussion

Comparing the VIS and NIR datasets, HARPS – N and GIANO – B RVs show a similar r.m.s scatter, 105 and 119 m s^{-1}, respectively (Tab. 3.18). Moreover, VIS and NIR semi-amplitudes are the same within the errors.

Fig. 3.32 shows the VIS orbital fit represented as dashed line, together with the phase-folded VIS RVs (blue diamonds). NIR RVs (red dots) are overplotted, clearly lying on the VIS curve.

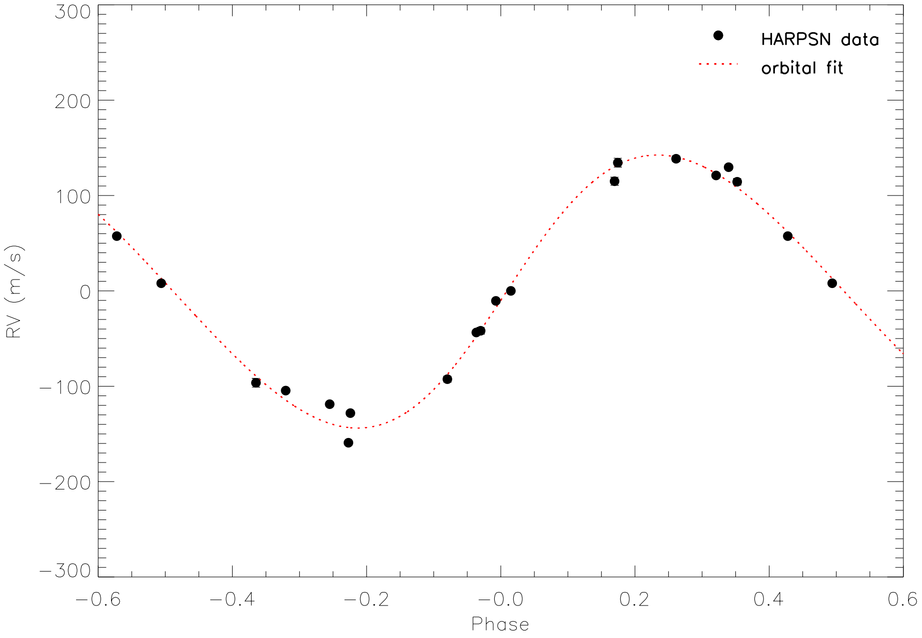

Figure 3.29: Orbital fit (dashed line) at 6.0981 days of HD 285507 with the HARPS – N data (black dots).

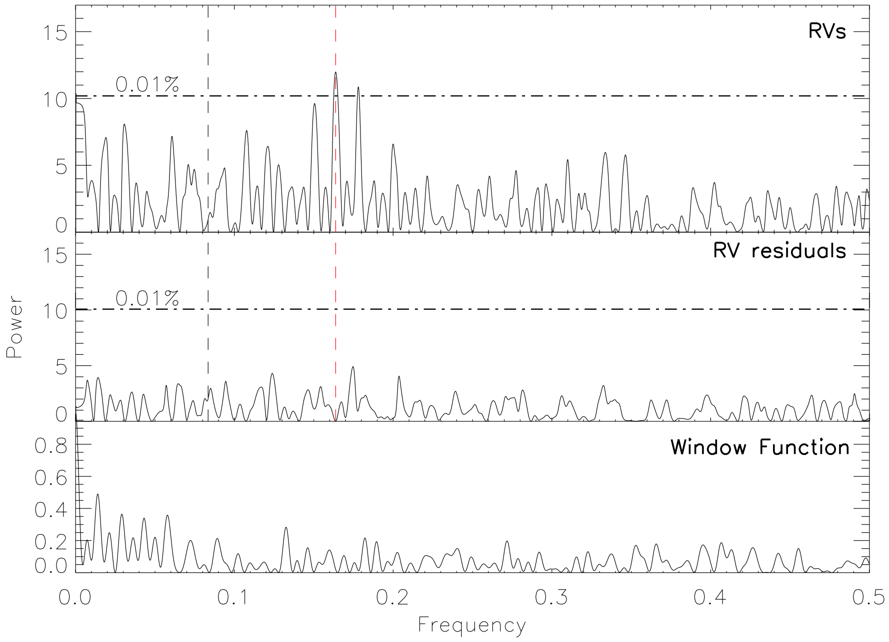

Figure 3.30: GLS of HD 285507 for GIANO – B data. The black vertical dashed line is the rotational period at 11.98 days, while the red vertical dashed line is the proposed planet period at 6.0881 days.

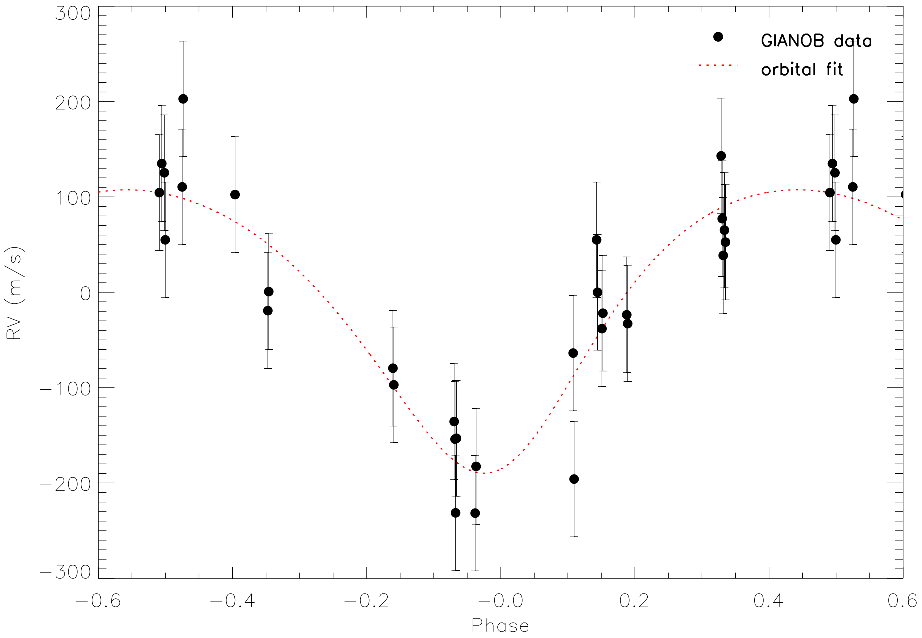

Figure 3.31: Orbital fit (dashed line) at 6.1061 days of HD 285507 with the GIANO – B data (black dots).

For a more consistent result, I performed the orbital fit analysis combining VIS and NIR data. Since the adopted tool computes the model by weighting the errors on RVs and since HARPS – N RV internal errors are about 2 orders of magnitude lower than the GIANO – B RV errors, I added the contribution of the stellar jitter to the HARPS – N data. Starting from the S-index provided by the DRS pipeline, I calculated the stellar jitter with method by Suárez Mascareño et al. (2015) for $B-V$ >1, resulting in about 5 m s^{-1}, and added it in quadrature to the HARPS – N errors (e.g. Cumming et al. 2008). The resulting orbital solution gives a RV semi-amplitude of 138.9 ± 2.9 m s^{-1}, a period 6.0966 ± 0.0028 days and an eccentricity of 0.046 ± 0.023. The model is represented in Fig. 3.33 as dashed line, while VIS and NIR RVs (blue diamonds and red dots, respectively) are overplotted.

The NIR RVs perfectly lie on the VIS orbital curve within the error bars. This leads to the confirmation of the Keplerian nature of RV variations, also supported by a strong correlation between VIS and NIR RVs (Fig. 3.34, Spearman correlation coefficient of 0.89, Pearson correlation coefficient of 0.94). Subtracting this trend from NIR RVs, the original NIR RV r.m.s. of 435 m s^{-1} goes down to 40 m s^{-1}.

I plotted this confirmed planet (red point) in the Period - Eccentricity diagram (Fig. 3.35). Although the visible fit is more accurate and in a very good agreement with the results by Quinn et al. (2014), I reported the VIS+NIR parameters in this plot for a more coherent analysis. The planet HD 285507b follows the general trend of this diagram, even if the eccentricity values are very scattered around that period. Figure 3.36 shows the Stellar age - Eccentricity diagram. It is clear that this diagram is quite poor at very young ages, where the eccentricities seem to be quite high. HD 285507b lies at intermediate eccentricity values, being the star not so young (∼625 Myr). The poor statistics does not allow us to understand the channel responsible for the HJs origins and filling out the left side of this diagram may be a great apportunity to put constraints to the planetary formation theories. In fact, the tidal migration channel is expected to have HJs with high eccentricities at younger ages, that then circularised their orbits by tidal dissipation, while low eccentricities characterize the disk migration origin channel.

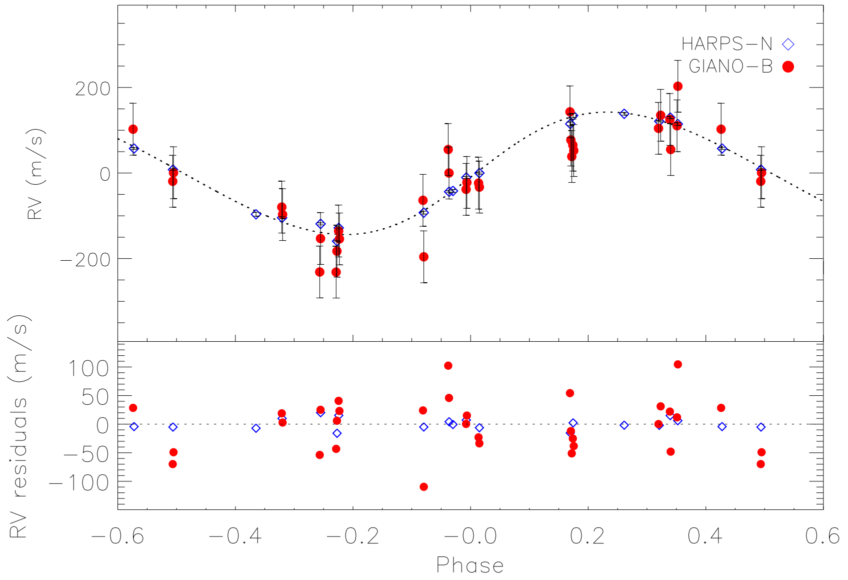

Figure 3.32: Visible orbital fit (black dashed line) of HD 285507 at 6.0981 days obtained with the visible data (HARPS – N, blue diamonds). GIANO – B RVs (red dots) are overplotted.

Table 3.19: Time series of HD 285507 from GIANO – B data. For each observation we list radial velocities (RV) and the bisector span (BIS) with the corresponding uncertainties.

JD-2450000	RV (km s^{-1})	σ_{RV} (km s^{-1})	BIS (km s^{-1})	σ_{BIS} (km s^{-1})
8044.6752199	-0.119	0.061	0.048	0.076
8044.6836459	-0.070	0.061	0.089	0.078
8050.6031019	-0.119	0.061	0.053	0.112
8050.6113194	-0.040	0.061	0.003	0.123
8051.6739699	0.049	0.061	0.030	0.086
8051.6823032	-0.083	0.061	-0.014	0.212
8088.5238773	0.168	0.061	0.017	0.076
8088.5321528	0.113	0.061	0.011	0.072
8103.5501041	0.215	0.061	0.017	0.100
8119.3289931	0.089	0.061	0.026	0.073
8119.3373032	0.080	0.061	0.057	0.071
8121.3872222	0.223	0.061	0.033	0.080
8121.3961111	0.316	0.061	-0.006	0.108
8133.3912268	0.217	0.061	0.003	0.066
8133.4135995	0.248	0.061	0.067	0.067

8184.3670602	0.033	0.061	0.021	0.088
8184.3753125	0.016	0.061	0.046	0.091
8187.3854282	0.178	0.061	-0.035	0.136
8187.3949537	0.165	0.061	0.173	0.154
8187.3558449	0.258	0.061	0.054	0.133
8187.3651389	0.190	0.061	0.074	0.125
8187.3742361	0.151	0.061	0.169	0.126
8188.3919097	0.238	0.061	0.079	0.076
8188.4001620	0.168	0.061	0.066	0.081
8189.3342593	0.093	0.061	-0.025	0.082
8189.3425694	0.113	0.061	0.017	0.084
8192.3764931	0.075	0.061	0.102	0.085
8192.3847338	0.091	0.061	0.093	0.092
8209.3489815	-0.023	0.061	0.015	0.161
8209.3572222	-0.041	0.061	0.031	0.138

Table 3.20: Time series of HD 285507 from HARPS – N data. For each observation we list radial velocities (RV) and the bisector span (BIS) with their related uncertainties.

JD-2450000	RV (km s^{-1})	σ_{RV} (km s^{-1})	BIS (km s^{-1})	σ_{BIS} (km s^{-1})
8044.6850138	37.913	0.002	0.04893	0.003
8050.6128093	37.953	0.003	0.02831	0.005
8051.6823658	37.979	0.003	0.02613	0.005
8088.5336132	38.028	0.002	0.03475	0.004
8102.5454368	38.210	0.003	0.04093	0.006
8103.5604001	38.129	0.002	0.05498	0.004
8119.3379541	38.072	0.002	0.01909	0.005
8121.3949551	38.186	0.003	0.05618	0.007
8133.3992812	38.193	0.001	0.05813	0.003
8143.4555451	38.030	0.003	0.01783	0.007
8147.5116964	37.976	0.005	0.04695	0.009
8184.3703359	37.967	0.002	0.03755	0.004
8187.3590862	38.187	0.004	0.02248	0.009
8187.3885047	38.206	0.005	0.06235	0.009
8188.3956073	38.202	0.002	0.03938	0.005
8189.3371032	38.080	0.002	0.05129	0.004
8192.3786570	38.061	0.002	0.01740	0.005
8209.3503459	37.944	0.002	0.04097	0.005

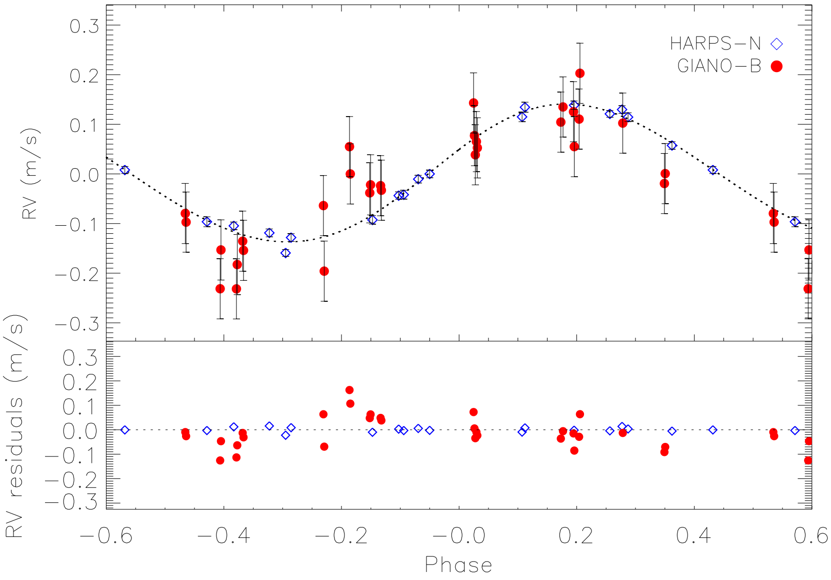

Figure 3.33: Orbital fit (black dashed line) of HD 285507 at 6.09722 days obtained combining the visible data (HARPS – N, blue diamonds), and GIANO – B RVs (red dots).

Table 3.21: Summary of the orbital parameters of HD 285507 resulting from the fitting model for different instruments.

Instrument	Period	K	e	ω
	(days)	(m s^{-1})		*deg*
GIANO – B	6.1061 ± 0.0122	148.5 ± 19.1	0.212 ± 0.134	193 ± 37
HARPS – N	6.0981 ± 0.0008	143.2 ± 1.1	0.084 ± 0.009	266 ± 4
HARPS – N + GIANO – B	6.0966 ± 0.0028	138.9 ± 2.9	0.046 ± 0.023	289 ± 27

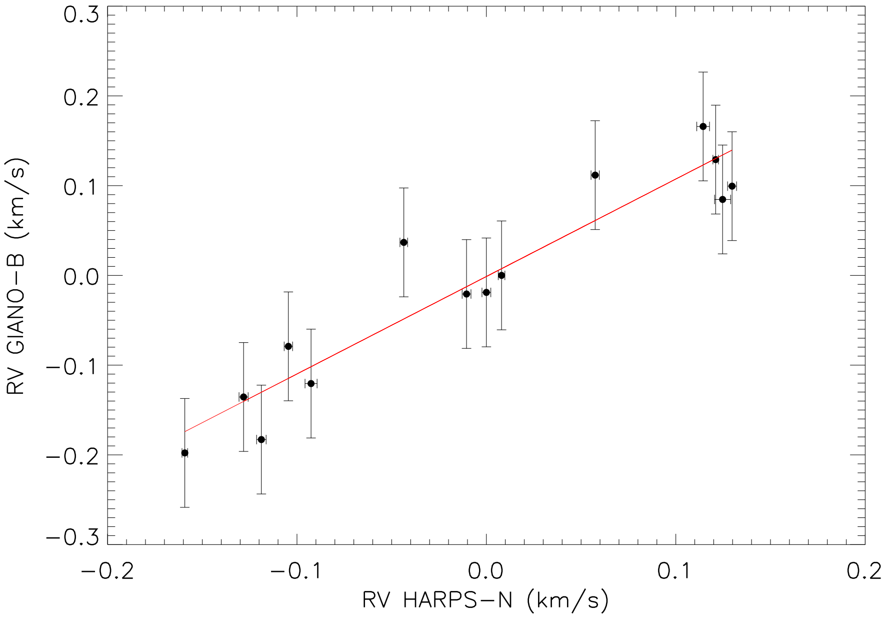

Figure 3.34: Correlation between VIS and NIR RVs of HD 285507.

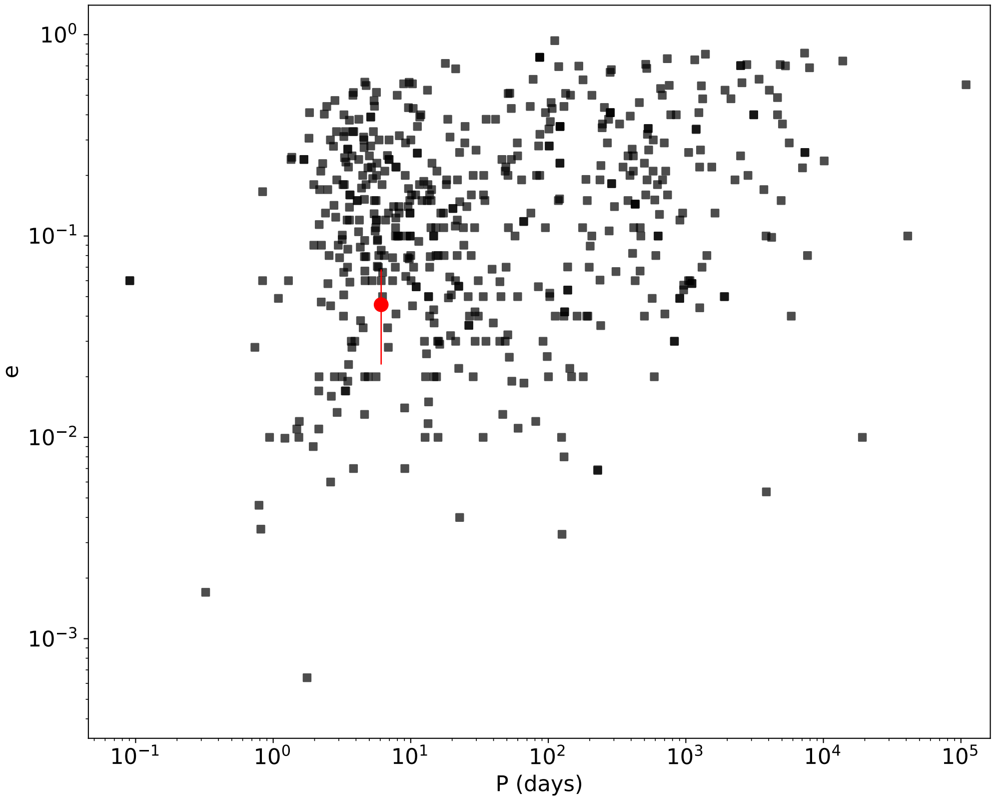

Figure 3.35: Period - Eccentricity diagram, in logarithmic scale. HD 285507 is highligthed in red. The error on period is smaller than the size of the point.

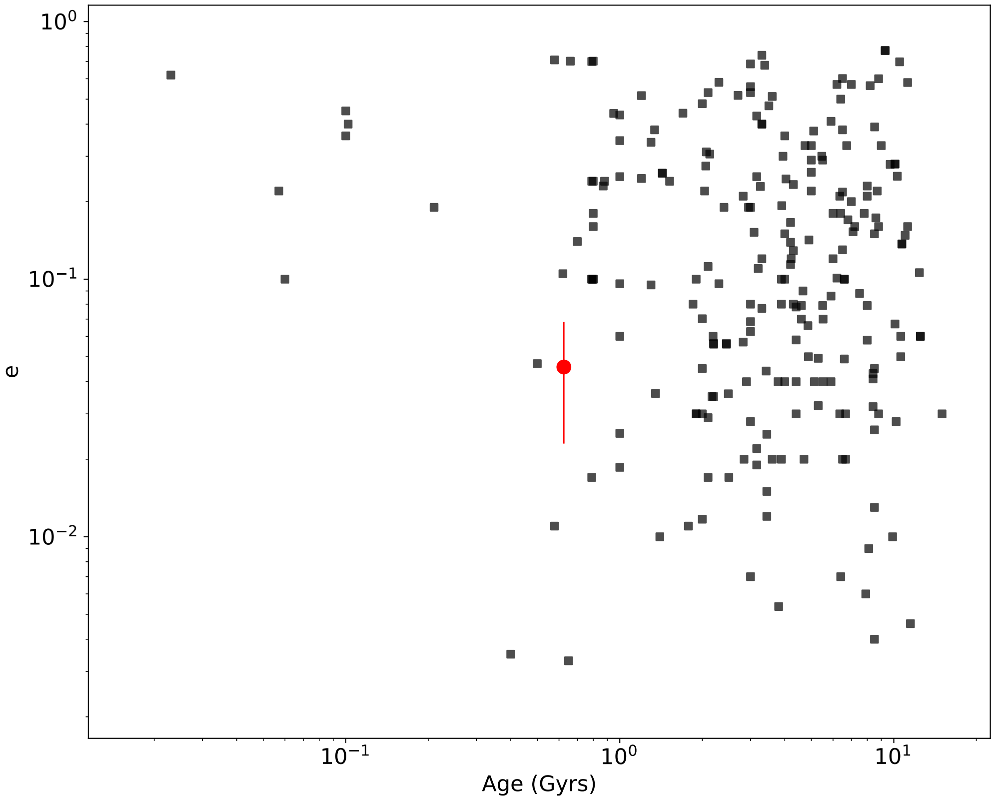

Figure 3.36: Stellar age - Eccentricity diagram, in logarithmic scale. HD 285507 is highligthed in red. The error on period is smaller than the size of the point.

3.5 AD Leo

In this Section I present the RV measurements of AD Leo (Gl 388, M4.5Ve, V=9.5, H=4.8, Reiners et al. 2013). AD Leo is a very close (distance of 4.9 pc, Pettersen & Coleman 1981) active star with an estimated age between 25 and 300 Myr (Shkolnik et al., 2009) and $vsini$ = 3 km s^{-1} (Reiners, 2007). Given its brightness and proximity, AD Leo is a very well studied star. Hawley & Pettersen (1991) observed AD Leo in the 1200-8000 Å wavelength region, reporting a giant flare lasted for more than 4 hours. Hunt-Walker et al. (2012), using MOST (Microvariability and Oscillations of Stars satellite) observations, captured 19 flares in 5.8 days and found a sinusoidal modulation in the light curve with a period of 2.23 days, attributing it to the rotation of a stellar spot. This period was consistent with the 2.24 d rotational period found by Morin et al. (2008) through the Zeeman Doppler imaging analysis. A further confirmation of this rotational period came from the HARPS RV variations found by Bonfils et al. (2013b): the periodogram analysis showed a peak at 2.22 days and the strong correlation between RVs and bisectors demonstrated the activity nature of the RV variation. Very similar results were found by Reiners et al. (2013), studying the Zeeman effect on RV measurements, interpreting the 2.22704 d as originating from the corotation of star spots on the stellar surface, since the line asymmetries were correlated with the RV modulation.

Very recently, Lavail et al. (2018) reported a sudden change in the surface magnetic field of AD Leo, through the study of magnetic maps using Zeeman Doppler imaging from ESPaDOnS spectropolarimetric data. The significant change in the shape of the circular polarisation profiles is attriduted to a strong decrease of the total magnetic field of about 20%, occuring between 2012 and 2016.

Finally, Tuomi et al. (2018) presented a photometric and spectroscopic analysis of AD Leo, proposing the presence of a planet orbiting the star in spin–orbit resonance in order to explain the RV variations from HARPS and HIRES spectra. They found a photometric period of 2.22791 days from ASAS photometry, and a spectroscopic period of 2.22579 days. Although the photometric and spectroscopic periods are very close and a strong correlation between HARPS RVs and bisector values is found, they performed tests on colour and time invariance of RVs. First they divided the 72 HARPS orders in six sets of 12 orders and calculated the weighted mean velocities, finding the signal to be independent on the selected wavelength range. Then they subdivided HARPS spectra in three different temporal subsets, threating them as independent datasets over a period of 60 days and they found a stable periodic variability, consistent with a time-invariant signal. These tests suggested the Keplerian nature of the RV variation rather than the activity nature.

We performed GIARPS observations over three months in 2018 in order to clarify the RV variations' nature in AD Leo, coupling VIS and NIR spectroscopy. Summary of the available data from HARPS – N and GIANO – B and their properties are presented in Table 3.22. The dataset is composed of 42 HARPS – N spectra and 25 GIANO – B spectra. HARPS – N RVs were processed by both HARPS – N DRS through the YABI workflow and TERRA pipeline and they are listed in Table 3.24.

GIANO-B data were reduced by the online GOFIO pipeline and divided in two different datasets, because instrumental operations between the two periods introduced instrumental drifts in our data (see Appendix D). The GIANO – B RVs were obtained with the method described in 2.9 and listed in Table 3.23.

Table 3.22: Summary of the spectroscopic data of AD Leo. For each dataset we list the instrument used for the observations, the number of spectra, the typical SNR, the RV nominal internal error (σ_{RV}), the RV r.m.s. scatter, and the peak-to-valley value of the RVs. We report the HARPS – N results from two different approach (DRS and TERRA).

Instrument	$\mathrm{N_{spectra}}$	SNR	σ_{RV} (km s^{-1})	RV r.m.s. (km s^{-1})	Peak-to-valley (km s^{-1})
GIANO – B (dataset 1)	12	180	0.019	0.019	0.063
GIANO – B (dataset 2)	13	186	0.017	0.019	0.055
HARPS – N (DRS)	42	74	0.001	0.030	0.097
HARPS – N (Terra)	42	74	0.001	0.022	0.074

HARPS – N DRS data The GLS and the orbital fit (using a Keplerian function) for HARPS – N data both for DRS and TERRA RVs were computed. The HARPS – N - DRS periodogram (Fig. 3.37) exhibits a significant periodicity at 2.2214 days, while the fitting model (Fig. 3.38) provides a period of 2.2237 ± 0.0002 days, a RV semi-amplitude of 45.0 ± 0.3 m s^{-1} and an eccentricity of 0.172 ± 0.005. These values are slightly lower (at the third decimal) than the photometric and spectroscopic periods found by Tuomi et al. (2018). After subtracting the VIS-DRS orbital fit, the VIS residuals have a scatter of 3.4 m s^{-1} and the corresponding periodogram exhibits a peak at 2.1343 days with a FAP of 0.6%. The corresponding fitting curve at 2.1345 days period is shown in Fig. 3.39. A trend can be seen, although the residual RVs are quite scattered around the fit.

HARPS – N TERRA data The HARPS – N - TERRA periodogram (Fig. 3.40) exhibits a highly significant periodicity at 2.2231 days, while the fitting model (Fig. 3.41) has a period of 2.2249 ± 0.0003 days, a RV semi-amplitude of 32.5 ± 0.3 m s^{-1} and an eccentricity of 0.168 ± 0.008. After subtracting the VIS-TERRA orbital fit, the residuals r.m.s is 2.6 m s^{-1}. The periodogram of the residual RVs show a peak at 11.1 days, while the Keplerian fit gives a period of 10.78 days. The phase-folded curve (a very unlikely fitting solution) of the residuals is shown in Fig. 3.42 and, since it seems to be driven by one or two points, it is clear that there is no variations.

Fig. 3.43 shows the RVs provided by the two different RV calculation methods and, as for V830 Tau (Sec. 3.3), the modulation amplitude is lower for TERRA RVs.

The different amplitudes obtained with different methods is the first hint indicating that the RV variations could be due to the activity rather than to a Keplerian signal, even if the RV signal could be composed by the two contributions and the DRS RVs are more affected by the activity exhibiting a larger amplitude, that can cover a possible Keplerian signal. A second hint for this hypothesis is the strong correlation between TERRA RVs and BIS obtained with the DRS (Fig. 3.50, Spearman r = -0.77, Pearson r = -0.78).

Since Tuomi et al. (2018) used TERRA for their RV calculation, I will consider my VIS RVs from TERRA pipeline in order to have a consistent comparison among RVs calculated with the same method (Fig. 3.44 shows the comparison between our RVs from TERRA pipeline and Tuomi's RVs).

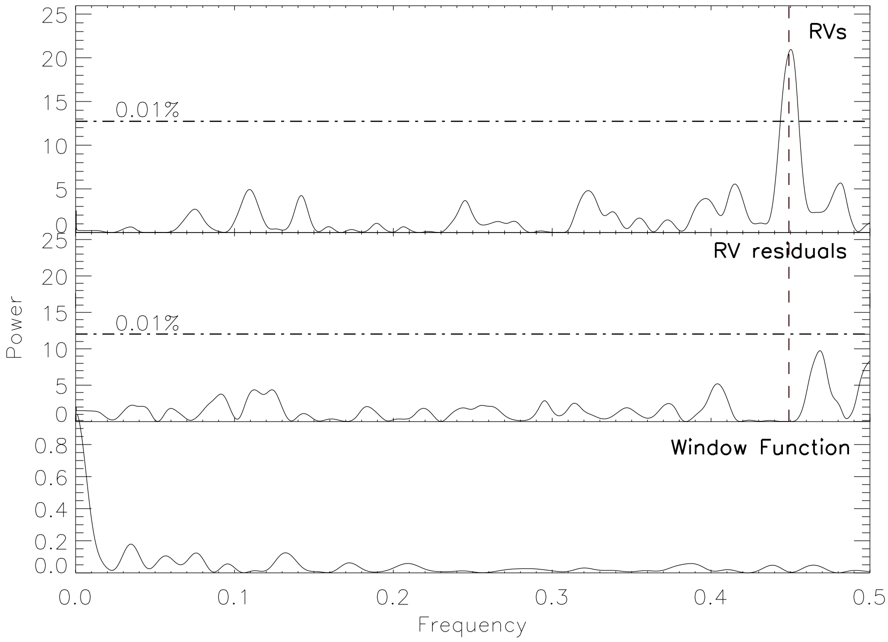

Figure 3.37: GLS of AD Leo for HARPS – N DRS data. The black vertical dashed line is the rotational period at 2.22791 days, while the red vertical dashed line is the proposed planet period at 2.22579 days (both periods by Tuomi et al. 2018).

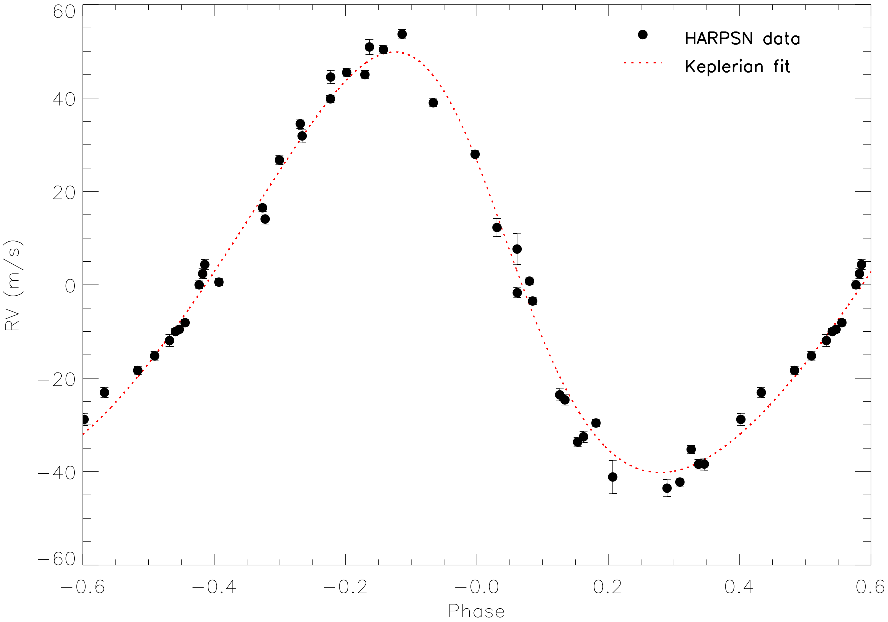

Figure 3.38: Keplerian fit (dashed line) for the HARPS – N DRS data (black dots) of AD Leo. The fitted period is of 2.2237 days.

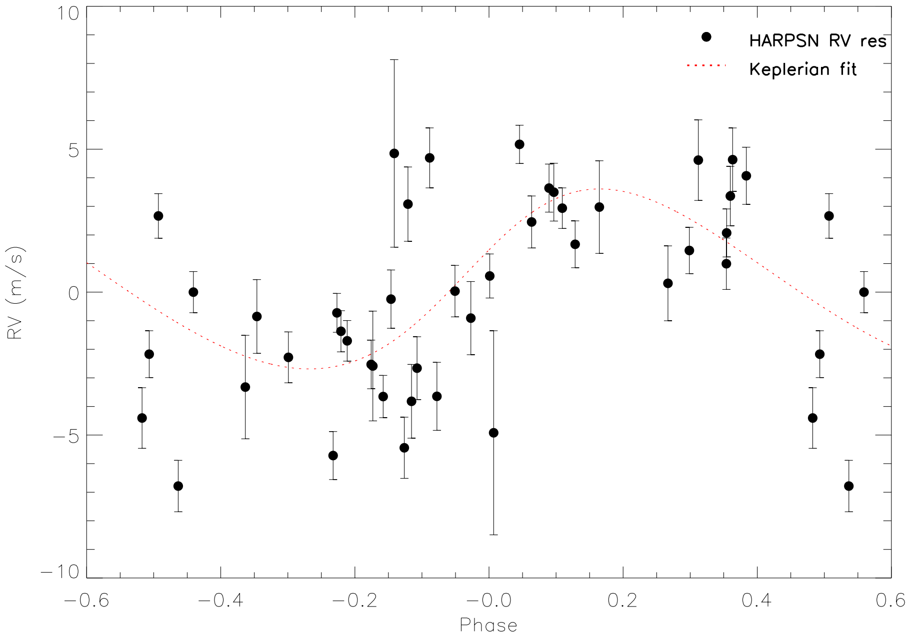

Figure 3.39: Keplerian fit (dashed line) of AD Leo with the residual HARPS – N DRS RVs (black dots). The fitted period is of at 2.1345 days.

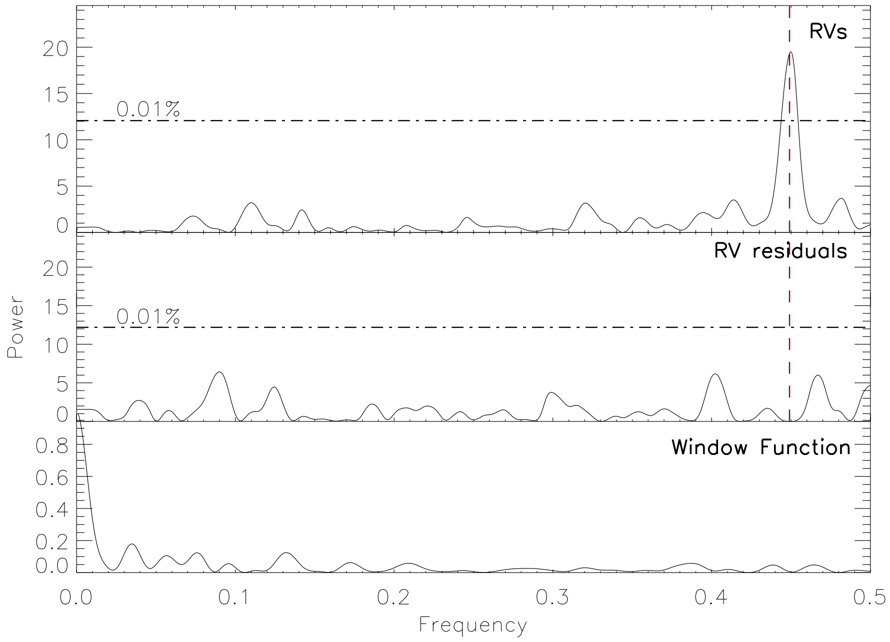

Figure 3.40: GLS of AD Leo for HARPS – N TERRA data. The black vertical dashed line is the rotational period at 2.22791 days, while the red vertical dashed line is the proposed planet period at 2.22579 days (both periods by Tuomi et al. 2018). The two lines are overimposed each other.

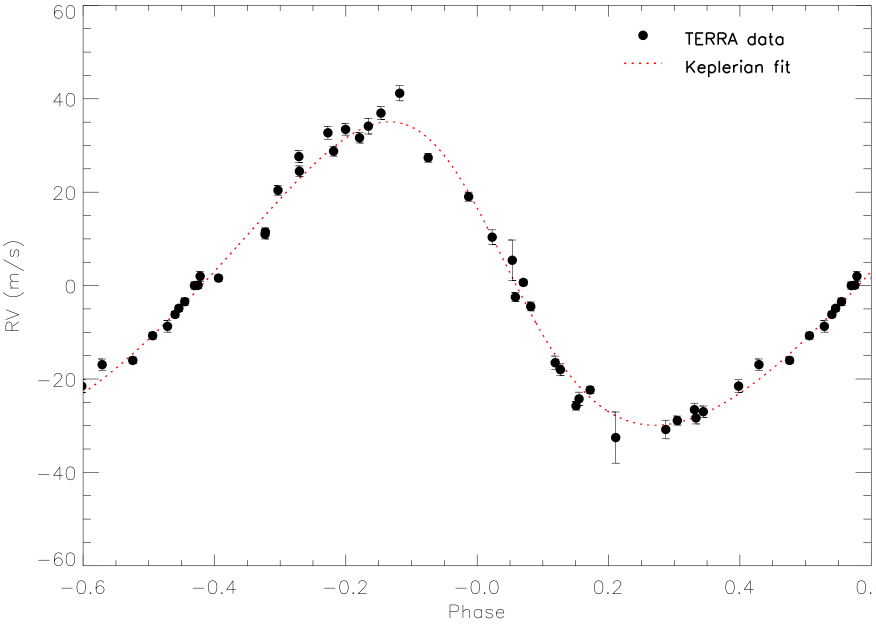

Figure 3.41: Keplerian fit (dashed line) at 2.2249 days of AD Leo with the HARPS – N TERRA data (black dots).

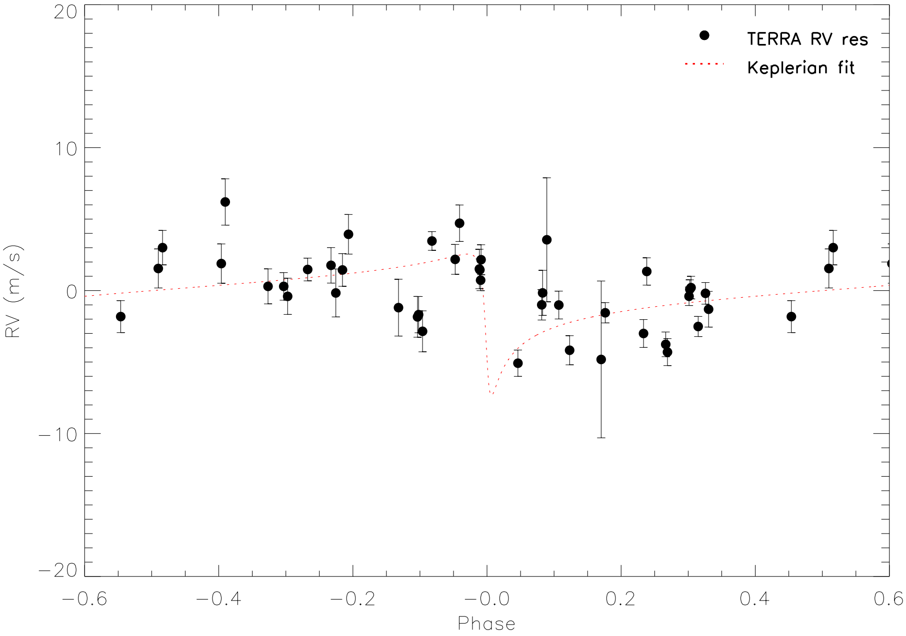

Figure 3.42: Keplerian fit (dashed line) at 10.78 days of AD Leo with the residual HARPS – N TERRA RVs (black dots).

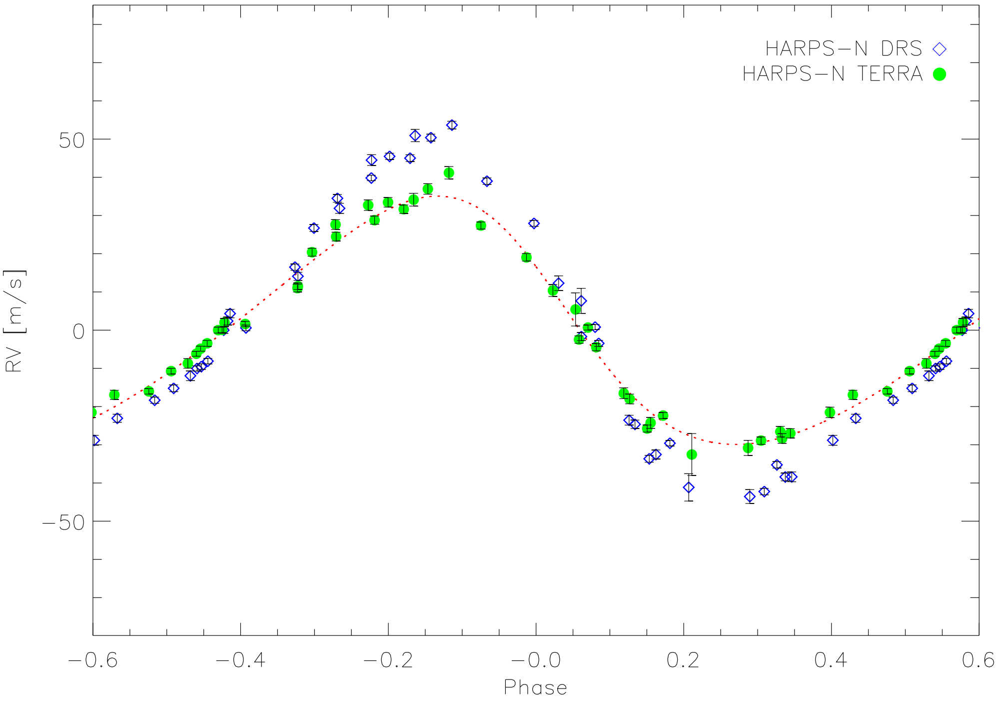

Figure 3.43: Comparison between DRS (blue diamonds) and TERRA (green dots) RVs with the TERRA orbital fit (dashed line).

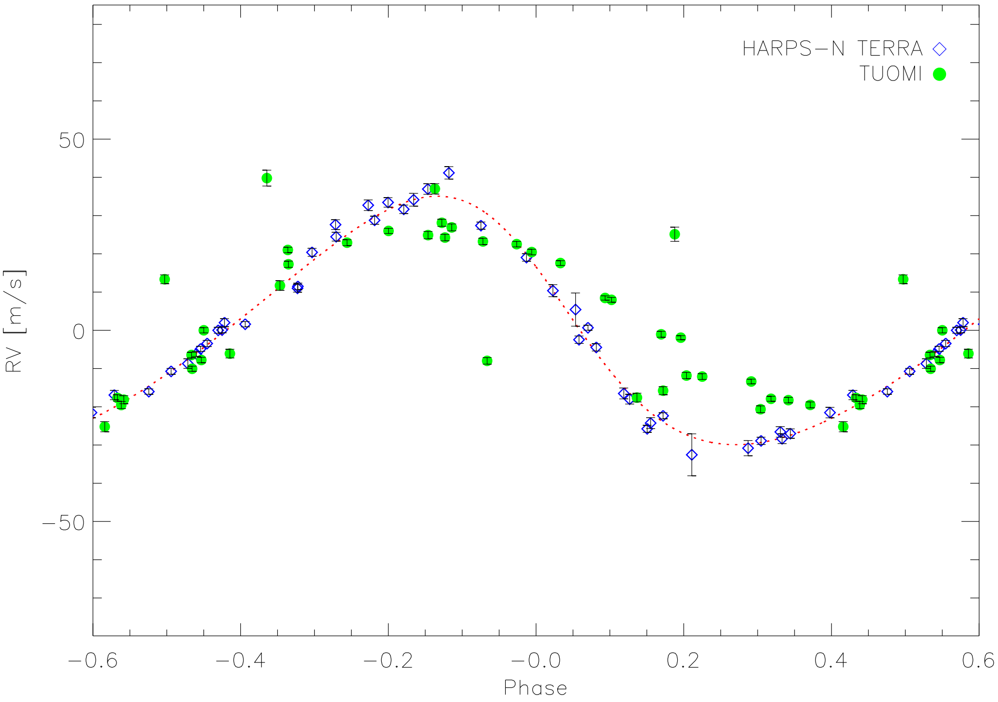

Figure 3.44: Comparison between our RVs from TERRA pipeline (blue diamonds, with the corresponding orbital fit, dashed line) and Tuomi's RVs (green dots) overimposed to our data.

HARPS − N TERRA and Tuomi's data I performed the GLS and orbital fit analysis putting together Tuomi's and our VIS-TERRA datasets. The maximum period of the periodogram is 2.2240 days (Fig. 3.45). The Keplerian fit of the whole dataset (Fig. 3.46) shows a period of 2.2273 ± 1.9 $\times 10^{-6}$ days, a RV semi-amplitude of 25.9 ± 0.1 m s^{-1} and an eccentricity of 0.108 ± 0.005. After subctracting the RV fit, the residuals show an r.m.s. of 8.4 m s^{-1}. The large dispersion is due to the different amplitude of the RV curves between our data and the ones presented by Tuomi et al. (2018). Again, this hints toward activity rather than Keplerian motion.

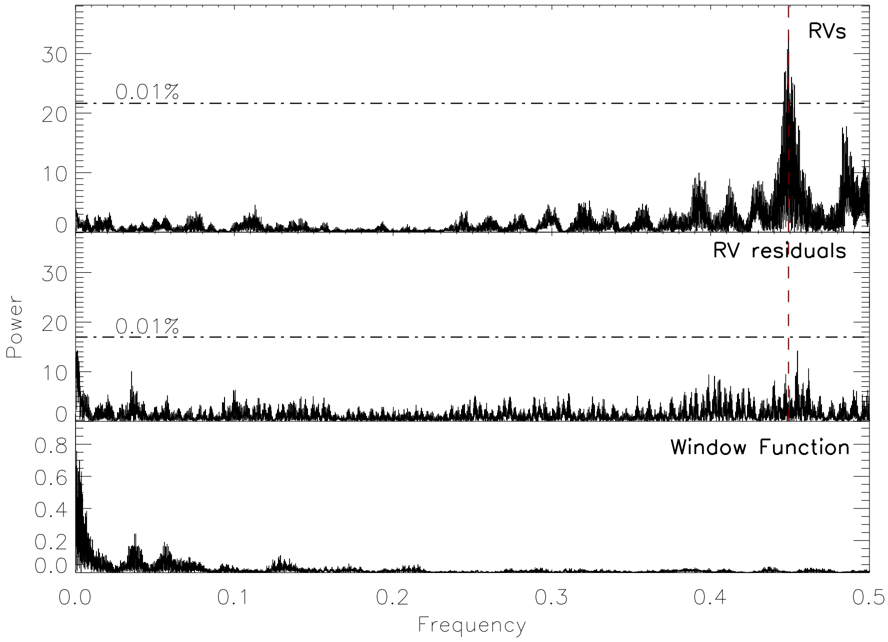

Figure 3.45: GLS of AD Leo for HARPS − N and Tuomi's data together. The black vertical dashed line is the rotational period at 2.22791 days, while the red vertical dashed line is the proposed planet period at 2.22579 days (both periods by Tuomi et al. 2018). The two lines are overimposed each other.

GIANO − B data The GLS and orbital fit analysis was also performed for GIANO − B data. The NIR periodogram (Fig. 3.47) shows a periodicity of 11.5228 days. This period could be due to the noise, due to the corresponding FAP value (0.1 %). The NIR orbital fit converges to a solution giving a period of 11.5125 ± 0.2918 days. Correcting the RVs for this fit, residual RVs show an r.m.s. of 10.3 m s^{-1} and a period of 2.2352 days (see Fig. 3.48), as can be seen in the periodogram of the residuals.

Summary of periods and semi-amplitudes obtained from data of the different instruments and different pipelines is reported in Tab. 3.25.

Fig. 3.49 shows the VIS-TERRA orbital fit represented as dashed line, together with the phase-folded VIS and NIR RVs (blue and red dots, respectively). The NIR RVs do not lie on the VIS orbital curve. We think that this strongly argues against a Keplerian nature of

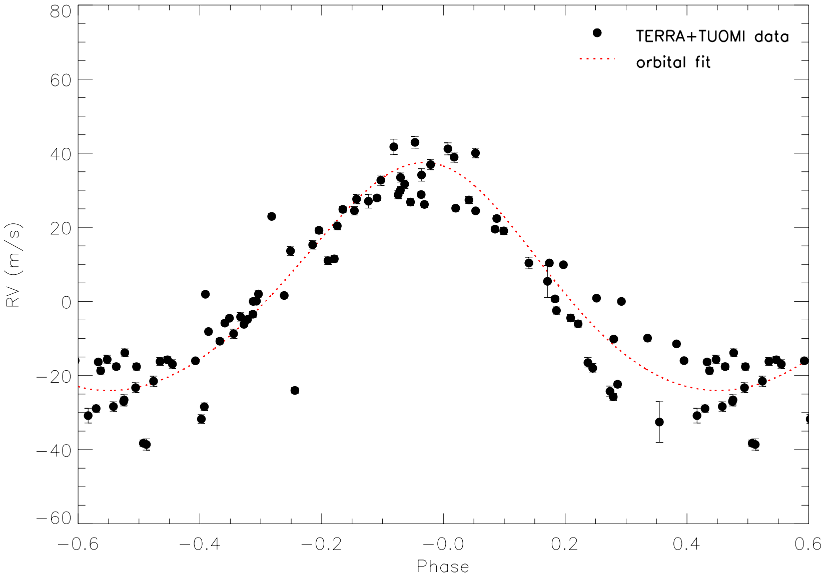

Figure 3.46: Keplerian curve (dashed line) at 2.2240 days of AD Leo with the HARPS – N - TERRA and Tuomi's data together.

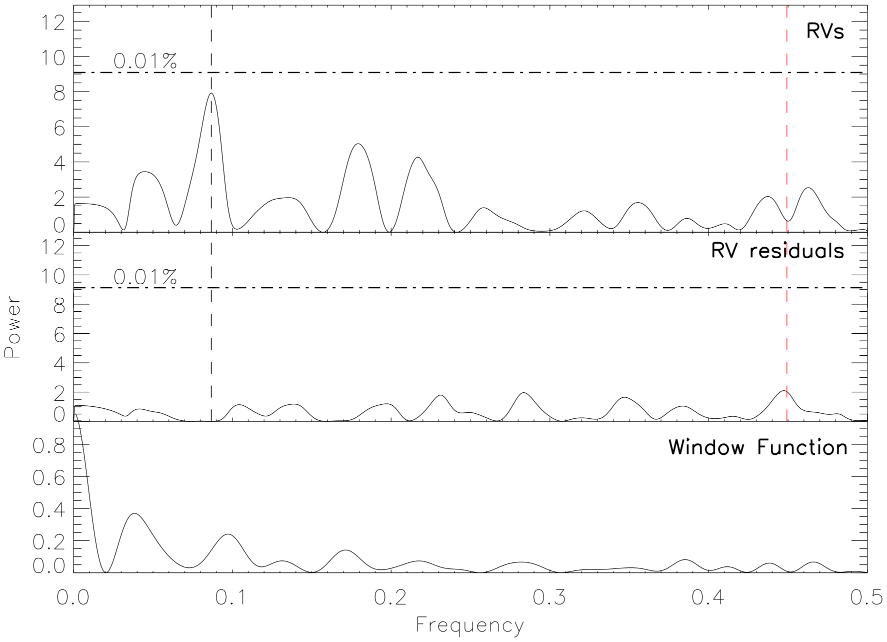

Figure 3.47: GLS of AD Leo for GIANO – B data. The black vertical dashed line indicates the maximum period of the NIR periodogram at 11.5 days, while the red dashed vertical line is the proposed orbital period. The residuals periodogram shows a peak at 2.2352 days.

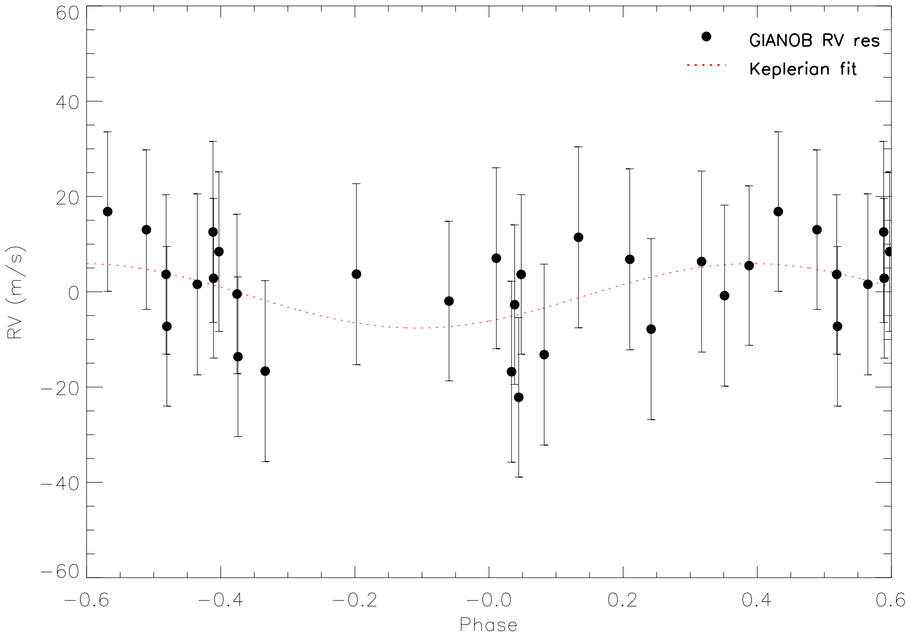

Figure 3.48: Keplerian fit (dashed line) of AD Leo with the GIANO – B residuals RVs (black dots) at a period of 2.2352 days.

RV variations, also supported by the strong correlation between VIS RVs (combining our and Tuomi's RVs) and BIS (Fig. 3.50). The r.m.s. of the RVs corrected for this trend results 14 m s^{-1} against the original r.m.s. of 22 m s^{-1}. Moreover, when I put the NIR residual RVs, that exhibit a period around 2.23 days, overplotted to the VIS Keplerian curve (see Fig. 3.51) they do not follow the VIS trend and are constant within the errors.

Table 3.23: Time series of AD Leo from GIANO – B data. For each observation we list radial velocities (RV) and the bisector span (BIS) with the corresponding uncertainties.

Dataset	JD-2450000	RV (km s^{-1})	σ_{RV} (km s^{-1})	BIS (km s^{-1})	σ_{BIS} (km s^{-1})
GIANO – B	8238.4196875	0.117	0.019	0.003	0.015
(dataset 1)	8238.5340394	0.143	0.019	-0.028	0.014
	8243.4145255	0.137	0.019	-0.059	0.015
	8243.4910995	0.129	0.019	0.001	0.019
	8244.4993866	0.115	0.019	-0.032	0.021
	8245.4103704	0.105	0.019	-0.009	0.017
	8245.4814583	0.090	0.019	-0.0069	0.018
	8246.4303472	0.080	0.019	-0.034	0.014
	8248.4392593	0.116	0.019	-0.033	0.015
	8248.4917361	0.127	0.019	-0.030	0.014
	8249.4360532	0.132	0.019	-0.052	0.014
	8249.4864583	0.109	0.019	-0.022	0.017
GIANO – B	8266.3748032	0.610	0.017	-0.046	0.018

(dataset 2)	8266.3928125	0.615	0.017	-0.052	0.016
	8266.4561343	0.592	0.017	-0.025	0.016
	8267.3783681	0.586	0.017	-0.060	0.015
	8267.3918634	0.566	0.017	-0.034	0.013
	8267.4001157	0.592	0.017	-0.033	0.014
	8268.3861343	0.587	0.017	-0.027	0.021
	8268.4542940	0.566	0.017	-0.027	0.031
	8269.3947685	0.569	0.017	-0.034	0.013
	8270.3949074	0.583	0.017	-0.039	0.013
	8275.3936458	0.621	0.017	-0.068	0.013
	8277.3923727	0.618	0.017	-0.065	0.013
	8279.4327662	0.596	0.017	0.024	0.013

Table 3.24: Time series of AD Leo from HARPS – N data (DRS and TERRA). For each observation we list radial velocities (RV) and the bisector span (BIS) with their related uncertainties.

	DRS				TERRA	
JD-2450000	RV (km s^{-1})	σ_{RV} (km s^{-1})	BIS (km s^{-1})	σ_{BIS} (km s^{-1})	RV (km s^{-1})	σ_{RV} (km s^{-1})
8213.4546160	12.593	0.001	-0.003	0.002	-0.027	0.001
8214.4570814	12.668	0.001	-0.010	0.001	0.029	0.001
8215.4127665	12.587	0.004	-0.005	0.007	-0.033	0.005
8216.4508868	12.645	0.001	-0.005	0.002	0.011	0.001
8236.4733936	12.642	0.001	-0.007	0.002	0.011	0.001
8238.3934517	12.618	0.001	-0.006	0.001	-0.006	0.001
8238.4062631	12.619	0.001	-0.004	0.001	-0.005	0.001
8238.4261108	12.620	0.001	-0.003	0.001	-0.003	0.001
8238.5406374	12.629	0.001	-0.004	0.001	0.002	0.001
8242.4077007	12.590	0.001	-0.001	0.003	-0.027	0.001
8243.4206503	12.674	0.001	-0.011	0.002	0.033	0.001
8243.4976917	12.679	0.002	-0.015	0.003	0.034	0.002
8244.5052941	12.585	0.002	-0.009	0.004	-0.031	0.002
8245.4166667	12.655	0.001	-0.010	0.002	0.020	0.001
8245.4873429	12.663	0.001	-0.010	0.002	0.028	0.001
8246.4262473	12.595	0.001	-0.004	0.002	-0.026	0.001
8248.4456851	12.626	0.001	-0.008	0.002	-0.002	0.001
8248.4977056	12.625	0.001	-0.006	0.002	-0.004	0.001
8249.4416895	12.613	0.001	-0.003	0.002	-0.011	0.001
8249.4920898	12.616	0.001	0.001	0.003	-0.009	0.001
8251.4265108	12.599	0.001	-0.004	0.003	-0.022	0.001
8251.4955782	12.605	0.001	-0.005	0.002	-0.017	0.001
8252.4399549	12.679	0.001	-0.013	0.002	0.037	0.001

8252.5033747	12.682	0.001	-0.014	0.002	0.041	0.002
8253.4437933	12.586	0.001	-0.003	0.002	-0.029	0.001
8253.5070279	12.590	0.001	-0.002	0.002	-0.028	0.001
8254.3885400	12.660	0.001	-0.012	0.003	0.024	0.001
8254.4851279	12.673	0.001	-0.012	0.003	0.033	0.001
8266.3792660	12.605	0.001	-0.005	0.003	-0.017	0.001
8266.3968916	12.604	0.001	-0.005	0.002	-0.018	0.001
8266.4600684	12.596	0.001	-0.008	0.002	-0.024	0.001
8267.3822946	12.628	0.001	-0.006	0.002	0.000	0.001
8267.3940411	12.631	0.001	-0.001	0.002	0.000	0.001
8267.4014015	12.633	0.001	-0.005	0.002	0.002	0.001
8268.3906816	12.640	0.002	-0.008	0.004	0.010	0.002
8268.4587770	12.636	0.003	-0.018	0.007	0.005	0.004
8269.3981431	12.610	0.001	-0.003	0.002	-0.016	0.001
8270.3987074	12.667	0.001	-0.013	0.002	0.027	0.001
8272.3909257	12.673	0.001	-0.010	0.002	0.032	0.001
8275.3970897	12.599	0.001	-0.003	0.001	-0.022	0.001
8277.3956075	12.629	0.001	-0.008	0.001	0.001	0.001
8279.4352346	12.656	0.001	-0.010	0.002	0.019	0.001

Table 3.25: Summary of the keplerian parameters of AD Leo resulting from the fitting model.

Instrument/Pipeline	Period (days)	K (m s^{-1})	e	ω *deg*
GIANO – B	11.5125 ± 0.2918	25.8 ± 7.1	0.16 ± 0.21	302 ± 83
HARPS – N (DRS)	2.2237 ± 0.0002	45.0 ± 0.3	0.17 ± 0.01	61 ± 2
HARPS – N (TERRA)	2.2249 ± 0.0003	32.5 ± 0.3	0.17 ± 0.1	64 ± 3
HARPS – N (TERRA) + TUOMI	$2.2273 \pm 1.9\times10^{-6}$	25.9 ± 0.1	0.11 ± 0.01	3.1 ± 0.1

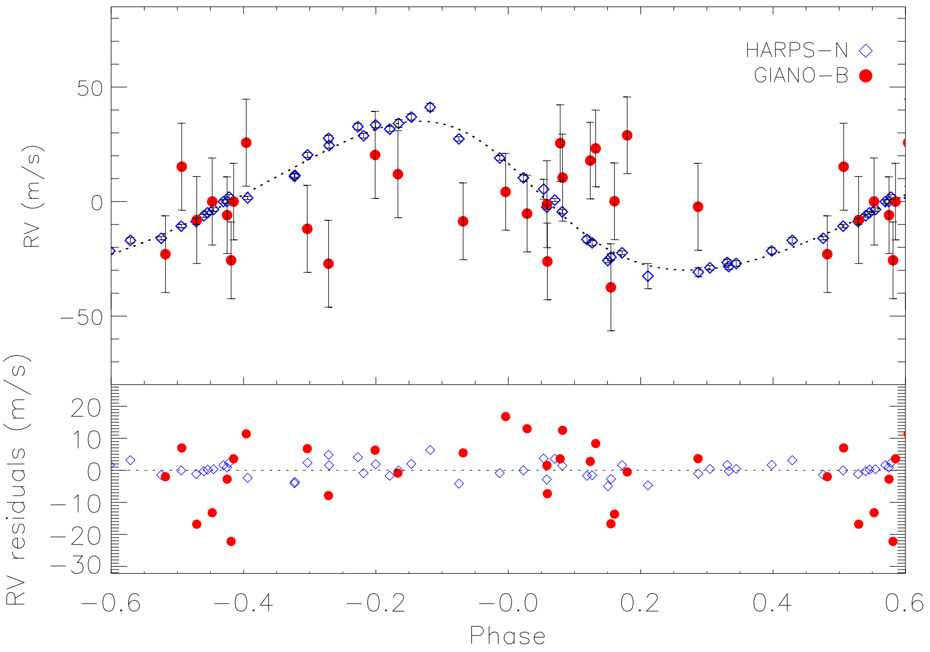

Figure 3.49: Keplerian fit (black dashed line) at 2.22485 days obtained with the visible data (HARPS – N, TERRA, blue diamonds), with GIANO – B RVs (red dots) overplotted.

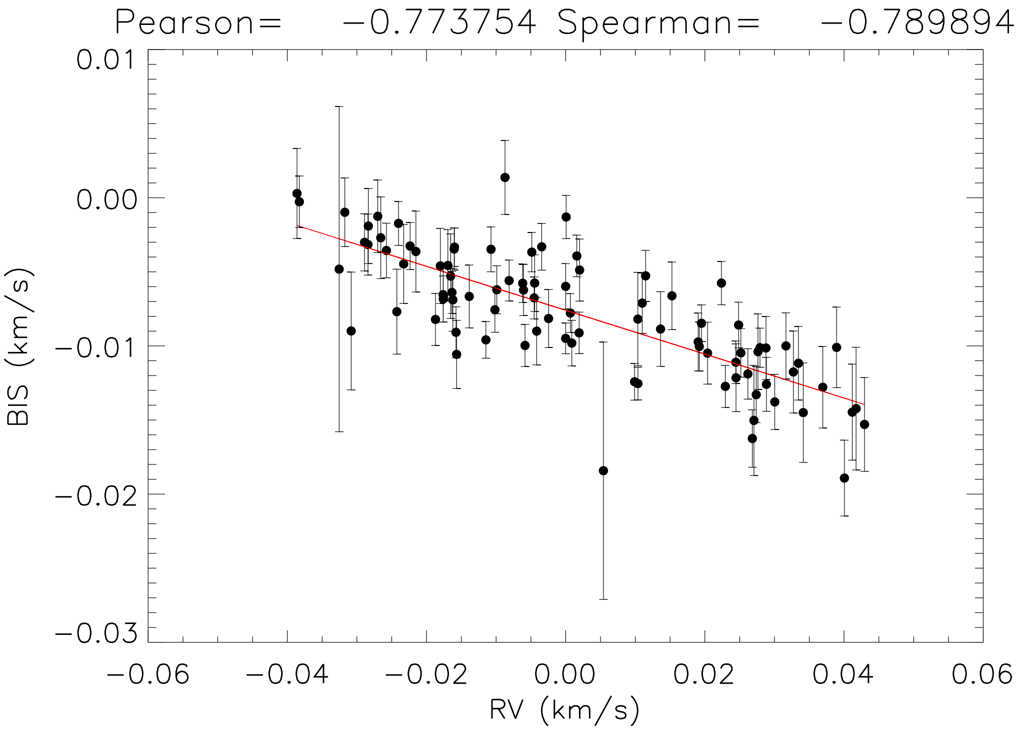

Figure 3.50: Correlation between VIS-TERRA (combining our and Tuomi's dataset) RVs and BIS of AD Leo.

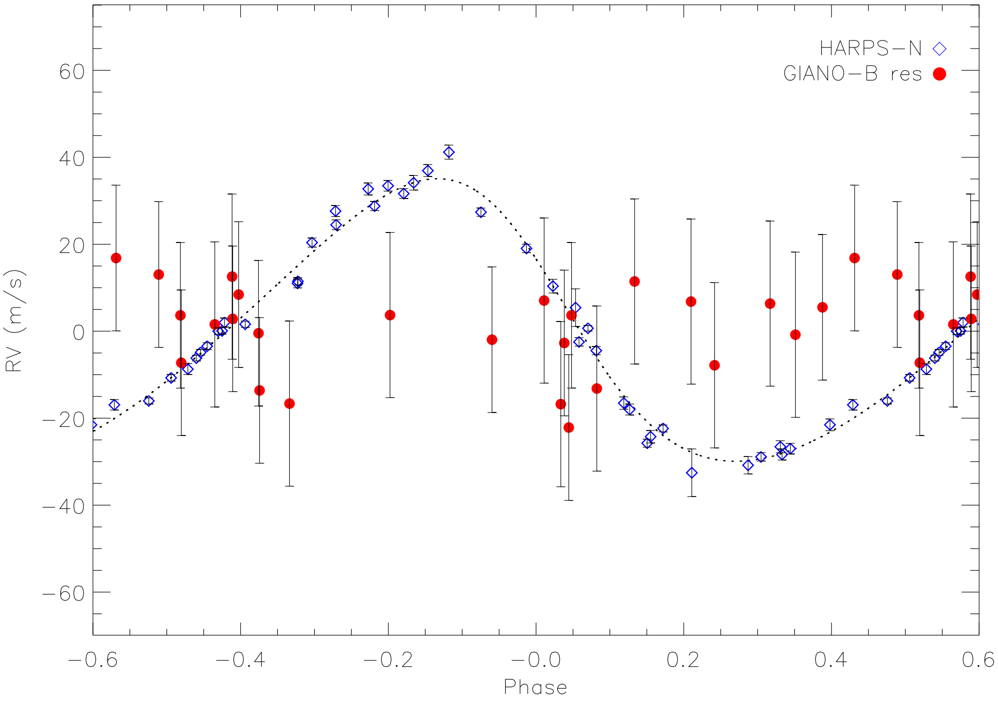

Figure 3.51: Keplerian fit (black dashed line) at 2.2249 days obtained with the visible data (HARPS – N, TERRA, blue diamonds), with GIANO – B residual RVs (red dots) overplotted.

3.6 GIANO – B Internal errors and RV Precision

The targets previously described allowed us to understand the GIANO – B performances and to assess the precisions of RV measurements. The characteristics of all the stars of our sample are reported in Tab. 3.26.

Table 3.26: List of stars of our sample together with the H magnitude, the SNR value, *vsini*, internal error and r.m.s scatter of RVs obtained from our analysis.

Star	SpType	Hmag	SNR	vsini $\mathrm{km\ s^{-1}}$	Internal error $\mathrm{m\ s^{-1}}$	RV r.m.s. scatter $\mathrm{m\ s^{-1}}$
V830 Tau	M0	8.6	27	30.5	769	946
HD 285507	K4.5	7.8	45	3.0	71	40
AD Leo	M4.5V	4.8	163	3.0	19	19
BD+20 1790	K5V	7.0	72	10.0	36	130
HD 3765	K2V	5.3	163	1.7	25	16
HD 159222	G1V	5.1	141	1.0	31	24

In Fig. 3.52 the internal errors and the RV scatter (that are consistent each other, see Fig. 3.53) are plotted as function of the SNR. The highest internal error correspond to the highest stellar *vsini* value, as can be see in Fig. 3.54 (the fitting curves are power functions to 3/2, since errors are expected to increase as the $(3/2)^{th}$ power of the *vsini*, Gray 1999). Fig. 3.55 shows the same result in terms of H magnitude. The stars with an H magnitude of about 5 have a precision of 8 $\mathrm{m\ s^{-1}}$ short-term and 16 $\mathrm{m\ s^{-1}}$ long-term, while the stars with H magnitude of about 8 reach a precision of ~100 $\mathrm{m\ s^{-1}}$.

The correlation, that we found between RV precisions and H magnitudes, can be represented with the following formula: err_{RV} ($\mathrm{m\ s^{-1}}$)$=10^{0.36Hmag-3.55}$.

It is important to note that the internal error is calculated considering only photon statistics. There are also other noise sources, due to the S/N ratio differences caused by the different exposure times used, and by variations in the conditions of the Earth's atmosphere. There are also instrumental effects, e.g. temperature drifts and differences due to the star itself, like variations in the stellar atmosphere due to magnetic activity, stellar oscillations, granulation, and so on. In addition, telluric lines may be not at rest with respect to the observer due to wind at different heights. Telluric lines are produced by a set of molecules (present at different heights) detectable at different wavelengths:

- H_2O (ubiquitous): <5 km
- O_2 (<1.3 μm): <5 km
- CO, CH_4 (K-band): 10-20 km
- CO_2 (H-band): >30 km

While in the visible range the strongest telluric lines are due to O_2 and H_2O molecules in layers at low altitude, in the NIR also the molecules formed in layers at high heights are

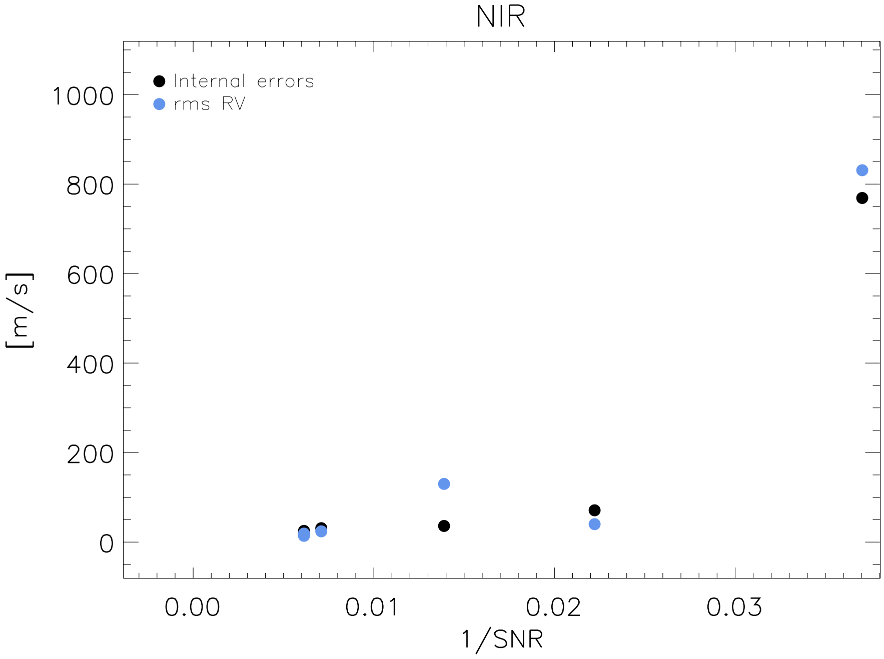

Figure 3.52: Internal errors (black points) and RV r.m.s. scatter (cyan points) of our sample as function of the the inverse of the signal to noise ratio.

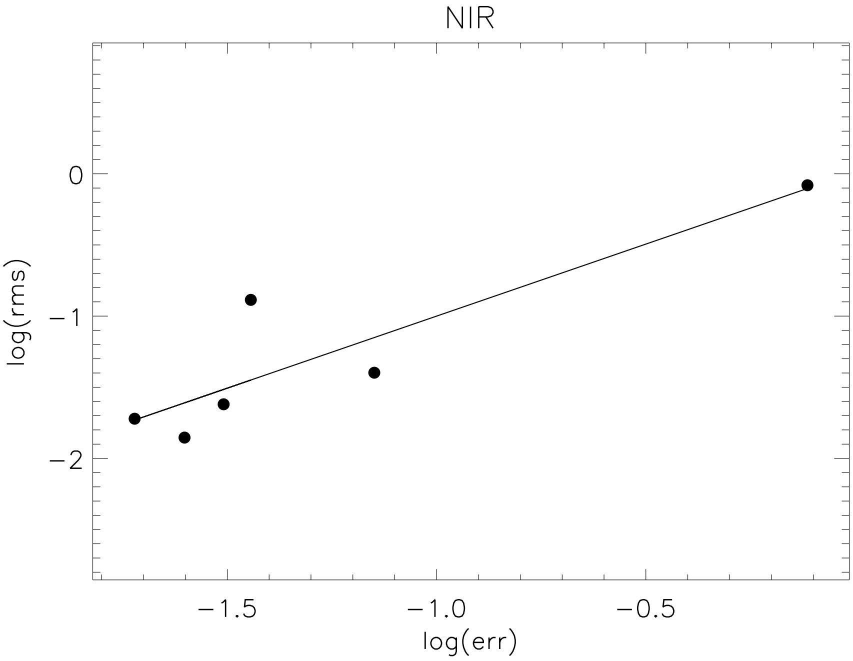

Figure 3.53: Logarithmic RV r.m.s. scatter as function of logarithmic internal errors.

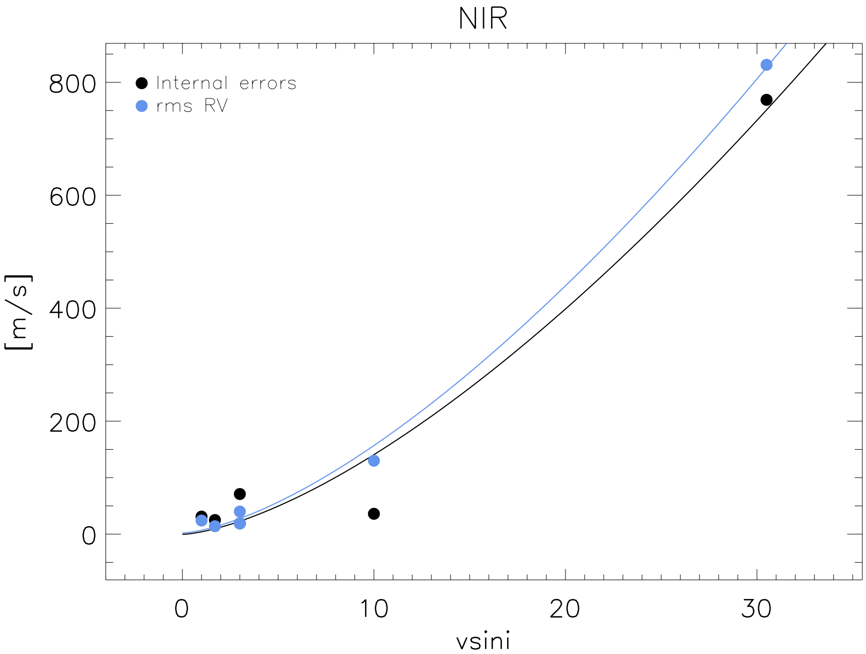

Figure 3.54: Internal errors (black points) and RV r.m.s. scatter (cyan points) of our sample as function of the stellar *vsini*).

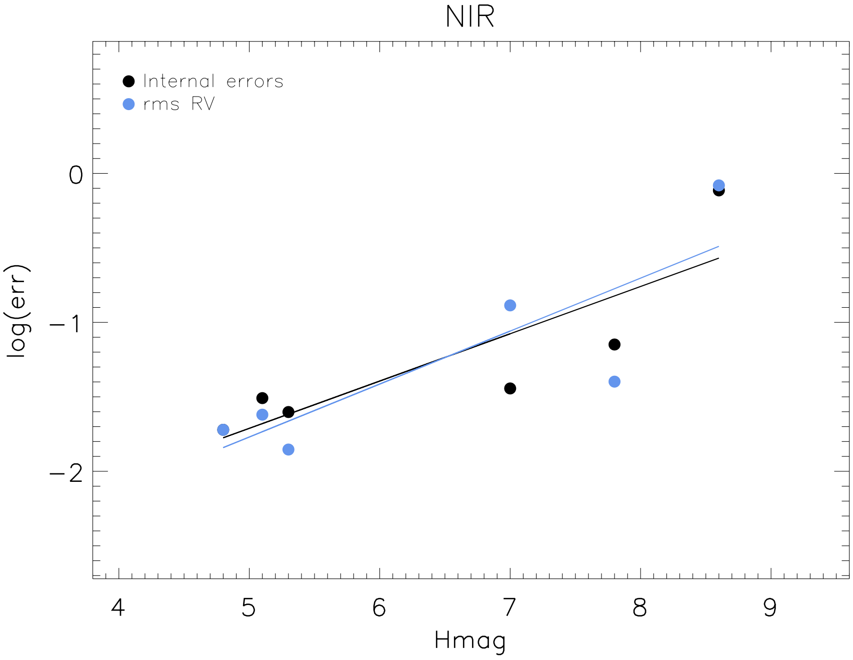

Figure 3.55: Logarithmic internal errors (black points) and RV r.m.s. scatter (cyan points) of our sample as function of the H magnitude.

significant. For these lines we expect winds whose velocity component along the line of sight may well be as large as 10 m s^{-1} that would reflect in offsets in the RVs.

Two main factors differentiate GIANO and HARPS – N: GIANO – B (as well as GIANO – A) is not an ultra-stabilized spectrograph as HARPS/HARPS – N (or even as the NIR arm of CARMENES). Such kind of control on the environmental conditions is not present for GIANO – B. Moreover, the wavelength calibration is not as stable as for HARPS – N. In fact, it is performed with an U-Ne lamp, showing errors of the order of 100 m s^{-1}. This can improve with the Fabry-Perot calibration, that will be soon available for GIANO – B.

Chapter 4

Conclusion and Future Perspectives

Despite the fact that about 500 Hot Jupiters have been discovered and studied over the past twenty years, the formation and evolution of this class of extrasolar planets is far to be clearly understood. Three main theories were proposed for the origin of Hot Jupiters, which I described in Section 1.2: in-situ formation, disk migration and tidal migration.

Observations of Hot Jupiters around young stars (Section 1.3) are crucial to investigate the first stage of the exoplanets' birth and they allow to associate the observed properties to the different theories, in order to understand the predominant origin channel. So far there is not a unique theory able to explain each observed features.

The investigation of the formation and migration histories may be carried out for example via intensive radial velocity (RV) monitoring of a sample of young stars, finding new planets and testing possible differences in the frequency of Hot Jupiters with age. However, the high level of stellar activity characterizing young stars induces RV variations able to mimic planetary signals, demanding a specific processing in order to investigate its actual contribution. In Section 1.3.1 I described some methods that have been developed for overcoming this issue: the correlation between RV measurements and bisector values, spectroscopic activity indicators such as the emission of H and K lines of Ca II in the visible range and the HeI and Brγ lines in the NIRthe Gaussian processes regression (see e.g. Haywood et al. 2014; Damasso et al. 2018), used to mitigate the contribution of the stellar activity noise in the RV data. This method does not assume any physical model about active regions, but it requires a large numbers of data to be reliable. A very powerful alternative is simultaneous multi-band high resolution spectroscopy (HRS), that is the focus of this PhD thesis, for example in the visible and near infrared ranges: since the impact of activity on RVs is expected to be typically three times lower in the NIR than in the VIS (see Prato et al. 2008; Mahmud et al. 2011; Crockett et al. 2012), observing in two different bands allow to disentangle wavelength-dependent activity-induced RV signals from those Keplerian that are achromatic. In principle, if the RV variation is due to a companion, the Doppler curves in VIS and NIR would present the same amplitude.

The building of new instrumentation allowing high precision HRS in the NIR range has been mainly pushed by the RV search of potentially habitable rocky planets around M-dwarf stars (see e.g. Reiners et al. 2010, Bonfils et al. 2013a and references therein). Some of those instruments, such as CARMENES (520 – 1710 nm, with spectral resolutions R=80,000 – 100,000, Quirrenbach et al. 2014; Reiners et al. 2018) or HARPS+NIRPS (0.95–1.8 nm, R ∼ 100,000, Conod et al. 2016), also guarantee contemporary VIS-NIR observations. In this framework, the GIARPS (GIANO – B + HARPS – N) project (Claudi et al., 2017), that I described in Chapter 2, has been conceived precisely to exploit the full potential of the simultaneous VIS and NIR HRS technique, allowing to have the two high resolution spectrographs of the Telescopio Nazionale Galileo (TNG, La Palma) working simultaneously: HARPS – N (High Accuracy Radial velocity Planet Searcher for the Northern emisphere) in the visible and GIANO – B in the NIR. This project was proposed and entirely funded and realized by GAPS2.0, a collaboration among most of Italian exoplanetary community, with the scientific aim to observe young stars at different ages and identify and characterize their planets, in order to better understand the realm of the planetary formation and evolution.

I collaborated for the first precursor result of GIARPS: the case of the detection of a substellar companion around the K giant star TYC 4282-605-1 (González-Álvarez et al., 2017). HARPS – N showed a RV variation, then confirmed by quasi-simultaneous VIS-NIR observations with HARPS – N and GIANO – A (Appendix C).

As Instrument Scientist of GIARPS, I took part to the GIARPS commissioning runs, that included three different parts: the commissioning for the preslit and the guiding camera in August/September 2016; the commissioning of the new GIANO configuration (GIANO – B) in November 2016, and finally the commissioning of GIARPS in March 2017. In particular, for the first one I organized the calibration plan, choosing calibration stars, mainly binaries for determining the scale of the astrometric field, and photometric standard stars in order to determine the photometric efficiency and to characterize the guiding camera and the field of view (limiting magnitude, field mask, bad pixels mask). The second commissioning concerned the verification of the functionality of some part of the systems, in particular the GIANO – B preslit alignment, the calibration units and the software (scheduler, sequencer, preslit software, autoguide). I selected some scientific proposals in order to perform the first GIANO – B observations and GIARPS observations for the third commissioning run, which was focused on the optimization of GIANO – B configuration, the sequencer and the autoguide, and the test of both instruments in GIARPS mode after the mounting of the dichroic, that allows GIANO – B to work simultaneously with HARPS – N. Furthermore, I selected different targets (point and extended sources) in order to test the online data reduction pipeline (nodding and stare mode) during early observations. For what concerns RVs, I developed an IDL code providing high precision values obtained using the telluric lines as a wavelength reference and the CCF method as computational technique (Carleo et al. 2016, Sec. 2.9), that is currently used to extract RV from GIANO spectra in the framework of the GAPS2.0 project.

In order to test the multi-wavelength methodology, a pilot program was performed in Autumn-Winter 2017, observing a number of very young HJs that have been claimed in the literature, this was followed by a GAPS2.0 Large Program started in April 2018 aiming to determine the frequency of very young HJs and their orbital parameters. In Chapter 3 I reported the results that I obtained with observations acquired with GIANO in all its configurations (GIANO – A and GIANO – B), before and after the GIARPS commissioning until the first semester of the Large Program.

Some RV standard stars were observed in order to test the instrumental RV stability (Section 3.1): HD 3765 was observed both with GIANO – A and GIANO – B, demonstrating that the short-term stability of GIANO (few days) is of ~ 8 m s^{-1} and the long-term stability (half a semester) is of ~ 16 m s^{-1}. The second RV-std star, HD 159222, showed a RV r.m.s. of ~ 24 m s^{-1}. This larger dispersion can be attributed to some aspects: HD 159222 is a G-type star, less suitable for NIR measurements, and its observations span one year during which some technical operations could have affected the instrumental stability (Appendix D).

In Section 3.2, I described my analysis performed on the star BD+20 1790, a very active star with a debated Hot Jupiter (Hernán-Obispo et al. 2010,Figueira et al. 2010a,Hernán-Obispo et al. 2015). GIANO and IGRINS NIR observations show that the NIR data have a peak-to-valley amplitude of 437.3 m s^{-1}, significantly lower than the VIS one (1853.6 m s^{-1}), demonstrating that the detected RV modulation is due to activity, and ruling out the presence of the previously announced hot-Jupiter planet.

I performed the same spectroscopic analysis for three more stars, V830 Tau (Sec. 3.3), HD 285507 (Sec. 3.4) and AD Leo (Sec. 3.5). No conclusive considerations can be done for V830 Tau, because of the high uncertainties in RVs, given the fast rotation and extremely high activity of this possibly still accreting star. An intensive monitoring is currently on going with GIARPS in order to obtain a larger dataset. While HD 285507 is a case of a confirmed planet, since HARPS − N and GIANO − B RVs show a similar r.m.s scatter and semi-amplitudes within the errors, AD Leo NIR RVs do not lie on the VIS orbital curve, strongly arguing against a Keplerian nature of RV variations.

These first results demonstrate the great potentiality of the multi-band high resolution spectroscopy when observing active stars. In the NIR regime the stellar activity is reduced, but not completely cancelled, and a RV signal could lead to wrong conclusions. For this reason, it is important to couple different bands, as VIS and NIR, in order to compare the corresponding results. In most cases multi-wavelength observations allow to almost immediately disentangle the nature of the RV variations.

The Large Program of GAPS2.0 just started, and the first analysed targets included already claimed Hot Jupiters in order to test both the multi-band methodology and the analysis tools for measuring RVs and dealing with the activity. The future plan concerns intensive observations of WTTS in Taurus and other young stars (age ≤ 200 Myr) taking full advantage of the GIARPS mode, aiming at a first determination of the frequency of HJs at younger ages. We will follow-up HJs TESS candidates around stars younger than 650 Myr and a suitable sample of TESS Hot Neptunes (HNs) candidates (estimated radius between 3 to 5 $R_{\oplus}$). Pre-selection of HJs candidates using TESS at intermediate age will allow an efficient use of telescope time considering the intrinsic rarity of HJs around mature solar-type stars. The follow-up of HNs candidates will allow us to obtain physical parameters and to compare the mass-radius relationship of these transitional objects with that of more and less massive objects. The most favorable cases will be observed in transmission spectroscopy in order to determine the characteristics of their atmospheres, that represent a further hint to understand the formation theories. In fact, also planet atmospheres evolve depending on the environment where the planet forms and encountered along its migration path. Moreover, a sample of young ($t < 650$ Myr) stars, without known stellar companions within 4”, will be observed with high cadence, complemented by few tens of young stars with TESS candidates. In addition to spectroscopic observations, quasi-simultaneous photometric monitoring will be performed using a network of small telescopes: REM observations (that produce simultaneously optical and NIR light curves), APACHE program (Giacobbe et al., 2012) at

Osservatorio Astronomico della Valle d'Aosta and EXORAP (EXOplanetary systems Robotic APT2 Photometry) program at Serra la Nave on Mt. Etna.

I will continue my collaboration and my work within the GAPS2.0 team: my NIR RV code, also thanks to the work performed in the last years in improving and optimizing, is currently the only one used within the collaboration to extract the GIANO-B RVs.

Acknowledgements

Appendix A

Data Reduction Software

Here I report the details of the DRS requirements and outputs as collected during the preparatory work for GIARPS.

A.1 DRS Requirements

A.1.1 General Requirements

GR1 The package will be accompanied by documentation that will provide the user with complete description of the DRS operation.

GR2 Online mode must have user feedback system that should provide information on the status of the processing as well as positive or negative outcome of the process.

GR3 Besides the general documentation (GR1), Offline DRS will provide additional documentation on how to install and operate the SW.

GR4 The input data to the package will be frames obtained with GIARPS and GIANO observation modes.

GR5 Unusable input data (low S/R-ratio, incompatible order layout) will produce warnings to the user, but not interrupt the reduction process.

GR6 Extracted spectra and associated files shall be written in FITS format.

GR7 The package shall read from the header fits all the necessary information about a target, as defined in the Instrumental Control Software (ICS) Document.

GR8 During the data reduction the package shall insert all the relevant information obtained through the process in the fits header.

GR9 The basic data reduction will be at first optimized for point sources (sky nodding and slit's nodding modes). As a goal, further implementation will allow the data reduction also for extended sources.

GR10 The DRS will be released with the possibility to measure RVs with the Cross Correlation technique, for both telluric lines and combined (cell + star) mask. As a goal, further implementation will allow the RV measurements also with the absorption cell technique (like AUSTRAL code by M. Endl, see Endl et al. 2000).

A.1.2 Online or Pipeline DRS

PR1 Real time data reduction at the telescope will be fully automatic, after each exposure.

PR2 The reduction time of a single frame should not interfere with the observations.

PR3 The software will make use of a pre-determined set of calibrations in order to provide a proper reduction of science frames. These data may consist of :

- A set of flat fields (10 frames);
- A set of dark frames (10 frames);
- An order definition frame, with a S/N-ratio per pixel of at least 10 in the orders that are to be extracted;
- Wavelength calibration frames.

PR4 Guaranteed that there are two positions on the slit, after selecting the input calibration files for the pipeline the package will perform pre-reduction processes. These should be prepared at the beginning of the observing night.

PR5 The wavelength solution, from associated calibration frames, should be made with an accuracy of 10%.

PR6 The Online DRS will save to the archive all the intermediate (reduced spectra, cleaned spectra) and final results of the reduction (calibrated spectra).

PR7 The Online DRS will display the average and RMS of dark current on the process terminal at the beginning of the night.

PR8 The Online DRS will display the SNR of the observed spectrum in (at least) three reference spectral regions on the process terminal during the night . The SNR should be computed in the same way as in the Exposure Time Calculator, ETC (defined mode), so that the observer can compare the expected SNR with the observed one and decide whether to extend exposure time. The wavelength regions should be easily identifiable by the observer.

PR9 A portion of the extracted spectrum in a representative wavelength range in the IR (e.g. a few interesting spectra lines, or a portion where the strength of telluric lines can be evaluated) will be showed in a graphical window.

A.1.3 Offline or User mode DRS

UR1 The Offline DRS will allow a fully automatic Data Processing (DP). In any case a user customization of the DP shall be also possible.

UR2 After the spectra extraction the offline DRS will provide radial velocity of the star if required by the user. Default: Telluric line technique. Goal: Absorption cell technique (like AUSTRAL).

UR3 The wavelength solution, from associated calibration frames, should be made with an accuracy of 10%.

UR4 The Offline DRS will save to the disk all the intermediate (reduced spectra, cleaned spectra) and final results of the reduction (calibrated spectra).

A.1.4 Implementation

IR1 The high level wrapper of the software shall be written in Python.

IR2 The reduction package will consist of a fixed set of algorithms that are optimized for GIARPS and GIANO data. The DRS responsible at the telescope should be able to perform the evaluation and calibration of the parameters of these algorithms.

IR3 The implemented software shall consist of modules (see below), allowing for stepwise future improvements of reduction routines.

- **IR3.01** Averaging of dark frames in order to construct a master dark frame.
- **IR3.02** Finding and tracing of order locations by fitting a polynominal to the position of the orders across the detector.
- **IR3.03** Summation and flat field frames in order to construct a master flat field frame.
- **IR3.04** Modeling and subtraction of scattered light from the inter-order regions.
- **IR3.05** Determination of wavelength solution by fitting a polynominal to the position of arc lines, either from separate calibration lamp spectra or from simultaneous interlaced calibration lamp spectra.
- **IR3.06** Pre-processing of science frames.
- **IR3.07** Extraction of observed spectral orders.
- **IR3.08** Normalization of extracted spectral orders through division by the 1D flat field.
- **IR3.09** Determination (in user mode) of the RV by Cross correlation evaluation of Doppler shift between telluric line and star spectra (see Section 7, RR3)
- **IR3.10** Determination (in user mode) of the RV by reconstruction of observed spectrum of the object plus the absorption cell as typical for Absorption Cell Technique (like AUSTRAL, see Section 7, RR4).

A.1.5 Radial Velocity Measurements

RR1 In the Offline mode the DRS will be able to measure the radial velocities with the telluric lines (default) or absorption cell (goal) techniques.

RR2 When the absorption cell technique will be available the user may choose among the two extraction modes.

RR3 The Offline DRS will perform the required steps (see below) in order to extract RVs with telluric lines technique:

- **RR3.01** The barycentric correction will be calculated.
- **RR3.02** Telluric and stellar spectra will be resampled with a constant step of 200m/s.
- **RR3.03** The signal to noise ratio of all spectra will be calculated.
- **RR3.04** Telluric and stellar spectra will be normalized to the continuum.
- **RR3.05** The stellar spectra cleaned from telluric lines will be created.
- **RR3.06** After finding the list of stellar lines, the DRS will create the stellar mask.

RR3.07 The telluric spectra cleaned from stellar lines will be created.

RR3.08 After finding the list of telluric lines, the DRS will create the telluric mask.

RR3.09 Stellar and telluric CCFs will be calculated, together with corresponding bisectors.

RR3.10 During the RV calculation the DRS will insert several keywords in the header fits of the spectra:

- Barycentric Julian Day
- Barycentric Earth RV
- final RV (CCF RV star – CCF RV tell)
- final error on RV
- CCF RV star
- CCF Intensity star
- CCF FWHM star
- CCF continuum star
- CCF RV tell
- CCF Intensity tell
- CCF FWHM tell
- CCF continuum tell
- Bisector Velocity Span star
- Bisector Velocity Span tell

RR3.12 The DRS will create a summary file including values in RR3.11

RR4 The Offline DRS will perform the required steps (see below, adapted from the AUSTRAL code by M. Endl, see Endl et al. 2000) in order to extract RVs with absorption cell technique.

RR4.01 Extraction of the spectrograph instrumental profile (IP), e.g. through a chi-square fitting between the spectra of a fast rotator B star taken with the cell and a model of the instrumental profile convolved with a oversampled spectrum of the absorption cell.

RR4.02 Deconvolution of the spectra of the target, taken without the cell, with the IP obtained in RR4.1 in order to obtain a clean "stellar template".

RR4.03 Reconstruction of a reference spectrum by using all the output obtained in RR4.1 and RR4.2 (Stellar template + IP + oversampled spectrum of the cell).

RR4.04 Radial velocity measurements are obtained through a chi-square fitting between the spectra of the target obtained with the absorption cell and the reference spectrum in RR4.3.

RR4.05 Radial velocity of the target spectra, as well as other interesting information (see RR3.11, RR3.12), will be saved into table files.

RR4.06 All the useful intermediate files (plots or textual) will be saved in dedicated directory.

A.1.6 Documentation

DR1 A user manual shall be released with the first version of both pipeline and user mode software. The user manual shall be updated every successive software version issue (if it is the case).

DR2 An installation manual shall be released with the first version of both pipeline and user mode software. The installation manual shall be updated every successive software version issue (if it is the case). If the offline DRS is offered web-based, an help-online should exist.

DR3 As goal, a maintenance manual, describing the internal layout of the reduction package and its software, and how the package can be developed further.

DR4 A commented source code shall be written for the DRS.

A.2 Proposed outputs for GIANO – B DRS

The GIANO-B DRS (GOFIO) is installed and functioning on the dedicated computer at TNG. An immediate next step is to have a user interface able to show information about spectra, in order to allow the observer to optimize the observational strategy during the night. The output already defined to be displayed on the user interface and the final fits format are listed in the following.

Interface

- Average and RMS of the dark current (from the dark calibration obtained in daytime)
- SNR of the extracted spectrum in the center of the spectral bands included in the GIANO-B spectra (Y, J, H and Ks)
- Portions of the extracted spectrum, representative in the NIR, showed in a graphical window (see Table A.1)

Intermediate and final data

- 2D non calibrated spectra (only bad-pixel correction and orders' straightening)[1]
- 2D calibrated spectra (orders' extraction and flat-field correction)
- Final output format to choose among: FITS files with one table (50orders x 2048 pixel), with information on the wavelength solution and a python procedure that convert the FITS files in ASCII files with wavelength and flux; FITS files with 3 tables (50x2048) with flux, wavelength and SNR per pixel.

Other possible outputs, as requested by the GIARPS Science Team are:

- Correction for the cosmic rays, including it in the online log

---

[1] Because of the optical design of GIANO the traces of the orders are curved on the detector and the spectral lines - i.e. the images of the slit at different wavelengths - are tilted. The pipeline uses a specific tool to straight the orders and the lines - i.e. after the correction, the slit-images are vertical in the whole spectrum.

- Visualization of the BERV (Barycentric Earth Radial Velocity) value
- If possible, the graphical window of the DRS interface showing the plots should be interactive, with the possibility to scale and move the spectrum.
- The combined (average) fits file of a number of AB nodding or C-Sky stare observations, after the default reduction of the single pairs.

Table A.1: List of the proposed features to be displayed in the GOFIO graphical window.

Element or molecule	Wavelength (nm)	GIANO – B spectral order	Science motivation
Silicates	1000	77	Tracer of silicates in the minor bodies of the Solar System
SrII,Fe,Si,Ca,Ti	1032-1040	74	Chemical analysis of dwarf and giant stars
HeI	1083	71	Diagnostic for young stellar objects, solar flares and coronal features
Paschenβ	1282	60	Diagnostic for young stellar objects
FeI	1564	49	Tracer of sunspots and solar cycle
CO2	1568-1580	49	Telluric absorption
H2	2120, 2240	36, 34	Diagnostics for young stellar objects and matter ejection (jets)
CO	2300	33[2]	Tracer of disks around pre-main sequence stars
CH4	2380-2420	32	Telluric absorption

---

[2] Feature at the edge of the order.

Appendix B

Calibration Plan for GIANO – B

The Calibration Plan consists in scientific, technical and instrument monitoring calibrations. In the following I describe in details the purpose and acquisition procedures for each calibration.

B.1 Science Calibration

Here the Science Calibrations for GIANO – B are described (a summary of these calibrations are reported in Table B.1.

Atmospheric Calibration

- *Phase*: Night
- *Frequency*: at least 1/night or 1/obs. program in multi-programs night
- *Purpose*: Calibration of telluric features to be removed from science spectra
- *Acquisition procedure*: Observe the spectrum of a featureless star (early-type star) with airmass within 0.1 from the science target, without the cell
- *Outputs*: Telluric spectrum
- *Duration*: 0.5 h

Cell Calibration

- *Phase*: Night
- *Frequency*: 1/night (on request) or 1/obs. program in multi-programs night
- *Purpose*: Calibration of the cell
- *Acquisition procedure*: Observe the spectrum of a featureless star (early-type star) with the cell
- *Outputs*: Cell spectrum
- *Duration*: 0.5 h

Sky background

- *Phase*: Night
- *Frequency*: 1/target acquisition
- *Purpose*: Remove sky background from science images

- *Acquisition procedure*: on slit nodding mode or on sky nodding mode
- *Outputs*: Sky background level
- *Duration*: it depends on the target integration time

Wavelength Calibration

- *Phase*: Night
- *Frequency*: 1/night
- *Purpose*: Perform wavelength calibration of the GIARPS spectra
- *Acquisition procedure*: Wavelength calibration of the lamp, identification of the Fabry-Perot lines, definition of the best values of $\delta\lambda$ e λ_0.
- *Outputs*: Pixel-wavelength
- *Duration*: $<0.5h$

Radial velocity standard

- *Phase*: Night
- *Frequency*: 1 / night (on request) or 1/obs. program in multi-programs night (on request)
- *Purpose*: Determine the RV trend to be removed from science spectra
- *Accuracy*: $10m\,s^{-1}$
- *Acquisition procedure*: Observe the spectrum of a RV standard star
- *Outputs*: RV-standard star spectrum
- *Duration*: 0.5 h

Dark current

- *Phase*: Day
- *Frequency*: 1/day
- *Purpose*: Remove dark level offset from flats and lamps
- *Acquisition procedure*: Take 10 dark frames (dark filter) with 600s of integration time (to be noted that starting from 600s frames it is possible to create frames with a minor time)
- *Outputs*: Zero level (dark) frames
- *Duration*: 2h

Flat fields

- *Phase*: Day
- *Frequency*: 1/day
- *Purpose*: Flat field correction and determine orders map
- *Acquisition procedure*: Take 10 flat frames
- *Outputs*: Flats fields echellogram frame
- *Duration*: $<0.5h$

Table B.1: Summary of the science calibrations with the corresponding frequency and duration.

Calibration name	Frequency	Duration
Atmospheric Calibration	1/night	0.5 h
Cell Calibration	1/night or 1/obs program	0.5 h
Sky background	1/night	Target integration time
Wavelength calibration	1/night	$<0.5h$
RV-standard star	1/night on request	0.5 h
Dark current	1/day	2 h
Flat fields	1/day	$<0.5h$

B.2 Technical Calibration

Here the Technical Calibrations for GIANO – B are described (a summary of these calibrations are reported in Table B.2.

Dark current

- *Phase*: Day
- *Frequency*: 3/year
- *Purpose*: Remove zero level offset, check dark current and identify hot pixels
- *Accuracy*: 10%
- *Acquisition procedure*: Take 50-100 dark frames with 600s of integration time (to be noted that starting from 600s frames it is possible to create frames with a minor time)
- *Outputs*: Detector dark current value, hot pixel map
- *Duration*: 9-17 h

Detector readout noise (RON

- *Phase*: Day
- *Frequency*: 3/year
- *Purpose*: Measure Detector RON
- *Accuracy*: 10%
- *Acquisition procedure*: Use the same frames taken to determine the dark current
- *Outputs*: Detector RON
- *Duration*: 9-17 h

Detector Gain

- *Phase*: Day
- *Frequency*: 2/year
- *Purpose*: Monitor detector gain factor
- *Accuracy*: 5%
- *Acquisition procedure*: Take 50-100 flat field frames with different flux levels
- *Outputs*: Detector Gain Factor
- *Duration*: 1 day

Total efficiency in the bands J,H,K

- *Phase*: Night
- *Frequency*: 1 / life (or on occurrence)
- *Purpose*: Determine the total efficiency and zero points of spectrograph
- *Accuracy*: 2-3% of the resulting efficiency
- *Acquisition procedure*: Take some photometric standards stars spectra (airmass=1)
- *Outputs*: efficiency and J,H,K zero points
- *Duration*: 1 night

Detector Persistence

- *Phase*: Day
- *Frequency*: 2 / year
- *Purpose*: Monitor the detector persistence after saturation
- *Accuracy*: 5%
- *Acquisition procedure*: Take 1 flat frame with different saturation levels (10-30-60-80%) and then take flat field frames of 10-60 seconds for 10-12 hours.
- *Outputs*: Detector Persistence (% as a function of time)
- *Duration*: 1 day

Time dependence of dark current

- *Phase*: Day + Night
- *Frequency*: 2 / year
- *Purpose*: Determine the dark current as function of time
- *Acquisition procedure*: Take dark frames of 600s every hour for 24 hours
- *Outputs*: Trend of the dark current as function of the temperature and the time.
- *Duration*: 24h

Cell and lamp line lists

- *Phase*: Day / Night
- *Frequency*: 1 / life
- *Purpose*: Determine the best signal and wavelength coverage, determine lamps and cell line lists
- *Acquisition procedure*: Take cell and lamps frames with different integration times
- *Outputs*: Line lists for the lamps and the cell.
- *Duration*: -

Time stability of dispersion function

- *Phase*: Day + Night
- *Frequency*: 2 / year
- *Purpose*: Determine the stability of dispersion as function of temperature
- *Acquisition procedure*: Take a lamp frame every half hour for 24 hours
- *Outputs*: Trend of the dispersion function dependent on the temperature and the time.
- *Duration*: 24h

Guide camera - Field mask

- *Phase*: Night
- *Frequency*: 1 / life (or to occurrence)
- *Purpose*: Determine the field mask
- *Accuracy*: 1 px^2
- *Acquisition procedure*: Take 1 sky frame with a deep exposure
- *Outputs*: Image of the field guide
- *Duration*: $<1h$

Guide camera - Astrometric field

- *Phase*: Night
- *Frequency*: 1 / life (or to occurrence)
- *Purpose*: Determine the scale and the angular offset from telescope axes
- *Acquisition procedure*: Take 1 image of an astrometric field
- *Outputs*: scale and axes orientation
- *Duration*: $<1h$

Guide camera - Bad pixels mask

- *Phase*: Day / Night
- *Frequency*: 1 / year
- *Purpose*: Determine the bad pixels mask
- *Accuracy*: 1 px^2
- *Acquisition procedure*: take 10 images of blank field
- *Outputs*: bad pixels mask
- *Duration*: $<0.5h$

Guide camera - Dark frame

- *Phase*: Day / Night
- *Frequency*: 4/ year
- *Purpose*: Determine the dark current frame value
- *Acquisition procedure*: take a dark frame
- *Outputs*: dark frame
- *Duration*: $<0.5h$

Guide camera - Photometric efficiency

- *Phase*: Night
- *Frequency*: 1 / life (or to occurrence)
- *Purpose*: Determine the limiting magnitude of the guiding camera
- *Accuracy*: 0.5 mag
- *Acquisition procedure*: Take 1 image of photometric standard star (airmass=1)
- *Outputs*: limiting magnitude in Z band for guiding
- *Duration*: $<1h$

Guide camera - A-B-C positions

- *Phase*: Night
- *Frequency*: 1 / night
- *Purpose*: Determine the positions A-B-C
- *Acquisition procedure*: Calculate the positions of A-B-C and inserted them in the Auto Guide inputs
- *Outputs*: Coordinates in pixels of A-B-C positions
- *Duration*: $<0.5h$

Table B.2: Summary of the technical calibrations with the corresponding frequency and duration.

Calibration name	Frequency	Duration
Dark current	3/year	9-17 h
Detector RON	3/year	9-17 h
Detector gain	2 / year	1 day
Total efficiency in the bands J,H,K	1 / life	1 night
Detector persistence	2 / year	1 day
Time dependence of dark current	2 / year	24 h
Cell and lamp line lists	1 / life	
Time stability of dispersion function	2 / year	24 h
Guide camera – Field mask	1 / life	$<1h$
Guide camera – Astrometric field	1 / life	$<1h$
Guide camera – Bad pixels mask	1 / year	$<0.5h$
Guide camera – Dark	4 / year	$<0.5h$
Guide camera – Photometric Efficiency	1 / life	$<1h$
Guide camera – A-B-C positions	1/night	$<0.5h$

B.3 Instrument Monitoring Calibration

Here the Instrument Monitoring Calibrations for GIANO – B are described (a summary of these calibrations are reported in Table B.3.

Bad Pixels Mask

- *Phase*: Day
- *Frequency*: 1 / year
- *Purpose*: Determine the mask of bad pixels
- *Acquisition procedure*: Take 10 flat-field frames
- *Outputs*: Detector static bad pixel map
- *Duration*: $<0.5h$

Orders Map

- *Phase*: Day / Night

- *Frequency*: 3 / year
- *Purpose*: Determine the map of the orders as function of time
- *Acquisition procedure*: Take 10 flat frames for 24 hours
- *Outputs*: Location of the orders as function of time
- *Duration*: 24 h

RON, dark current map and intensity

- *Phase*: Day
- *Frequency*: 1-2/month
- *Purpose*: Check RON, dark current map and intensity as function of time
- *Acquisition procedure*: Take Dark frames (as in scientific calibrations)
- *Outputs*: RON, dark current map and intensity as function of time
- *Duration*: 0.5 h

Transparency, halogen lamp intensity, orders map

- *Phase*: Day
- *Frequency*: 1-2/month
- *Purpose*: Check transparency, halogen lamp intensity, orders map as function of time
- *Acquisition procedure*: Take Flat field frames (as in scientific calibrations)
- *Outputs*: transparency, halogen lamp intensity, orders map as function of time
- *Duration*: 0.5 h

Dispersion function, calibration lamp intensity

- *Phase*: Day
- *Frequency*: 1-2/month
- *Purpose*: Monitor the dispersion function, calibration lamp intensity as function of time
- *Acquisition procedure*: lamp frames (as in scientific calibrations)
- *Outputs*: dispersion function, calibration lamp intensity as function of time
- *Duration*: 0.5 h

Dark current map

- *Phase*: Day
- *Frequency*: 1 / week
- *Purpose*: Determine the dark shape
- *Acquisition procedure*: Take 10 dark frames as function of the flat
- *Outputs*: Detector Persistence (% as a function of time)
- *Duration*: $<0.5h$

Calibration lamp

- *Phase*: Day
- *Frequency*: 2 / month
- *Purpose*: Monitor the dispersion function at different y-positions and different orders
- *Acquisition procedure*: Take 1 frame of the lamp

- *Outputs*: lamp or Fabry-Perot frame
- *Duration*: $<0.5h$

Table B.3: Summary of the instrument monitoring calibrations with the corresponding frequency and duration.

Calibration name	Frequency	Duration
Bad Pixels Mask	1 / year	$<0.5h$
Orders Map	3 / year	24 h
RON,dark current map, itensity	1-2/ month	0.5 h
Transparency, halogen lamp intensity, orders map	1-2/ month	0.5 h
Dispersion function, calibration lamp intensity	1-2/ month	0.5 h
Dark current map	1 / week	$<0.5h$
Calibration lamp	2 / month	$<0.5h$

Appendix C

First quasi-simultaneous GIANO and HARPS – N observations

In this Appendix I report the paper by González-Álvarez et al. (2017), that represents the first result of VIS and NIR data using GIANO – A and HARPS – N, even if not in their simultaneous mode yet. I contributed to this work both helping in the data reduction and providing the code used to extract the NIR RVs.

A&A 606, A51 (2017)
DOI: 10.1051/0004-6361/201731124

Astronomy & Astrophysics

The GAPS Programme with HARPS-N at TNG

XV. A substellar companion around a K giant star identified with quasi-simultaneous HARPS-N and GIANO measurements[★]

E. González-Álvarez[1,2], L. Affer[1], G. Micela[1], J. Maldonado[1], I. Carleo[3,4], M. Damasso[4,5], V. D'Orazi[3], A. F. Lanza[6], K. Biazzo[6], E. Poretti[7], R. Gratton[3], A. Sozzetti[5], S. Desidera[3], N. Sanna[8], A. Harutyunyan[9], F. Massi[8], E. Oliva[8], R. Claudi[3], R. Cosentino[9], E. Covino[10], A. Maggio[1], S. Masiero[1], E. Molinari[9,11], I. Pagano[6], G. Piotto[3,4], R. Smareglia[12], S. Benatti[3], A. S. Bonomo[5], F. Borsa[7], M. Esposito[10], P. Giacobbe[5], L. Malavolta[3,4], A. Martinez-Fiorenzano[9], V. Nascimbeni[3,4], M. Pedani[9], M. Rainer[7], and G. Scandariato[6]

[1] INAF–Osservatorio Astronomico di Palermo, Piazza Parlamento 1, 90134 Palermo, Italy
e-mail: `egonzalez@astropa.unipa.it`
[2] Dipartimento di Fisica e Chimica – Università degli Studi di Palermo, via Archirafi 36, 90123 Palermo, Italy
[3] INAF–Osservatorio Astronomico di Padua, Vicolo dell'Osservatorio 5, 35122 Padova, Italy
[4] Dipartimento di Fisica e Astronomia G. Galilei, Università di Padova, Vicolo dell'Osservatorio 2, 35122 Padova, Italy
[5] INAF–Osservatorio Astrofisico di Torino, via Osservatorio 20, 10025 Pino Torinese, Italy
[6] INAF–Osservatorio Astrofisico di Catania, via S. Sofia 78, 95123 Catania, Italy
[7] INAF–Osservatorio Astronomico di Brera, via E. Bianchi 46, 23807 Merate, Italy
[8] INAF–Osservatorio Astronomico di Arcetri, Largo Enrico Fermi, 5, 50125 Firenze, Italy
[9] Fundación Galileo Galilei-INAF, Rambla José Ana Fernandez Pérez 7, 38712 Breña Baja, TF, Spain
[10] INAF–Osservatorio Astronomico di Capodimonte, Salita Moiariello 16, 80131 Napoli, Italy
[11] INAF–IASF Milano, via Bassini 15, 20133 Milano, Italy
[12] INAF–Osservatorio Astronomico di Trieste, via Tiepolo 11, 34143 Trieste, Italy

Received 8 May 2017 / Accepted 14 June 2017

ABSTRACT

Context. Identification of planetary companions of giant stars is made difficult because of the astrophysical noise, that may produce radial velocity variations similar to those induced by a companion. On the other hand any stellar signal is wavelength dependent, while signals due to a companion are achromatic.

Aims. Our goal is to determine the origin of the Doppler periodic variations observed in the thick disk K giant star TYC 4282-605-1 by HARPS-N at the Telescopio Nazionale *Galileo* (TNG) and verify if they can be due to the presence of a substellar companion.

Methods. Several methods have been used to exclude the stellar origin of the observed signal including detailed analysis of activity indicators and bisector and the analysis of the photometric light curve. Finally we have conducted an observational campaign to monitor the near infrared (NIR) radial velocity with GIANO at the TNG in order to verify whether the NIR amplitude variations are comparable with those observed in the visible.

Results. Both optical and NIR radial velocities show consistent variations with a period at 101 days and similar amplitude, pointing to the presence of a companion orbiting the target. The main orbital properties obtained for our giant star with a derived mass of $M = 0.97 \pm 0.03\ M_\odot$ are $M_\mathrm{P} \sin i = 10.78 \pm 0.12\ M_\mathrm{J}$; $P = 101.54 \pm 0.05$ days; $e = 0.28 \pm 0.01$ and $a = 0.422 \pm 0.009$ AU. The chemical analysis shows a significant enrichment in the abundance of Na I, Mg I, Al I and Si I while the rest of analyzed elements are consistent with the solar value demonstrating that the chemical composition corresponds with an old K giant (age = 10.1 Gyr) belonging to local thick disk.

Conclusions. We conclude that the substellar companion hypothesis for this K giant is the best explanation for the observed periodic radial velocity variation. This study also shows the high potential of multi-wavelength radial velocity observations for the validation of planet candidates.

Key words. stars: individual: TYC 4282-605-1 – techniques: radial velocities – planetary systems – infrared: stars

1. Introduction

Several physical mechanisms related to the host star characteristics may mimic the presence of a planet. They include granulation and activity phenomena such as spots, plages and even cycles as well as radial and non-radial pulsations (Hatzes & Cochran 2000; Dumusque et al. 2011). These phenomena may occur on several time scales and produce radial velocity (RV) variations hardly distinguishable from those induced by a low-mass companion.

The K giant stars usually have masses in the 0.2–10 $M_\odot$ mass range and radii between 2 and 100 $R_\odot$. Their precise evolutionary stage is difficult to determine because the evolutionary tracks of the stars belonging to the red giant branch, red clump (for solar

---

[★] Based on observations collected at the Italian Telescopio Nazionale *Galileo* (TNG), operated on the island of La Palma by the Fundación Galileo Galilei of the INAF (Istituto Nazionale di Astrofisica) at the Spanish Observatorio del Roque de los Muchachos of the Instituto de Astrofísica de Canarias, in the frame of the programme Global Architecture of Planetary Systems (GAPS).

metallicity) and asymptotic giant branch fall close and can intersect with each other in the H-R diagram (Chaplin & Miglio 2013).

The variability of these objects can be quite complex. Luminous red-giants are known to exhibit regular and semiregular light curves, with periods of tens and hundreds of days, and additional long-term modulations not yet fully understood (Wood et al. 2004). Several mechanisms have been suggested, such as rotational modulation, additional pressure or gravity pulsation modes, mass loss effects induced by companions, amongst others. The space mission CoRoT disclosed the huge asteroseismic potential of G-K giants: the regular patterns due to solar-like oscillations and the progressive shift of frequency of maximum oscillation power were both observed (De Ridder et al. 2009). Further detailed investigations of the pulsational properties allowed asteroseismologists to investigate the internal stellar structure (see Chaplin & Miglio 2013; Hekker & Christensen-Dalsgaard 2017, for reviews).

Surface features and non-radial pulsations are expected to produce changes in the shape of the spectral line profile which can be misinterpreted with velocity shifts. These changes can be measured using spectral line bisectors that are correlated with RV in case of distortion of the lines. The measurements of the bisector require very high resolution spectra and a stable instrument. The absence of variations in the spectral line shape is a necessary condition but it is not sufficient to prove the existence of planetary companion.

Photometric observations are useful to understand the long-period RV variations as they constitute an independent measure of the time scales of rotation and pulsation periods. A photometric variability on the same time scale of the RV variations would immediately exclude the planetary companion hypothesis. Photometric analysis, together with the monitoring of the Ca II H and K lines (measured using the same spectra as to derive RVs) and bisector analysis are very helpful to reject the companion hypothesis and should always be used when possible.

As mentioned before, the pulsations in K giants are excited by p-modes spanning a large interval of periods. The amplitudes of the RV variations are expected to show an atmospheric gradient as it happens for Cepheids (see Fig. 7 in Nardetto et al. 2017). The processes of stellar origin are chromatic, therefore measurements of the RV in more than one spectral band may be helpful to discriminate the origin (stellar or Keplerian) of the observed variations. Pulsations cause light variations, and in this case the photometric amplitudes are also different at visible and infrared wavelengths (Percy et al. 2001).

A similar behaviour is expected in the case of activity, where the variations are due to the difference of temperature between the unperturbed photosphere and the spot. On the contrary the planetary signal is independent from the spectral band, therefore the comparison of the RV amplitude variations in the two bands may provide an effective way to discriminate stellar and Keplerian variations.

In this paper we present the analysis of the RV variations of the giant star TYC 4282-605-1 observed with HARPS-N at the TNG. These observations were obtained within the Global Architecture of Planetary Systems (GAPS, see Covino et al. 2013) observing programme. The GAPS programme started its operations in August 2012 taking advantage of the high performance of the HARPS-N spectrograph (Cosentino et al. 2012), mounted at the Italian telescope TNG in La Palma, Canary Islands.

The observations showed a periodic signal in RV that could be attributed to a planet. Since we cannot exclude a possible alternative explanation, we acquired additional data in the near infrared (NIR) with the GIANO spectrograph (Oliva et al. 2006) at the TNG, to obtain quasi-simultaneous observations in optical and NIR to discriminate between a stellar and Keplerian origin of the periodicity observed in the optical band.

Table 1. Stellar parameters of TYC 4282-605-1 from literature.

Parameters	Value
α (J2000)	22 55 29.2581^a
δ (J2000)	+62 14 20.849^a
B [mag]	12.105 ± 0.01^a
V [mag]	10.58 ± 0.01^a
$B-V$ [mag]	1.52 ± 0.01
J [mag]	7.667 ± 0.023^b
H [mag]	6.963 ± 0.033^b
K [mag]	6.778 ± 0.021^b
μ_α [mas yr^{-1}]	44.2 ± 3.5^c
μ_β [mas yr^{-1}]	6.8 ± 3.5^c
$U_{\rm LSR}$ [km s^{-1}]	−154.4 ± 50.4^d
$V_{\rm LSR}$ [km s^{-1}]	−63.0 ± 17.9^d
$W_{\rm LSR}$ [km s^{-1}]	−48.5 ± 19.0^d

References. $^{(a)}$ Zacharias et al. (2012); $^{(b)}$ Cutri et al. (2003); $^{(c)}$ Høg et al. (2000); $^{(d)}$ this work (see text).

In Sect. 2 we derive the stellar parameters and discuss the chemical analysis. Section 3 describes the observations with HARPS-N, the RV analysis of the collected spectra, the effects of the stellar contribution to RV variation through the study of the bisector as asymmetry indicator and finally the chromospheric emission from Ca II H and K lines. Section 4 describes the photometric analysis. Our methods of extracting the RV in NIR are given in Sect. 5 together with observations, data reduction of the GIANO spectrograph and the consistency between optical and NIR data. Finally, the conclusions are presented in Sect. 6.

2. Stellar properties

2.1. Stellar parameters

TYC 4282-605-1 is a K giant star with a visible magnitude of $V = 10.581 \pm 0.01$ mag (stellar parameters summarised in Table 1) misclassified as an M star in Lépine & Gaidos (2011) and for this reason it was included in the original M stars sample in the GAPS programme. The first collected spectra showed soon its earlier type and low gravity. Notwithstanding that the star was misclassified, we decided to continue monitoring this target because of the large variations of RV observed in the first few observations.

Our HARPS-N data (see Sect. 3) were used to determine the stellar parameters through the higher signal-to-noise ratio (S/N) co-added spectrum with a value of ~400 at 5500 Å. Our analysis yielded a temperature of $T_{\rm eff} = 4300 \pm 50$ K, a surface gravity $\log g = 2.0 \pm 0.2$ dex, a microturbulent velocity $\xi = 1.19 \pm 0.2$ km s^{-1} and an iron abundance of $[{\rm Fe/H}] = -0.07 \pm 0.16$ dex with a method based on measurements of equivalent widths (EWs) that relies on the excitation and ionisation equilibria of Fe lines, explained accurately in Sect. 2.2.

To measure the projected rotational velocity ($v \sin i$), we performed a spectral synthesis using the *synth* driver within MOOG code (version 2014, Sneden 1973) and fixing the stellar parameters ($T_{\rm eff}$, $\log g$, ξ) at the values derived through the EWs method. We followed the prescriptions given by D'Orazi et al. (2011),

Table 2. Stellar parameters of TYC 4282-605-1 derived in this work.

Parameters	Value
Derived from HARPS-N spectra	
$T_{\rm eff}$ (K)	4300 ± 50
log g (dex)	2.0 ± 0.2
ξ (km s^{-1})	1.19 ± 0.2
[Fe/H] (dex)	−0.07 ± 0.16
$v \sin i$ (km s^{-1})	3.0 ± 0.5
Estimated from isochrones[a]	
Mass ($M_\odot$)	0.97 ± 0.03
Radius ($R_\odot$)	16.21 ± 4.01
log L ($L_\odot$)	1.91 ± 0.18
d (pc)	700 ± 143
Age (Gyr)	10.1 ± 0.05

References. (a) Bressan et al. (2012).

and fixed the macroturbulence velocity to the value derived from the relation by Valenti & Fischer (2005). Further details on the procedure of spectral synthesis are given in other works within the GAPS project (see, e.g. Covino et al. 2013; Damasso et al. 2015; Esposito et al. 2014). The resulting $v \sin i$ is reported in Table 2.

For the estimation of the stellar mass, radius, luminosity and age (listed in Table 2) we used the isochrones by Bressan et al. (2012) shown in Fig. 1. From the spectroscopic parameters ($T_{\rm eff}$ and log g) extracted in this work we identified the evolutionary track followed by TYC 4282-605-1, classifying this object as a 10.1 Gyr star, being therefore an old giant star with mass 0.97 ± 0.03 $M_\odot$.

Thanks to the empirical calibration of $T_{\rm eff}$ versus colour and [Fe/H] of giant stars proposed by Alonso et al. (1999) we obtained the bolometric correction ($BC(V) = -0.636 \pm 0.003$, as a function of $T_{\rm eff}$ and [Fe/H]) and the colour excess ($E_{B-V} = 0.24 \pm 0.01$) that allowed us to estimate the distance of the star according to the following equations:

$$M_{\rm bol} = M_{{\rm bol}_\odot} - 2.5 \log \frac{L}{L_\odot}; \quad M_{{\rm bol}_\odot} = 4.75 \tag{1}$$

$$M_{\rm bol} = M_V + BC(V) \tag{2}$$

$$M_V = m_V + 5 - 5 \log d({\rm pc}) - A_V \tag{3}$$

where the total extinction, A_V, is defined as $A_V = 3.1 \times E_{B-V}$, M_V is the absolute magnitude in V band, $m_V = 10.581 \pm 0.01$ is the apparent V magnitude provided by the UCAC4 catalogue and d is the distance of the star measured in parsec. The computation yields the star at a distance of 700 ± 143 pc from the Sun.

Since the star has been observed by *Gaia* and included in the first data release (Gaia Collaboration 2016), we have computed the stellar mass using its *Gaia* parallaxes of $\pi = 2.74 \pm 0.56$ mas using the relation $g = G\frac{M}{R^2}$ where g is measured spectroscopically and R is computed from $L = \sigma T_{\rm eff}^4 4\pi R^2$. The resulting mass is 0.26 ± 0.15 $M_\odot$. Such low mass in unexpected for an evolved giant unless the star has lost substantial fraction of it mass. In this case we should find chemical anomalies that are not evident from our analysis (see Sect. 2.2). Since the discrepancy of our parallax with the *Gaia* one is at only the 2σ level, before applying the Lutz-Kelker correction, we assume a stellar distance of $d = 700 \pm 143$ pc as determined by isochrones.

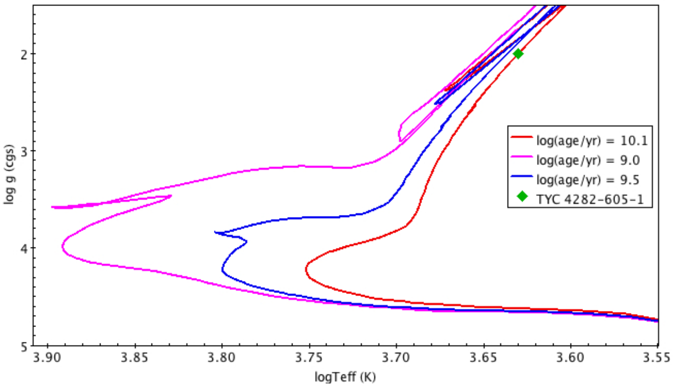

Fig. 1. Isochrones by Bressan et al. (2012) place the target (green diamond) as an old giant star with log (age/yr) = 10.1 (red line). The rest of the estimated parameters (mass, radius, luminosity) are listed in Table 2.

2.2. Chemical analysis

Chemical abundance of individual elements C, Na, Mg, Al, Si, Ca, Ti, Cr, Fe, Ni, Cu, Y, Ba, and La were obtained using the MOOG code together with ATLAS9 atmosphere models (Kurucz 1993), with no overshooting. Abundances of Na, Mg, Al, Si, Ca, and Ni were obtained using lines of the neutral atoms (X I), while for Ti, Cr, and Fe we have exploited lines of both neutral and single ionised species (X II). The lines selected in the chemical analysis of these elements were taken from Maldonado et al. (2015).

For the above mentioned species we have carried out EW analysis, using the driver *abfind* in MOOG; the ARES code (Sousa et al. 2007) has been used to measure EW values, but we have carefully double checked each single spectral feature using the task *splot* in IRAF[1]. For C, Cu, Y, Ba and La we have instead performed spectral synthesis calculations using the driver *synth*, and including hyperfine structure and isotopic splitting, as needed. The abundance of C I has been determined by synthesing the CH band at 4300 Å using the line list by Plez (priv. comm.), whereas for Cu we have used the line at 5782 Å, including HFS information by Steffen (1985). As for neutron-capture elements we have employed lines at 4883.68 Å and 4900.12 Å for Y II, the line at 5853.69 Å for BaII, and LaII lines at 4322.51 Å and 6390.48 Å. We refer the reader to our previous papers for details on oscillator strengths and atomic parameters for these spectral features (e.g. D'Orazi et al. 2012, 2017).

The first step is the determination of the atmospheric parameters and iron abundance by means of the spectroscopic analysis, following the standard procedure. Effective temperature ($T_{\rm eff}$) has been derived by zeroing the slope between abundances from Fe I lines and the excitation potential of the spectral features. Similarly, microturbulence values (ξ) has been obtained imposing no spurious trend between abundances from Fe I and the reduced EWs (that is EW/λ). The surface gravity (log g) comes from the ionisation balance, that is $\Delta[A(\text{Fe II}) - A(\text{Fe I})] = 0$. The solution is reached when all the three conditions are simultaneously satisfied, better than 1σ from the error on slopes for temperature and microturbulence and better than roughly one-third the error bar in FeI and FeII features (i.e. the standard deviation from the mean). We have obtained $T_{\rm eff} = 4300 \pm 50$ K, $\log g = 2.00 \pm 0.2$ dex, $\xi = 1.19 \pm 0.20$ km s^{-1}. By adopting

---

[1] IRAF is the Image Reduction and Analysis Facility, a general purpose software system for the reduction and analysis of astronomical data. IRAF is written and supported by National Optical Astronomy.

Table 3. Derived abundances for TYC 4282-605-1.

Ion	$\langle A(\mathrm{X})\rangle_\odot{}^1$	$\langle A(\mathrm{X})\rangle^1$	n	$[\mathrm{X/Fe}]^2$
C I	8.43 ± 0.07	8.20 ± 0.08	1	−0.23 ± 0.15
Na I	6.38 ± 0.01	6.57 ± 0.04	3	0.26 ± 0.16
Mg I	7.62 ± 0.02	7.91 ± 0.04	2	0.36 ± 0.13
Al I	6.48 ± 0.01	6.82 ± 0.09	2	0.41 ± 0.15
Si I	7.60 ± 0.01	7.78 ± 0.03	13	0.25 ± 0.05
Ca I	6.42 ± 0.02	6.46 ± 0.03	12	0.11 ± 0.18
Ti I	5.02 ± 0.01	4.97 ± 0.02	15	0.02 ± 0.17
Ti II	5.04 ± 0.01	4.91 ± 0.05	5	−0.06 ± 0.06
Cr I	5.68 ± 0.01	5.63 ± 0.03	18	0.02 ± 0.16
Cr II	5.67 ± 0.01	5.67 ± 0.06	3	0.07 ± 0.06
Ni I	6.29 ± 0.01	6.28 ± 0.02	37	0.06 ± 0.05
Cu I	4.25 ± 0.05	4.19 ± 0.07	1	0.01 ± 0.15
Y II	2.19 ± 0.05	2.06 ± 0.04	2	−0.06 ± 0.20
Ba II	2.13 ± 0.05	2.08 ± 0.08	1	0.02 ± 0.25
La II	1.05 ± 0.04	0.97 ± 0.01	2	−0.01 ± 0.20
	$\langle A(\mathrm{X})\rangle_\odot{}^1$	$\langle A(\mathrm{X})\rangle^1$	n	$[\mathrm{Fe/H}]^2$
Fe	7.50 ± 0.01	7.43 ± 0.02	222	−0.07 ± 0.19

Notes. (1) Line-to-line scatter errors as $\sigma\sqrt{n}$, (2) final uncertainties due to the propagation of errors in stellar parameters plus the line-to-line scatter errors.

these atmospheric stellar parameters we have inferred an iron abundance of A(Fe I) = 7.43 ± 0.01 (rms = 0.134, 207 lines) and A(Fe II) = 7.43 ± 0.03 (rms = 0.102, 15 lines)[2].

Our results are reported in Table 3, which includes abundances for the species under scrutiny in this study along with corresponding uncertainty. The solar abundances adopted throughout the manuscript are given in Col. 2 and have been employed to derive the [X/Fe] ratios listed in Col. 5[3]. Two kind of internal (random) errors affect our abundance values, that is errors due to EW measurements (or to the determination of best fit via spectral synthesis) and errors related to atmospheric parameters. For the first source of errors, assuming Gaussian statistics, the line-to-line scatter errors are computed as $\sigma/\sqrt{n}$, where σ is the standard deviation of the derived individual abundances from the n lines. For species for which only one spectral line is available (i.e., Cu and Ba) we have repeated the measurement several times by changing the continuum displacement and other criteria and inspected the corresponding variation in the resulting abundances. In order to estimate uncertainties due to stellar parameters we have instead proceeded in the standard way, that is by varying one parameter at the time and inspecting the corresponding change in the resulting abundance. The total uncertainties for the derived abundances are then calculated by summing in quadrature line-to-line scatter errors and those related to the stellar parameters (Col. 5).

Our findings point to a significant enrichment in the abundances of Na I, Mg I, Al I and Si I while Ca I, Ti I, II, Cr I, II and Ni I are consistent with the solar value. The same result holds for heavy elements (Cu I, Y II, Ba II and La II) for which we retrieve a solar-scaled abundance pattern.

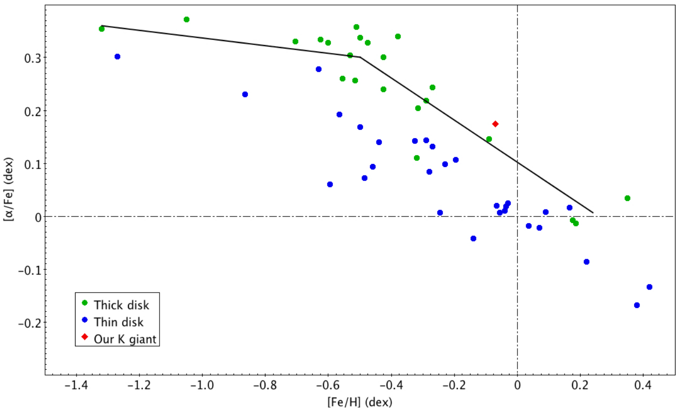

Fig. 2. Mean α-elements abundance ratio ([O, Mg, Si, Ca, Ti/Fe]) as a function of [Fe/H] by Alves-Brito et al. (2010). The symbols are explained in the figure.

To investigate the nature of the enhancement of some of the studied elements we decided to compare our results with the work by Alves-Brito et al. (2010) for a sample of giant stars in the local disk. The authors show a chemical distinction between the local thin and thick disks stars. Their results suggest that the local thick disk stars have α-enhancements relative to solar abundances in K giants higher than those stars located in the local thin disk. As shown in Fig. 2 the [α/Fe] chemical pattern of TYC 4282-605-1 clearly follows the performed linear fit for [α/Fe] vs. [Fe/H] of local thick disk stars. We demonstrated thus that the chemical composition of our target supports that it is an old K giant (age = 10.1 Gyr) belonging to local thick disk.

This result is confirmed by the kinematic velocities. Calculation of the space velocity with respect to the Sun is based on the procedure presented by Johnson & Soderblom (1987), corrected for the effect of differential galactic rotation (Scheffler & Elsasser 1988), by adopting a solar Galactocentric distance of 8.5 kpc and a circular velocity of 220 km s^{-1}. The correction of space velocity to the local standard of rest is based on a solar motion, $(U, V, W)_\odot$ = (10.0, 5.2, 7.2) km s^{-1}, as derived from HIPPARCOS data by Dehnen & Binney (1998). TYC 4282-605-1 shows kinematic properties typical of the thick disk population (see Table 1) following the distributions of the space velocities for the thick disk sample calculated by Bensby et al. (2004).

3. HARPS-N observations and radial velocity analysis

We collected 48 spectra of TYC 4282-605-1 with HARPS-N at TNG in the four seasons from August 2012 to November 2015. Spectra were obtained with an integration time of 900 s and an average S/N of 70 at 5500 Å. The main characteristics of HARPS-N, very similar to HARPS at ESO, are the very high stability, the high spectral resolution of R = 115 000 and the large wavelength coverage from 3800 to 6900 Å.

The reduction of the spectra and the RV measurements were obtained using the latest version (Nov. 2013) of the HARPS-N instrument Data Reduction Software (DRS) pipeline with a K5 binary mask. The measurement of the RVs is based on the weighted cross-correlation function (CCF) method (Baranne et al. 1996; Pepe et al. 2002). In Table A.1, we list the RVs and their corresponding errors. We obtained the first three spectra with the simultaneous Th-Ar calibration lamp, while the rest of the spectra, obtained with a new charge-coupled device (CCD) after the failure of the previous one, were collected with the sky background in the second fiber. We have verified that our results do not change considering or excluding the first

---

[2] The derived abundances are expressed in the usual scale, $A(\mathrm{X}) = \log(N_\mathrm{X}/N_\mathrm{H}) + 12$.

[3] $[\mathrm{X/Fe}] = [\mathrm{X/H}]-[\mathrm{Fe/H}]$, where $[\mathrm{X/H}] = A(\mathrm{X}) - A(\mathrm{X})_\odot$.

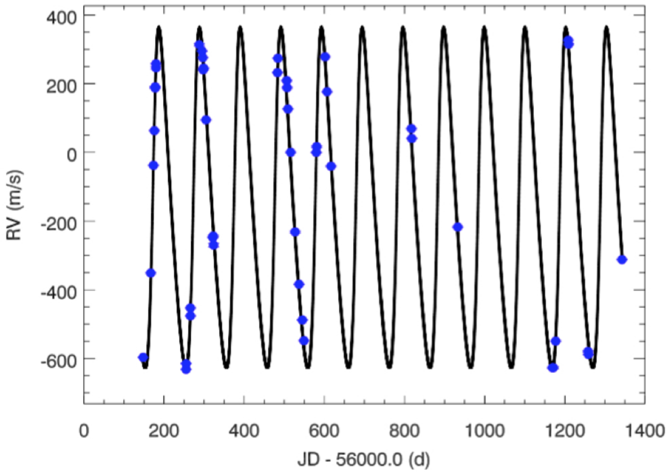

Fig. 3. Radial velocity measurements from the four observing seasons with HARPS-N (blue dots). Removal of median of RV has been applied to the data set before plotting. The curve represents the orbital solution (see Table 4).

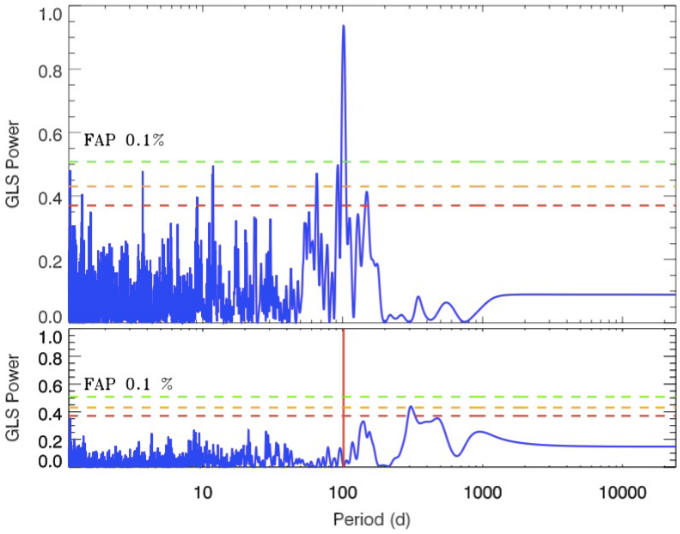

Fig. 4. *Top panel*: GLS periodogram of RVs measured with HARPS-N with a significant peak at 101.54 days, the horizontal dashed lines represent the false alarm probabilities (FAP) of 0.1% (green line), 1% (orange) and 10% (red), respectively. *Botton panel*: periodogram of the residuals data after subtracting the orbital fit. The red solid line indicates the location of the maximum period found with the RV.

three data points, and that a systematic correction offset is not needed. The RV measurements for the four seasons are shown in Fig. 3 after removal of median RV with a standard deviation of 337.5 m s^{-1} much more larger than the average error (1.8 m s^{-1}), pointing to an intrinsic variability.

To detect a possible periodic signal in our data we used the Generalized Lomb-Scargle periodogram (GLS, Zechmeister & Kürster 2009), which is the most common method in case of unevenly spaced times and it is characterised by a simple statical behaviour. The GLS periodogram allows us to identify significant periods in the data which can be used as starting estimates for the algorithm if their amount of power is higher than a confidence level.

The GLS periodogram reveals a clear periodicity with a highly significant peak at period P = 101.54 days in the top panel of Fig. 4 with a power much higher than the lowest false alarm probability (FAP) fixed at 0.1% (green line) and estimated through a bootstrap method with 10 000 iterations. To verify the presence of possible aliasing phenomenon, we plot the window function in Fig. 5 showing that the strong peak around 101 days, corresponding to 0.01 days^{-1} in the domain of frequencies, is not related with a periodicity in the sampling.

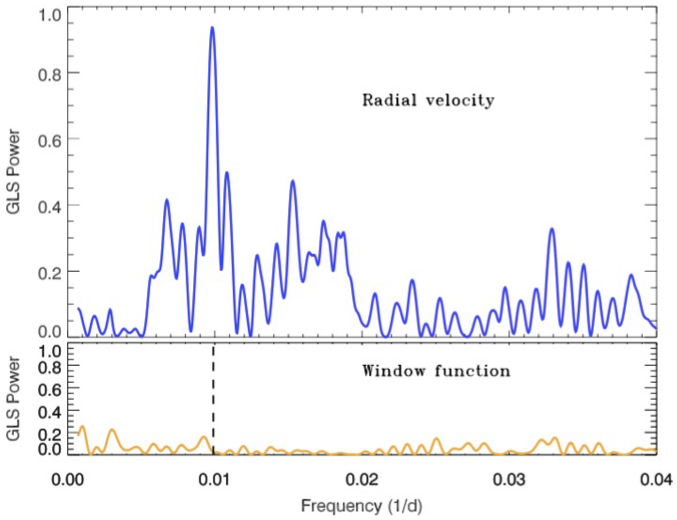

Fig. 5. GLS periodogram of the TYC 4282-605-1 RVs (*upper panel*) and the corresponding window function (*lower panel*). The strong peak found around 101 days corresponds with the value in frequency of 0.01 days^{-1}.

Assuming the companion hypothesis we used the RVLIN code[4] (see Wright & Howard 2009) to obtain the best Keplerian fit and derive the orbital parameters listed in Table 4. The orbital solution and RV data are presented in Fig. 3 as a function of the time.

In order to obtain the residuals data we use the orbital fit to remove the period and its harmonics simultaneously. The periodogram of the residuals (bottom panel of Fig. 4) does not show other significant peaks, but a marginal long term signal between 300−500 days is present. The RV and residuals measurements (rms = 23.02 m s^{-1}) phase-folded are shown in Fig. 6. Our solution resulted in a semi-amplitude, $K_{\rm opt}$ = 495.2 ± 5.1 m s^{-1}, eccentricity, e = 0.28±0.01, semi-major axis, a = 0.422±0.009 AU and a minimum mass for the companion, $M_{\rm P} \sin i$ = 10.78 ± 0.12 $M_{\rm J}$, assuming the stellar mass of 0.97 ± 0.03 $M_{\odot}$ previously derived. We estimated the errors of the derived orbital parameters through a bootstrap (10 000 re-sampling) analysis.

3.1. Bisector analysis

Stellar activity and pulsations can cause deformations in the line profile of the spectral lines producing a shift of the centroid of the line. This effect can be quantified by several asymmetry indicators, including the bisector. In presence of surface inhomogeneities or surface deformations we expect some (anti) correlation between RV and the CCF bisector velocity span (BVS). The top panel of Fig. 7 shows the BVS as a function of the RV measurements. No significant correlation was found with Spearman correlation coefficient of ρ = −0.17. The bottom panel of the same figure shows the correlation between BVS and RV residuals having a value of ρ = 0.47. In Fig. 9 the GLS periodogram of the BVS is shown and no significant peak is found at the

---

[4] The code is available at `http://exoplanets.org/code/`

Table 4. Best fit orbital parameters.

Parameter	Units	Value
P	Period (day)	101.54 ± 0.05
$T_{\rm P}$	Periastron time (JD-2 400 000)	56479.28 ± 0.57
e	Eccentricity	0.28 ± 0.01
ω_*	Argument of periastron (deg)	288.94 ± 2.38
K	RV semi-amplitude (m s^{-1})	495.2 ± 5.1
γ	Systemic velocity (m s^{-1})	−12 361.54 ± 3.58
$M_{\rm P} \sin i$	Minimum mass ($M_{\rm J}$)	10.78 ± 0.12
a	Semi-major axis (AU)	0.422 ± 0.009

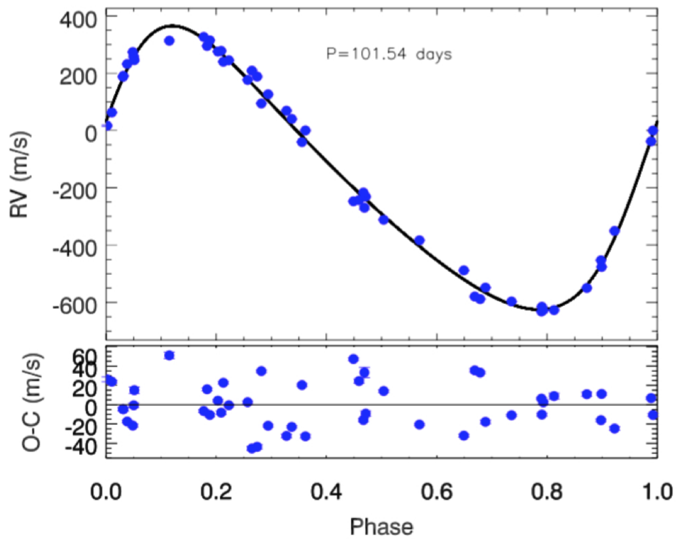

Fig. 6. *Top panel*: radial velocity data of the four observing seasons of HARPS-N phased to the correspond orbital period. The solid line is the orbital solution. *Bottom panel*: residual RV variations after subtracting the orbital solution. The residuals show standard deviation value of 23.02 m s^{-1}.

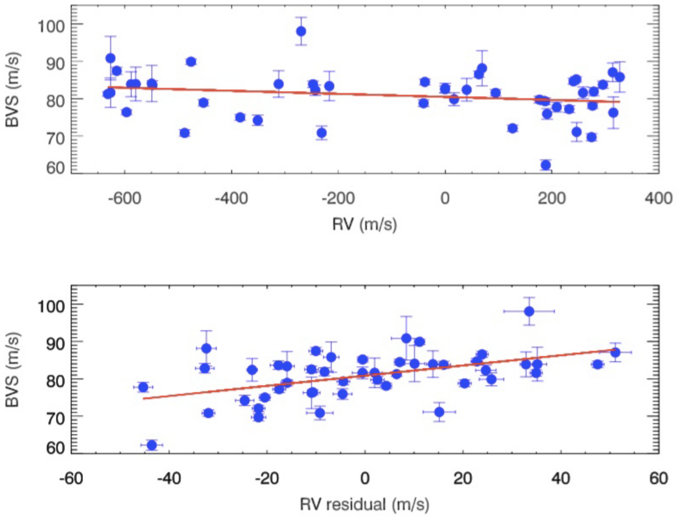

Fig. 7. Correlation between bisector velocity span (BVS) with RV measurements (*top panel*) and with residuals of RV (*bottom panel*).

101 days period, indicating that the modulation found in the RV is probably not connected to stellar activity or pulsations. That instead may be responsible for the long term (>300 days) signal and for the correlation between BVS and RV residuals likely related to the stellar rotation. The lack of a correlation does not imply necessarily the presence of a companion as the origin of the RV periodicity but it is a necessary condition.

3.2. Chromospheric emission, S-index

Stellar activity can produce RV variations and create a signal that could be misinterpreted as an exoplanet. Some apparent RV offsets are related to the magnetic activity of the star and surface features such as spots. Also, the convection patterns of the stellar surface can suffer local or global changes due to the magnetic activity. When a star has a large convection layer hotter and bluer material can emerge from its convection cells (e.g. stellar granulation) and it causes apparent blueshifts to the integrated stellar spectrum (Anglada-Escudé & Butler 2012). For these reasons, one could expect apparent RV jitter whenever the magnetic field of the star experiences changes. One way to disentangle the effects of activity is to measure activity indicators such as the Mount Wilson S-index (Noyes et al. 1984). This index measures the relative flux of the Ca II H and K lines in emission ($\lambda_{\rm K}$ = 3933.664 Å and $\lambda_{\rm H}$ = 3968.470 Å) compared with a local continuum (e.g. Lovis et al. 2011). These lines in emission are formed in the hot plasma of the chromospheres of stars, and their intensity varies with the strength of the stellar magnetic field.

The width of the chromospheric lines in giant stars is larger than in main-sequence stars because of the Wilson-Bappu effect (e.g. Linsky 1980; Park et al. 2013). Nevertheless, their width can still be sensitive to the activity level of the star, that is, to the level of non-thermal heating of its chromosphere, as found by Elgaroy et al. (1997). Therefore, we shall use the chromospheric S-index to look for a possible correlation with the RV variation that can indicate activity as the physical cause of the observed RV modulation, although the sensitivity of the method is lower than in the case of main-sequence stars. We checked that the band passes defined by Lovis et al. (2011) for main-sequence star are adequate for our giant and we used HARPS-TERRA (Template-Enhanced Radial velocity Re-analysis Application) software (Anglada-Escudé & Butler 2012) that incorporates the automatic measurements of the S-index and its corresponding errors using the necessary information provided by the HARPS DRS.

Another argument in favour of the companion interpretation at 101 days is shown in Fig. 8 through the low Spearman correlation coefficient between the S index with RV (ρ = 0.15, in the top panel) and with the RV residuals (ρ = 0.29, middle panel), respectively. Figure 9 shows the GLS periodograms for S index, BVS and residual RVs in order to check that there is not activity effects correlated at 101 days. As a result, the activity has been

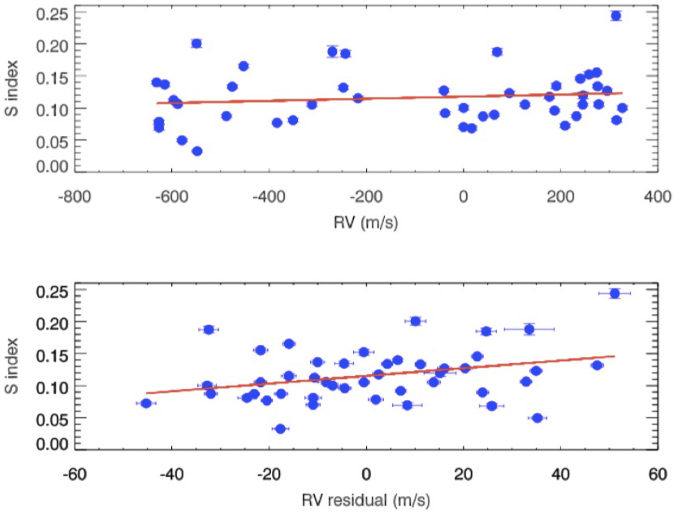

Fig. 8. Correlation between RV (*top panel*) and RV residual (*bottom panel*) with S-index.

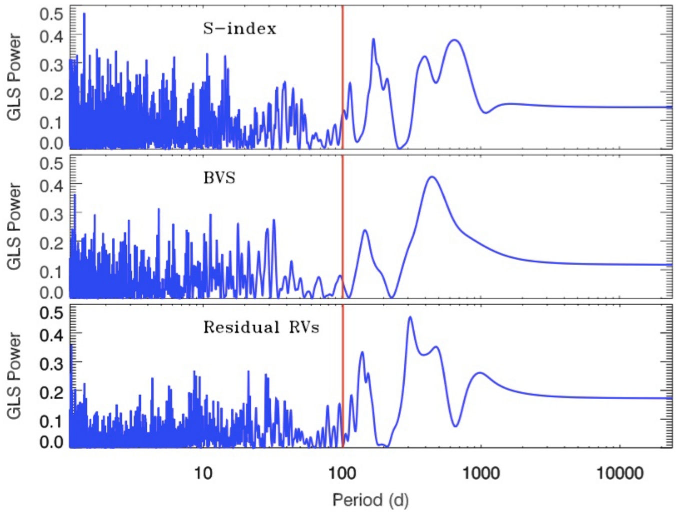

Fig. 9. GLS Periodograms of S index, BVS and residual RV. There is no significant period at 101 days (red line).

excluded as being responsible of the significant signal found in optical band.

3.3. The case of a pulsating star

The physical parameters listed in Table 2 and the RV curve shown in Fig. 6 suggest the possibility that TYC 4282-605-1 is a pulsating star. Therefore, we must discuss it on the basis of what described in Sect. 1.

We note that the RV curve has a reverse shape of that expected from a radial pulsation mode (see Fig. 2 in Nardetto et al. 2017, for a close comparison with the RV curve of δ Cep).

A rising branch steeper than the descending one in the RV curve implies a descending branch steeper than the rising one in the photometric light curve, but such a shape is not very common in pulsating stars. These light curves seem to be confined to few unusual cases, like V1719 Cyg stars. However, these variables show only slight asymmetric RV curves (see Fig. 3 in Poretti & Antonello 1988) and therefore the RV curve of TYC 4282-605-1 would be unique.

The line profiles have also to change during pulsation, to reflect the outward and inward motion of the atmosphere (see Fig. 1 in Nardetto et al. 2017). In particular, variations of the full-width half-maximum (FWHM) and of the bisector span values are expected over the pulsation period. No periodicity has been observed in the bisector spans of TYC 4282-605-1 (Fig. 9). We also analyzed the FWHM values and we did not find any variability as well.

Therefore, the detailed analysis of the HARPS-N spectra does not support pulsation as the cause of the RV curve shown in Fig. 6 upper panel. On the other hand, the scatter observed in the residuals (Fig. 6, lower panel) could be due to solar-like oscillations and/or granulation effects (Kjeldsen & Bedding 2011). For comparative purposes, solar-like oscillations are visible with an amplitude up to 60 $\mathrm{m\,s^{-1}}$ and apparent periodicity around 1 d in HD 170053, a red giant very similar to TYC 4282-605-1 (Poretti et al. 2015). Unfortunately, the time sampling of the HARPS-N spectra of TYC 4282-605-1 is not suitable for detecting amplitude and time scale of such short-period oscillations.

4. Photometric analysis

Any detected photometric variability on the same time scale of the RV variations makes the companion hypothesis questionable (Hatzes 2002). We checked for evidence of a $P \sim 100$ days periodicity in the light curve obtained by the APACHE survey (A PAthway to the Characterization of Habitable Earths, Sozzetti et al. 2013). More than 6350 photometric points in standard Cousin I-band have been collected over three observing seasons between 2012 and 2014, with the time span covering a total of 782 days. The differential light curve was derived by using UCAC4 762-068173, 761-069159, 761-069142 and 762-068154 as comparison stars. For the present analysis we have considered the nightly mean values of the total light curve assuming the standard deviation of the mean as the uncertainty for each binned value. We discarded four nights over a total of 109 because of the photometry scarce quality resulting in errors larger than 0.02 mag. We calculate the GLS periodogram in the frequency range 0.00125–0.1 $\mathrm{d^{-1}}$ (10–800 days) to search for possible periodic modulation, limiting our investigation to periods lower than the observational time span (Fig. 10). The highest peak occurs at $P \sim 530$ days (0.00189 $\mathrm{d^{-1}}$), with p-value = 0.1% estimated through a bootstrap (with re-sampling) analysis. Despite the statistical significance, we cannot conclude anything about the physical nature of this signal, but only ascertain the existence of a possible long-term variability, due to the poor sampling of our dataset and the fact that it does not cover the minimum two cycles necessary for verifying the actual periodic modulation.

However we note that the signal could coincide with the long-term signal found in the activity indicators (bisector, S-index) and present in the residuals of the radial velocity (see Fig. 9) likely linked to the rotation of the star. We note that the light curve (see Fig. 10, second panel) presents an offset between the first season and the rest of the observations. The increase occurring between the first and second season seems to correspond to a decrease of S-index (see upper panel of Fig. 10). This is suggestive of an activity long-term effect, with higher activity during the first season (low photometry and high S-index) and low activity level during the second and third seasons.

What is more relevant here is that the periodogram, that considers the three observing seasons, does not show significant signals at or close to $P \sim 101$ days. The same result is obtained when the observing seasons have been analysed separately and

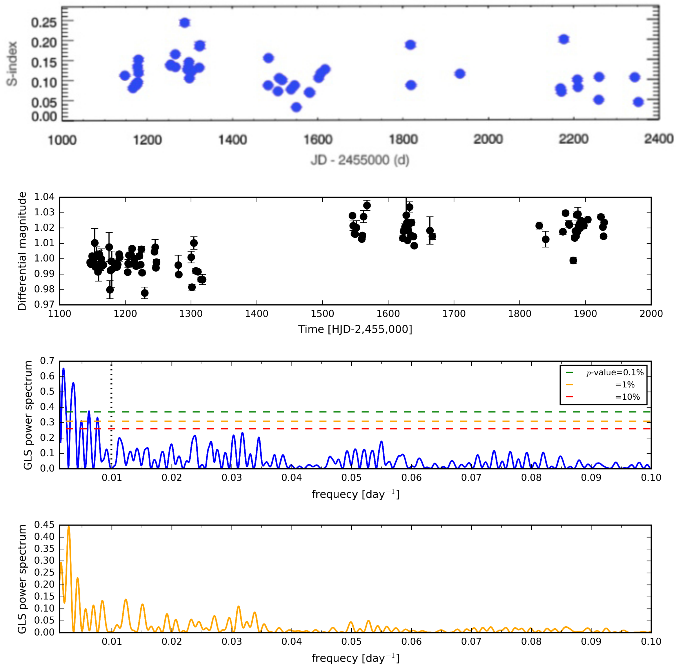

Fig. 10. *Upper panel*: time serie of the S-index. *Middle-upper panel*: differential light curve of TYC 4282-605-1 collected by the APACHE survey. *Middle-bottom panel*: generalized Lomb-Scargle (GLS) periodogram of the differential light curve. The dotted vertical line marks the orbital period of the TYC 4282-605-1 companion. *Bottom panel*: spectral window function of the APACHE observations.

this also occurs for the residuals (not showed). This lack of photometric signal at 101 days is another point against radial pulsation as origin of the RV variability (see Sect. 3.3).

5. GIANO NIR observations

5.1. Observations and data reduction

We have collected seven NIR spectra from May 2015 to August 2015 (time coverage 100 days) with GIANO at the TNG, with the epochs of observation previously selected to optimise the covering phase found with HARPS-N optical data.

GIANO is the NIR high resolution spectrograph of the TNG that was originally designed for direct feeding of light at the Nasmyth-B focus (Oliva et al. 2006). The instrument provides cross dispersed echelle spectroscopy at a resolution of 50 000 over the 0.95–2.45 micron spectral range in a single exposure (Y, J, H and K bands). In July 2012 the spectrometer was provisionally positioned in Nasmyth-A focus fed via fibers (Origlia et al. 2014). The spectrometer was offered to the community in 2015 (TNG call AOT31). In the meantime, a more appropriate interface for direct light-feeding was designed and built, and the spectrograph in the new configuration is now called GIANO-B. This new interface, that also includes a dichroic for simultaneous observations of GIANO-B and HARPS-N (GIARPS, Claudi et al. 2016), was succesfully implemented and commisioned between August 2016 and March 2017.

Our observations were collected with the previous configuration of GIANO. It was fiber-fed with two fibers of 1 arcsec angular diameter at a fixed angular distance of 3 arcsec on sky. An image slicer subdivides the light beam from each fiber so the echellogram is composed by four traces instead of two. A typical 2D output of GIANO can be seen and is explained in detail in Appendix B. The GIANO spectrograph is equipped with a 2048 × 2048 HAWAII-2 detector, allowing us to image almost the whole spectral range over 49 orders, with only small missing regions at the longest wavelengths.

Since GIANO is not equipped yet with a gas absorption cell for high precision radial velocities measurements, we obtained the RVs by using the telluric lines as a reference. However, our method can be easily adapted with absorption cells that are now planned in an upgrade of this instrument.

To extract and wavelength-calibrate the GIANO spectra, we have used the ECHELLE package in IRAF and some new, ad hoc scripts that have been grouped in a package named GIANO TOOLS[5]. The GIANO data reduction manual[6] with a detailed description is available on the TNG website and in Appendix B we reported the main steps followed in the reduction of the spectra obtained with GIANO and used in this work.

Observations of science targets are performed by nodding-on-fiber technique, i.e. target and sky are taken in pairs and alternatively acquired on fiber A and B, respectively, for an optimal subtraction of the detector noise and background. From each pair of exposure, an (A-B) 2D-spectrum is computed and then is extracted and summed to get a final 1D wavelength-calibrated spectrum with the best possible signal-to-noise ratio. The spectra in this work were obtained with 600 s integration time for each nodding.

2D-spectra of halogen lamps are used to map the geometry of the four spectra in each order, for optimal extraction purposes. The four spectra in each order are independently extracted and wavelength-calibrated, to minimise feature smearing in wavelength due to the small distortion of the slit image along the spatial direction. The instrument is stable enough that flat-fields taken during the daytime are perfectly suited for this purpose.

Each extracted spectrum is wavelength-calibrated by using the U-Ne lamp reference spectra taken at the end of the night. We use a set of approximately 30 bright lines (mostly Ne lines) distributed over a few orders to obtain a first fit, then the optimal wavelength solution is computed by using ~300 U-Ne lines distributed over all orders.

5.2. Radial velocity computations

In the computation of the RVs in the NIR an ensemble of interface definition language (IDL) procedures was used. It was created to measure RVs with the Cross Correlation Function (CCF) method (Baranne et al. 1979). A brief summary of the procedure is explained in the following and more details can be found in Carleo et al. (2016).

- Pre-reduction: spectrum normalisation. The first step is to have a uniform wavelength scale of the spectra and it is necessary re-sample the original ones in order to have a constant step in RV and reduce the RV errors. The re-sampling should be made with the same steps for stellar and telluric lines. In order to re-sample the individual order of the input spectrum we make use of a third degree cubic spline interpolation and a continuum normalisation.

- Subtraction of telluric contribution. The goal is to obtain the stellar spectrum cleaned from telluric lines. First a median spectrum of the Earth atmosphere was created in order to

---

[5] Available on `http://www.tng.iac.es/instruments/giano/`

[6] `http://www.bo.astro.it/giano/documents/handbook_giano_v1.2.0.pdf`

Table 5. Measurements of radial velocity with GIANO.

Epoch [BJD]	RV [km s^{-1}]	Error [km s^{-1}]
57 169.709	–12.869	0.016
57 174.706	–13.005	0.026
57 177.701	–12.942	0.017
57 208.728	–12.078	0.014
57 210.714	–12.133	0.017
57 236.601	–12.676	0.021
57 259.755	–12.959	0.014

subtract it from the normalised stellar spectra. In the same way, the telluric spectrum cleaned from stellar contribution is obtained. Therefore, for each science observation we obtained two cleaned spectra: the stellar spectrum without telluric lines, and the telluric spectrum without the stellar contribution, both of them are used in order to derive the stellar and telluric RV.

- Stellar mask. We use the CCF method, correlating the spectrum with a mask. It was necessary to prepare two masks, for the stellar and telluric spectra, respectively. It is important that the same mask is used for all the stellar spectra in order to obtain the variations of RVs rather than in their absolute values. From the re-sampled, normalised and cleaned spectra (star and telluric), we built a list of stellar lines and masks.
- Telluric mask. The line list of the telluric target, just like stellar mask, is obtained by considering the median telluric spectrum. Using the line list obtained with the normalised spectra of the telluric standard it is possible to build the telluric mask. We chose only the telluric lines with a similar intensity to the stellar lines.
- Subtraction of stellar contribution. The stellar and telluric spectra can contaminate each other, therefore we subtract the stellar template in order to obtain telluric spectrum without stellar contribution.
- High precision RVs. The subtraction of the telluric RV from the star RV gives the final RV for each spectrum, $\mathrm{RV} = \mathrm{RV}_{\mathrm{star}} - \mathrm{RV}_{\mathrm{tell}}$ and the internal errors are obtained taking into account the weight of each order and assuming that S/N is given only by statistics of photons. The total error for one specific order is the combination of the telluric and stellar contribution.

The RV errors computed as above vary from epoch to epoch with a mean value about 18 m s^{-1}. The final RV and the corresponding error for each epoch is listed in Table 5.

5.3. Consistency between optical and IR data

In order to confirm or reject the companion hypothesis of the RV variations observed in the K giant, we used a set of high precision optical and NIR RVs to search for consistency between the two wavelength domains.

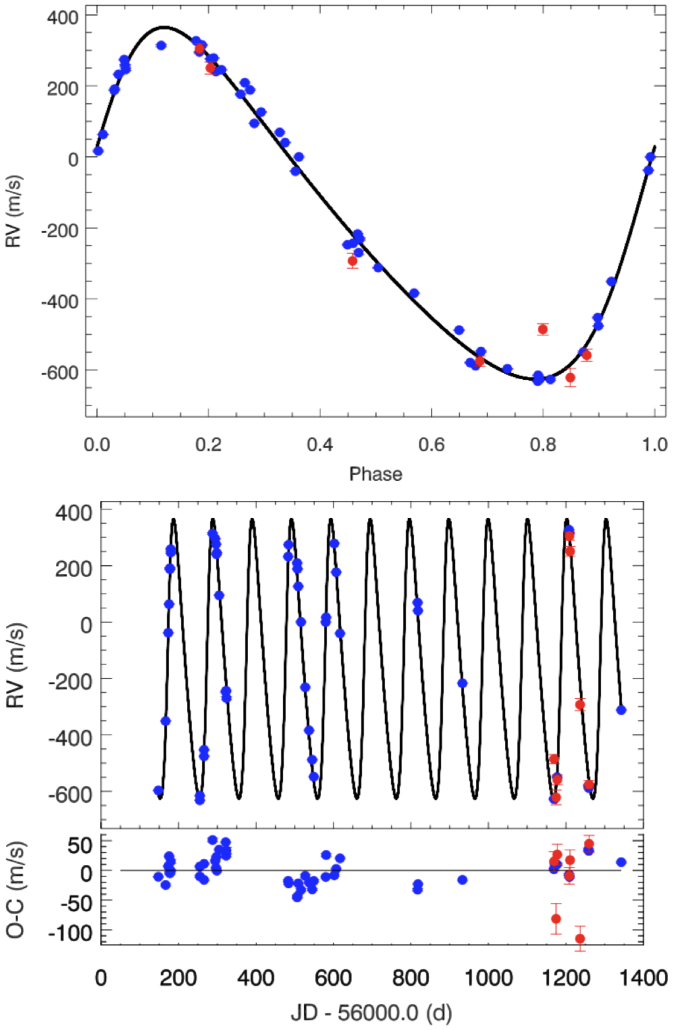

Fig. 11. GIANO NIR radial velocity with red circles and HARPS-N optical RVs with blue circles. The best fit Keplerian model obtained from optical data is plotted with a solid black line. The *top panel* shows the RV data in function of the phase. The *bottom panel* shows the RV as a function of the time and the residuals information. The NIR radial velocities (in red) are in excellent agreement with the optical data (in blue).

The orbital parameters that characterise a Keplerian orbit have been derived from the optical RVs (see Table 4). Because of the smaller number of data points in NIR than in the optical, we only fitted the Keplerian orbit to the GIANO RVs for the RV semi-amplitude (K_{IR}) and systemic velocity (γ_{IR}), keeping the other parameters (P, T_{P}, e) fixed at the values derived from the optical RVs. The obtained values in NIR are $\gamma_{\mathrm{IR}} = -12\,560.42 \pm 6.46$ m s^{-1} and $K_{\mathrm{IR}} = 477.6 \pm 9.5$ m s^{-1}. The different value between center of mass RV (γ) in optical and NIR enables us to determine the offset between the two datasets. It is important to note that before the observations with GIANO, we have simulated several possible strategies in order to have the best phase coverage and number of observations. We obtained the best results concentrating the observations at phases close to the minimum and maximum, with few observations at the other phases.

The seven NIR Doppler points from GIANO plotted in Fig. 11 were corrected by offset and median of RV, but were not used for fitting. In Fig. 11 we find that the GIANO data follow the Keplerian model predicted by HARPS-N RVs. The NIR data have an excellent phase coverage (one full period) and have consistent amplitude (1.5σ) with the optical data. Our results support the hypothesis of an orbiting companion around the K giant star TYC 4282-605-1 with the orbital parameters list on Table 4.

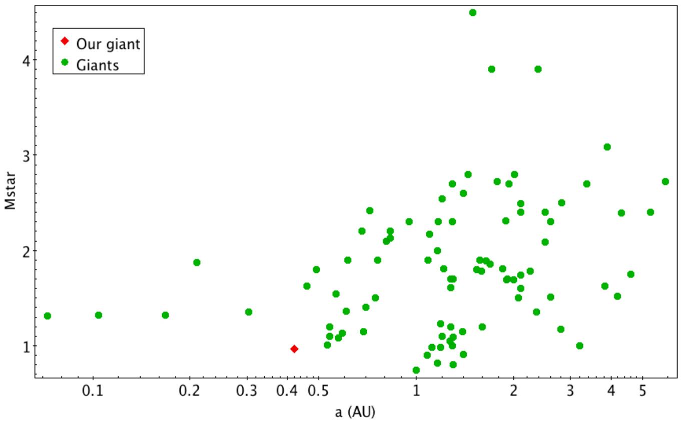

Fig. 12. Observed orbital distance vs. the stellar mass for known planets orbiting giant stars taken from Heidelberg group (`https://www.lsw.uni-heidelberg.de/users/sreffert/giantplanets/giantplanets.php`).

6. Summary and conclusions

We have reported the discovery of a sub-stellar companion around K giant star TYC 4282-605-1. We note that this is the first time that IR+optical RV measurements were used to confirm a planet discovery around a K giant. The main orbital properties are the following: $M_{\rm P} \sin i = 10.78 \pm 0.12$ $M_{\rm J}$; $P = 101.54 \pm 0.05$ days; $e = 0.28 \pm 0.01$; $a = 0.422 \pm 0.009$ AU.

It is possible to establish an upper-limit to the mass of the low-mass companion taking advantage of the knowledge of the eccentricity and imposing that the minimum distance from the star cannot be smaller than the stellar radius (16 $R_\odot$). We obtain an upper limit of 40 $M_{\rm J}$ resulting in a range of mass between 10 and 40 $M_{\rm J}$ for our sub-stellar companion.

Our planet is rather close to its parent star with $a \sin i/R \sim 5$. This poses it close to the limiting value $a/R \sim 3$ that Villaver et al. (2014) estimated from the fast tidal decay of the planetary orbits in their models. Indeed they find that only three planets around red giant branch (RGB) stars have $a/R < 10$ considering the observations collected till September 1st 2013. Our star is less massive than most of the RGB hosts that have masses between 1.2 and 2.8 $M_\odot$ (cf. Fig. 12 in Villaver et al. 2014) so the radius inflation during its ascent along the red giant branch was slower giving a longer remaining lifetime to the planet. The orbit of our planet is significantly eccentric and allows us to apply the theory by Verbunt & Phinney (1995) to estimate the decrease of the eccentricity due to tides inside the red giant host after it left the main sequence. Considering Eqs. (6) and (9) of Verbunt & Phinney (1995), we estimate that $e \sim 0.35$ when the star ended its main-sequence evolution because tides did not have time to circularise and shrink the orbit given that the star was still on the initial phase of the red giant branch ascent. If our star were a red clump giant or were ascending the asymptotic giant branch, that is, if it were a core or shell helium-burning object that previously reached the red giant tip, the planet would have been engulfed during the phase of rapid radius increase during the red giant branch ascent and would not be there. We expect that the planet will be engulfed by the star in the next evolutionary phase and indeed today it is one of the closest planet to its host star (see Fig. 12, see also Fig. 12 in Villaver et al. 2014). In other words, the presence of the planet and its eccentric orbit are a strong argument in favour of our previous estimate of the evolutionary phase and mass of our star.

Our goal was to determine the origin of the periodic variability found with HARPS-N in optical band using also NIR radial velocity measurements. The comparison between the amplitude variations in two different bands allowed us to understand the origin of the periodicity of RV time series.

We obtained NIR RVs with the GIANO spectrograph derived by an ensemble of IDL procedures created to measure RVs with the CCF method. The NIR RVs are in excellent agreement with the optical data obtained with HARPS-N, following the best Keplerian model prediction and being consistent in amplitude. Thus, we confirm the presence of a substellar companion around the giant star after a careful analysis to exclude a stellar origin of the signal thanks to the study of the photometric light curve, the bisector time series and the RV analysis in NIR with GIANO.

In this work we have also studied the chemical abundance of the K giant to explain the nature of the enhancement found for some of α-elements. Based on the study done by Alves-Brito et al. (2010) and the derived kinematic properties for the target, we can conclude that our K giant it is compatible with a star located in the local thick disk.

We have shown the capability of GIANO to discern the presence of a companion around a giant star and further studies would benefit from the ongoing efforts to use HARPS-N and GIANO-B in a simultaneous way. Thanks to the GIARPS project (GIANO-B + HARPS-N) it is possible to take in a single exposure a high resolution spectrum from 0.383 nm to 2.45 nm. This upgrade will make future observations more efficient, providing precious information on the origin of the radial velocity variations.

Acknowledgements. This work was supported by WOW from INAF through the *Progetti Premiali* funding scheme of the Italian Ministry of Education, University, and Research. The research leading to these results has received funding from the European Union Seventh Framework Programme (FP7/2007-2013) under Grant Agreement No. 313014 (ETAEARTH). We thank the referee Artie Hatzes for his useful comments.

References

Alonso, A., Arribas, S., & Martínez-Roger, C. 1999, A&AS, 140, 261
Alves-Brito, A., Meléndez, J., Asplund, M., Ramírez, I., & Yong, D. 2010, A&A, 513, A35
Anglada-Escudé, G., & Butler, R. P. 2012, ApJS, 200, 15
Baranne, A., Mayor, M., & Poncet, J. L. 1979, Vist. Astron., 23, 279
Baranne, A., Queloz, D., Mayor, M., et al. 1996, A&AS, 119, 373
Bensby, T., Feltzing, S., & Lundström, I. 2004, A&A, 421, 969
Bressan, A., Marigo, P., Girardi, L., et al. 2012, MNRAS, 427, 127
Carleo, I., Sanna, N., Gratton, R., et al. 2016, Exper. Astron., 41, 351
Chaplin, W. J., & Miglio, A. 2013, ARA&A, 51, 353
Claudi, R., Benatti, S., Carleo, I., et al. 2016, in Proc. SPIE Conf. Ser., 9908, 99081A
Cosentino, R., Lovis, C., Pepe, F., et al. 2012, in Ground-based and Airborne Instrumentation for Astronomy IV, Proc. SPIE, 8446, 84461V
Covino, E., Esposito, M., Barbieri, M., et al. 2013, A&A, 554, A28
Cutri, R. M., Skrutskie, M. F., van Dyk, S., et al. 2003, VizieR Online Data Catalog: II/246
Damasso, M., Biazzo, K., Bonomo, A. S., et al. 2015, A&A, 575, A111
De Ridder, J., Barban, C., Baudin, F., et al. 2009, Nature, 459, 398
Dehnen, W., & Binney, J. J. 1998, MNRAS, 298, 387
D'Orazi, V., Biazzo, K., & Randich, S. 2011, A&A, 526, A103
D'Orazi, V., Biazzo, K., Desidera, S., et al. 2012, MNRAS, 423, 2789
D'Orazi, V., Desidera, S., Gratton, R. G., et al. 2017, A&A, 598, A19
Dumusque, X., Santos, N. C., Udry, S., Lovis, C., & Bonfils, X. 2011, A&A, 527, A82
Elgaroy, O., Engvold, O., & Joras, P. 1997, A&A, 326, 165
Esposito, M., Covino, E., Mancini, L., et al. 2014, A&A, 564, L13
Gaia Collaboration (Prusti, T., et al.) 2016, A&A, 595, A1
Hatzes, A. P. 2002, Astron. Nachr., 323, 392
Hatzes, A. P., & Cochran, W. D. 2000, AJ, 120, 979
Hekker, S., & Christensen-Dalsgaard, J. 2017, A&ARv, 25, 1

Høg, E., Fabricius, C., Makarov, V. V., et al. 2000, A&A, 355, L27

Johnson, D. R. H., & Soderblom, D. R. 1987, AJ, 93, 864

Kjeldsen, H., & Bedding, T. R. 2011, A&A, 529, L8

Kurucz, R. 1993, ATLAS9 Stellar Atmosphere Programs and 2 km s^{-1} grid, Kurucz CD-ROM No. 13., Cambridge, Mass.: Smithsonian Astrophysical Observatory, 13

Lépine, S., & Gaidos, E. 2011, AJ, 142, 138

Linsky, J. L. 1980, ARA&A, 18, 439

Lovis, C., Dumusque, X., Santos, N. C., et al. 2011, ArXiv e-prints [arXiv:1107.5325]

Maldonado, J., Eiroa, C., Villaver, E., Montesinos, B., & Mora, A. 2015, A&A, 579, A20

Nardetto, N., Poretti, E., Rainer, M., et al. 2017, A&A, 597, A73

Noyes, R. W., Hartmann, L. W., Baliunas, S. L., Duncan, D. K., & Vaughan, A. H. 1984, ApJ, 279, 763

Oliva, E., Origlia, L., Baffa, C., et al. 2006, in Proc. SPIE, 6269, 626919

Origlia, L., Oliva, E., Baffa, C., et al. 2014, in Ground-based and Airborne Instrumentation for Astronomy V, Proc. SPIE, 9147, 91471E

Park, S., Kang, W., Lee, J.-E., & Lee, S.-G. 2013, AJ, 146, 73

Pepe, F., Mayor, M., Galland, F., et al. 2002, A&A, 388, 632

Percy, J. R., Wilson, J. B., & Henry, G. W. 2001, PASP, 113, 983

Poretti, E., & Antonello, E. 1988, A&A, 199, 191

Poretti, E., Mathias, P., Barban, C., et al. 2015, in Asteroseismology of Stellar Populations in the Milky Way, eds. A. Miglio, P. Eggenberger, L. Girardi, & J. Montalbán, Astrophys. Space Sci. Proc., 39, 101

Scheffler, H., & Elsasser, H. 1988, Science, 240, 1680

Sneden, C. 1973, ApJ, 184, 839

Sousa, S. G., Santos, N. C., Israelian, G., Mayor, M., & Monteiro, M. J. P. F. G. 2007, A&A, 469, 783

Sozzetti, A., Bernagozzi, A., Bertolini, E., et al. 2013, in Eur. Phys. J. Web Conf., 47, 03006

Steffen, M. 1985, A&AS, 59, 403

Valenti, J. A., & Fischer, D. A. 2005, ApJS, 159, 141

Verbunt, F., & Phinney, E. S. 1995, A&A, 296, 709

Villaver, E., Livio, M., Mustill, A. J., & Siess, L. 2014, ApJ, 794, 3

Wood, P. R., Olivier, E. A., & Kawaler, S. D. 2004, ApJ, 604, 800

Wright, J. T., & Howard, A. W. 2009, ApJS, 182, 205

Zacharias, N., Finch, C. T., Girard, T. M., et al. 2012, VizieR Online Data Catalog: I/322

Zechmeister, M., & Kürster, M. 2009, A&A, 496, 577

Appendix A: Additional table

Table A.1. Measurements of radial velocity with HARPS-N.

Epoch [JD]	RV [km s^{-1}]	Error [km s^{-1}]
56 147.839	−12.784	0.001
56 166.789	−12.538	0.002
56 173.522	−12.225	0.001
56 175.743	−12.124	0.001
56 177.793	−12.000	0.001
56 177.875	−11.996	0.002
56 179.774	−11.929	0.002
56 179.888	−11.941	0.003
56 254.898	−12.819	0.001
56 254.972	−12.802	0.001
56 265.822	−12.640	0.001
56 265.943	−12.663	0.001
56 287.877	−11.873	0.003
56 294.842	−11.892	0.001
56 296.838	−11.911	0.001
56 297.838	−11.947	0.001
56 298.862	−11.942	0.001
56 304.837	−12.093	0.001
56 321.813	−12.435	0.001
56 322.841	−12.430	0.002
56 323.836	−12.457	0.005
56 483.194	−11.955	0.001
56 484.233	−11.913	0.001
56 506.194	−11.978	0.002
56 507.145	−11.999	0.002
56 509.159	−12.061	0.001
56 516.042	−12.187	0.002
56 527.155	−12.418	0.003
56 537.019	−12.571	0.001
56 545.210	−12.675	0.001
56 549.192	−12.735	0.002
56 580.046	−12.187	0.001
56 581.044	−12.170	0.003
56 602.066	−11.909	0.002
56 606.945	−12.011	0.001
56 616.947	−12.228	0.001
56 817.168	−12.118	0.002
56 818.143	−12.147	0.001
56 932.895	−12.404	0.002
57 169.103	−12.814	0.002
57 171.085	−12.814	0.003
57 177.087	−12.737	0.002
57 208.095	−11.860	0.002
57 209.211	−11.872	0.002
57 258.008	−12.766	0.002
57 258.998	−12.775	0.001
57 342.797	−12.499	0.001
57 350.926	−12.607	0.005

Appendix B: Reducing GIANO spectra

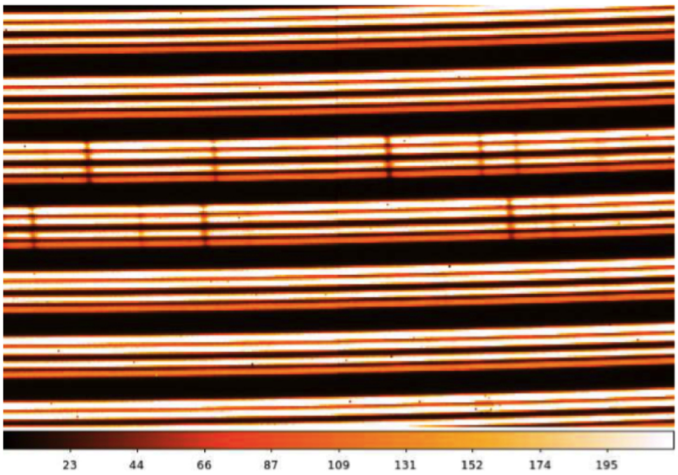

Fig. B.1. Zoom-in on a GIANO image of a continuum lamp. Note that each order is split in four parallel tracks due to the insertion of an image slider that divides the image of the two fibers.

A typical 2D output from a GIANO integration with the previous fibers configuration, is shown in Fig. B.1. The whole frame contains 49 groups of 4 arc-shaped tracks where each group represents a spectral order. Any group is composed of two pairs of arcs, each pair corresponding to the output of one of the two optical fibres used to transfer the signal from the telescope focal plane to the spectrograph. Within each order, wavelength increases from right to left. In addition, wavelength decreases with increasing order. One of the goals of the reduction procedure is to find the curve that best fits the signal peak in each sub-track and to count the signal as a function of position within apertures centred on these curves (called traces). In order to obtain an accurate extraction we need a set of calibration frames (dark frames, flat-field frames and reference lamp spectra) and follow the following steps:

- Dark and frame subtraction. Dark subtraction is only needed by flat-fields and lamp reference spectra. The dark frames to subtract, must have been taken with the same integration time as the image to be corrected. We have to combine all the dark with the same integration time and then subtract the final image from all the calibration files (flats and UNe).
  It is important to remember that the images taken in cycle AB do not need the dark subtraction but it is necessary to remove any residual scattered and diffuse light contribution. For these reasons we subtract frame B from frame A for every target taken in cycle AB and the resulting 2D spectra will exhibit the target signal in all sub-tracks and have most of the bias removed. If there are more than one subtracted AB pair of frames from the same target we have to combine them together before extracting the spectra.
  Then, it is necessary to apply bad-pixel corrections to all flat-field frames, calibration-lamp frames and A-B frames. The correction can be done by using the GIANO TOOLS task called CLEAN-UP.

- Flat-field correction. The spectrograph efficiency varies with the spectral order and produce differences in peak counts between the four tracks of each order due to the different efficiencies of the two fibres and the positioning of the source in the fibre.
  CCDs and NIR detectors exhibit pixel-to-pixel variations in their quantum efficiency. These need being corrected in order to increase the signal-to-noise ratio. The issue is more complicated for images of echelle spectra, due to the large fraction of the detector area (between orders) exposed to a very low flux. To avoid various degrading effects on the noise

statistics, flat-field corrections should only be made inside each aperture.

There are two possibles ways of flat-field spectra correction:

- Construct a 2D flat-field map by deriving a flat-field correction only inside the apertures and divide each frame by this map.

- Extract the 1D spectrum from each aperture of the flat-field image, normalise it, and divide all extracted (1D) unflatted spectra by the corresponding normalised flat-field 1D spectra.

Here we described the 2D technique because making a 2D flat-field frame allows us to define the traces for all orders and check that the subsequent spectrum extraction works. Both methods are equivalent and the same results are obtained.

First of all, we have to combine together all flat-field frames to enhance the signal-to-noise ratio. This is the image we will use to construct the 2D flat-field map and also to find and fit the traces.

- Find traces. Following the previous step a final average flat-field image that has the highest signal-to-noise ratio is obtained. Then we fit polynomials to the signal tracks because these polynomials define the traces associated to each track. An intermediate step is necessary in order to remove the scattered component because a high level of scattered light can drive small spurious peaks between the central orders exhibiting more counts than the peaks at the highest order. Using the task GIANO FIND TRACE it is possible to construct the scattered light map necessary as a reference file when we will determine the traces.

- Fit traces and construct a 2D flat-field frame. It is necessary to derive a polynomial curve fitting the corresponding signal across the detector by using APFLATTEN. It determine the traces that will be used to extract the spectra from any frame. This IRAF task allows us to check the trace and spectrum fits when we follow the procedure and it gives a final image corresponding with a normalised flat frame.
  Then we have to correct all the images (lamp spectra and science frame) dividing (pixel by pixel) each frame by the normalised flat.

- Cloning frame. There are 196 traces and 49 orders on the detection (four traces for each order). In fact, for each order there is a bottom trace, a mid-lower one, a mid-upper one and a topmost one. Each trace must be extract and calibrate independently to obtain four 1D for each detection. For this reason we need to make four copies of each detection. The task to use is $copyfile$ of GIANO TOOLS. We do the same for the lamp, obtaining four sets of frames for the four different traces.

- Spectrum extraction. The task used for extracting spectra is DOECSLIT. However, we first need to run APEDIT in order to associate the traces already found in the flat-field frame to science frame through GIANO FIND TRACE and APFLATTEN.
  Before to run APEDIT, we have to split the traces found and re-arrange them in the correct order. To this purpose, we use the GIANO TOOLS task SPLIT FILE operating on the non normalised flat-field frame. The output of this task are four sets of frames for the flat (lower, middown, midup and topmost).
  The next step is to run APEDIT and check that the aperture locations have been set correctly for each frame. We must run APEDIT for all the four track group (lowest, middown, midup and topmost), so that every frame will have its trace set associated.
  The next step is DOECSLIT to extract and wavelength calibrate the 1D spectra. This task also has to be done four times, for the four groups of frames. The output file is the extracted spectra in 1D.

- Combining the extracted 1D spectra together. At this point, we have four different 1D spectra for each target. It is necessary to combine them together to increase the S/N. The output of each fibre is split into two spots, both feeding the slit. This means that the exposure time is exactly that of the single A or B frame after summing together the pair of 1D spectra corresponding to the same fibre. Consequently, if we add together all four 1D spectra extracted from an AB subtracted frame, the effective exposure time will be twice that of the single A or B frame. If you average together the four 1D spectra, the exposure time will be half that of the single A or B frame.

Appendix D

AD Leo: From RV measurements to 'technical' problems

This document is aimed to show how the radial velocity (RV) analysis of AD Leo, acquired with GIANO-B, reflects some issues due to different causes that I describe below. Table D.1 lists all the available spectra for this star.

The first 4 dates have been eliminated from the RV analysis, since the K band is completely lost because of a possible presence of a plexiglass piece in the optical path that shaded the whole K band.
I performed the RV measurement for the remaining spectra and I found some anomalous RV values (shifts of 3-10 km s^{-1} from the average, much greater than the slit's width), both for telluric and stellar spectra, in specific nights (see Table D.2), in particular 12-13-15-27-29 May.

In order to understand the origin of these shifts in RV values, I performed a deeper analysis, checking the raw data, that allowed to point out some tricky points regarding the data reduction and the instrumental stability. I list these points in the following :

- *Data reduction*:
  - The reduced data on the TNG archive are those of the online pipeline. It means that the wavelength calibration is performed with the last (in time) available UNe lamp: if we are in the middle of an observing run the lamp would be that one of one night before, but when GIANO-B is not used for the observations, the UNe lamp could be that one of some days or weeks before.
  - Some nights (15 and 27 May) the UNe lamp was not acquired, so the reduction was performed by GOFIO with the last (2 and 10 days before, respectively) available lamp.
  - For some reason, the night of 13 May was reduced by GOFIO with the lamp of 09 May, even if some closest lamps were available.
  - Some spectra (e.g. 29 May) was reduced by GOFIO with an UNe lamp without any features (the information about the used lamp are stored in the file headers).
- *Instrumental stability*

Table D.1: Available spectra of AD Leo.

Date	JD	Baricentric Correction ($\mathrm{km\ s^{-1}}$)	airmass
04apr18	2458212.94627310	-20.5708	1.01
05apr18	2458213.94841430	-20.9365	1.01
06apr18	2458214.90298610	-21.1652	1.03
07apr18	2458215.94186340	-21.6198	1.01
29apr18	2458237.91968750	-27.3526	1.05
29apr18	2458238.03403940	-27.5863	1.64
04may18	2458242.91452550	-28.1355	1.06
04may18	2458242.99109950	-28.2979	1.37
05may18	2458243.99938660	-28.4454	1.46
06may18	2458244.91037040	-28.3898	1.06
06may18	2458244.98145830	-28.5405	1.34
07may18	2458245.93034720	-28.5559	1.12
09may18	2458247.93925930	-28.7898	1.17
09may18	2458247.99173610	-28.8864	1.48
10may18	2458248.93605320	-28.8719	1.17
10may18	2458248.98645830	-28.9774	1.46
12may18	2458250.92091440	-29.0188	1.13
12may18	2458250.99048610	-29.1427	1.55
13may18	2458251.93503470	-29.1082	1.20
13may18	2458251.99835650	-29.2141	1.67
15may18	2458253.88331020	-29.1075	1.06
15may18	2458253.97953700	-29.2943	1.52
27may18	2458265.87480320	-29.0349	1.12
27may18	2458265.89281250	-29.0709	1.18
27may18	2458265.95613430	-29.1721	1.62
28may18	2458266.87836810	-28.9938	1.14
28may18	2458266.89186340	-29.0197	1.19
28may18	2458266.90011570	-29.0348	1.22
29may18	2458267.88613430	-28.9363	1.17
29may18	2458267.95429400	-29.0432	1.66
30may18	2458268.89476850	-28.8801	1.22
31may18	2458269.89490740	-28.8001	1.24
05jun18	2458274.89364580	-28.2804	1.30
07jun18	2458276.89237270	-28.0161	1.33
09jun18	2458278.93276620	-27.7709	1.78

Table D.2: Radial velocities of AD Leo for each observing night, with the corresponding Julian date, stellar RV and telluric RV.

Night Date	JD	RV (km s^{-1})	RVstar (km s^{-1})	RVtell (km s^{-1})
29apr18	2458237.91968750	0.4446	0.2385	-0.2061
29apr18	2458238.03403940	0.3908	-0.0107	-0.4015
04may18	2458242.91452550	0.3681	-0.0799	-0.4480
04may18	2458242.99109950	0.3569	0.3346	-0.0223
05may18	2458243.99938660	0.4015	0.2730	-0.1285
06may18	2458244.91037040	0.4014	0.3867	-0.0147
06may18	2458244.98145830	0.3520	0.3390	-0.0130
07may18	2458245.93034720	0.3825	0.2775	-0.1050
09may18	2458247.93925930	0.4163	0.2526	-0.1637
09may18	2458247.99173610	0.3688	0.3279	-0.0409
10may18	2458248.93605320	0.4051	0.4501	0.0450
12may18	2458250.92091440	1.0437	-11.1650	-12.2087
12may18	2458250.99048610	0.9159	-11.9642	-12.8801
13may18	2458251.93503470	0.4066	-10.8026	-11.2092
13may18	2458251.99835650	0.3793	-11.0562	-11.4355
15may18	2458253.88331020	1.1090	-3.4518	-4.5609
15may18	2458253.97953700	1.1026	-3.0758	-4.1784
27may18	2458265.87480320	0.3857	8.3342	7.9484
27may18	2458265.89281250	0.8961	8.1596	7.2635
27may18	2458265.95613430	0.4031	8.3280	7.9249
28may18	2458266.87836810	0.2673	-0.5249	-0.7921
28may18	2458266.89186340	0.2698	-0.1819	-0.4516
28may18	2458266.90011570	0.2686	-0.1935	-0.4621
29may18	2458267.88613430	0.1930	7.5703	7.3773
29may18	2458267.95429400	0.2726	7.8576	7.5849
30may18	2458268.89476850	0.2714	-0.1759	-0.4473
31may18	2458269.89490740	0.2809	-0.1935	-0.4744
05jun18	2458274.89364580	0.2751	-0.0806	-0.3556
07jun18	2458276.89237270	0.2580	-0.3127	-0.5708
09jun18	2458278.93276620	0.2905	0.0642	-0.2263

Table D.3: This table lists the lamp used by the online reduction for each observing night, the shifts in pixel position of the UNe lamp acquired at the end of the observing night and the shifts in pixel position of the tellurics of the observing night. Three dates (10-12-28 May) have not been reduced from online GOFIO. For 15 and 27 May observing nights the corrisponding UNe lamps have no features.

Night Date	Lamp used in online GOFIO (night date)	Lamp Position of the corresponding night (x,y)	Telluric position (x,y)	Notes
29apr18	27apr18	427, 538	895, 868	
04may18	03may18	427, 538	895, 868	
05may18	04may18	427, 538	895, 868	
06may18	05may18	427, 538	895, 868	
07may18	06may18	427, 538	895, 868	
09may18	08may18	427, 538	895, 868	
10may18	-	427, 538	895, 868	No reduced data
12may18	-	431, 538	899, 868	No reduced data
13may18	09may18	431, 538	899, 868	
15may18	13may18	-	896, 868	15may18 (empty lamp)
27may18	16may18 (empty)	-	892, 873	27may18 (empty lamp)
28may18	-	424, 545	892, 873	No reduced data
29may18	28may18 (empty)	424, 545	892, 873	
30may18	29may18	424, 545	892, 873	
31may18	29may18	424, 545	892, 873	
05jun18	03jun18	424, 545	892, 873	
07jun18	06jun18	424, 545	892, 873	
09jun18	08jun18	424, 545	892, 873	

I checked the pixel position of a specific feature of the UNe lamps and found out that they have shifts in specific periods. I also checked the pixel position of a specific feature of the tellurics, in order to understand if these shifts affected both the lamp and the scientific spectra or only one of these. Table D.3 shows the pixel positions for each lamp and for each telluric in the same night. The shifts affect both lamp and telluric spectra. There is a jump in x direction on 12 May, another little shift in x on 15 May, and then a jump both in x and y directions on 27 May. In two cases, 15 and 27 May, the lamp was not available, so only the shift of the tellurics is reported.
I'd like to stress that the correct lamp to use for each observation is that one acquired at the end of the night, while it is clear form the table that this is not the case. Considering that one pixel is 3 km s^{-1}, the shifts in pixel (Table D.3) perfectly correspond to the shifts in RVs (Table D.2).

D.1 Actions

D.1.1 27-28-29 May

From the Table D.2 we see that the three nights (27-28-29 May) have alternating RV shifts, while do not have any pixel shift (Table D.3). In this case the problem is the lamp used for the wavelength calibration. The night of 29 May was reduced by GOFIO with the lamp of 27 May (namely GIANO-B.2018-05-28T05-06-35), which has no features. I performed a new reduction with the lamp of the same night (GIANO-B.2018-05-30T05-03-11) and the shift disappeared. The night of 27 May was reduced by GOFIO with the lamp of 10 days before (GIANO-B.2018-05-16T08-40-47), that is empty (no features). Since I could not perform a new reduction with the lamp of the same night, that results empty too, I reduced the spectra using the lamp of 28 May (GIANO-B.2018-05-29T04-26-40). The shift disappeared. Fig. D.1 and Fig. D.2 show the situation before and after my new reduction, respectively. In praticular a zoom of three spectra (10 May, 27 May, 29 May) is plotted: in Fig. D.1 the three spectra as downloaded from the TNG archive, in Fig. D.2 the three spectra after my new reduction of 27 and 29 May spectra, with the night of 10 May as reference.

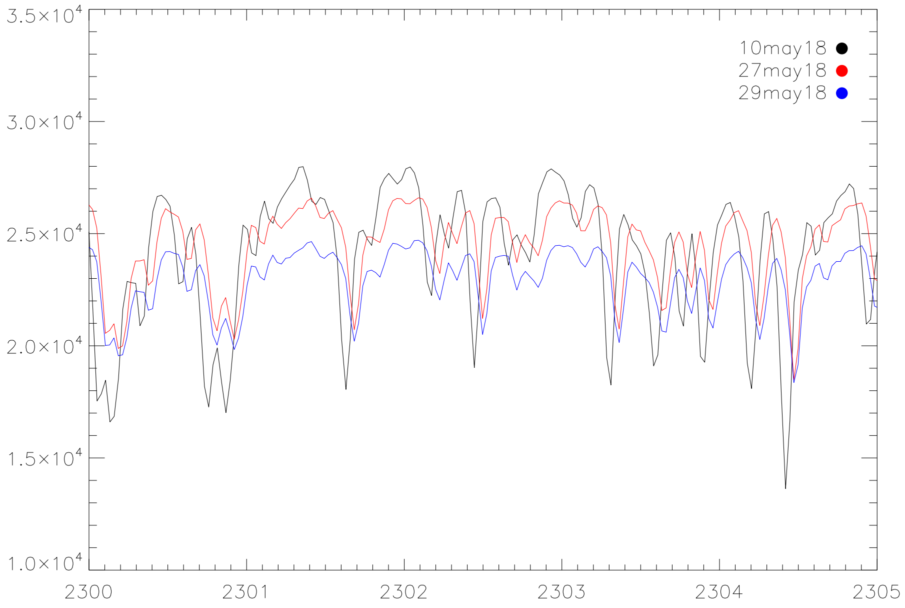

Figure D.1: Spectra of 10 May ('good' night), 27 and 29 May as downloaded from TNG archive.

D.1.2 12-13-15 May

The night of 12 May was not reduced by GOFIO online, so I reduced the spectra with the lamp of the same night (GIANO-B.2018-05-13T05-51-44), but the RVs show a shift. So I tried a reduction with the lamp of 09 May (GIANO-B.2018-05-10T04-17-59). The shift remains. The night of 13 May was reduced by GOFIO with the lamp of 09 May (GIANO-B.2018-05-10T04-17-59), so I reduced the spectra with the lamp of the same night. The shift remains.

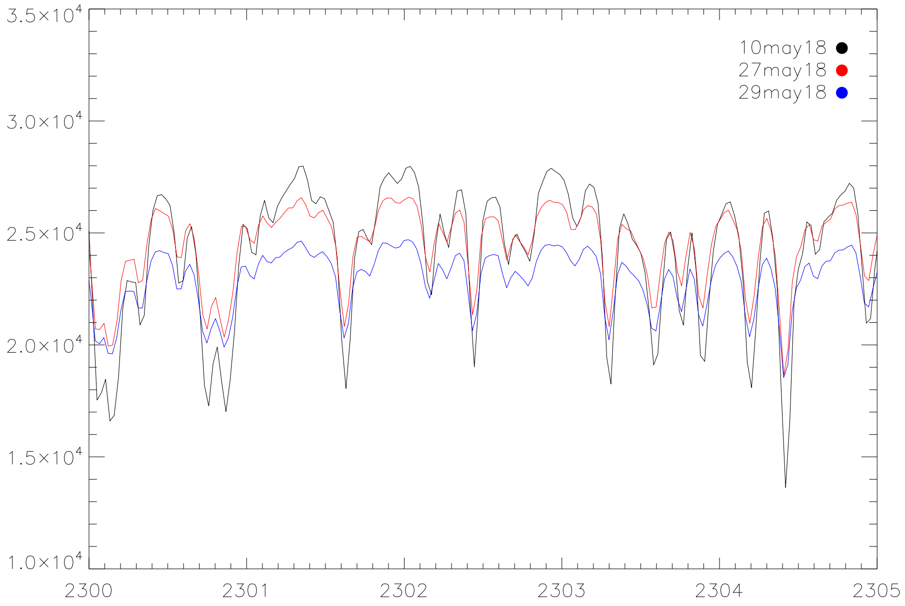

Figure D.2: Spectra of 10 May ('good' night) and 27 and 29 May after my new reduction.

The night of 15 May was reduced by GOFIO with the lamp of the 13 May night (GIANO-B.2018-05-14T05-36-29). Since the lamp of the same night is empty, I tried the reduction of the spectra with the lamp of 14 May (GIANO-B.2018-05-15T05-40-29) and the lamp of 28 May (GIANO-B.2018-05-29T04-26-40). The shift changes in both cases but doesn't match with the 'good' nights. These three dates cannot be used for the RV calculation, since the wavelength calibration is not reliable.

D.1.3 New RV calculation with the TNG archive spectra

Since it seems that there are two different instrumental configurations before and after the period 12-15 May, the final analysis of AD Leo was performed considering two different datasets: the first one from 29 Apr to 10 May 2018, and the second one from 27 May to 9 Jun 2018. As these two periods seem to be stable, I used the automatic reduced data from TNG archive (that means the lamp used for the wavelength calibration is that one of one or two days before the observing night). The RVs of these two datasets don't show any large shift in RVs (Table D.4), even if the lamp used was not the correct one. To note that during this last step I discovered an additional spectrum of 10 May that I didn't consider before, and I added it in the analysis.

D.1.4 New RV calculation with the re-reduced spectra

A further check was performed: I reduced the first dataset of AD Leo (from 29 Apr to 10 May 2018) with the corresponding lamp acquired at the end of the observing night. Fig. D.3 shows the GIANO-B RVs from the spectra from TNG archive reduced with the lamp of one or two nights before the observing night (green points) and the GIANO-B RVs reduced with the lamp of the same night (red points). The two GIANO-B RV measurements are consistent

Table D.4: New radial velocities of AD Leo for each observing night, with the corresponding Julian date, stellar RV and telluric RV.

Night Date	JD	RV ($km\ s^{-1}$)	RVstar ($km\ s^{-1}$)	RVtell ($km\ s^{-1}$)
29apr18	2458237.9196875	0.2608	0.1161	-0.1447
29apr18	2458238.0340394	0.1945	-0.1719	-0.3664
04may18	2458242.9145255	0.1767	-0.2651	-0.4418
04may18	2458242.9910995	0.1475	0.1208	-0.0268
05may18	2458243.9993866	0.1562	0.0283	-0.1279
06may18	2458244.9103704	0.1586	0.1594	0.0008
06may18	2458244.9814583	0.1426	0.1447	0.0022
07may18	2458245.9303472	0.1402	0.0036	-0.1366
09may18	2458247.9392593	0.1402	-0.0276	-0.1678
09may18	2458247.9917361	0.1001	-0.0086	-0.1087
10may18	2458248.9360532	0.0791	0.0649	-0.0141
10may18	2458248.9864583	0.0295	0.0040	-0.0255
27may18	2458265.8748032	0.5739	0.0110	-0.5629
27may18	2458265.8928125	0.5780	-0.0295	-0.6075
27may18	2458265.9561343	0.5392	0.0495	-0.4897
28may18	2458266.8783681	0.5407	-0.3430	-0.8837
28may18	2458266.8918634	0.5008	-0.0543	-0.5551
28may18	2458266.9001157	0.5134	-0.0512	-0.5646
29may18	2458267.8861343	0.5618	0.3468	-0.2149
29may18	2458267.9542940	0.5418	0.3700	-0.1718
30may18	2458268.8947685	0.5324	0.0419	-0.4905
31may18	2458269.8949074	0.5475	0.0420	-0.5055
05jun18	2458274.8936458	0.5350	0.1158	-0.4192
07jun18	2458276.8923727	0.5094	-0.1487	-0.6582
09jun18	2458278.9327662	0.4922	0.1909	-0.3013

within the error bars.

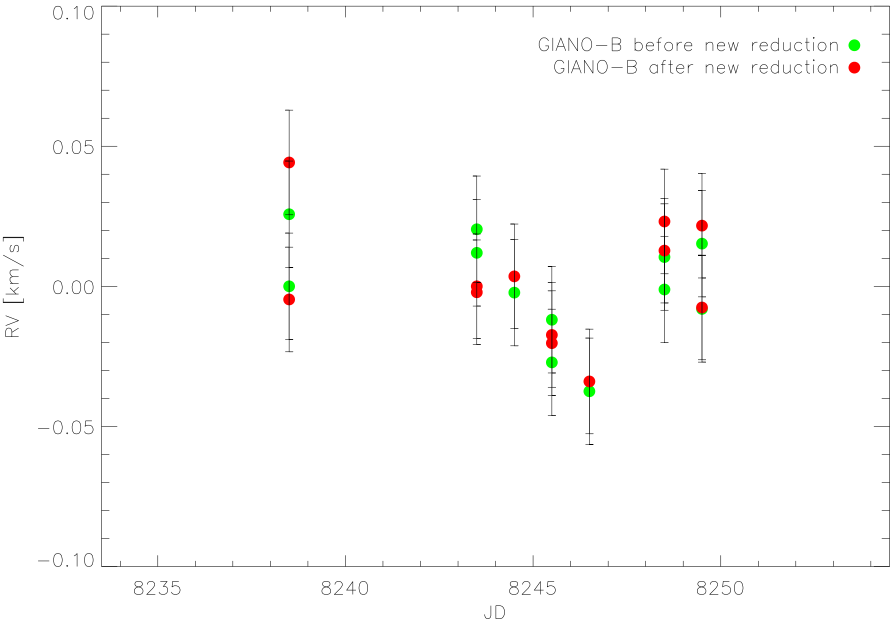

Figure D.3: Comparison between the GIANO-B RVs of AD Leo from the TNG archive (green points) and from the data reduced with the lamp of the end of the night (red points).

I can conclude that, when GIANO-B has a stable period, the lamp used for the wavelength calibration can be taken within few nights from the observing night.

D.2 Conclusions

It is known that the high precision RVs need a precise wavelength calibration. My analysis aimed to understand anomalous RV values of AD Leo (a star of GAPS-2 sample) that are very discrepant from the average. Concluding:

- There are some periods during which the instrument was not stable. We attested that technical operations, including the whole system alignment, were performed. It is important to inform the scientific community about possible technical operation, since in this case it is not a possible to threat a dataset as only one.

- Some nights were reduced with lamps very far from the observing nights. That caused RV shifts. It is crucial to reduce the spectra with the lamp of the same night (end of the night). If that is not possible, the lamp should be the closest lamp (maximum few nights). A set of GIANO-B calibrations could be acquired even if GIANO-B will not be operative during the night, in order to always have the 'closest' lamp.

- The TNG archive has the data reduced by the online pipeline, that means the spectra are reduced with the lamp of the latest night. Those data are often useless and the user needs to reduce everything again. The archive from which a user downloads reduced data should contain the data reduced with the lamp of the same observing night.

Bibliography

Albrecht, S., Winn, J. N., Johnson, J. A., et al. 2012, ApJ, 757, 18

Anglada-Escudé, G., Amado, P. J., Barnes, J., et al. 2016, Nature, 536, 437

Anglada-Escudé, G., Boss, A. P., Weinberger, A. J., et al. 2012, ApJ, 746, 37

Anglada-Escudé, G. & Butler, R. P. 2012, ApJS, 200, 15

Bailes, M. 1996, in Astronomical Society of the Pacific Conference Series, Vol. 105, IAU Colloq. 160: Pulsars: Problems and Progress, ed. S. Johnston, M. A. Walker, & M. Bailes, 3–+

Bailey, III, J. I., White, R. J., Blake, C. H., et al. 2012, ApJ, 749, 16

Baranne, A., Mayor, M., & Poncet, J. L. 1979, Vistas in Astronomy, 23, 279

Barman, T. S., Hauschildt, P. H., & Allard, F. 2005, ApJ, 632, 1132

Baruteau, C., Crida, A., Paardekooper, S.-J., et al. 2014, Protostars and Planets VI, 667

Batten, A. H. 1983, Bulletin d'Information du Centre de Donnees Stellaires, 24, 3

Batygin, K., Bodenheimer, P. H., & Laughlin, G. P. 2016, ApJ, 829, 114

Bean, J. L., Seifahrt, A., Hartman, H., et al. 2010, ApJ, 713, 410

Beaulieu, J. P., Kipping, D. M., Batista, V., et al. 2010, MNRAS, 409, 963

Bell, C. P. M., Mamajek, E. E., & Naylor, T. 2015, MNRAS, 454, 593

Benatti, S. 2018, Geosciences, 8, 289

Berta, Z. K., Irwin, J., Charbonneau, D., Burke, C. J., & Falco, E. E. 2012, AJ, 144, 145

Birkby, J. L., de Kok, R. J., Brogi, M., et al. 2013, MNRAS, 436, L35

Bitsch, B., Crida, A., Libert, A.-S., & Lega, E. 2013, A&A, 555, A124

Blake, C. & Shaw, M. 2011a, in AAS/Division for Extreme Solar Systems Abstracts, Vol. 2, 20.13

Blake, C. H. & Shaw, M. M. 2011b, PASP, 123, 1302

Boisse, I., Bonfils, X., & Santos, N. C. 2012, A&A, 545, A109

Boisse, I., Bouchy, F., Hébrard, G., et al. 2011, A&A, 528, A4

Bonfils, X., Bouchy, F., Delfosse, X., et al. 2013a, in European Physical Journal Web of Conferences, Vol. 47, 05004

Bonfils, X., Delfosse, X., Udry, S., et al. 2013b, A&A, 549, A109

Boss, A. P. 1995, in Bulletin of the American Astronomical Society, Vol. 27, American Astronomical Society Meeting Abstracts, 1379

Boss, A. P. 1997, Science, 276, 1836

Bouchy, F., Doyon, R., Artigau, É., et al. 2017, The Messenger, 169, 21

Brogi, M., Giacobbe, P., Guilluy, G., et al. 2018, ArXiv e-prints [e-print[arXiv]1801.09569]

Caccin, B., Cavallini, F., Ceppatelli, G., Righini, A., & Sambuco, A. M. 1985, A&A, 149, 357

Carleo, I., Benatti, S., Lanza, A. F., et al. 2018, A&A, 613, A50

Carleo, I., Sanna, N., Gratton, R., et al. 2016, Experimental Astronomy, 41, 351

Casasayas-Barris, N., Palle, E., Yan, F., et al. 2018, ArXiv e-prints [e-print[arXiv]1805.03102]

Charbonneau, D., Berta, Z. K., Irwin, J., et al. 2009, Nature, 462, 891

Chatterjee, S., Ford, E. B., Matsumura, S., & Rasio, F. A. 2008, ApJ, 686, 580

Chaturvedi, P., Chakraborty, A., Anandarao, B. G., Roy, A., & Mahadevan, S. 2016, MNRAS, 462, 554

Chincarini, G., Zerbi, F., Antonelli, A., et al. 2003, The Messenger, 113, 40

Cincunegui, C., Díaz, R. F., & Mauas, P. J. D. 2007, A&A, 469, 309

Claret, A., Hauschildt, P. H., & Witte, S. 2012, A&A, 546, A14

Claudi, R., Benatti, S., Carleo, I., et al. 2017, European Physical Journal Plus, 132, 364

Claudi, R., Benatti, S., Carleo, I., et al. 2016, in Proc. SPIE, Vol. 9908, Ground-based and Airborne Instrumentation for Astronomy VI, 99081A

Conod, U., Blind, N., Wildi, F., & Pepe, F. 2016, in Proc. SPIE, Vol. 9909, Adaptive Optics Systems V, 990941

Cosentino, R., Lovis, C., Pepe, F., et al. 2012, in Proc. SPIE, Vol. 8446, Ground-based and Airborne Instrumentation for Astronomy IV, 84461V

Covino, E., Esposito, M., Barbieri, M., et al. 2013, A&A, 554, A28

Crifo, F., Jasniewicz, G., Soubiran, C., et al. 2010, A&A, 524, A10

Crockett, C. J., Mahmud, N. I., Prato, L., et al. 2012, ApJ, 761, 164

Croll, B., Albert, L., Lafreniere, D., Jayawardhana, R., & Fortney, J. J. 2010, ApJ, 717, 1084

Cumming, A., Butler, R. P., Marcy, G. W., et al. 2008, PASP, 120, 531

Cumming, A., Marcy, G. W., & Butler, R. P. 1999, ApJ, 526, 890

Cunha, D., Santos, N. C., Figueira, P., et al. 2014, A&A, 568, A35

Cutri, R. M., Skrutskie, M. F., van Dyk, S., et al. 2003, VizieR Online Data Catalog, 2246

Damasso, M., Bonomo, A. S., Astudillo-Defru, N., et al. 2018, ArXiv e-prints [e-print[arXiv]1802.08320]

D'Angelo, G., Durisen, R. H., & Lissauer, J. J. 2010, Giant Planet Formation (Seager, S.), 319–346

David, T. J., Mamajek, E. E., Vanderburg, A., et al. 2018, ArXiv e-prints [e-print[arXiv]1801.07320]

Dawson, R. I. & Johnson, J. A. 2018, ArXiv e-prints [e-print[arXiv]1801.06117]

de Kok, R. J., Brogi, M., Snellen, I. A. G., et al. 2013, A&A, 554, A82

de Mooij, E. J. W. & Snellen, I. A. G. 2009, A&A, 493, L35

Deeg, H. 1998, in Astronomical Society of the Pacific Conference Series, Vol. 134, Brown Dwarfs and Extrasolar Planets, ed. R. Rebolo, E. L. Martin, & M. R. Zapatero Osorio, 216–+

Del Moro, D., Berrilli, F., Duvall, Jr., T. L., & Kosovichev, A. G. 2004, Sol. Phys., 221, 23

Delorme, P., Collier Cameron, A., Hebb, L., et al. 2011, MNRAS, 413, 2218

Desidera, S., Carolo, E., Gratton, R., et al. 2011, A&A, 533, A90

Desidera, S., Gratton, R., Claudi, R., et al. 2006, in Tenth Anniversary of 51 Peg-b: Status of and prospects for hot Jupiter studies, ed. L. Arnold, F. Bouchy, & C. Moutou, 119–126

Desort, M., Lagrange, A.-M., Galland, F., Udry, S., & Mayor, M. 2007, A&A, 473, 983

Dittmann, J. A., Irwin, J. M., Charbonneau, D., et al. 2017, Nature, 544, 333

Donati, J.-F., Hébrard, E., Hussain, G. A. J., et al. 2015, MNRAS, 453, 3706

Donati, J. F., Moutou, C., Malo, L., et al. 2016, Nature, 534, 662

Donati, J.-F., Yu, L., Moutou, C., et al. 2017, MNRAS, 465, 3343

Dressing, C. D. & Charbonneau, D. 2013, ApJ, 767, 95

Dressing, C. D. & Charbonneau, D. 2015, ApJ, 807, 45

Duffell, P. C., Haiman, Z., MacFadyen, A. I., D'Orazio, D. J., & Farris, B. D. 2014, ApJ, 792, L10

Dumusque, X., Boisse, I., & Santos, N. C. 2014, ApJ, 796, 132

Dumusque, X., Borsa, F., Damasso, M., et al. 2017, A&A, 598, A133

Dumusque, X., Santos, N. C., Udry, S., Lovis, C., & Bonfils, X. 2011, in IAU Symposium, Vol. 276, The Astrophysics of Planetary Systems: Formation, Structure, and Dynamical Evolution, ed. A. Sozzetti, M. G. Lattanzi, & A. P. Boss, 527–529

Dürmann, C. & Kley, W. 2015, A&A, 574, A52

Endl, M., Kürster, M., & Els, S. 2000, A&A, 362, 585

Esposito, M., Covino, E., Mancini, L., et al. 2014, A&A, 564, L13

Evans, T. M., Aigrain, S., Gibson, N., et al. 2015, MNRAS, 451, 680

Evans, T. M., Sing, D. K., Wakeford, H. R., et al. 2016, ApJ, 822, L4

Fedele, D., van den Ancker, M. E., Henning, T., Jayawardhana, R., & Oliveira, J. M. 2010, A&A, 510, A72

Fűrész, G., Szentgyorgyi, A. H., & Meibom, S. 2008, in Precision Spectroscopy in Astrophysics, ed. N. C. Santos, L. Pasquini, A. C. M. Correia, & M. Romaniello, 287–290

Figueira, P., Adibekyan, V. Z., Oshagh, M., et al. 2016, A&A, 586, A101

Figueira, P., Kerber, F., Chacon, A., et al. 2012, MNRAS, 420, 2874

Figueira, P., Marmier, M., Bonfils, X., et al. 2010a, A&A, 513, L8

Figueira, P., Pepe, F., Lovis, C., & Mayor, M. 2010b, A&A, 515, A106

Figueira, P., Santos, N. C., Pepe, F., Lovis, C., & Nardetto, N. 2013, A&A, 557, A93

Fischer, D. A., Anglada-Escude, G., Arriagada, P., et al. 2016, PASP, 128, 066001

Fortney, J. J., Lodders, K., Marley, M. S., & Freedman, R. S. 2008, ApJ, 678, 1419

Gagné, J., Plavchan, P., Gao, P., et al. 2016, ApJ, 822, 40

Giacobbe, P., Damasso, M., Sozzetti, A., et al. 2012, in European Planetary Science Congress 2012, EPSC2012–755

Gillon, M., Jehin, E., Lederer, S. M., et al. 2016, Nature, 533, 221

Gillon, M., Triaud, A. H. M. J., Demory, B.-O., et al. 2017, Nature, 542, 456

Goldberg, L. & Müller, E. A. 1953, ApJ, 118, 397

Goldreich, P. & Tremaine, S. 1980, ApJ, 241, 425

Gomes da Silva, J., Santos, N. C., Boisse, I., Dumusque, X., & Lovis, C. 2014, A&A, 566, A66

Gomes da Silva, J., Santos, N. C., Bonfils, X., et al. 2011, A&A, 534, A30

Gomes da Silva, J., Santos, N. C., Bonfils, X., et al. 2012, A&A, 541, A9

González-Álvarez, E., Affer, L., Micela, G., et al. 2017, A&A, 606, A51

Gratton, R. G., Bonanno, G., Bruno, P., et al. 2001, Experimental Astronomy, 12, 107

Gray, D. F. 1999, in Astronomical Society of the Pacific Conference Series, Vol. 185, IAU Colloq. 170: Precise Stellar Radial Velocities, ed. J. B. Hearnshaw & C. D. Scarfe, 243

Griffin, R. & Griffin, R. 1973, MNRAS, 162, 255

Gully-Santiago, M. A., Herczeg, G. J., Czekala, I., et al. 2017, ApJ, 836, 200

Hanson, M. M., Conti, P. S., & Rieke, M. J. 1996, ApJS, 107, 281

Harutyunyan, A., Rainer, M., Hernandez, N., et al. 2018, in Ground-based and Airborne Instrumentation for Astronomy VII, Proc. SPIE, TBD

Haswell, C. A. 2010, *Transiting exoplanets* (The Open University)

Hatzes, A. P., Cochran, W. D., & Johns-Krull, C. M. 1997, ApJ, 478, 374

Hatzes, A. P., Endl, M., Cochran, W. D., et al. 2018, AJ, 155, 120

Hawley, S. L. & Pettersen, B. R. 1991, ApJ, 378, 725

Haywood, R. D., Collier Cameron, A., Queloz, D., et al. 2014, MNRAS, 443, 2517

Hermes, J. J. 2017, Timing by Stellar Pulsations as an Exoplanet Discovery Method (Springer Living Reference Work), 6

Hernán-Obispo, M., Gálvez-Ortiz, M. C., Anglada-Escudé, G., et al. 2010, A&A, 512, A45

Hernán-Obispo, M., Tuomi, M., Gálvez-Ortiz, M. C., et al. 2015, A&A, 576, A66

Herrero, E., Ribas, I., Jordi, C., et al. 2016, A&A, 586, A131

Huélamo, N., Figueira, P., Bonfils, X., et al. 2008, A&A, 489, L9

Hunt-Walker, N. M., Hilton, E. J., Kowalski, A. F., Hawley, S. L., & Matthews, J. M. 2012, Publications of the Astronomical Society of the Pacific, 124, 545

Hunter, A. A., Macgregor, A. B., Szabo, T. O., Wellington, C. A., & Bellgard, M. I. 2012, Source Code for Biology and Medicine, 7, 1

Ida, S. & Lin, D. N. C. 2008, ApJ, 673, 487

Isaacson, H. & Fischer, D. 2010, ApJ, 725, 875

Israelian, G., Delgado Mena, E., Santos, N. C., et al. 2009, Nature, 462, 189

Jeffries, R. D. 1995, MNRAS, 273, 559

Johns-Krull, C. M., McLane, J. N., Prato, L., et al. 2016, ApJ, 826, 206

Johnson, J. A., Aller, K. M., Howard, A. W., & Crepp, J. R. 2010, PASP, 122, 905

Jurić, M. & Tremaine, S. 2008, ApJ, 686, 603

Kaeufl, H.-U., Ballester, P., Biereichel, P., et al. 2004, in Proc. SPIE, Vol. 5492, Ground-based Instrumentation for Astronomy, ed. A. F. M. Moorwood & M. Iye, 1218–1227

Koen, C. 2016, MNRAS, 463, 4383

Kopparapu, R. K. 2013, ApJ, 767, L8

Kozai, Y. 1962, AJ, 67, 591

Kreidberg, L., Bean, J. L., Désert, J.-M., et al. 2014, ApJ, 793, L27

Lagrange, A.-M., Boccaletti, A., Milli, J., et al. 2012, A&A, 542, A40

Lagrange, A.-M., Desort, M., Galland, F., Udry, S., & Mayor, M. 2009, A&A, 495, 335

Lagrange, A.-M., Desort, M., & Meunier, N. 2010, A&A, 512, A38

Lagrange, A.-M., Meunier, N., Chauvin, G., et al. 2013, A&A, 559, A83

Lamm, M. H., Bailer-Jones, C. A. L., Mundt, R., Herbst, W., & Scholz, A. 2004, A&A, 417, 557

Landolt, A. U. 1992, AJ, 104, 340

Lanza, A. F. 2010, A&A, 512, A77

Lanza, A. F. 2016, in Lecture Notes in Physics, Berlin Springer Verlag, Vol. 914, Lecture Notes in Physics, Berlin Springer Verlag, ed. J.-P. Rozelot & C. Neiner, 43

Lanza, A. F., Boisse, I., Bouchy, F., Bonomo, A. S., & Moutou, C. 2011, A&A, 533, A44

Lanza, A. F., Malavolta, L., Benatti, S., et al. 2018, ArXiv e-prints [e-print[arXiv]1804.07039]

Lavail, A., Kochukhov, O., & Wade, G. A. 2018, MNRAS, 479, 4836

Lee, E. J. & Chiang, E. 2016, ApJ, 817, 90

Lee, E. J. & Chiang, E. 2017, ApJ, 842, 40

Lee, E. J., Chiang, E., & Ormel, C. W. 2014, ApJ, 797, 95

Lin, D. N. C. & Papaloizou, J. 1986, ApJ, 309, 846

López-Santiago, J. 2005, PhD thesis, Universidad Complutense de Madrid, Spain

Lovis, C., Dumusque, X., Santos, N. C., et al. 2011, ArXiv e-prints [e-print[arXiv]1107.5325]

Lovis, C., Mayor, M., Pepe, F., et al. 2006, Nature, 441, 305

Mace, G., Kim, H., Jaffe, D. T., et al. 2016, in Proc. SPIE, Vol. 9908, Ground-based and Airborne Instrumentation for Astronomy VI, 99080C

Mahmud, N. I., Crockett, C. J., Johns-Krull, C. M., et al. 2011, ApJ, 736, 123

Maiolino, R., Rieke, G. H., & Rieke, M. J. 1996, AJ, 111, 537

Makarov, V. V., Beichman, C. A., Catanzarite, J. H., et al. 2009, ApJ, 707, L73

Malavolta, L., Nascimbeni, V., Piotto, G., et al. 2016, A&A, 588, A118

Mandell, A. M., Drake Deming, L., Blake, G. A., et al. 2011, ApJ, 728, 18

Martínez-Arnáiz, R., Maldonado, J., Montes, D., Eiroa, C., & Montesinos, B. 2010, A&A, 520, A79

Mayor, M., Bonfils, X., Forveille, T., et al. 2009, A&A, 507, 487

Mayor, M., Pepe, F., Queloz, D., et al. 2003, The Messenger, 114, 20

Mayor, M. & Queloz, D. 1995, Nature, 378, 355

McLaughlin, D. B. 1924, ApJ, 60

Meunier, N. & Delfosse, X. 2009, A&A, 501, 1103

Meunier, N., Lagrange, A.-M., & De Bondt, K. 2012, A&A, 545, A87

Mohler, O. C., Pierce, A. K., McMath, R. R., & Goldberg, L. 1953, ApJ, 117, 41

Morin, J., Donati, J.-F., Petit, P., et al. 2008, MNRAS, 390, 567

Mullally, F. 2009, Journal of Physics Conference Series, 172, 012056

Nardetto, N., Mourard, D., Kervella, P., et al. 2006, A&A, 453, 309

Noyes, R. W., Hartmann, L. W., Baliunas, S. L., Duncan, D. K., & Vaughan, A. H. 1984, ApJ, 279, 763

Nugroho, S. K., Kawahara, H., Masuda, K., et al. 2017, AJ, 154, 221

Oke, J. B. 1990, AJ, 99, 1621

Oliva, E., Origlia, L., Baffa, C., et al. 2006, in Proc. SPIE, Vol. 6269, Society of Photo-Optical Instrumentation Engineers (SPIE) Conference Series, 626919

Origlia, L., Oliva, E., Baffa, C., et al. 2014, in Proc. SPIE, Vol. 9147, Ground-based and Airborne Instrumentation for Astronomy V, 91471E

Pallé, E., Zapatero Osorio, M. R., Barrena, R., Montañés-Rodríguez, P., & Martín, E. L. 2009, Nature, 459, 814

Park, C., Jaffe, D. T., Yuk, I.-S., et al. 2014, in Proc. SPIE, Vol. 9147, Ground-based and Airborne Instrumentation for Astronomy V, 91471D

Pepe, F., Mayor, M., Galland, F., et al. 2002, A&A, 388, 632

Pepe, F., Mayor, M., Queloz, D., et al. 2004, A&A, 423, 385

Pepe, F. A., Cristiani, S., Rebolo Lopez, R., et al. 2010, in Proc. SPIE, Vol. 7735, Ground-based and Airborne Instrumentation for Astronomy III, 77350F

Perri, F. & Cameron, A. G. W. 1974, Icarus, 22, 416

Perryman, M., Hainaut, O., Dravins, D., et al. 2005, ArXiv Astrophysics e-prints [e-printarXiv:astro-ph/0506163]

Pettersen, B. R. & Coleman, L. A. 1981, ApJ, 251, 571

Plavchan, P., Latham, D., Gaudi, S., et al. 2015, ArXiv e-prints [e-print[arXiv]1503.01770]

Prato, L., Huerta, M., Johns-Krull, C. M., et al. 2008, ApJ, 687, L103

Queloz, D. 1995, in IAU Symposium, Vol. 167, New Developments in Array Technology and Applications, ed. A. G. D. Philip, K. Janes, & A. R. Upgren, 221

Queloz, D., Henry, G. W., Sivan, J. P., et al. 2001, A&A, 379, 279

Quinn, S. N., White, R. J., Latham, D. W., et al. 2014, ApJ, 787, 27

Quirrenbach, A., Amado, P. J., Caballero, J. A., et al. 2014, in Proc. SPIE, Vol. 9147, Ground-based and Airborne Instrumentation for Astronomy V, 91471F

Radick, R. R., Lockwood, G. W., Henry, G. W., Hall, J. C., & Pevtsov, A. A. 2018, ApJ, 855, 75

Rafikov, R. R. 2005, ApJ, 621, L69

Rafikov, R. R. 2006, ApJ, 648, 666

Rainer, M., Harutyunyan, A., Carleo, I., et al. 2018, in Ground-based and Airborne Instrumentation for Astronomy VII, Proc. SPIE, TBD

Rasmussen, C. E. & Williams, C. K. I. 2006, Gaussian Processes for Machine Learning (MIT Press)

Redfield, S., Endl, M., Cochran, W. D., & Koesterke, L. 2008, ApJ, 673, L87

Reiners, A. 2007, A&A, 467, 259

Reiners, A., Bean, J. L., Huber, K. F., et al. 2010, ApJ, 710, 432

Reiners, A., Ribas, I., Zechmeister, M., et al. 2018, A&A, 609, L5

Reiners, A., Shulyak, D., Anglada-Escudé, G., et al. 2013, A&A, 552, A103

Rice, J. B., Strassmeier, K. G., & Kopf, M. 2011, ApJ, 728, 69

Rizzuto, A. C., Mann, A. W., Vanderburg, A., Kraus, A. L., & Covey, K. R. 2017, AJ, 154, 224

Robert, C. M. T., Crida, A., Lega, E., Méheut, H., & Morbidelli, A. 2018, ArXiv e-prints [e-print[arXiv]1808.00381]

Roberts, D. H., Lehar, J., & Dreher, J. W. 1987, AJ, 93, 968

Robertson, P., Bender, C., Mahadevan, S., Roy, A., & Ramsey, L. W. 2016, ApJ, 832, 112

Robertson, P., Endl, M., Cochran, W. D., & Dodson-Robinson, S. E. 2013, ApJ, 764, 3

Robinson, R. D., Cram, L. E., & Giampapa, M. S. 1990, ApJS, 74, 891

Roettenbacher, R. M. & Kane, S. R. 2017, ApJ, 851, 77

Rogers, T. M., Lin, D. N. C., & Lau, H. H. B. 2012, ApJ, 758, L6

Rossiter, R. A. 1924, ApJ, 60

Rothman, L. S., Rinsland, C. P., Goldman, A., et al. 1998, J. Quant. Spectrosc. Radiative Transfer, 60, 665

Rudolf, N., Günther, H. M., Schneider, P. C., & Schmitt, J. H. M. M. 2016, A&A, 585, A113

Saar, S. H. & Donahue, R. A. 1997, ApJ, 485, 319

Sameshima, H., Matsunaga, N., Kobayashi, N., et al. 2018, PASP, 130, 074502

Santos, N. C., Gomes da Silva, J., Lovis, C., & Melo, C. 2010, A&A, 511, A54

Schlichting, H. E. 2014, ApJ, 795, L15

Schrijver, C. J. & Zwaan, C. 2000, Solar and Stellar Magnetic Activity (Cambridge University Press)

Sedaghati, E., Boffin, H. M. J., MacDonald, R. J., et al. 2017, Nature, 549, 238

Seemann U. et al. . 2018, in Ground-based and Airborne Instrumentation for Astronomy VI, Proc. SPIE, 10706

Seifahrt, A. & Käufl, H. U. 2008, A&A, 491, 929

Seifahrt, A., Käufl, H. U., Zängl, G., et al. 2010, A&A, 524, A11

Setiawan, J., Henning, T., Launhardt, R., et al. 2008, Nature, 451, 38

Shara, M. M., Hurley, J. R., & Mardling, R. A. 2016, ApJ, 816, 59

Shkolnik, E., Liu, M. C., & Reid, I. N. 2009, ApJ, 699, 649

Sing, D. K., Désert, J.-M., Lecavelier Des Etangs, A., et al. 2009, A&A, 505, 891

Sing, D. K. & López-Morales, M. 2009, A&A, 493, L31

Sissa, E., Gratton, R., Desidera, S., et al. 2016, A&A, 596, A76

Sithajan, S., Ge, J., & Wang, J. 2016, in American Astronomical Society Meeting Abstracts, Vol. 227, American Astronomical Society Meeting Abstracts #227, 137.19

Skowron, J., Shin, I.-G., Udalski, A., et al. 2015, ApJ, 804, 33

Smette, A., Sana, H., Noll, S., et al. 2015, A&A, 576, A77

Snellen, I. A. G., Albrecht, S., de Mooij, E. J. W., & Le Poole, R. S. 2008, A&A, 487, 357

Sosnowska, D., Lodi, M., Gao, X., et al. 2012, in Proc. SPIE, Vol. 8451, Software and Cyberinfrastructure for Astronomy II, 84511X

Spalding, C. & Batygin, K. 2015, ApJ, 811, 82

Stevenson, K. B., Bean, J. L., Seifahrt, A., et al. 2014, AJ, 147, 161

Stober, G., Sommer, S., Schult, C., Chau, J. L., & Latteck, R. 2013, AGU Fall Meeting Abstracts, SA51B

Strassmeier, K., Washuettl, A., Granzer, T., Scheck, M., & Weber, M. 2000, A&AS, 142, 275

Strassmeier, K. G., Fekel, F. C., Bopp, B. W., Dempsey, R. C., & Henry, G. W. 1990, ApJS, 72, 191

Suárez Mascareño, A., Rebolo, R., González Hernández, J. I., & Esposito, M. 2015, MNRAS, 452, 2745

Swain, M. R., Tinetti, G., Vasisht, G., et al. 2009, ApJ, 704, 1616

Swain, M. R., Vasisht, G., & Tinetti, G. 2008, Nature, 452, 329

Tinetti, G., Deroo, P., Swain, M. R., et al. 2010, ApJ, 712, L139

Title, A. M., Tarbell, T. D., Topka, K. P., et al. 1989, ApJ, 336, 475

Toomre, A. 1964, ApJ, 139, 1217

Torres, C. A. O., Quast, G. R., Melo, C. H. F., & Sterzik, M. F. 2008, Young Nearby Loose Associations (Reipurth, B.), 757

Tozzi, A., Oliva, E., Iuzzolino, M., et al. 2016, in Proc. SPIE, Vol. 9908, Ground-based and Airborne Instrumentation for Astronomy VI, 99086C

Tozzi, A., Oliva, E., Origlia, L., et al. 2014, in Proc. SPIE, Vol. 9147, Ground-based and Airborne Instrumentation for Astronomy V, 91479N

Tuomi, M., Jones, H. R. A., Barnes, J. R., et al. 2018, AJ, 155, 192

Vacca, W. D., Cushing, M. C., & Rayner, J. T. 2003, PASP, 115, 389

Vogt, S. S., Allen, S. L., Bigelow, B. C., et al. 1994, in Proc. SPIE, Vol. 2198, Instrumentation in Astronomy VIII, ed. D. L. Crawford & E. R. Craine, 362

Wheatley, P. J., Louden, T., Bourrier, V., Ehrenreich, D., & Gillon, M. 2017, MNRAS, 465, L74

White, R. J., Gabor, J. M., & Hillenbrand, L. A. 2007, AJ, 133, 2524

Winn, J. N., Fabrycky, D., Albrecht, S., & Johnson, J. A. 2010, ApJ, 718, L145

Wolszczan, A. & Frail, D. A. 1992, Nature, 355, 145

Wu, Y. & Murray, N. 2003, The Astrophysical Journal, 589, 605

Yang, J., Boué, G., Fabrycky, D. C., & Abbot, D. S. 2014, ApJ, 787, L2

Yu, L., Donati, J.-F., Hébrard, E. M., et al. 2017, MNRAS, 467, 1342

Yuk, I.-S., Jaffe, D. T., Barnes, S., et al. 2010, in Proc. SPIE, Vol. 7735, Ground-based and Airborne Instrumentation for Astronomy III, 77351M

Zechmeister, M. & Kürster, M. 2009, A&A, 496, 577